Dynamics, Stability and Scaling of Turbulent Methane Oxy-Combustion

by

Nadim Walid Chakroun

B.S., Mechanical Engineering,
Purdue University (2012)
S.M., Mechanical Engineering,
Massachusetts Institute of Technology (2014)

Submitted to the Department of Mechanical Engineering
in partial fulfillment of the requirements for the degree of

Doctor of Philosophy in Mechanical Engineering

at the

MASSACHUSETTS INSTITUTE OF TECHNOLOGY

February 2018

Signature redacted

Author .....
Department of Mechanical Engineering
January 12, 2018

Signature redacted

Certified by .....
Ahmed F. Ghoniem
Ronald C. Crane Professor, Department of Mechanical Engineering
Thesis Supervisor

Signature redacted

Accepted by .....
Rohan Abeyaratne
Chairman, Department Committee on Graduate Students

Dynamics, Stability and Scaling of Turbulent Methane Oxy-Combustion

by

Nadim Walid Chakroun

Submitted to the Department of Mechanical Engineering
on January 12, 2018, in partial fulfillment of the
requirements for the degree of
Doctor of Philosophy in Mechanical Engineering

Abstract

Carbon capture and storage (CCS) is an important strategy for reducing CO_2 emissions, with oxy-fuel combustion being one of the most promising technologies because of it is high efficiency and low cost. In oxy-combustion, $CH_4/O_2/CO_2$ mixtures burn at low temperatures ($\approx$1700 K), high pressures ($\approx$40 bar), where laminar burning velocities are about 7 times lower than in traditional CH_4/Air mixtures. Thus oxy-fuel combustors are more prone to blowoff and dynamic instabilities. In this thesis we examine turbulent oxy-combustion flame stabilization physics at the large and small scales using experimental studies and numerical simulations.

Experimental measurements are used to establish the stability characteristics of flame macrostructures in a swirl stabilized combustor. We show that the transition in the flame macrostructure to a flame stabilized along both the inner and outer shear layers (Flame IV), scales according to the extinction strain rate, similar to air flames. To achieve accurate scaling, extinction strain rates must be computed at the thermal conditions of the outer shear layer, emphasizing the role of heat interactions with the wall boundary layer. Care must be exercised while modeling the chemical structure of oxy-flames. We show that the kinetics of CO_2 (used as a diluent in oxy-combustion) is important in determining the consumption speed and flame extinction strain rate. Specifically, the extinction strain rate was found to be heavily impacted by the reaction $CO_2 + H \rightleftarrows CO + OH$.

Large Eddy Simulations (LES) models, first validated for various combustor geometries, fuels and oxidizers, are used to examine the stabilization mechanisms of these flames. First, we demonstrate the importance of choosing the correct global chemical kinetics mechanism in predicting the flow structures in multi-dimensional simulations and develop a priori criterion of selecting a reduced mechanism based on the extinction strain rate. Besides flame macrostructures, recirculation zone lengths are found to linearly scale with extinction strain rates. This scaling holds regardless of fuel or oxidizer type, Reynold's number, inlet temperature, or combustor geometry. It is thus very important that a chemical mechanism is able to correctly predict extinction strain rates if it is to be used in CFD simulations. We use the validated LES

framework to model the transition to Flame IV in the swirl combustor for methane oxy-combustion mixtures. The 3D turbulent flame structure strongly resembles a 1D strained adiabatic laminar flame structure in the combustor interior, and non-adiabatic flames near the combustor wall. The results support the earlier conclusions regarding the use of the extinction strain rate and the wall thermal boundary condition in scaling and modeling turbulent combustion dynamics.

Thesis Supervisor: Ahmed F. Ghoniem
Title: Ronald C. Crane Professor, Department of Mechanical Engineering

This thesis is dedicated to my late grandmother

Acknowledgments

I begin by thanking Prof. Ghoniem, my thesis supervisor, for all of his support and guidance during the two years of my Masters work and the three and a half years of my PhD. On top of being a great advisor, he is also a mentor and a friend.

I am also grateful to Santosh Shanbhogue, Soufien Taamallah, Dan Michaels, Gaurav Kewlani, Yuval Dagan, Georgios Dimitrakopoulos, XiaoYu Wu and Akhilesh Bakshi for all their valuable support and helpful discussions which helped improve the quality of the work in this thesis.

I also would like to thank my PhD committee members: Prof. Green, Prof. Lermusiaux and Prof. Marzouk for their graciousness and feedback during our meetings.

I have had the pleasure of working alongside very distinguished colleagues and lab-mates in the Reacting Gas Dynamics group over the past five and a half years which also made for a friendly and rewarding atmosphere.

A big thanks to the sponsors and funders of this work, KFUPM and KAUST.

This thesis was mostly written at the Jaho and Explorateur cafes in Downtown Boston and it was also a delight meeting and interacting with so many different people there.

Outside work, I am lucky to have a lot of caring and fun friends which made my time in Boston very enjoyable and I cherish all the experiences we had together. I am definitely going to miss all the parties and clubs we went to, all the trips to NYC and DC, "studying" at coffee shops together, playing tennis, soccer and basketball, and exploring the city, just to name a few. They were also essentially my family away from home.

Most importantly I could not have been able to accomplish this incredible feat without the love and support of my family. It has definitely been tough being away from home for over 9 years during this long academic journey. But their unwavering support and encouragement helped me through it. To my parents, Walid and May, my brother, Rami, and sister Leah, this thesis is for all of you as well. We are incredibly grateful to have such loving and inspiring parents who never stop reminding us that

we have no limits and no reason why we could not study at the top universities in the world. My life accomplishments will never be complete until I see my brother and sister also reach the pinnacle of their fields. This thesis is also dedicated to my late grandmother who passed away just a few months before I was able to finish. She always used to keep asking how long I had left so I could move back home and see her more often. I am disheartened that she won't be around to witness her vision finally become a reality, but I know that she is currently looking down from heaven very proud and bragging about me to everyone just as she did while she was here.

A final thanks to God for giving me the strength and peace of mind that I can always rely on.

"Education is the most powerful weapon which you can use to change the world."
-Nelson Mandela

Contents

List of Figures

List of Tables

Chapter 1

Introduction

Greenhouse gas (GHG) emissions are the leading contributers to climate change. Combustion of fossil fuels results in the formation of significant amounts of carbon dioxide (CO_2), the primary GHG released into the atmosphere. At the global scale, CO_2 emissions accounted for approximately 65% of all GHG emissions in 2014 [24]. According to the Environmental Protection Agency (EPA), about 26% of all global GHG emissions were produced by the electricity generation sector. It is also estimated that the world CO_2 emissions from electricity production will increase by approximately 43% by 2035, from 30.2 billion metric tons in 2008 to 43.2 billion metric tons [25]. Much of this growth in emissions is attributed to the developing non-OECD countries which continue to rely on fossil fuels to meet their growing energy demand. By 2040 these non-OECD countries are expected to contribute as much as 69% of the world's total emissions, whereas the OECD emissions, totaling about 14 billion metric tons, represent the balance [25].

The agreement reached in Paris in late 2015 at the 21st Conference of the Parties (COP21) was a pivotal moment in the fight against global warming and decarbonizing our energy systems. Its main aims were to peak global emissions as soon as possible and reach net-zero emissions in the second half of this century, as well as to keep the global temperature rise well below 2°C while pursuing efforts to limit it to 1.5°C. The International Energy Agency (IEA) developed different policy scenarios to model this shift towards reducing emissions from the energy sector. Two of these scenarios are

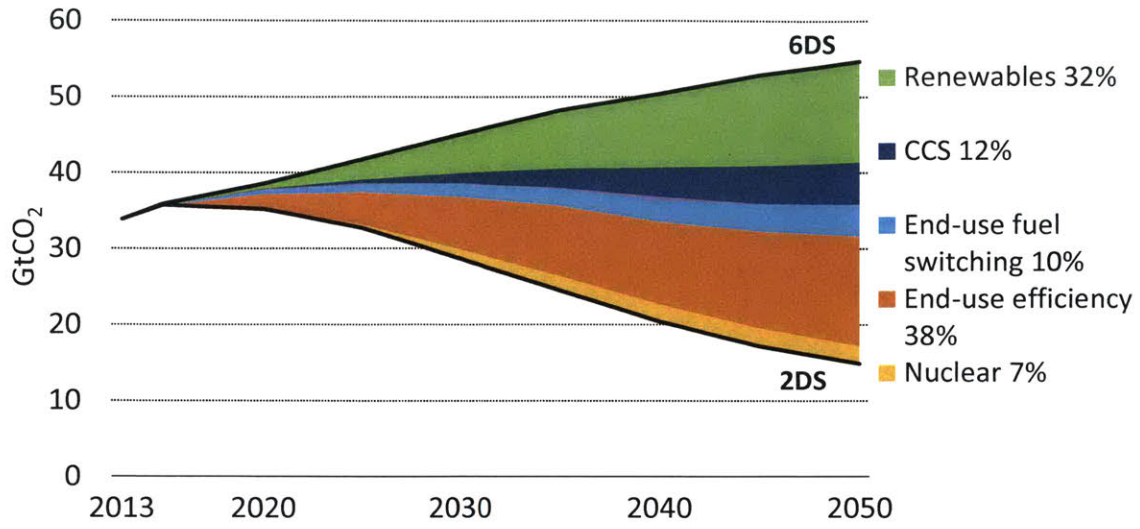

Figure 1-1: Global energy related CO_2 reductions by technology area (data from [1])

shown in Figure 1-1 along with strategies to achieve these emissions reductions. One of these scenarios is a business-as-usual case and is referred to as 6DS. This largely assumes an extension of current trends, and so primary energy demand and and process-related CO_2 emissions would grow by about 60% from 2013 to 2050. Since there is no effort to stabilize atmospheric concentrations of GHGs, average global temperature rise above pre-industrial levels would be projected to reach 4°C by the end of the century and 5.5°C in the long-term.

The most stringent scenario is the 2DS. As shown in the figure, the 2DS sets the target of cutting emissions by almost 60% by 2050 in order to limit the average global temperature increase to 2°C. It lays out an energy system deployment pathway and emissions trajectory consistent with these targets with carbon emissions from fuel combustion and industrial processes projected to decline after 2050 until carbon neutrality is reached. The 2DS identifies changes that help ensure a secure and affordable energy system in the long run.

A portfolio of low-carbon technologies is needed to reach the 2DS cost-effectively [1]. One of these promising technologies is Carbon Capture and Storage (CCS). In this technology, CO_2 released from power plants is separated, liquefied, compressed and transported to a site for underground injection in secure geological formations,

including natural underground reservoirs, or depleted oil and gas fields. The integration of these CCS technologies with the power generation plants has not yet been fully demonstrated commercially [27, 28]. Oxy-fuel combustion is one of the promising CCS options [29], the other ones being post-combustion CO_2 capture and pre-combustion CO_2 capture [30]. The main difference between these technologies is the location at which the CO_2 is removed in the cycle. In oxy-fuel combustion, the fuel is burned in oxygen diluted with CO_2 or water or a mixture of both, at stoichiometric conditions so that the products consist of only carbon dioxide and water. Water can then be easily separated from the carbon dioxide by condensation. A diluent is added to the fuel and oxidizer to moderate the temperatures of combustion and the resulting products. Due to the simplicity of the carbon capture system in oxy-fuel combustion, the CO_2 capture rate is very high ($\approx$98%) [30].

Oxy-combustion efforts in both research and implementation has often been associated with coal since coal power plants produce about two times as much CO_2 per MWh than natural gas power plants [31]. On the other hand, natural gas' share of the world's electricity generation is expected to grow from 22% in 2010 to 24% in 2040 [25] and applying the same concept to this fuel has been suggested. Estimated cost of electricity by source [32], suggest that natural gas power plants with CCS are competitive with other zero carbon energy sources.

Methane oxy-combustion cycles require combustors that can burn fuel and an oxygen stream along with some diluent, so that the CO_2 in the flue gases can easily be captured by condensing out the water. In order to control the flame temperature in these combustors, the oxidizer is diluted with either H_2O or CO_2 depending on the cycle layout. In the Semi-Closed Oxy-fuel Combustion Combined Cycles (SCOC-CC), CO_2 is used as the dilution medium [33, 34, 35, 36, 37]. Using CO_2 as the diluent is our main focus in this thesis since these types of cycles have the highest efficiency and lower costs [38]. The air separation unit (ASU) needed to produce the oxygen stream for the combustor consumes a significant fraction of the plant power and is a cost intensive process [38], therefore these oxy-fuel cycles typically operate at stoichiometric conditions (equivalence ratio = 1).

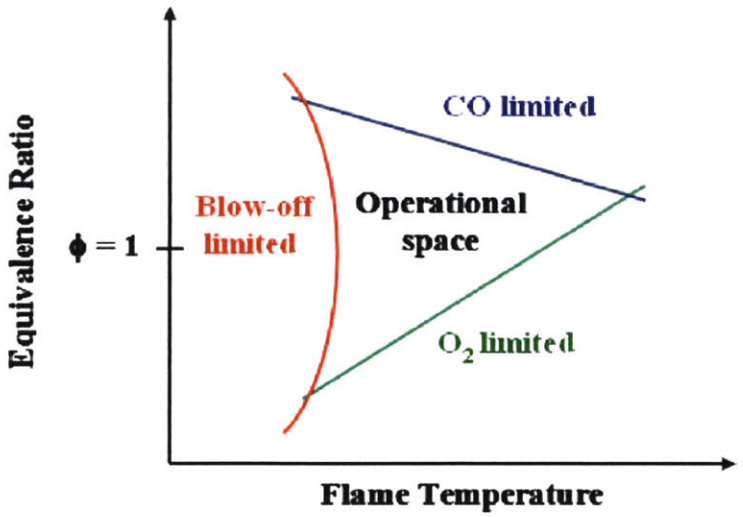

Figure 1-2: Operational space for oxy-combustion (adapted from [2])

Flame speed calculations have shown that the oxy-flame has a laminar burning velocity about 7 times lower than the air-equivalent mixture. The lower burning velocity of the oxy-flame negatively impacts the stability of these flames by increasing their propensity to blowoff and increasing flame length. Figure 1-2 shows the issues associated with oxy-combustion in the equivalence ratioflame temperature coordinates [2]. High flame temperatures and equivalence ratios result in excessive CO emissions. High flame temperatures and low equivalence ratios, meanwhile, are associated with high O_2 emissions. On the other hand, too low flame temperatures causes blowoff. Therefore there is a limited range of equivalence ratios and flame temperatures which minimizes the operational issues associated with oxy-combustion.

Premixed and non-premixed methane oxy-combustion were both examined experimentally in our swirl combustor [39]. However it was reported that the non-premixed case resulted in long flames with bright and sooty tips whereas the premixed case had a more compact flame. These observations of the non-premixed oxy-flame can also be seen in another recent study [40]. 1-D flame calculations have also shown that diffusion flames result higher CO and lower CO_2 in the products compared to premixed flames. These findings coupled with the fact that premixed flames generally have

more uniform outlet temperature profiles [41], have led us to focus solely on studying premixed oxy-combustion flames in this thesis.

1.1 Swirl Combustion Stability and Scaling

A number of important and critical issues face the operation and design of combustors, all of which are impacted by the fuel and oxidizer properties. These are: blowout, flashback, combustion instability, autoignition, emissions and flame compactness. A number of studies have looked at blowout both experimentally [39] and numerically [2] for methane oxy-combustion. Both agree that CO_2 diluted oxy-combustion flames blowoff at higher temperatures for a given Reynolds number than air combustion flames. This was explained by the fact that $CH_4/O_2/CO_2$ flames have slower kinetics making them easier to blowoff [42]. Premixed combustion, especially, is susceptible to combustion instabilities [43], which result from the acoustic coupling of heat release rate fluctuations that accompany unsteady flow oscillations (ex. vortex shedding) or equivalence ratio oscillations, causing extinction, flashback, excessive structural vibrations and even system damage and failure [44, 45].

These combustion instabilities in oxy-fuel combustors is not a well understood topic but it has been gaining interest in the literature recently [46, 47, 48]. In oxy-fuel cycles with CO_2 recycle, combustor inlet temperatures are on the order of 700 K while the outlet temperatures are set to 1600 K due to materials limitations [38]. In a study by Altay et al. [49], it was found that, in a backward-step combustor, thermoacoustic instabilities (associated with increase in pressure oscillations) shift to lower equivalence ratios (or lower adiabatic flame temperatures) as the inlet temperature is raised. Results of Shroll et al. show that the sound pressure levels in an oxy-fuel swirl combustor start to rise for mixtures whose adiabatic flame temperatures are around 1850 K at 300 K inlet temperature [46]. Therefore we expect that during the practical operation of high inlet temperature oxy-combustors, combustion instabilities will be a major issue.

We begin by reviewing the work that has been done on combustion instability

characterization in gas turbine combustors. Previously, in pour lab the onset of thermo-acoustic instabilities and their link to the mean flame configurations were investigated in a swirl combustor for an CH_4/H_2/Air mixture [3]. Four different flame configurations were observed: (I) columnar flame, (II) bubble-columnar flame, (III) single conical flame, and (IV) double conical flame. These configurations are shown in Figure 1-3 along with the sound pressure levels and frequencies. Transitions II to III, III to IV and IV to V (not shown) do show strong changes in the acoustic signature. When these results were compared to those of the uncoupled case of the short combustor, the same configurations as those observed in Figure 1-3 were still seen [3]. However in the transition from III to IV in the short combustor, unlike that of the long combustor, occurred without the onset of instability. But during this transition, the flame starts to appear intermittently in the outer recirculation zone (ORZ), also known as ORZ flame flickering. This observed flame flickering occurs in a same range of equivalence ratios at which the long combustor exhibits its first unstable mode, highlighting the importance of this flame transition. Modeling and understanding this flame transition for oxy-combustion is a main focal point of this thesis as will be shown in the forthcoming chapters.

In the multiple studies performed for various fuels (methane, hydrogen, syngas, propane) and oxidizers (air, oxy) looking at their stability in the swirl combustor [46, 50, 51], there was a noticeable similarity in the pressure level data as a function of equivalence ratio or flame temperature between all of these different operating conditions. This implied that some form of a universal scaling parameter might exist which would collapse this data regardless of fuel concentration. Indeed it was reported first by Speth et al. [50], then Altay et al. [49], then Hong et al. [5] and most recently by Shanbhogue et al. [51], that a strained consumption speed or extinction strain rate could collapse these pressure data for the multiple fuels and combustor geometries.

Shanbhogue et al. [51] conducted experiments with CH_4/H_2 mixtures on the swirl combustor using PIV and chemiluminescence measurements, and they successfully scaled the flame shape, flow structure and combustor stability according to the extinction strain rate. This scaling indicates that the flame response to stretch dominates

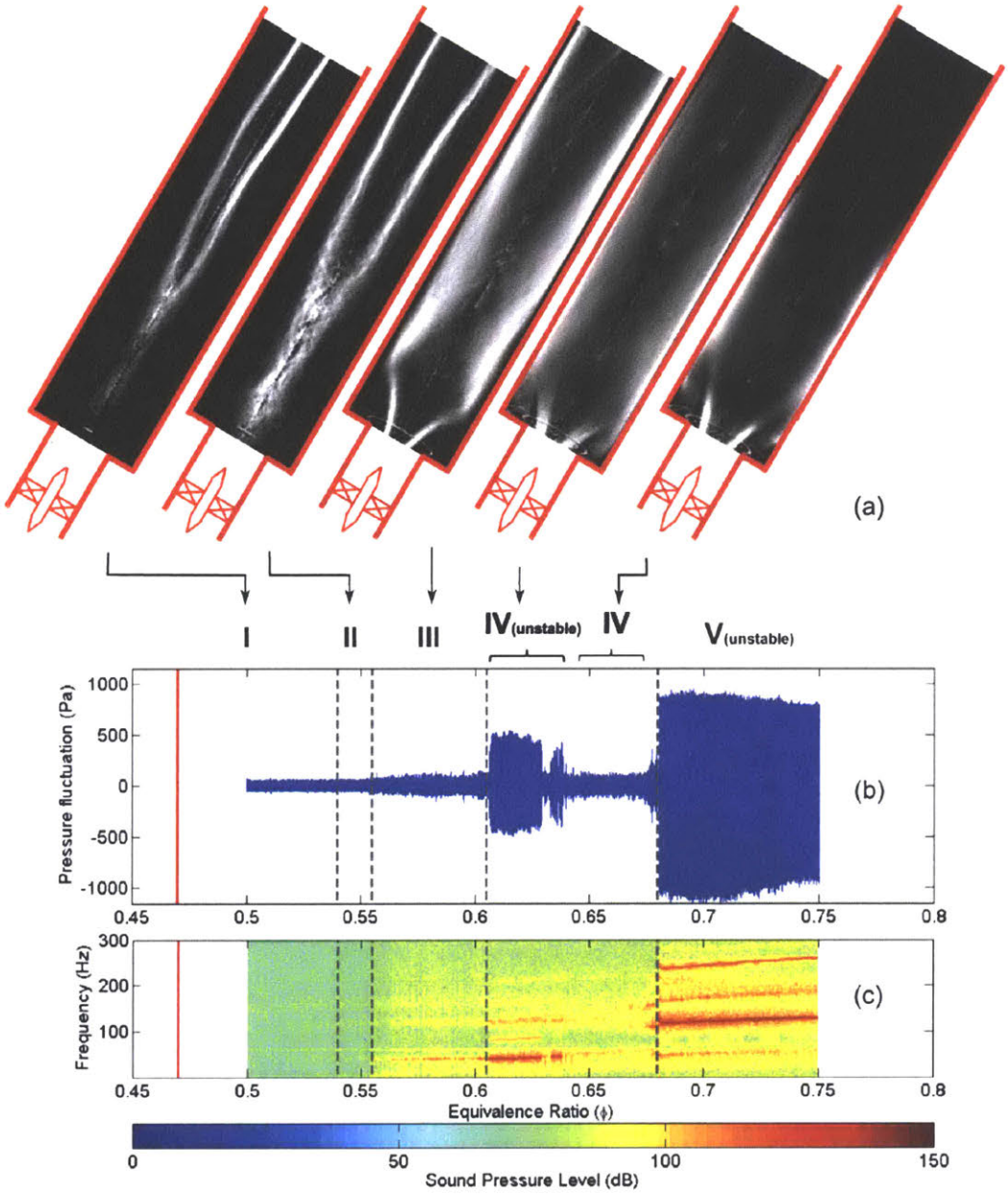

Figure 1-3: Correspondence between the flame macrostructures and thermo-acoustic modes in the long combustor for 100% CH_4. (a) Flame macrostructures (I to IV, V not shown). (b) Pressure fluctuations. (c) Spectrogram. [3]

the flame location as it can stabilize in regions with high strain rate. This observation was also seen in simulations by Michaels et al. [6] on a bluff body combustor as will be explained in the next section.

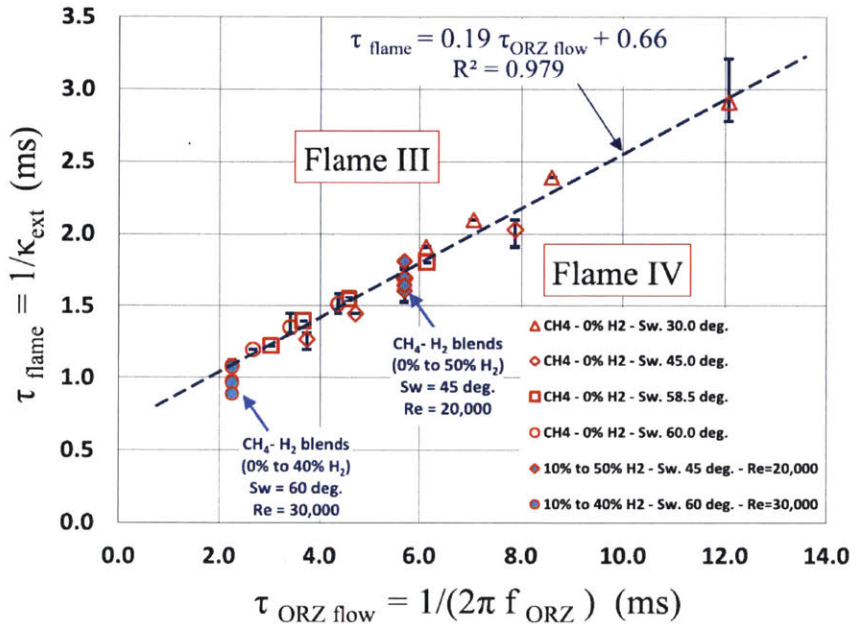

Figure 1-4: Characteristic ORZ flow time versus characteristic flame time for CH_4/Oxy, CH_4/Air and CH_4/H_2/Air flames. The flame times were all computed at 400 K, reflecting the actual conditions in the ORZ [4].

Taamallah et al. [4] also studied the physical mechanism leading to a flame transitioning to the ORZ in air combustion (Flame III to IV). For each operating condition, there was a critical ϕ_{onset} at which the flame appears in the ORZ and ultimately stabilizes along the OSL. They found that the appearance of the flame in the ORZ starts intermittently and is associated with a flame spinning along with the predominately azimuthal ORZ flow at a clearly defined frequency f_{ORZ}. The survival of a flame in the ORZ was represented as a balance between a characteristic flame time τ_{flame} (taken as the inverse of the extinction strain rate K_{ext}) and the ORZ flow time $\tau_{ORZ\ flow}$ (taken as the inverse of the ORZ spinning frequency f_{ORZ}), as can be seen in Figure 1-4.

1.2 Scaling in Other Geometries

Next, we show that the extinction strain rate scaling observed in the literature for the swirl combustor, is also seen in other geometries such as the backward-facing step and bluff body combustors.

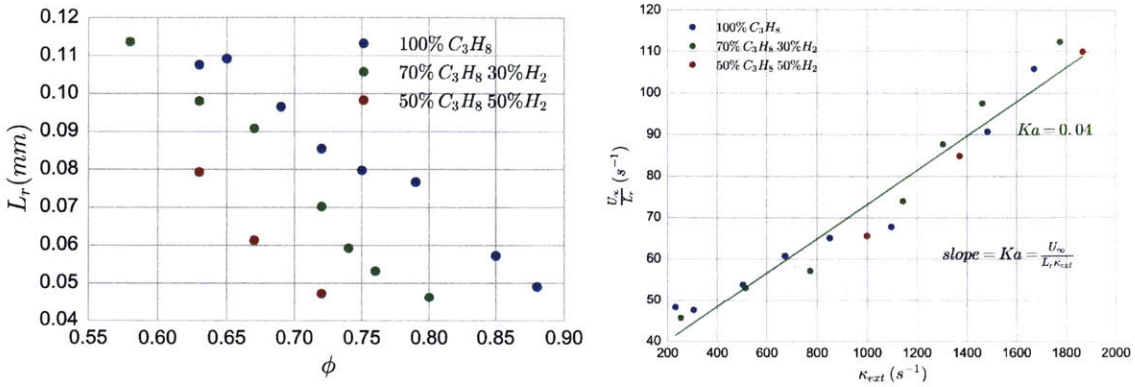

Figure 1-5: (Left) Measured data showing recirculation zone length as a function of equivalence ratio for different fuel compositions. (Right) Same data as is the left plot, but now plotted as a function of extinction strain rate. The y-axis is the inlet velocity divided by recirculation zone length and has the same units as the x-axis, which is a chemical time scale. Using this representation, the slope of the graph is the Karlovitz number (a chemical time/flow-time). Data reproduced from Ref. [5]

Wake flows are the preferred mode of flame stabilization in lean premixed combustion because they create recirculation zones that can anchor flames. However coupling between the flow dynamics and system acoustics can result in combustion instabilities [45]. The combustor geometry also determines the size and structure of the recirculation zone and these recirculating flows in the wake of a bluff body, behind a sudden expansion or downstream of a swirler, are pivotal for anchoring the flame and expanding the stability range. Hong et al. [5] investigated the impact of fuel composition on the recirculation zone structure for C_3H_8/H_2/Air mixtures in a backward-facing step combustor. The results in Figure 1-5 show the spread in the recirculation zone length data when plotted as a function of equivalence ratio, whereas the scatter is significantly reduced when the data are plotted versus the extinction strain rate.

Cocks et al. [52] questioned the ability of LES to predict the large scale dynamics in reacting flows, e.g. the recirculation zone features. They used the same combustor geometry which is also tested in our work, triangular bluff body combustor, as will be explained later. It has been recently demonstrated that in CFD simulations, predicting the extinction strain rate is an important indicator that a multi dimensional simulation can be expected to reproduce for accurate flow and combustion features.

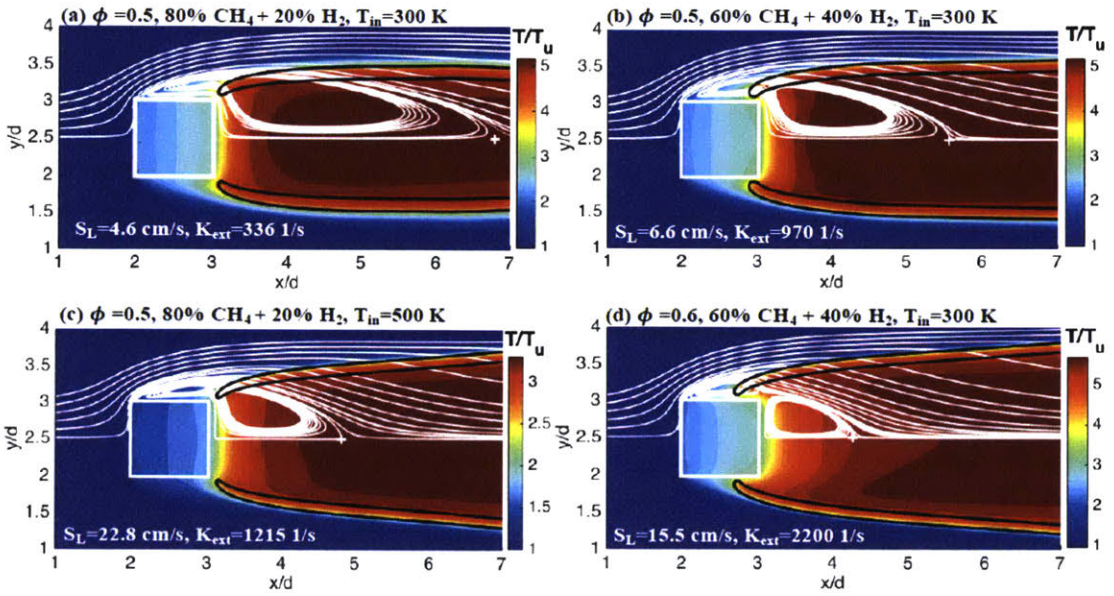

Figure 1-6: Temperature contours for reactive mixtures, with overlaid contour of 10% from the maximum heat release (black line), streamlines (white lines), and a + mark for identifying the downstream stagnation point. The bluff body is plotted as a white square. (reproduced from [6]).

In Michaels et al. [6], DNS of laminar premixed bluff body stabilized CH_4/H_2/Air flames at various temperature ratios were conducted. Results shown in Figure 1-6 illustrate that the higher the extinction strain rate of the mixture (either by increasing equivalence ratio or H_2 percentage), the shorter the recirculation zone and the flame leading edge moves further upstream. The next question to ask is, since these recirculation zone lengths appear to change with K_{ext}, can K_{ext} be used as a surrogate to scale these lengths? The answer is shown in the plots in Figure 1-7. When the laminar burning velocity was considered in defining the chemical time scale, the recirculation zone length data is widely scattered and no clear trend is observed. However when

the data is plotted using the extinction strain rate to define the chemical time scale, there is a clear trend revealing that the recirculation zone length correlates well with a chemical time scale based on the flame extinction strain rate of the inlet mixture [6].

These scaling results observed, suggest that regardless of combustor geometry, flow regime, fuel or oxidizer, and inlet temperature, recirculation zone lengths might be correlated with the extinction strain rate. This will be studied in greater detail in Chapter 5 and how this can be applied to oxy-combustion mixtures. Next we review the work that has specifically focused on modeling methane oxy-combustion mixtures both experimentally and numerically.

1.3 Methane Oxy-Combustion Modeling

To retrofit or re-design existing natural gas based power generation plants, thorough understanding of the fundamental differences in the flame characteristics associated with the substitution of N_2 with CO_2 as the diluent is needed. Unlike N_2, CO_2 is not inert but impacts the kinetics primarily through the reaction $CO_2 + H \rightleftarrows CO + OH$ [9, 2]. Due to the high concentrations of CO_2 under oxy-fuel conditions, the forward reaction is primary responsible for the chemical effect of CO_2 at medium to high temperatures [13].

The oxy-fuel combustor requires significant modeling and experimental investigations due to the increased instability of CO_2 recycled oxy-fuel flames [53]. Most of the modeling so far on oxy-fuel combustion has been focused on coal. More work is needed especially for modeling and simulating premixed methane oxy-combustion in a gas turbine combustor. CFD modeling is also an important industrial tool for acquisition of in-depth knowledge, as well as design and optimization. It can effectively provide details on the velocity, temperature and concentration variations that are not easily obtained through experimental measurements. In this section, we review the literature on methane oxy-combustion starting from chemical kinetics modeling and then presenting results from a selection of CFD and experimental studies.

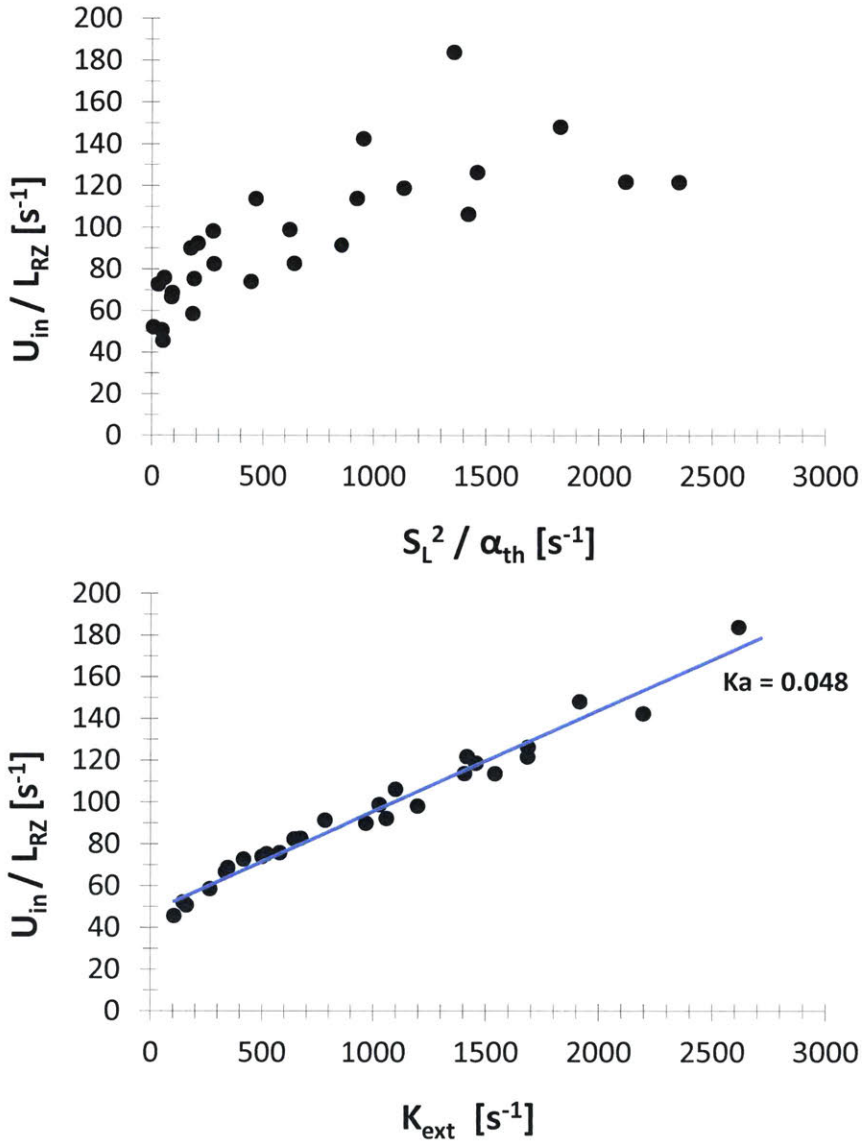

Figure 1-7: Flow vs chemical time scales for different fuels and inlet temperatures from DNS simulations of premixed laminar CH_4/H_2/Air mixtures in a bluff body stabilized combustor. The flow time scale is associated with a recirculation zone length while the chemical time scale is either represented by the flame speed (top) or extinction strain rate (bottom) of the chemical mechanism. Figures were generated using data from Michaels et al. [6].

1.3.1 Numerical Modeling

The choice of reaction mechanism plays an important role in modeling oxy-combustion flames. In a highly CO_2 rich environment, reaction rates are much different than from conventional methane air-combustion due to the chemical effect of CO_2; mainly influencing the reaction: CO + OH $\leftrightarrow$ CO_2 + H. Until now there is no clear consensus on which reaction mechanism should be used for oxy-combustion whether it is which detailed mechanism for simpler calculations or which reduced/global mechanisms for CFD modeling of oxy-combustion.

Detailed Mechanisms

Detailed reaction mechanisms for oxy-combustion are not very plentiful and there are so far only a few mechanisms that have been tested under these conditions. There are also not many comprehensive comparative studies analyzing which mechanism best captures effects in these high-CO_2, and close to stoichiometric environments. The three detailed mechanisms which are commonly used in the literature for oxy-combustion of methane are, the GRI-Mech 3.0 [54], the mechanism developed by Glarborg et al. [13, 55, 56], and the recently developed AramcoMech 1.3 mechanism by Metcalfe et al. [57]. This new mechanism has recently started to appear in literature studies on methane oxy-combustion mixtures [9, 58]. Unlike the other two mechanisms, the AramcoMech 1.3 is based on a recent O-H model [59] and includes an improved rate constant for the reaction H + O_2 = OH+ O [60]. However it doesn't include a model for nitrogen oxides (NO_x) formation but as has been shown, these compounds are negligible for realistic O_2 purities [61], therefore it should not be a problem when using the AramcoMech 1.3. Table 1.1 compares the number of species and reactions of these three detailed mechanisms for oxy-fuel combustion.

Recently, Bongartz et al. [9] performed a comparison of these mechanisms by looking at burning velocities, ignition delay times and CO concentrations. Figures 1-8 to 1-10 show some of these results. All three mechanisms correctly capture the extent of the decrease in burning velocity for a CH_4-air flame diluted with CO_2 (see

Mechanism	No. of Species	No. of Reactions
GRI-Mech 3.0	53	325
Glarborg et al.	49	350
AramcoMech 1.3	124	766

Table 1.1: Detailed mechanisms for methane oxy-combustion

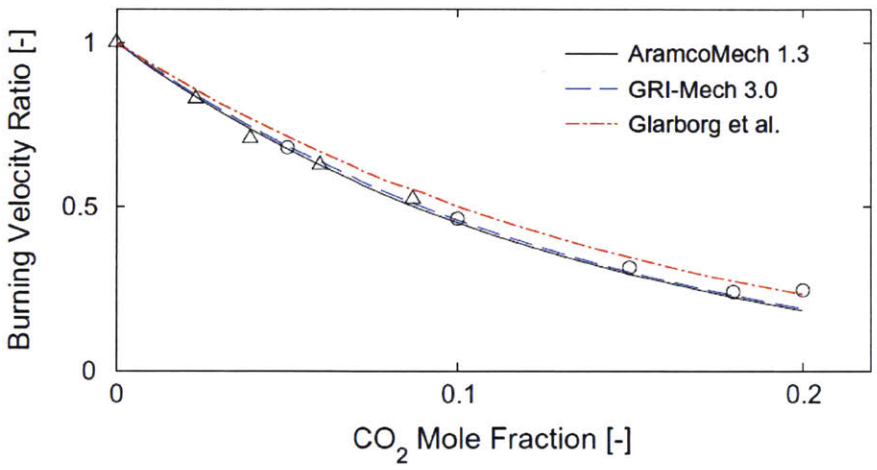

Figure 1-8: The modeling results (lines) are shown along with the experimental data (symbols) of Halter et al. [7] (○) and Kishore et al. [8] (△) for the reduction of the laminar burning velocity of stoichiometric CH_4-air flames with CO_2 addition (T = 300 K, p = 1 atm) (reproduced from [9]).

Figure 1-8) This trend is well established in the literature and it has been shown that both thermal and chemical effects are responsible for the reduction in laminar burning velocity when adding CO_2 to CH_4-air flames [62, 7, 8].

With H_2O dilution of CH_4-air flames, the impact on the burning velocity of CH_4 has also been looked at in a number of studies [10, 11, 12, 63]. Figure 1-9 shows this effect on the burning velocity at two pressures comparing the mechanisms' results with the experimental data. All three mechanisms agree with the data equally well at atmospheric pressure but the AramcoMech 1.3 appears to perform better at the higher pressure.

Bongartz et al. [9] also showed that all of the mechanisms were able to reproduce the inhibiting effect of large CO_2 concentrations on CO oxidation observed by Abin et

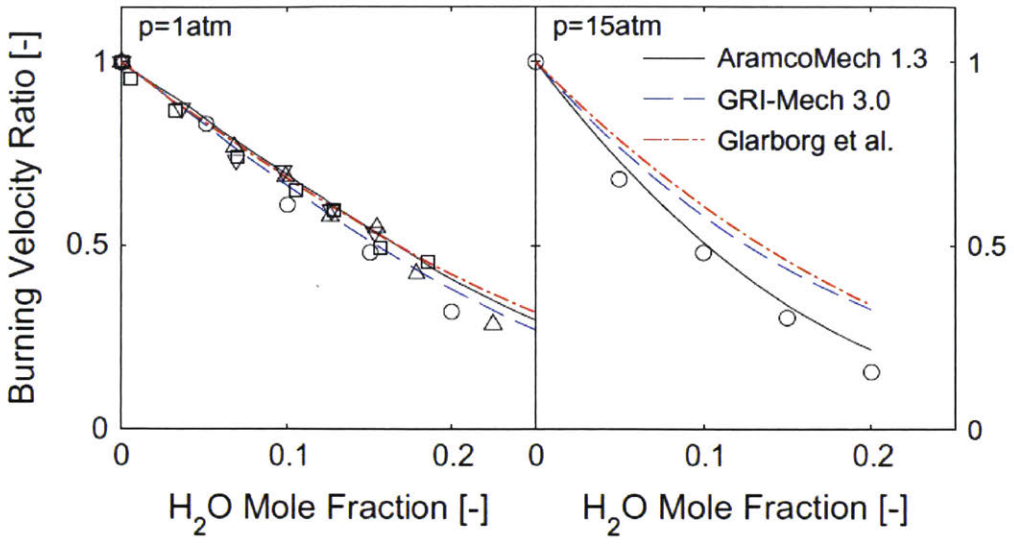

Figure 1-9: The modeling results (lines) are shown along with the experimental data (symbols) of Albin et al. [10] ($\triangle$,$\triangledown$), Mazas et al. [11] ($\square$), and Babkin and V'yun [12] ($\circ$) for the reduction of the laminar burning velocity of stoichiometric CH_4-air flames with H_2O addition at atmospheric pressure (reproduced from [9]).

al. [64] both for lean and rich conditions. Moreover the mechanisms also captured the inhibiting effect of larger concentrations of H_2O on CO oxidation, at the extremely lean conditions ($\phi \approx 0.04$) observed by Glarborg et al. [65].

Looking now at CO formation for CH_4 oxidation in the atmospheric reactor of Glarborg and Bentzen [13], all of the mechanisms predict the effect of CO_2 on CO concentrations (see Figure 1-10). At the more practical stoichiometric condition, the AramcoMech 1.3 appears to have a better agreement with the experimental data compared to the other mechanisms.

The GRI and Glarborg mechanisms were also compared by calculating their laminar burning velocities and extinction strain rates in a counterflow non-premixed flame configuration in a study by Watanabe et al. [18]. The calculations were compared to experimental data by Maruta et al. [66] in a similar flame configuration and inflow conditions. The results of the extinction strain rate calculations will be shown later in Figure 3-8. But the calculations showed that the Glarborg mechanism with radiation seems to have the best agreement with the experimental data for the oxy flame. This

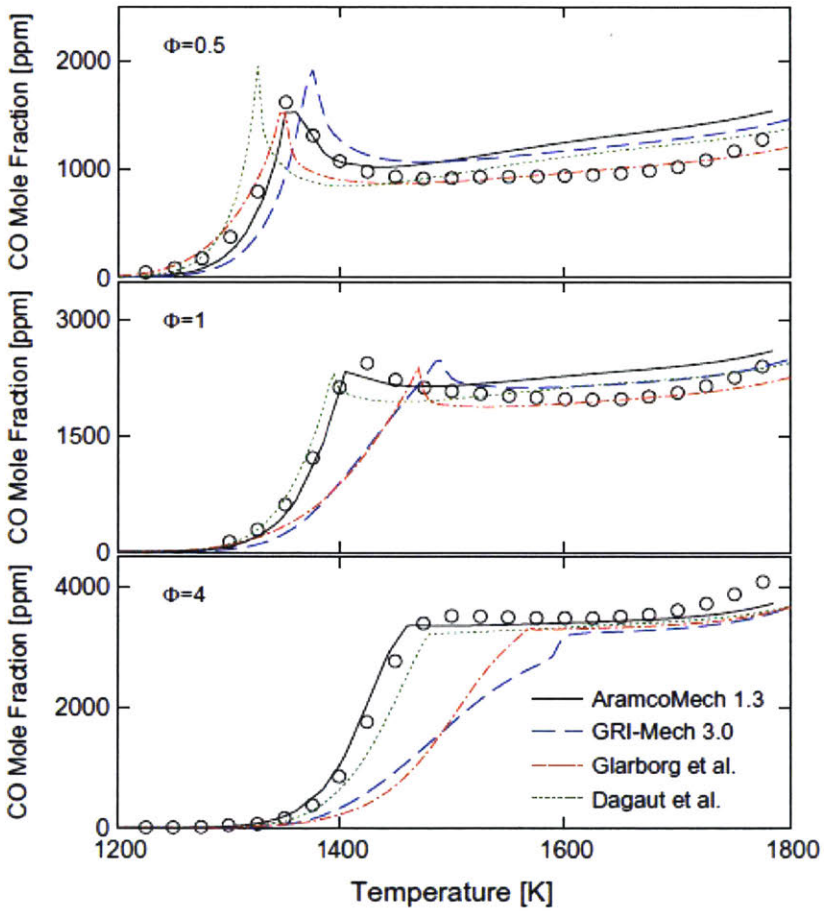

Figure 1-10: Comparison between modeling results (lines) and experimental data (symbols) from the atmospheric $CH_4/O_2/CO_2/N_2$ flow reactor of Glarborg and Bentzen [13] on CO formation in CH_4 oxidation in the presence of CO_2. The modeling was done assuming a residence time of $\tau \approx 960/T$ s and constant temperature. Inlet conditions: $X_{CO} \approx 1000$ ppm, $X_{CO2} = 77\text{-}95\%$, balance N_2. (reproduced from [9]).

importance of radiation has also been seen in other studies [2, 67, 68, 69, 70, 71, 72, 73].

Although the GRI-Mech 3.0 is still commonly used in oxy-combustion calculations [74, 53, 75, 76, 19], recently, the Glarborg mechanism has been able to model and capture experimental observations [16, 18]. Therefore, we can use this mechanism in methane oxy-fuel combustion studies with adequate agreement.

Reduced and Global Mechanisms

We showed in the previous section that there are detailed reaction mechanisms which are valid under oxy-fuel combustion conditions. However in computational fluid dynamics (CFD) modeling, it is computationally expensive to implement these detailed mechanisms. A number of reduced and global mechanisms have been proposed to model oxy-flames kinetics in these CFD studies.

Frassoldati et al. [14] compared the popular Westbrook and Dryer (WD) [77] and Jones and Lindstedt (JL) [78] mechanisms for methane oxy-combustion and found that the original JL mechanism performs slightly better. Therefore they then focused on tuning the JL mechanism for the combustion of methane in pure oxygen using a laminar diffusion flame. They reported improved agreement of temperature and CO_2 profiles for their modified JL mechanism over the original JL mechanism, as seen in Figure 1-11. "DKM" refers to a detailed kinetic mechanism previously developed and validated for hydrocarbons up to 16 C atoms by the authors [79].

Almost simultaneously, Andersen et al. [15] presented their own modified oxy-fuel versions of the WD and JL mechanisms each for CO_2 dilution. They left the fuel consumption reactions unchanged and modified the CO-CO_2 reactions to better fit plug flow reactor results obtained using the detailed mechanism by Glarborg and Bentzen [13] under CO_2-diluted oxy-fuel condition. They found the modified mechanisms to give a closer agreement for CO concentrations (see Figure 1-12) and equilibrium values and also improve the prediction of a turbulent diffusion flame.

Once again for the global mechanisms proposed for modeling oxy-combustion, there is no obvious mechanism that stands out as being the best. In Chapter 5, we test different reduced mechanisms in LES of a swirl combustor to evaluate their

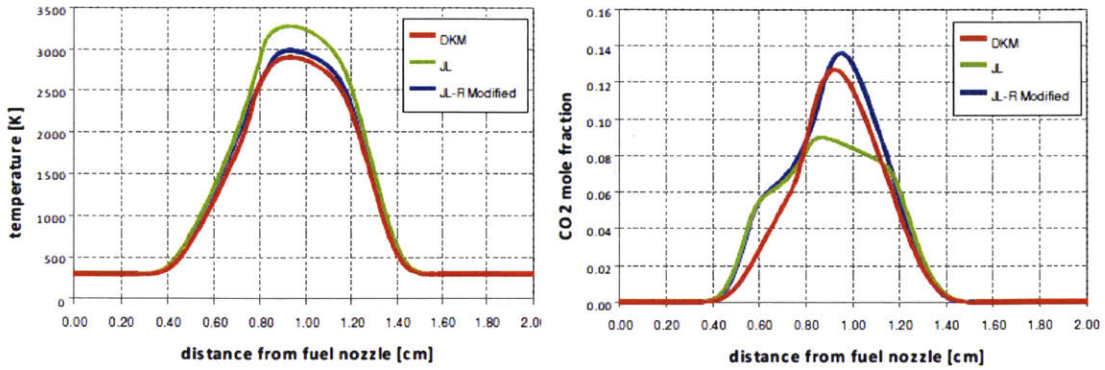

Figure 1-11: Calculated temperature and CO_2 mole fraction profiles showing the comparison between detailed and global kinetic mechanisms (10% N_2 in oxidizer stream) for a laminar diffusion flame (reproduced from [14]).

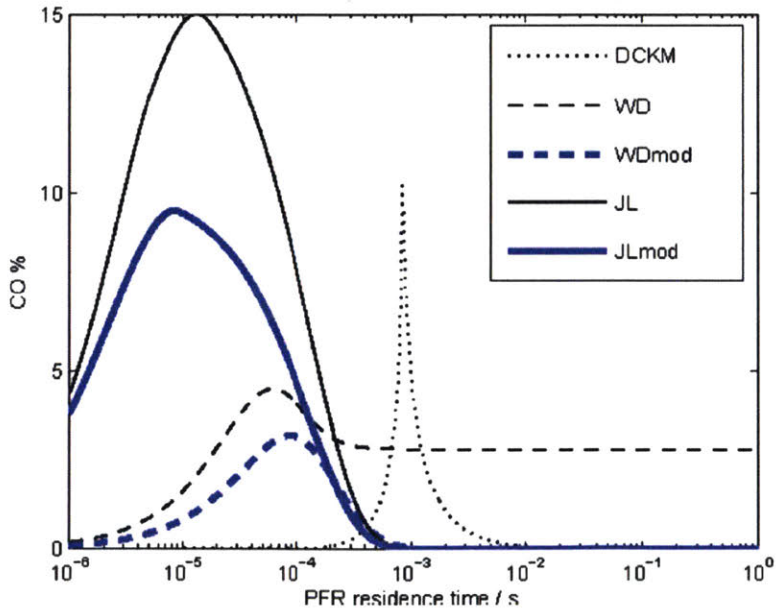

Figure 1-12: CO concentrations in plug flow calculations. Comparison between the DCKM (detailed kinetic model by Glarborg & Bentzen [13], WD, JL, and modified mechanisms at 1600 K and $\lambda = 1.2$ under oxy-firing conditions (28% O_2 and 72% CO_2) (reproduced from [15]).

performance.

CFD Simulations

Numerical CFD modeling of oxy-fuel gas turbine combustors can help to predict the system performance and also help develop the fundamental understanding of the combustion dynamics, flame stability as well as predicting velocities, temperatures and concentration variations inside the combustor. But most of the studies that have been done on natural gas oxy-combustion has focused on furnaces and boilers or on diffusion combustors [73, 80, 81, 82, 29]. Nemitallah et al. [29] investigated an atmospheric diffusion oxy-combustion flame in a gas turbine combustor. To model the reaction kinetics, they used the 3-step WD mechanism modified by Andersen [15] that was mentioned in the previous section. They reported a good prediction of temperatures and CO emission trends in the simulations compared to experiment. Since the reaction mechanism was validated by Andersen et al. [15] using diffusion flames, this agreement is not unexpected. Premixed methane oxy-combustion in the swirl combustor is less addressed.

Moreover, the CFD modeling in the literature for oxy-combustion has also mostly focused on reproducing quantities such as adiabatic flame temperature or emissions. Studies on more complex and practical insights such as the response to strain, predicting flow structures, and predicting flame macrostructures, have been limited. We will explore these important characteristics in LES of premixed practical combustors in this thesis.

1.3.2 Experimental Investigations

There have been a number of experimental studies on premixed and partially premixed methane oxy-combustion in swirl combustors.

The effects of swirl number, quarl angle and flame temperature on the stabilization and shapes of premixed air and oxy-flames were analyzed by Jourdaine et al. [83] in a swirl combustor. The CO_2-diluted flames were found to be less stable than the

N_2-diluted flames at Re < 20,000, however the flame shapes were matching when the swirl numbers and adiabatic flame temperatures were the same for both. Runyon et al. [84] also studied the flame structures and emissions that result from premixed methane-oxygen and methane-air mixtures in a swirl-stabilized burner at varying thermal power pressure similar to Shroll et al. [46]. The oxy-flames demonstrated stable combustion at a range of thermal powers and pressures (up to 3 bar). The size of the central recirculation zone was also found to increase in size by about 14% for the CO_2 diluted flame over the N_2 diluted case. Amato et al. [2] showed the operability boundaries of a CO_2 diluted system to be significantly reduced compared to methane-air mixtures in a premixed swirl combustor, mainly due to the slower kinetics of the $CH_4/O_2/CO_2$ mixture. The CO_2 diluted mixture was found to blow off at temperatures about 300K hotter than the air mixture for a given nozzle exit velocity.

Shroll et al. [46] examined the dynamic stability characteristics of premixed methane oxy-fuel flames and methane air flames in a swirl stabilized combustor. They reported similar flame structures for air and oxy flames in each of the dynamic modes [46]. These flame structures were similar to the ones described previously in Section 1.1. At the highest flame temperature, the combustor is unstable at the first harmonic of the combustor's natural frequency. The flame was very compact at these low dilution levels and the dominant instability frequency corresponds to that of the first harmonic of the combustor's natural frequency. Then as the temperature was reduced, the combustor jumps to fundamental mode and then to a low frequency mode (below the combustor's natural frequency), before eventually blowing off.

Throughout this reduction in temperature, the flame length increases and the flow structures switch between a double-helix type and a spiral type breakdown. The transitions between these different instability modes, for both the air and oxy cases, were shown to be predominately a function of the mixture adiabatic flame temperature. But the dominant frequencies for the high, medium and low frequency modes are shifted higher for air due to the differences in acoustic properties of the reactants and products between air and oxy-combustion [46].

Building upon the previous work of Shroll et al. [46], Watanabe et al. [16] investigated the structure of these flames but under stable conditions experimentally in a swirl stabilized combustor. High speed chemiluminescence images were taken along with planar laser-induced fluorescence (PLIF) measurement of OH radicals which were used to study the instantaneous flame front at the microscale, and flame photographs were also used to describe the average flame configuration or macro-structure. Finally, flame extinction characteristics were computed in the twin flame configuration using CHEMKIN-PRO to help explain some of the experimental results.

In Watanabe et al. [16], flame configuration IV, where the flame appears in the outer shear layer, was the focus of the tests. It was found that as the equivalence ratio is reduced, the flame length increases for both the air and oxy cases, this was also observed in [46]. Similar flame shapes and macro-structures were observed for both cases as the equivalence ratio was reduced until $\phi = 0.6$. At this equivalence ratio, as seen in Figure 1-13, the flames are wrinkled for both cases but surprisingly a flame is not stabilized in the outer shear layer (OSL) for the air flame, unlike the oxy case. Since the air flame has a higher laminar flame speed than the oxy flame, one would expect the air flame to be "stronger", moving to the ORZ earlier. When chemiluminescence images were used to compare the dynamic flame shapes for air and oxy flames (Figure 1-14), with decreasing equivalence ratio, the intensity of the chemiluminescence decreases in both air and oxy cases and a toroidal flame shape is also observed in the ORZ (except for air at $\phi = 0.6$). For $\phi = 0.6$, the oxy flame is flickering and rotating but the outer toroidal-shaped flame is rarely observed for the air case. It was shown that the extinction strain rate plays a role in the combustion dynamics and flame configurations [16]. This type of analysis was used to explain the observed differences at $\phi = 0.6$.

Figure 1-15 shows the extinction strain rate of air and oxy-flames for equivalence ratios 0.6-0.68. As can be seen, at low ϕ the extinction strain rate is higher for oxy than air but at high ϕ the opposite is true. This means that at these low ϕ, oxy flames can sustain higher strains than air flames, which might explain why the oxy flame has a flame stabilizing in the ORZ but air does not. Heat loss plays a major

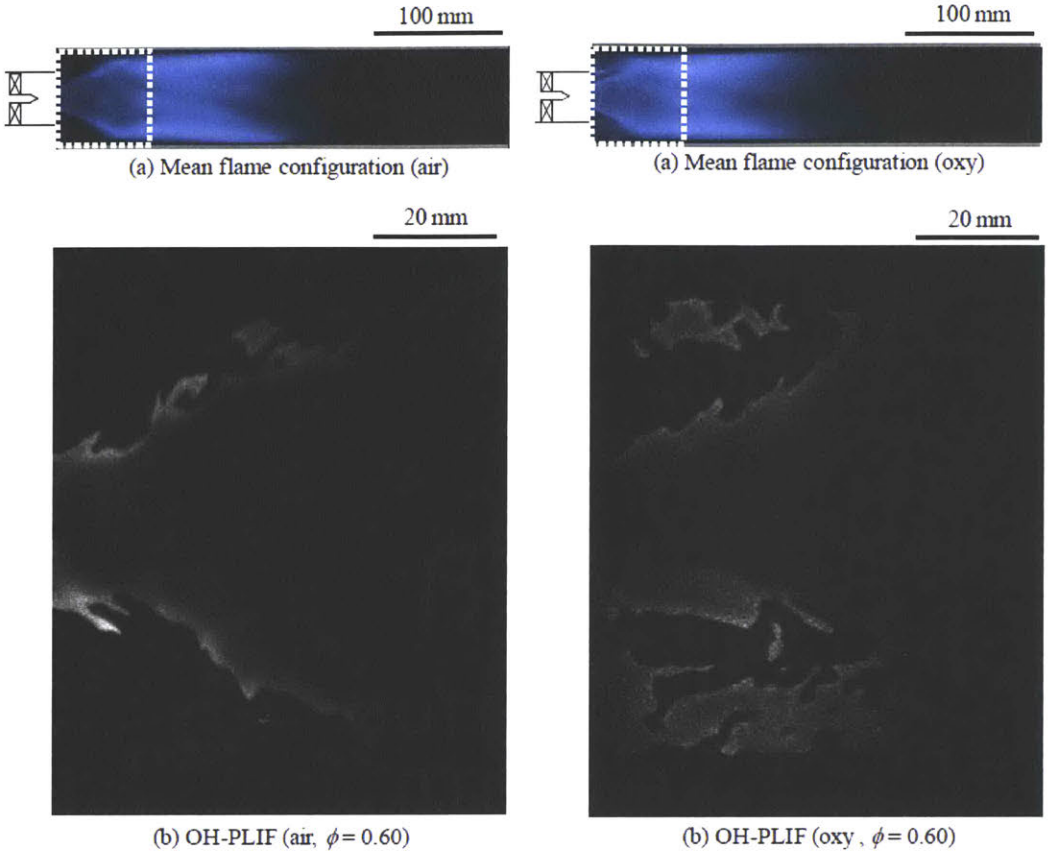

Figure 1-13: Mean flame configuration and OH-PLIF images of air and oxy-flames at $\phi = 0.60$ [16]

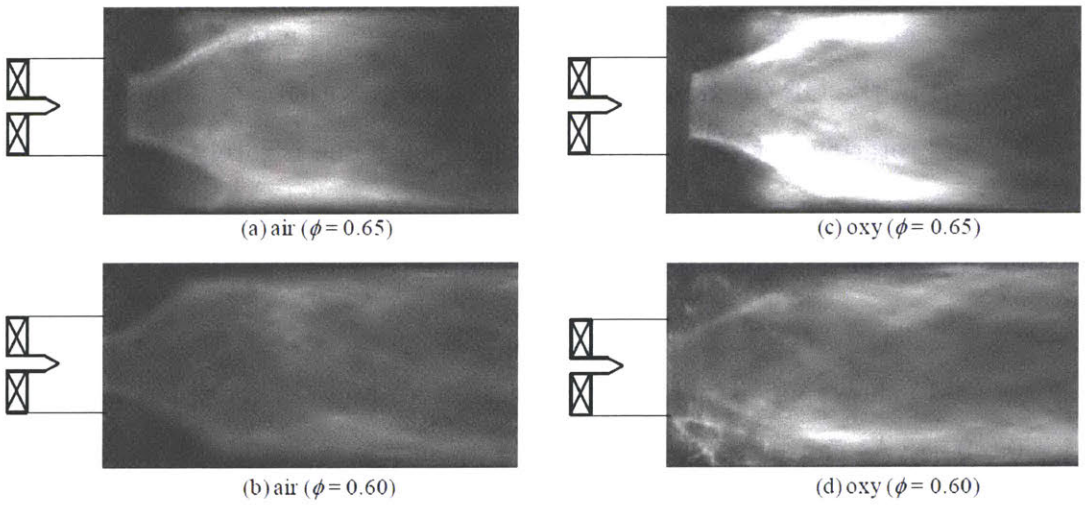

Figure 1-14: Chemiluminescence images of air and oxy-flames [16]

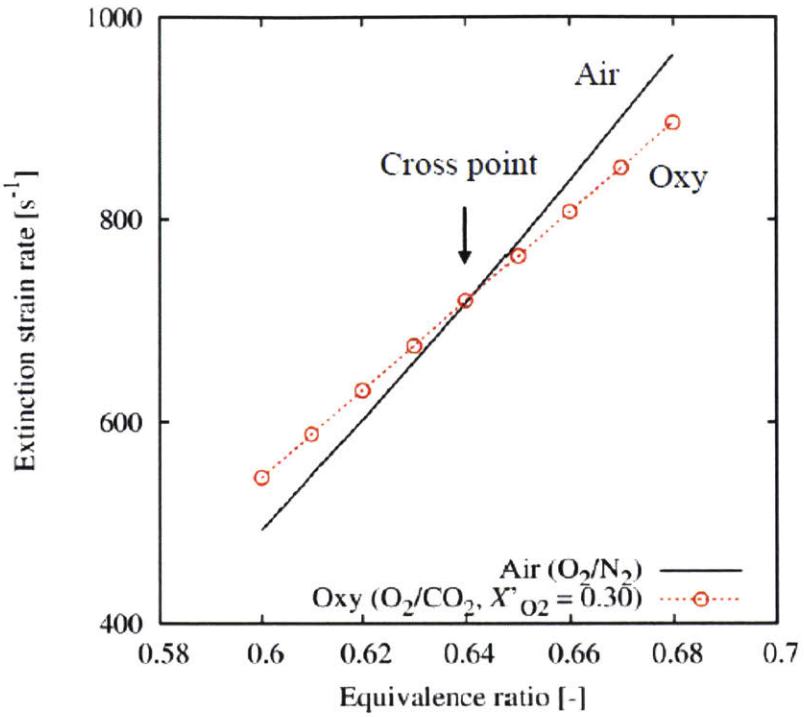

Figure 1-15: Extinction strain rates of premixed twin air and oxy-flames ($CH_4/O_2/N_2$ vs. $CH_4/O_2/CO_2$) [16]

role in the extinction of flames in the ORZ due to their proximity to the combustor wall. Thus they are vulnerable to extinction earlier than those in the inner shear layer.

The Lewis number of the oxy-flame is lower than unity while it is around 1 for the air-flame, and it was also found that the OH radical concentration to be higher for the oxy case at $\phi = 0.6$. Therefore it was determined that the combined effects of these two results is what lead to oxy-flames appearing to be "stronger" than air-flames at $\phi = 0.6$ [16].

Looking at CO emissions now, the important and critical pollutant in oxy-combustion is carbon monoxide (CO). Williams et al. [61] showed that in a premixed, 20 kW swirl-stabilized combustor, CO emissions do not become significant until an equivalence ratio greater than 0.95. Also at this near-stoichiometric limit, CO emissions rise faster for oxy-combustion than air-combustion.

Ditaranto and Hals [48] presented acoustic mode results from a 2 kW premixed, expansion-stabilized combustor. They reported thermo-acoustic instabilities occurring as the O_2 content in the oxidizer was increased, hence CO_2 decreased, with stoichiometric operation similar to other studies [46, 83]. They also found that the different instability modes can be triggered depending on the ratio of flame speed to inlet velocity.

From this extensive review, a number of gaps exist in the literature and unexplained observations arise which will be answered in this thesis with the main aim of advancing the fundamental knowledge on oxy-combustion flames.

1.4 Thesis Overview

1.4.1 Objectives

The overall goals of this work:

- Establishing the stability characteristics for flame macrostructure transitions for turbulent oxy flames in a gas turbine combustor.

- Investigating the role of kinetics versus transport on the response to strain of methane oxy-flames.

- Examining the importance of chemical kinetics modeling in LES of premixed flames for multiple geometries, fuels and oxidizers.

- Understanding and modeling the flame macrostructure transition mechanism for oxy-flames in the swirl combustor.

- To further aide in the design of oxy-combustors for power plants, experiments will be conducted and LES models will be validated for oxy-combustion.

1.4.2 Outline

A combined experimental and numerical approach will be used to take advantage of both types of tools in exploring the combustion dynamics of oxy-fuel flames. Having access to both advanced experimental tools and numerical capabilities is not very common and so using these facilities in our lab will put us in an advantageous position. These tools are presented in Chapter 2.

In Chapter 3, flame stabilization of air and oxy-combustion mixtures are modeled and scaled in the experimental swirl combustor. The extinction strain rate is found to be an important parameter for modeling these methane-oxy flames. Subsequently, these effects are investigated further in Chapter 4 to identify the role of transport and chemistry on the response to strain of these flames.

Rigorous LES simulations are performed in Chapters 5 and 6 to study the turbulence-chemistry effect on premixed flames. Chapter 5 focuses on the impact of chemical kinetics modeling on the prediction of important flow structures such as recirculation zones in multiple geometries, and for different fuels and oxidizers. In Chapter 6, the flame macrostructure transition phenomenon is simulated and used to study the flame microstructures and to understand the interplay between the flow and flame dynamics in an oxy-fuel gas turbine combustor. Finally, Chapter 7 wraps up with the summary of this thesis and the list of publications.

Chapter 2

Experimental and Numerical Setups

2.1 Experimental

2.1.1 Combustor Description

All experimental data presented in this thesis were obtained from the fully premixed atmospheric swirl-stabilized combustor at the Reacting Gas Dynamics Laboratory at MIT. It is similar to setups used in previous studies [50, 39] and similar to those found in modern gas turbines. The major advantage of this setup at MIT is having access

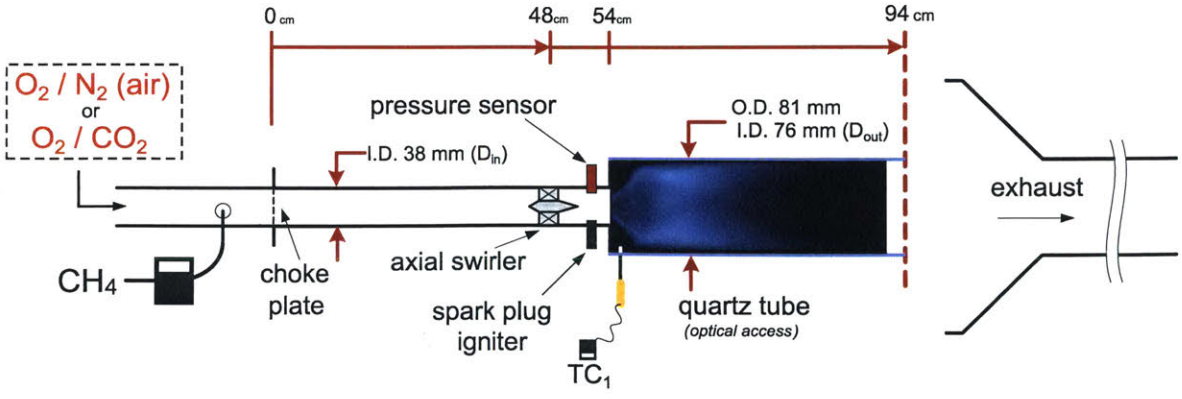

Figure 2-1: Overview of the swirl combustor experimental setup.

to several modern diagnostics techniques for combustion phenomena including high speed selective chemiluminescence, high speed particle imaging velocimetry (PIV) and planar laser induced fluorescence (PLIF). High speed chemiluminescence can be used to track dynamics larger than the flame thickness scale as only the flame brush can be inferred from this relatively large exposure time technique. PLIF can provide us with enough spatial resolution to identify the flame front and explore the way it interacts with the turbulent flow but without temporal resolution (10 Hz). Lastly two-dimensional, two-component high-speed particle imaging velocimetry (PIV) system can be used to interrogate the reacting flow field and provide us with instantaneous and mean velocities in the flow. Along with the optical diagnostics, temperature measurements can be performed. A K-type sheathed thermocouple with a diameter of 1/16 inches and a response time around 1 s will be used to obtain these measurements at various locations within the combustor. One of these possible positions is shown in the Figure.

The 50kW axisymmetric swirl-stabilized combustor operates at atmospheric pressure with a fixed swirl number. The axial swirler blade angle is fixed throughout experiments in this thesis ($\alpha_{sw} = 45°$). The corresponding swirl number can be estimated using the expression [45]:

$$Sw = \frac{2}{3} \left(\frac{1-(D_{cb}/D_{in})^3}{1-(D_{cb}/D_{in})^2}\right) tan(\alpha_{sw}) \approx 0.7$$

with α_{sw} being the blade angle, D_{in} the inlet tube diameter (38 mm) and D_{cb} the centerbody diameter (9 mm).

Methane, oxygen and carbon dioxide gases are supplied by Sierra C100M Smart-Trak digital mass flow controllers with a mass flow rate uncertainty of $\pm 1\%$ of maximum capacity. A Sierra Instruments 780S Flat-Trak flow meter was used to measure the air flow rate with the same uncertainty. Subsequent relative error on the equivalence ratio is 2% of maximum capacity. For example, setting ϕ at $\phi_{set\ point} = 0.59$ for a CH_4/air at $Re_{inlet} = 20{,}000$ led to a measured $\phi_{mean} = 0.5919$ and a standard deviation $\phi_{std} = 0.0024$.

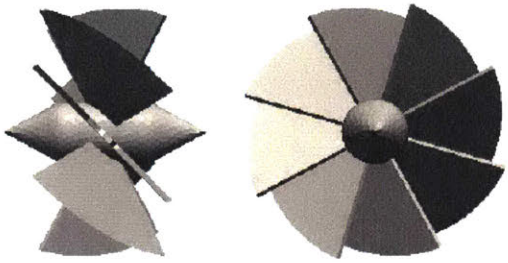

Figure 2-2: The axial eight-vane swirler with 45° vane angle used in the experiment [17].

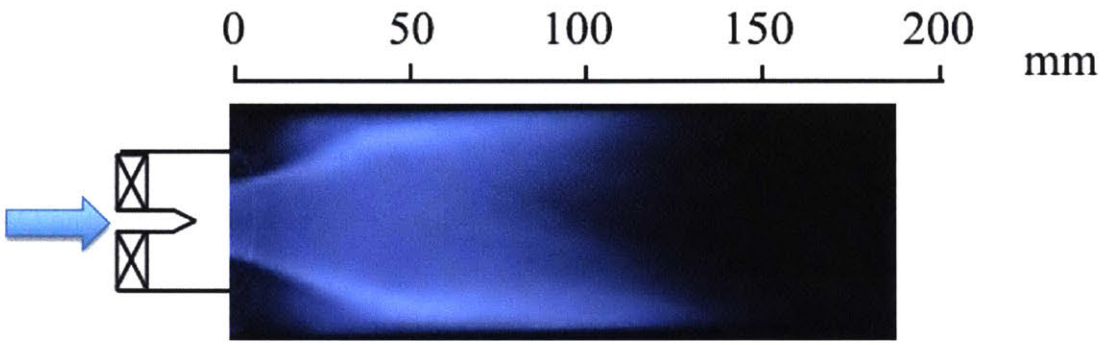

Figure 2-3: Example of a flame macrostructure captured using the digital camera without a filter for methane oxy-combustion at ϕ=0.65 and Re=20,000.

After the premixed reactants enter the combustor through the 38 mm diameter inlet pipe, the flow is choked, and then passes through the swirler (shown in Figure2-2. The flow then expands into a 400 mm long and 76 mm diameter combustion chamber with a quartz tube for optical access.

2.1.2 Diagnostics Tools

The main experimental diagnostics tools utilized are described in this section. Mean flame images are taken using a Nikon D5100 SLR camera. These are used to describe the time-averaged flame shape, or flame "macrostructure" (see Figure 2-3) because this long exposure time technique averages out micro-scale features of the flame such as instantaneous wrinkles on the flame surface.

High speed chemiluminescence data is acquired at 1 kHz with an infrared (IR)

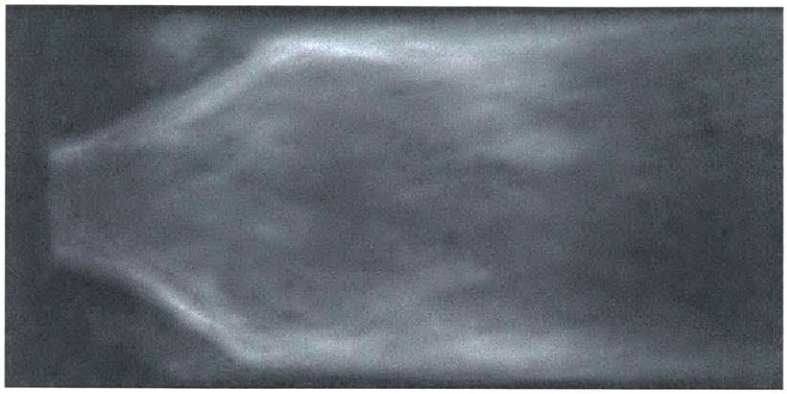

Figure 2-4: Example of a flame chemiluminescence image with an IR filter for methane oxy-combustion at ϕ=0.65 and Re=20,000 (flow is from left to right).

blocking filter (2-mm CG-BG-39 Schott glass) using a 1280×1024 pixel high-speed NAC GX-1 CMOS camera mounted above the combustor field of view as shown later in Figure 3-4). Chemiluminescence is used to identify the flame transition to the ORZ and also compute f_{ORZ} (frequency in ORZ) as will be explained and shown in detail in the next chapter. An example of a flame chemiluminescence image is shown in Figure 2-4.

We also use a two dimensional, two-component high-speed particle imaging velocimetry (PIV) system to interrogate the flow field and compare it for air and oxy-combustion. Aluminum oxide Al_2O_3 seeding particles (diameter between 0.9 and 2.2 micron) are introduced into the main air flow upstream of the swirler. A dual pulse Nd:YLF laser at 1kHz with pulse energies of 25 mJ/pulse is used along with sheet optics (a spherical lens with a focal length of 1000 mm and a cylindrical lens with a focal length of -20 mm) to produce a light sheet of wavelength 527 nm less than 1 mm thick. A 1280 x 1024 pixel NAC GX-1 CMOS camera is used with an F-mount Nikon 60 mm lens to collect the scattered light at a 1 KHz rate. The PIV measurements are then processed using the LaVision DaVis 7.2 software. An example of PIV results is shown in Figure 2-5.

In addition to optical diagnostics, temperature measurements are performed; a K-type sheathed thermocouple (TC_1) is used to measure the temperature in the ORZ. It is inserted through a hole in the quartz tube 15 mm downstream of the sudden

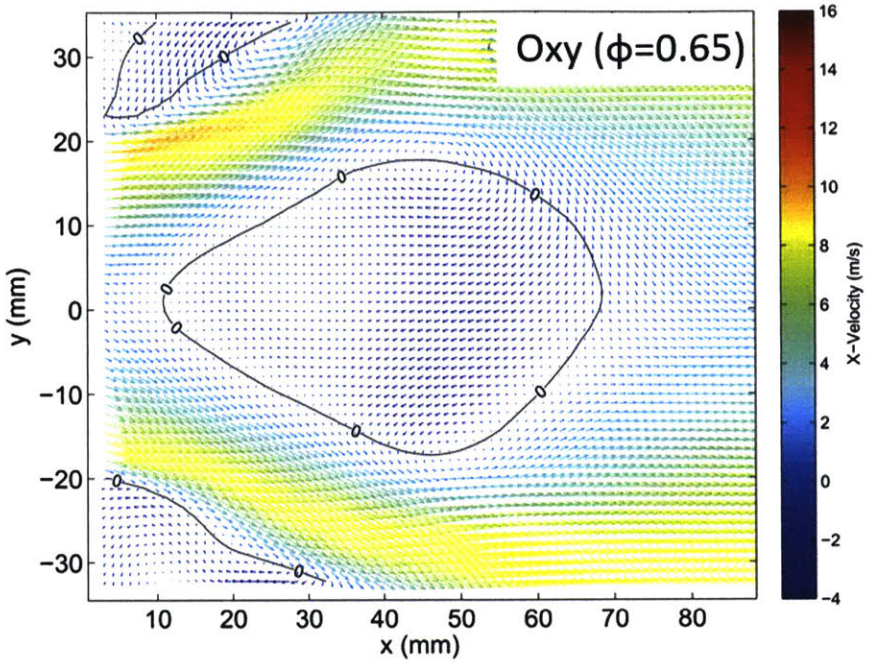

Figure 2-5: Example of PIV results for methane oxy-combustion at ϕ=0.65 and Re=20,000 (flow is from left to right).

expansion side wall and 5 mm into the ORZ (as shown in Figure 2-1). TC_1 has a sheath diameter of 1/16 inch and a response time around 1 s and a 20 Hz sampling rate. Multiple measurements were made to evaluate an uncertainty of $\pm$ 5 K. TC_1 is used to measure the relatively low temperature of the unburnt reactants in the ORZ before the appearance of a flame in that zone. The measurement error due to radiative heat exchange between the probe and its surroundings is neglected. The sensitivity of the measurement to the thermocouple depth into the ORZ was evaluated and found to be less than 2%; this also suggests that the ORZ temperature is fairly homogeneous at the conditions studied in this thesis.

2.2 Numerical

2.2.1 Large Eddy Simulations

Large Eddy Simulations (LES) is a major tool that is utilized in this thesis. It serves as an important numerical approach for investigating combustion dynamics phenom-

ena, giving access simultaneously to any variable needed as well as any location in the domain as opposed to experimental diagnostics. The LES code is similar to the one described in previous studies by Kewlani et al. [85, 86, 87]. This code is implemented using OpenFOAM's C++ libraries based on finite volume spatial discretization. Implicit second order temporal schemes are used along with a combination of first and second order schemes for spatial discretization. For the turbulent combustion model, the artificially thickened flame (ATF) approach is used [88].

LES resolves the large scales of the flow but models the smallest (and most expensive) scales of the solution, rather than resolving them as DNS does. The governing equations for LES are obtained by applying a spatial filter to the conservation equations of mass, momentum and energy, and species transport equations. This low pass filter operation eliminates the small scales of the solution. The sub-grid-scale stresses resulting from the filtering operation are unknown, and require modeling. These terms can be modeled using different approaches but in our code the one-equation eddy viscosity model [89] is implemented. Also for these reacting flows, since the density cannot be considered constant, and to simplify the equations, Favre or density-weighted filtering is applied [85]. Applying these filters to each term in the partial differential equations governing the flow (ideal gas, mass, momentum, species, energy) results in the following equations.

LES Filtered Governing Equations

The Favre filtered Navier-Stokes equations that are solved are shown below, following general form (using Poinsot et al. notations [90]). Several terms are neglected in our implementation based on the specific flow conditions we are simulating in this thesis.

$$\overline{p} = \overline{\rho} R \widetilde{T} \quad (Equation\ of\ state) \tag{2.1}$$

$$\frac{\partial \overline{\rho}}{\partial t} + \frac{\partial \overline{\rho}\widetilde{u}_j}{\partial x_j} = 0 \tag{2.2}$$

$$\begin{aligned} \frac{\partial \overline{\rho}\widetilde{u}_i}{\partial t} + \frac{\partial \overline{\rho}\widetilde{u}_i\widetilde{u}_j}{\partial x_i} &= -\frac{\partial \overline{p}}{\partial x_i} + \underbrace{f_i}_{C} \\ &\quad + \frac{\partial}{\partial x_i}(\underbrace{\overline{\tau}_{ij}}_{A} - \underbrace{\overline{\rho}(\widetilde{u_i u_j} - \widetilde{u}_i\widetilde{u}_j)}_{B}) \end{aligned} \tag{2.3}$$

$$\begin{aligned} \frac{\partial \overline{\rho}\widetilde{Y}_k}{\partial t} + \frac{\partial \overline{\rho}\widetilde{u}_i\widetilde{Y}_k}{\partial x_i} &= \underbrace{\frac{\partial}{\partial x_i}(\overline{V_{k,i}Y_k}}_{I} - \underbrace{\rho(\widetilde{u_i Y_k} - \widetilde{u}_i\widetilde{Y}_k))}_{J} \\ &\quad + \underbrace{\overline{\dot{\omega}_k}}_{K} \end{aligned} \tag{2.4}$$

$$\begin{aligned} \frac{\partial \overline{\rho}\widetilde{h}_s}{\partial t} + \frac{\partial \overline{\rho}\widetilde{u}_i\widetilde{h}_s}{\partial x_i} &= \underbrace{\overline{\frac{Dp}{Dt}}}_{D} + \frac{\partial}{\partial x_i}(\underbrace{\lambda\overline{\frac{\partial T}{\partial x_i}}}_{E_1} - \underbrace{\rho(\widetilde{u_i h_s} - \widetilde{u}_i\widetilde{h}_s))}_{E_2} \\ &\quad + \underbrace{\overline{\tau_{ij}\frac{\partial u_i}{\partial x_j}}}_{F} - \underbrace{\frac{\partial}{\partial x_i}(\overline{\rho\sum_{k=1}^{N} V_{k,i}Y_k h_{s,k}})}_{G} \\ &\quad + \underbrace{\overline{\dot{\omega}_T}}_{H} \end{aligned} \tag{2.5}$$

where t is the time and x_i the space variable (Einstein notation was used). ρ, u_i and p represent the density, the spatial components of velocity and pressure of the gaseous mixture respectively. μ is the molecular viscosity. h_s and T and λ are the sensible enthalpy, the temperature and the thermal diffusivity. Y_k is the mass fraction of species k. The over bars and tildes represent the spatially filtered and density-weighted filtered values with a filter width Δ respectively.

The terms (A to K) in the system of governing equation are detailed below. These

are in some cases modeled and other cases neglected:

- A: molecular or resolved viscous stress modeled as $\tau_{ji} = -\frac{2}{3}\mu\frac{\partial \widetilde{u}_k}{\partial x_k}\delta_{ji} + \mu(\frac{\partial \widetilde{u}_j}{\partial x_i} + \frac{\partial \widetilde{u}_i}{\partial x_j})$ for a Newtonian fluid.
- B: The sub-grid scale (sgs) stress is unknown and results from the LES filtering operation. It represents the effect of the sub-grid stresses on all the scales equal or larger than the filter level. This term requires modeling and we use the Boussinesq hypothesis and the Prandtl's one-equation model based on the turbulent kinetic energy (TKE) [89]; this requires solving an additional PDE for k the turbulent kinetic energy.
- C: Body forces like gravity forces are neglected. The Froude number is estimated based on the conditions studied in this thesis: Fr $\approx$ 45; gravity forces are thus neglected.
- D: Heating due to compressibility effects. This term is characterized by the dimensionless Eckert number $\mathrm{E}_{ck} = \frac{U^2}{c_p\,\Delta T}$. In this study $\mathrm{E}_{ck} \approx 10^{-4}$ thus the heating due to compressibility effects can be neglected compared with heat release from combustion. This is generally the case in reacting flows and the term is neglect in our model.
- E_1: The laminar thermal diffusion flux is approximated by Fourier's law using the molecular thermal diffusivity.
- E_2: The unresolved sensible enthalpy flux is modeled using the gradient assumption analogous to Fourier's law but using a subgrid scale thermal diffusivity (α_{sgs}). α_{sgs} is calculated from ν_{sgs} and a turbulent or sgs Prandtl number.
- F: The viscous dissipation term is neglected as the Brinkman number ($Br = \frac{\mu\,U^2}{k\,\Delta T}$) associated with this term is small compared to one $Br \approx 10^{-5}$.
- G: Heat transport due to species diffusion. This Dufour effect is neglected.
- H: Heat release due to chemical reactions.
- I: The laminar species diffusion flux is approximated by Fick's law using the mass diffusivity.

- J: The unresolved species flux is modeled using also the gradient assumption analogous to Fick's law but using a subgrid scale mass diffusivity (D_{sgs}). D_{sgs} is calculated from ν_{sgs} and a turbulent or sgs Schmidt number (Sc_{sgs}). Sc_{sgs} is assumed equal to the laminar Schmidt number.
- K: The filtered reaction rate requires modeling. This is the subgrid scale combustion model. We use the artificially thickened flame (ATF) model allowing the use of an Arrhenius type reaction rate as described in the next section.

Turbulent Combustion Modeling

The species transport equation, after applying Fick's law to the species diffusion flux, becomes:

$$\frac{\partial \overline{\rho}\widetilde{Y_k}}{\partial t} + \frac{\partial \overline{\rho}\widetilde{u}_i\widetilde{Y_k}}{\partial x_i} = \frac{\partial}{\partial x_i}(\overline{\rho}D_k\frac{\partial \widetilde{Y_k}}{\partial x_i}) - \frac{\partial}{\partial x_i}\overline{\rho}(\widetilde{u_iY_k} - \widetilde{u}_i\widetilde{Y_k}) + \overline{\dot{\omega}_k}$$

$\overline{\dot{\omega}_k}$ is the filtered reaction rate which requires modeling. This is the sub-grid scale combustion model.

We use the ATF model allowing the use of an Arrhenius type reaction rate [88]. This involves artificially thickening the flame front so that it can be resolved on the LES grid, in a DNS-like approach, while maintaining the same laminar flame speed and turbulence-flame interaction. This approach has some advantages over other combustion models since it allows the use of suitably detailed reaction chemistry and can be applied to different combustion regimes; allowing for accurate predictions of flame stabilization and combustion dynamics [91, 92].

In the ATF model, the molecular diffusivity (D) and reaction rate ($\overline{\dot{\omega}}$) are modified accordingly using a thickening factor, F, (FD & $\overline{\dot{\omega}}/F$) to maintain the same flame speed [86]. When the flame is thickened, however, this leads to a modified turbulence-chemistry interaction and the wrinkling of the flame front is reduced. To account for the wrinkling effect of the unresolved features on the thickened flame front, an efficiency function, E, is introduced. This efficiency function is implemented following

the algebraic expression proposed by Colin et al. [88]. A dynamic thickening approach is implemented [93] wherein the thickening factor and the diffusivity are represented locally (F_{loc} & D_{loc}). The filtered species conservation equation then takes the form:

$$\frac{\partial \overline{\rho}\widetilde{Y}_k}{\partial t} + \frac{\partial \overline{\rho}\widetilde{u}_i\widetilde{Y}_k}{\partial x_i} = \frac{\partial}{\partial x_i}\left(\overline{\rho}F_{loc}ED_{eff,loc,k}\frac{\partial \widetilde{Y}_k}{\partial x_i}\right) + \frac{E\overline{\dot{\omega}_k}}{F_{loc}} \tag{2.6}$$

where,

$$F_{loc} = 1 + (F-1)\Psi(c) \tag{2.7}$$

$$D_{eff,loc,k} = \frac{\mu}{Sc}EF_{loc} + (1-\Psi(c))\frac{\mu_{sgs}}{Sc_{sgs}} \tag{2.8}$$

with $\Psi(c) = 16[c(1-c)]^2$ is a locally defined function based on the reaction progress variable: $c = \left(1 - \frac{Y_{fuel}}{Y_{fuel}^{inlet}}\right)$. μ and Sc are the dynamic viscosity and the Schmidt number respectively.

Following the expression proposed by Colin et al. [88] for modeling the efficiency function in terms of the dimensionless wrinkling factor, Ξ, local filter width, Δ, unstrained laminar flame speed, S_L^0, thickness of the laminar (δ_L^0) and thickened flames (δ_L^1), and local sub-grid scale velocity fluctuation, u'_Δ :

$$E = \frac{\Xi(\delta = \delta_L^0)}{\Xi(\delta = \delta_L^1)} \geqslant 1 \tag{2.9}$$

$$\Xi = 1 + \alpha\left(\frac{2ln2}{3C_{ms}(Re_t^{1/2}-1)}\right)\frac{u'_\Delta}{S_L^0}\Gamma\left(\frac{u'_\Delta}{S_L^0}, \frac{\Delta}{\delta_L^0}\right) \tag{2.10}$$

$$\Gamma\left(\frac{u'_\Delta}{S_L^0}, \frac{\Delta}{\delta_L^0}\right) = 0.75\left(\frac{\Delta}{\delta_L^0}\right)^{2/3} exp\left[-1.2\left(\frac{u'_\Delta}{S_L^0}\right)^{-0.3}\right] \tag{2.11}$$

The term $\alpha\frac{u'_\Delta}{S_L^0}\Gamma$ expresses the increase in flame wrinkling due to the turbulent stretch. While the function Γ represents the dimensionless stretch of a flame with velocity S_L^0 and thickness δ_L^0 impacted by a range of vortices. This function, Γ,

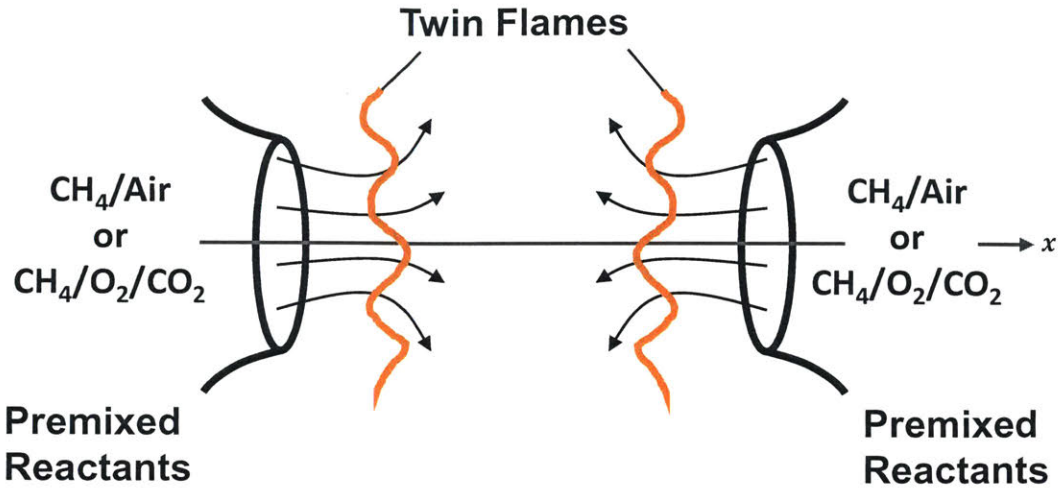

Figure 2-6: Numerical premixed laminar twin flame configuration setup

attempts to estimate the strain effect of the flow on the flame. When the flame propagation estimated using this combustion model is weak, either due to the effects of strain or temperature, extinction occurs as the convection-diffusion balance is upset and so reaction rates are very low and this impacts the species conservation equations. This formulation has also been used extensively in very recent studies [94, 95].

Reactions are taken into account using an appropriate chemical mechanism depending on the mixture type. Choosing this mechanism is one of the most important aspects of this combustion model since it greatly impacts the results as will be discussed later in Chapter 5.

2.2.2 Chemkin

CHEMKIN-PRO is used to perform all of the consumption speed and extinction strain rate calculations in this thesis.

A one-dimensional strained flame model (OPPDIF module) is used to compute the consumption speed at different strain rates. The laminar premixed flame is stabilized in a planar stagnation flow, and extinction occurs when higher strain rates push the opposed twin flames closer together. Figure 2-6 shows this setup. The distance between the two nozzles is set to 1.4 cm. 1000 grid points is also the maximum number

allowed to resolve the computational domain. We use an absolute tolerance of 1 x 10^{-9} and relative tolerance of 1 x 10^{-4} to determine convergence of the governing equations. The strain rate is taken as the maximum axial velocity gradient on the inlet's side just before the flame. CHEMKIN-PRO outputs the different properties of the mixture at each position along the flame and then the consumption speed, S_c, of the flame is calculated using:

$$Sc = \frac{\int_{-\infty}^{\infty} \dot{q}'''/c_p dx}{\rho_u(T_b - T_u)} \tag{2.12}$$

where $\dot{q}'''$ is the volumetric heat release rate, c_p is the specific heat of the mixture, x is the axial coordinate, ρ_u is the unburned mixture density, and T_u and T_b are the unburned and burned temperatures, respectively. Extrapolating the consumption speed to a strain rate of zero gives the laminar burning velocity. Multicomponent and thermal diffusion effects are also included in every numerical simulation.

The extinction strain rate, K_{ext}, is calculated using the premixed twin flame configuration where twin flames are formed near the stagnation plane of the two opposed CH_4/Air or $CH_4/O_2/CO_2$ flows (see figure 2-6). The extinction strain rate is obtained from curves of the maximum temperature and the strain rate. Besides the adiabatic flame, gaseous radiation for oxy-flames was included using an optically thin radiation model with a Plank mean absorption coefficient. The simple optically thin model has been frequently used in studies to examine the effects of CO_2 dilution on the flame radiation for $CH_4/O_2/CO_2$ mixtures [96, 97, 98]. In recent work [18] simulations adopting this radiation model were found to produce the most accurate extinction strain rates when compared to experimental results (shown later in Figure 3-8). By using this radiation model, we are considering the maximum impact of radiation on extinction for these mixtures since it generally over-predicts radiative losses. Effects of radiation led to changes on the order of 10% and 1% for oxy-flames and air-flames respectively. Therefore, we only included radiation in the oxy-flame computations.

This setup is used in most of the laminar flame profiles and calculations we show in the forthcoming chapters to compare with turbulent flames. However in Section

6.3, unlike before where both jets are identical mixtures of premixed reactants, in these results, we model one jet containing a premixed unreacted mixture and another containing equilibrium products of the mixture, but at various product temperatures. We use this to compute flame profiles under different levels of heat loss with product temperatures extracted from LES simulations as will be explained later.

Chapter 3

Scaling Flame Stabilization Modes in the Swirl Combustor

3.1 Introduction

In this chapter, we establish the stability characteristics for flame macrostructure transitions of turbulent oxy-flames in a gas turbine combustor. We compare the conditions leading to the stabilization of turbulent methane air and oxy-flames in the outer recirculation zone (ORZ) of our lean premixed acoustically decoupled swirl combustor. The appearance of a flame in the ORZ is an important flame macrostructure transition that was previously shown to be associated with the onset of thermo-acoustic instability under acoustically coupled conditions [3]. The study discussed in this chapter was also motivated in part by an early observation for methane-air flames where it was shown that a Karlovitz number criterion, based on the extinction strain rate, could adequately model the flame transition in the ORZ [4].

3.1.1 Literature Review

Changing the diluent from N_2 to CO_2 impacts the combustion process because of the differences in thermo-physical properties, chemical kinetics and radiative properties [67, 13, 2, 46, 99]. N_2 and CO_2 have sizable differences in density, specific heat

capacity and diffusivities. CO_2 dilution impacts the chemical kinetics by affecting the radical pool mainly through the reaction $CO_2 + H \rightleftarrows CO + OH$ [9]. Moreover, the CO_2 dominated combustion products lead to more radiative heat exchange with the surroundings, compared to air-flames.

These differences impact the flame macrostructures and there have been a number of studies on premixed methane oxy-flames in swirl-stabilized combustion systems [46, 99, 83, 2, 100]. Shroll et al. [46] investigated thermo-acoustic stability of premixed $CH_4/O_2/CO_2$ and $CH_4/O_2/N_2$ mixtures in a swirl combustor. Oxy-flames were kept at stoichiometric conditions, which is the practical operating condition owing to the relatively large O_2-production cost; variable CO_2 dilution levels were used to keep the same adiabatic flame temperature as the air-flame. They found that the transition between thermo-acoustic modes is mainly a function of adiabatic flame temperature.

Watanabe et al. [99] compared air and oxy-flames in the same premixed swirl combustor considered in this thesis. Different flame shapes were observed when comparing air and oxy-flames with the same inlet Reynolds number (Re), swirl number (Sw), adiabatic flame temperature (T_{ad}), and equivalence ratio (ϕ).

The effects of swirl number and adiabatic flame temperature on the lean stability and shapes of premixed air and oxy-flames were analyzed by Jourdaine et al. [83]. Air and oxy-flame shapes matched when the swirl number and flame temperature were the same for both, at Reynolds numbers less than 20,000.

Amato et al. [2] focused on the lean blowoff limit and showed that the operability boundaries of a CO_2 diluted system reduces significantly compared to methane-air mixtures in a premixed swirl combustor; this was attributed to the slower kinetics of $CH_4/O_2/CO_2$. The CO_2 diluted mixture was found to blowoff at adiabatic flame temperatures 300 K higher than the air mixture for a given nozzle exit velocity, showing that the adiabatic flame temperature does not govern the flame static stability.

Work on oxy-combustion has been also carried-out in a swirl combustor by Kutne et al [100] at atmospheric conditions. The O_2 mole fraction in the oxidizer mixture, as well as the equivalence ratio and thermal power were varied to also study the flame macrostructure and static stability at lean conditions. Here, an enhanced stability was

found as the O_2 fraction in the oxidizer was raised; they attributed this observation to the change in laminar burning velocity and Reynolds number.

Several researchers reported the existence of different flame shapes or macrostructures in swirl-stabilized combustion with air as the oxidizer. These have been previously documented as functions of different parameters such as the fuel composition, equivalence ratio, Reynolds number, swirl number, as well as centerbody geometry [101, 102, 103, 104, 105]. Similar swirling flame macrostructures have also been reported for oxy-flames under stoichiometric conditions [46]. Most of these studies reported the following flame macrostructures: columnar tubular flames (flame I); bubble-columnar flames (flame II); single conical flames stabilized along the inner shear layer, ISL, (flame III); and a double conical flame with an additional flame front stabilized in the outer recirculation zone and along the outer shear layer, OSL, (flame IV). These different shapes were illustrated in Figure 1-3.

Recently, it was demonstrated that there is a strong correlation between these flame macrostructures, the transitions among them, and the different thermo-acoustic modes observed in a swirl-stabilized combustor [3]. The sharp and sudden transition to limit-cycle pressure oscillations was concomitant with the flame shape transition from flame III to IV in acoustically decoupled combustion. For this reason, examining the conditions for flame shape transitions is of critical importance.

Efforts to model this transition have recently been carried out [4, 106]. Taamallah et al. [4], studied the physical mechanism leading to a flame transitioning to the ORZ in methane-air combustion. For each operating condition, there was a critical ϕ_{onset} at which the flame appears in the ORZ and ultimately stabilizes along the OSL. They found that the appearance of the flame in the ORZ starts intermittently and is associated with a flame spinning along with the predominately azimuthal ORZ flow at a clearly defined frequency, f_{ORZ}. It was shown that f_{ORZ} is a surrogate for the flow conditions in that zone and is weakly affected by chemistry. The associated Strouhal number ($St = \frac{f_{ORZ} \cdot D_{in}}{U_{in,bulk}}$) was shown to be independent of the inlet velocity but the kinematic viscosity was not varied to extend that independence to the Reynolds number. This will be tested in the current work. For air flames, the survival of a

flame in the ORZ was represented as a balance between a characteristic flame time, τ_{flame}, (taken as the inverse of the extinction strain rate, K_{ext}) and the ORZ flow time, τ_{flow}, (taken as the inverse of the ORZ spinning frequency, f_{ORZ}). f_{ORZ} can also be interpreted as a surrogate for the bulk strain rate in the ORZ; following this interpretation, the flame can survive in the ORZ when its extinction strain rate is higher than the prevailing strain rate.

3.1.2 Objectives

In this chapter, we investigate the transition from flame III to flame IV for methane oxy-combustion in the swirl combustor. The hypothesis is that the appearance of the oxy flame in the ORZ is governed by the balance between the extinction strain rate and prevailing strain rate in the ORZ as was shown previously for methane air-combustion [4]. The following questions will be answered:

1. How does the critical ϕ at which the flame appears in the ORZ change when switching from air to oxy flames ?

2. In order to isolate the chemical effects when comparing air and oxy flames, what inflow parameters lead to similar underlying flow conditions in the ORZ ?

3. Can the extinction strain rate be used as a scaling parameter for flame stabilization in oxy-combustion, and how similar are the scaling curves for CH_4/Air, CH_4/H_2/Air and $CH_4/O_2/CO_2$ mixtures ?

3.2 Results and Discussion

When comparing air and oxy-combustion, certain parameters need to be held constant in order to isolate the desired effect. Some studies keep the inlet Reynolds number constant to satisfy dynamic similarity. Others keep the thermal input constant to make it easier to test the retrofitting of existing air combustors. Other studies compare air and oxy-flames at the same adiabatic flame temperature in order to have

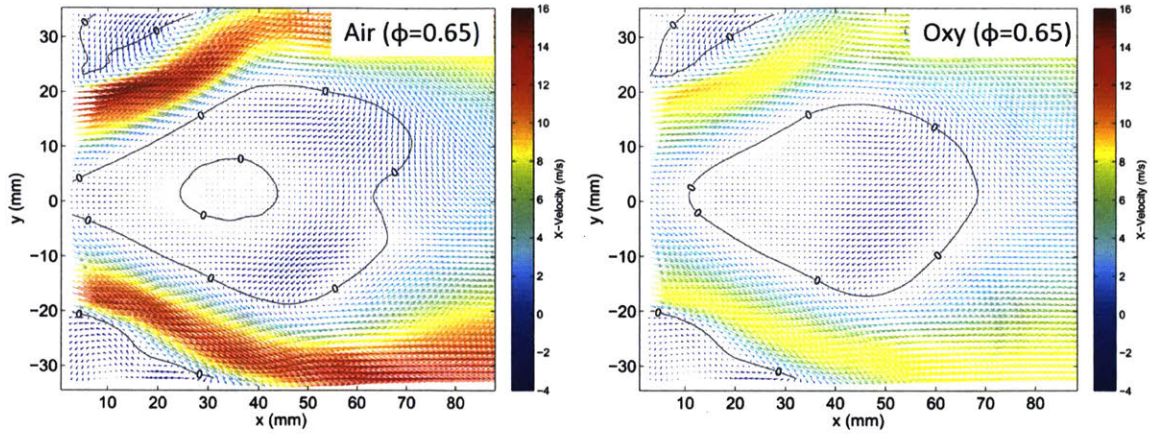

Figure 3-1: Time-averaged PIV data for air (left) and oxy (right) at Re=20,000 and ϕ=0.65. The zero axial velocity contours are indicated by the black lines.

similar combustor and turbine inlet temperatures, a major constraint in gas turbine combustion. The choice of inlet parameter to hold constant for comparisons is crucial and an important part of this work.

In this study, we vary equivalence ratio (ϕ), the inlet velocity (U_{in}) and the inlet Reynolds number (Re_{in}) in order to compare air and oxy-combustion and isolate thermo-chemical effects (Table 3.1); all other parameters are held constant (including the inlet temperature to the combustor at 300 K). For oxy-combustion, the CO_2 mole fraction (x_{CO_2}) is adjusted to obtain the same T_{ad} at the same ϕ, when compared to combustion in air. For example, at T_{ad} = 1666 K for CH_4/Air combustion for ϕ=0.60; in order to obtain the same T_{ad} for a $CH_4/O_2/CO_2$ mixture at ϕ=0.60, we impose x_{CO_2}= 0.642.

Inlet Gas	ϕ	**Flame Shape**	**Re (x 1000)**	U_{in} **(m/s)**
$CH_4 + O_2 + N_2$	0.56 - 0.65	III - IV	10 - 35	4-15
$CH_4 + O_2 + CO_2$	0.57 - 0.64	III - IV	14 - 35	4-10

Table 3.1: Experimental testing conditions in the swirl combustor

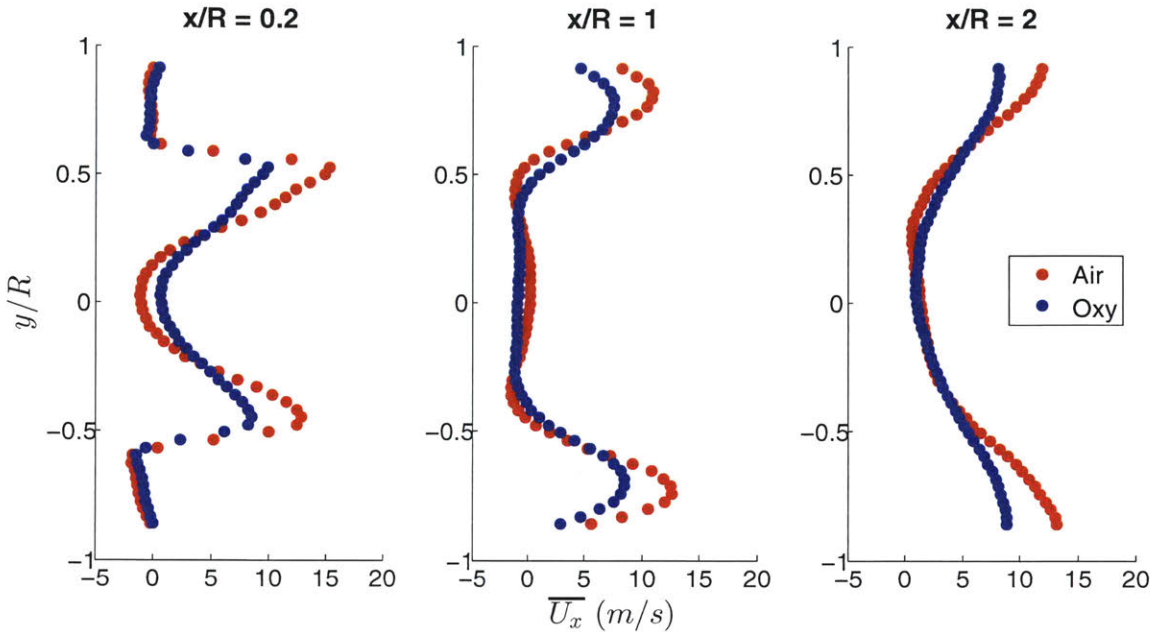

Figure 3-2: Mean axial velocity profiles at Re=20,000 and ϕ=0.65 comparing air and oxy mixtures at several axial (x/R) locations in the swirl combustor.

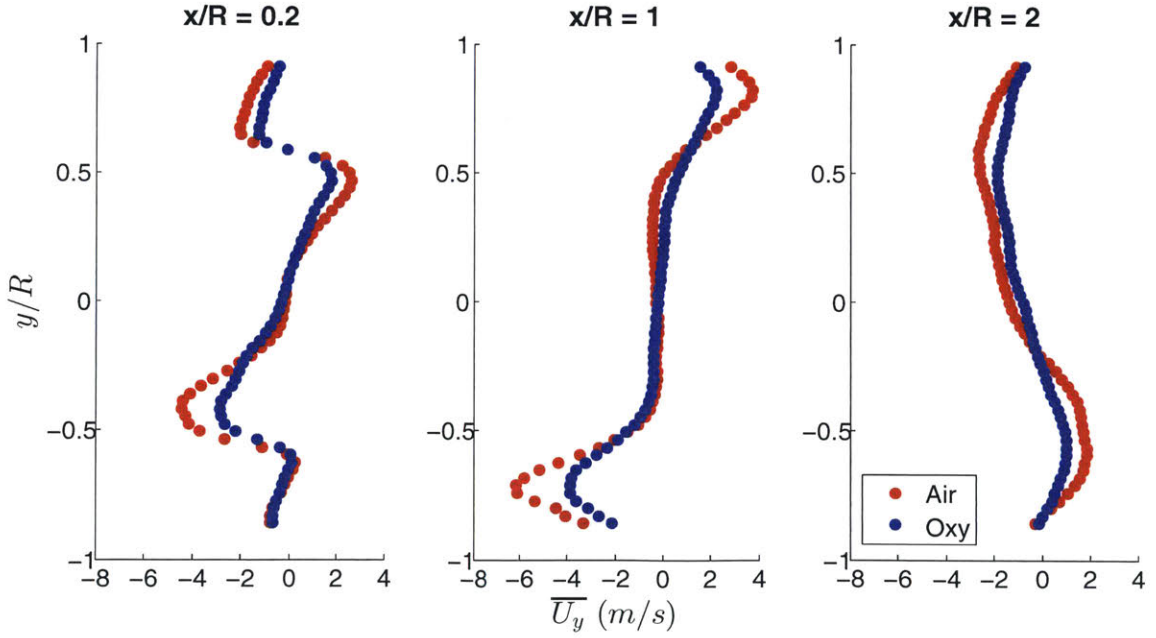

Figure 3-3: Mean transverse velocity profiles at Re=20,000 and ϕ=0.65 comparing air and oxy mixtures at several axial (x/R) locations in the swirl combustor.

3.2.1 Flow Fields

We begin by comparing the flow fields of the air and oxy combustion mixtures using the PIV data available at Re=20,000 and ϕ=0.65. The velocity vectors for these mixtures are plotted in Figure 3-1 along with the zero axial velocity contours. At the same Reynolds number, the two mixtures have vastly different flow fields. Each mixture has distinct recirculation zones, as indicated by the black lines, especially the inner recirculation zone (IRZ). The IRZ in oxy-combustion is shorter and begins after the sudden expansion (x=0).

The axial velocity magnitudes in the jets are also much higher for the air mixture. In order to keep the Reynolds number fixed, due to the density differences of the mixtures (N_2 vs CO_2), the inlet bulk velocity is lower for oxy than air (U_{in}=5.4 vs 8.4 m/s at Re=20,000). If we plot the axial and transverse velocity profiles at several axial locations, this difference is clearly seen (Figures 3-2 and 3-3). 'R' refers to the radius of the combustor (R = 37.5 mm). The velocities in the jet regions for the air case are about 1.5 times those of the oxy case mainly due to the differences in inlet velocities.

Therefore we observe that by keeping the Reynolds number constant when comparing the two mixtures, there are still significant differences in the flows which can lead to very different flow fields in the ORZ. Hence the effect of chemistry cannot be isolated. The next step is to investigate which inlet conditions should be chosen in order to maintain similar flow fields (and strain rates) in the ORZ. The important question to answer is, is it more relevant to impose the same inlet Reynolds number or the same inlet velocity ?

3.2.2 ORZ Flow Dynamics

During the transition from flame III to IV for both air and oxy-flames it was observed that the appearance of the flame in the ORZ to be intermittent over a range of equivalence ratios and associated with a flame spinning frequency (f_{ORZ}). This ORZ flame is spinning azimuthally at that clearly defined frequency, f_{ORZ}, predominately

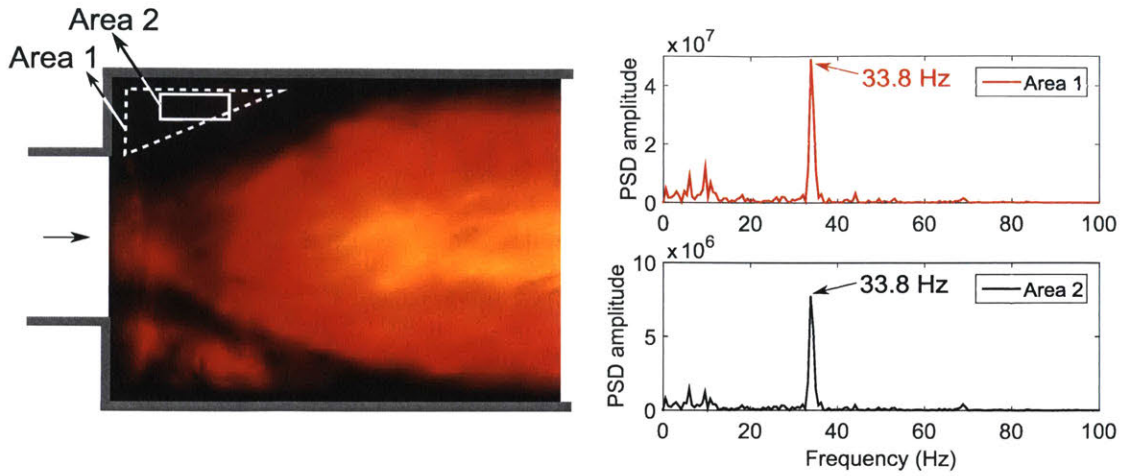

Figure 3-4: Left : A sample of oxy-flame chemiluminescence image (at U_{in}=9.9 m/s and ϕ=0.67) showing the field of view and two different choices for the area used to integrate the ORZ flame signal. Right : FFT obtained using two areas covering the ORZ.

dictated by the flow and independent of the fuel and equivalence ratio as was shown by Taamallah et al. [4]. High speed chemiluminescence data is acquired during these transitions for each mixture and a Fast Fourier Transform (FFT) algorithm is applied to the chemiluminescence signal integrated over an area that encompasses the ORZ in order to obtain f_{ORZ}. The frequency extracted from the images is found to be insensitive to the choice of the area over which the signal is integrated, as shown in Figure 3-4.

This measured f_{ORZ} is used as a surrogate for the flow conditions in the ORZ. Figure 3-5 depicts f_{ORZ} for both air and oxy flames plotted as a function of both Re_{in} and U_{in}. The spinning frequency of the ORZ flame linearly increases with increasing inlet Reynolds number and inlet velocity. However we observe that when f_{ORZ} is plotted versus the inlet velocity, the air and oxy flames' plots collapse despite the different densities and dynamic viscosities. This shows that the ORZ flow dynamics are only dictated by the bulk inlet velocity rather than the inlet Reynolds number. This is also seen in Figure 3-6 where the Strouhal number is independent of the Reynolds number at a constant value of 0.12 regardless of the two mixtures.

The above result has the important implication that, in order to maintain similar flow conditions in the ORZ when comparing air versus oxy combustion, it is more

relevant to fix U_{in} rather than Re_{in}.

3.2.3 Flame III to IV Transition

After examining the ORZ flow dynamics, next we compare the equivalence at which the flame appears in the ORZ for air and oxy-flames, ϕ_{onset}. This is done by raising ϕ gradually starting from close to lean blow-off conditions. When the flame appears in the ORZ, ϕ_{onset} is recorded along with high speed flame chemiluminescence during the intermittent transition. The chemiluminescence images were used to compute the ORZ flame spinning frequencies (f_{ORZ}) shown earlier. Each ϕ_{onset} measurement is repeated three times; mean values are shown along with error bars.

First, air and oxy combustion are compared at the same inlet Re_{in} in Figure 3-7a which illustrates the dependence of ϕ_{onset} on Re_{in}. At larger Re_{in}, a higher ϕ is required for both air and oxy flames in order for the transition to an ORZ flame to take place. Moreover, for a fixed Re_{in}, the air flame requires a ϕ about 0.01 higher to stabilize in the ORZ.

The trends are different when ϕ_{onset} is plotted versus U_{in} (Figure 3-7b). The air flames now transition at earlier equivalence ratios than oxy flames. This is closer to what might be expected since oxy flames are considered "weaker" than air flames due to their lower laminar burning velocity (S_L^0) for the same T_{ad} and ϕ [62]. Another interesting observation here is the existence of a crossover point at an equivalence ratio of about 0.56 where the air and oxy flames both have an OSL-stabilized flame at the same inlet bulk velocity of about 3 m/s.

Using the results from the previous section, we now know that the experimental results in Figure 3-7b are more relevant if we want to purely isolate the thermochemical effects on the ORZ flame transition. In order to study the two time scales present in the mixtures, we can represent the flow time scale using f_{ORZ} derived from Figure 3-5b since it is only dependent on U_{in}. The next unknown becomes, which flame property can be used to represent the flame time scale to help explain the trends we see in Figure 3-7b? Figure 3-7 also shows the laminar burning velocity of the two data points closest to the crossover point around ϕ=0.56. As can be seen, there are

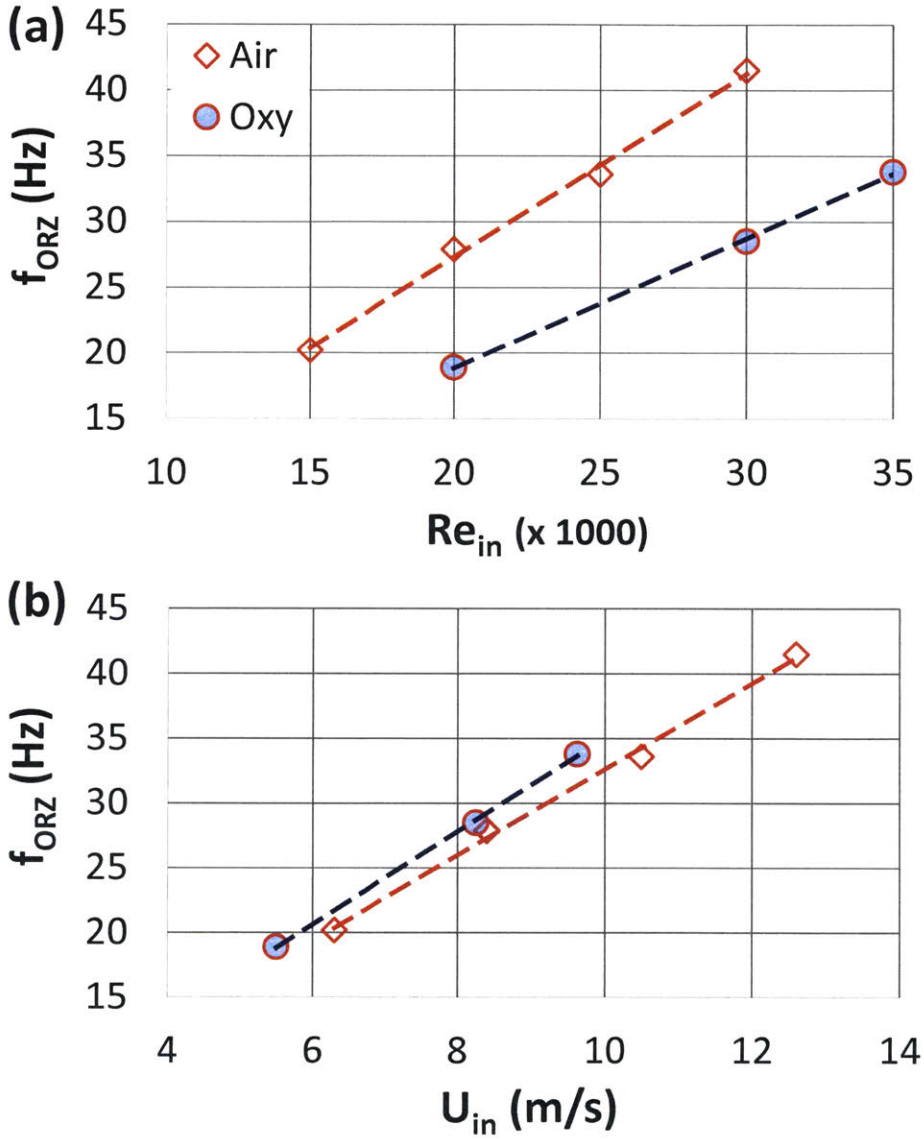

Figure 3-5: ORZ flame spinning frequency as a function of: (a) Re_{in}, (b) U_{in}.

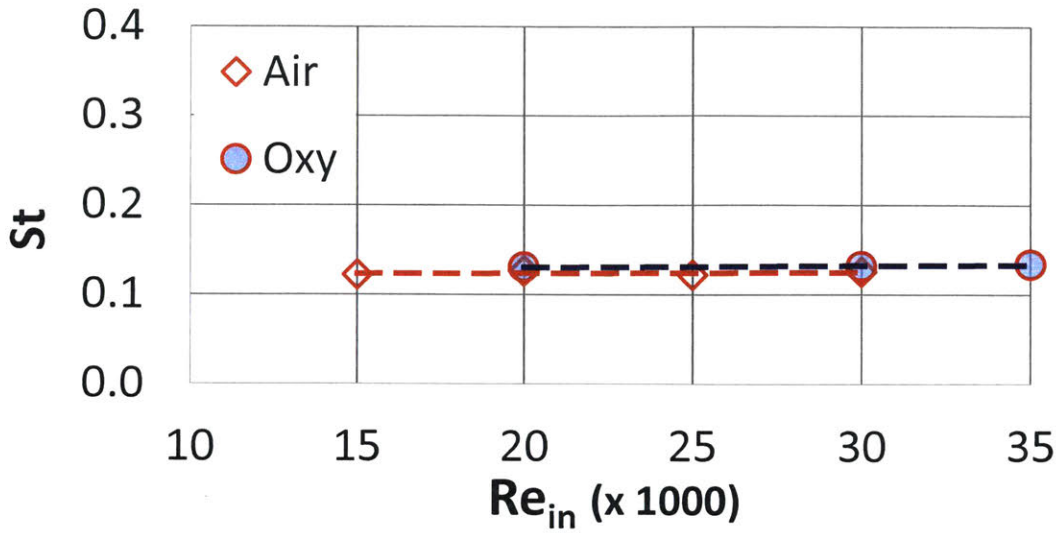

Figure 3-6: Strouhal number's ($St = \frac{f_{ORZ} D_{in}}{U_{in}}$) dependence on the inlet Reynolds number.

differences in flame speeds of the two mixtures at the same inlet velocity and equivalence ratio transition. Thus it fails to explain this transition adequately and another flame property is needed. In the next section, we test the use of the extinction strain rate as a surrogate for the flame time scale as it has been recently shown to be of importance in understanding premixed flame stabilization [107, 4, 6].

3.2.4 Flame III to IV Scaling

Extinction Strain Rates

Extinction strain rate (K_{ext}) calculations are performed using CHEMKIN-PRO [108]. Details about these calculations were explained in section 2.2.2. The air-flame (CH_4/ O_2/N_2) is modeled using the commonly used GRI-Mech 3.0 [54]. It involves 53 species and 325 elementary reactions. In this chapter, the oxy-flame ($CH_4/O_2/CO_2$) kinetics are modeled using the mechanism proposed by Mendiara and Glarborg [109]. It involves 49 species and 350 elemental reactions. This mechanism has been recently developed specifically for methane oxy-combustion with GRI-Mech 3.0 as the starting point and with nitrogen chemistry removed. In a previous study [18] we also showed that the Glarborg mechanism had a better extinction strain rate agreement

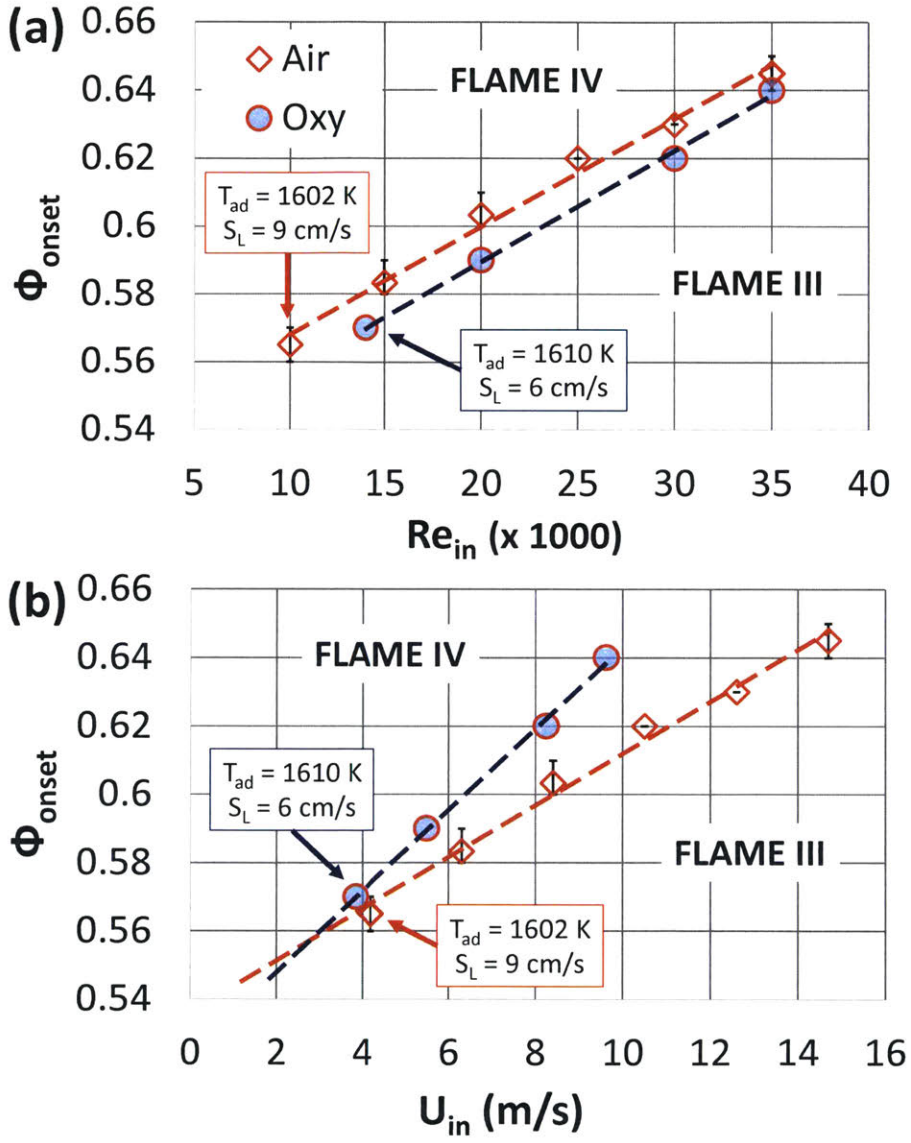

Figure 3-7: Effect of (a) Re_{in} and (b) U_{in} on the critical equivalence ratio. Each measurement is repeated three times and subsequent error bars are displayed.

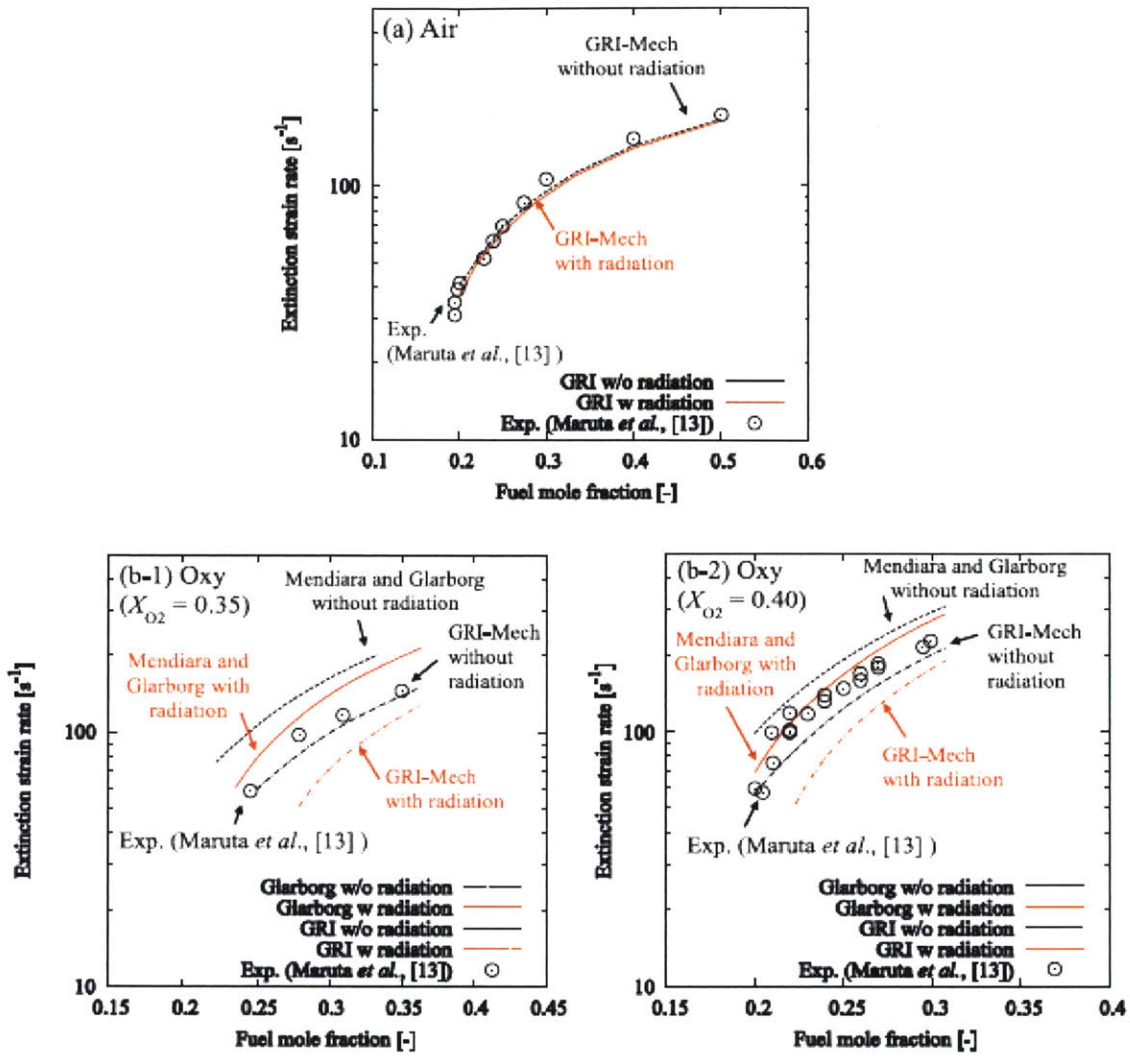

Figure 3-8: Characteristic flame time versus characteristic ORZ flow time for Oxy and air flames. Flame time computed at 300 K and 400 K. (Figure adapted from Ref. [18])

with non-premixed experiments by Maruta et al [66], compared to calculations using GRI-Mech 3.0 (see Figure 3-8). The results using GRI-Mech 3.0 underpredicted extinction strain rates. Premixed experimental extinction strain rates for these oxy-combustion mixtures are not yet available in the literature in order to further validate the mechanism under the conditions studied in this thesis. Recent studies have also used this mechanism and have found good agreement in their results [99, 18]. Gaseous radiation for oxy-flames was included using an optically thin radiation model.

The computed extinction strain rates are plotted as a function of equivalence ratio

	U_{in} (m/s)	Re_{in} (10^3)	ϕ	T_{ad} (K)	T_{ORZ} (K)
Air	8.4	20	0.59	1648	407
Oxy	8.4	29.5	0.59	1648	402
	5.7	20	0.58	1630	398

Table 3.2: Measured T_{ORZ} for air and oxy flames just before the appearance of an ORZ flame.

for air and oxy-flames (Figure 3-9), first with atmospheric reactant inlet temperatures (T_{in} = 300 K). Air and oxy flames' K_{ext} increases with ϕ but at different rates; this leads to the existence of an equi-extinction strain rate K^*_{ext} point at $\phi^* \approx 0.70$ where oxy and air flames are equally resistant to the strain rate (such a crosspoint was observed in previous studies [99]). We also noticed a crosspoint in Figure 3-7b with the existence of an experimental equi-transition point; however this occurred at a lower equivalence ratio ($\approx$ 0.56).

The choice of computing K_{ext} at T_{in} = 300 K was made using the fact that the reactants entering the combustor are at atmospheric conditions. However, since we are mainly investigating the stabilization of a flame in the ORZ, it would make more sense to understand the thermal conditions present in that zone and compute extinction strain rates at those conditions. Using a thermocouple placed inside the ORZ, temperature measurements are recorded and are shown in Table 3.2. T_{ORZ} is the steady state ensemble-averaged temperatures of the ORZ recirculating reactants, at ϕ just before the ORZ flame appearance.

While the inlet temperature of the combustor is ambient, we see that the average ORZ temperature, T_{ORZ}, is higher and closer to 400 K. There is a minor variation in this temperature with inlet velocity and mixture type. It is also important to note that the measured ORZ temperature varies with ϕ. For example, for air-combustion, it ranged from 374 K at U_{in} = 5.5 m/s and ϕ = 0.56, to 419 K at U_{in} = 12.6 m/s and ϕ = 0.63.

Since we now know that the temperatures in the ORZ are in fact closer to 400 K, K_{ext} is recomputed using this new inlet temperature and results are shown in Figure

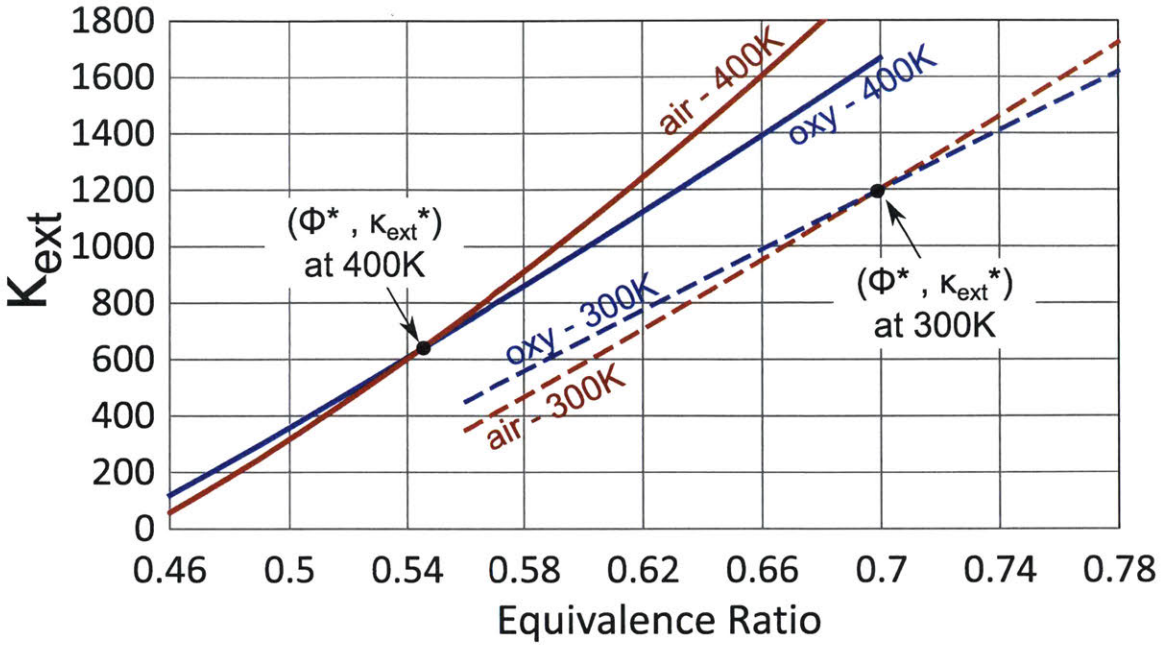

Figure 3-9: Calculated extinction strain rates for air and oxy flames at 300 K and 400 K inlet temperatures.

3-9. K_{ext} increases with T_{in} as might be expected for both air and oxy flames but interestingly enough, the crosspoint we saw earlier at 300 K has now shifted to $\phi \approx 0.55$. The higher T_{in} has a weaker effect on the oxy-flame's slope which causes the crossover point to shift to leaner conditions. The exact reason for this will be investigated further in the next chapter. This new calculated crossover equivalence ratio of 0.55, is in much better agreement with the experimental crosspoint we observed earlier in Figure 3-7b with $\phi \approx 0.56$.

ORZ Scaling Curves

Using the results from Figures 3-5b and 3-9, we replace the axes of Figure 3-7b by their respective characteristic time scales. We define a characteristic ORZ flow time based on f_{ORZ}, $\tau_{ORZ\ flow} = 1/2\pi f_{ORZ}$, and a characteristic flame time based on K_{ext}, $\tau_{flame} = 1/K_{ext}$. At each ϕ_{onset} required for the transition from Flame III to IV, the imposed flow time is plotted against the associated flame time scale computed at both $T_{in} = 300$ and 400 K (Figure 3-10). From Table 3.2 we know that the reactants in the ORZ are at temperatures closer to 400 K. The importance of taking into account

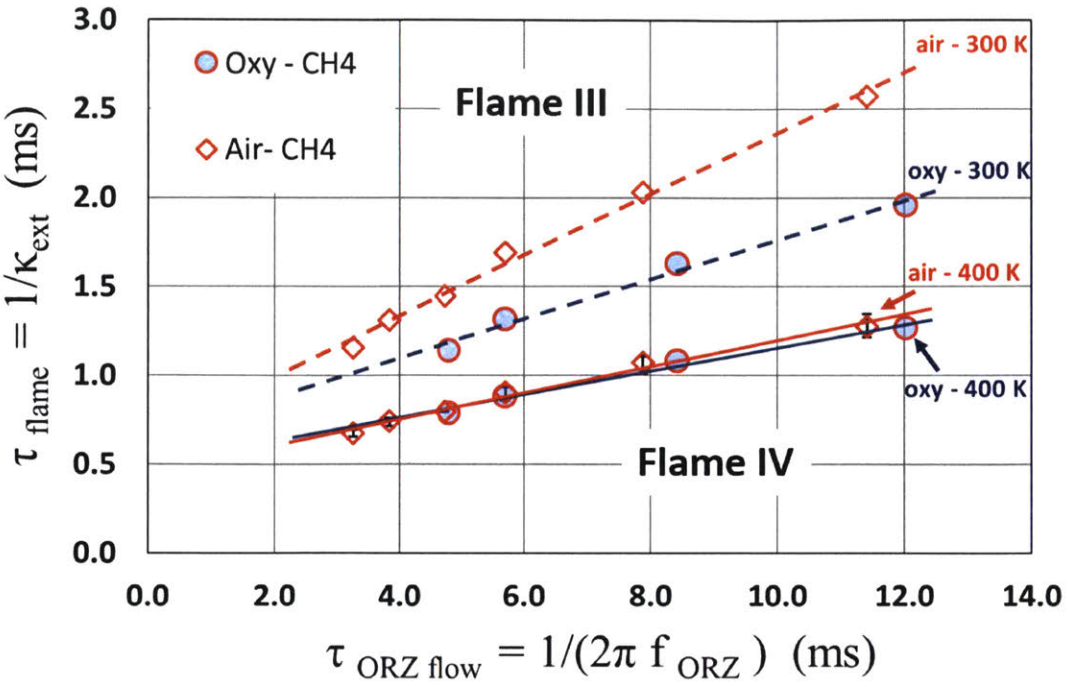

Figure 3-10: Characteristic flame time versus characteristic ORZ flow time for air and oxy flames. Flame time is computed at 300 K and 400 K.

the preheating of the ORZ reactants is clearly seen in the figure; both the air and oxy data only collapse into a single line that splits the flow-flame times space into flames III and IV regions, at 400 K. This is not the case when τ_{flame} is computed at T_{in} = 300 K. *Therefore this proves that modeling and scaling flame stabilization also requires an accurate understanding of the thermal conditions present in that zone of interest.*

Taking this scaling a step further, data from a previous study on CH_4/H_2/Air flames [4] are reproduced and plotted in Figure 3-11 along with the oxy data from the current work. The extinction strain rates of the data points from this previous study were recomputed at T_{in}=400 K to better account for the temperatures in the ORZ. The figure shows results for multiple swirl numbers, Reynolds numbers, fuels and oxidizers. Despite all the different variables between the data points, we once again observe that the results fit relatively well along a line separating the conditions between Flame III and Flame IV. Specifically, the fact that the CH_4/H_2/Air mixtures with relatively fast chemistry (high S_L^0) [110], and the $CH_4/O_2/CO_2$ mixtures with

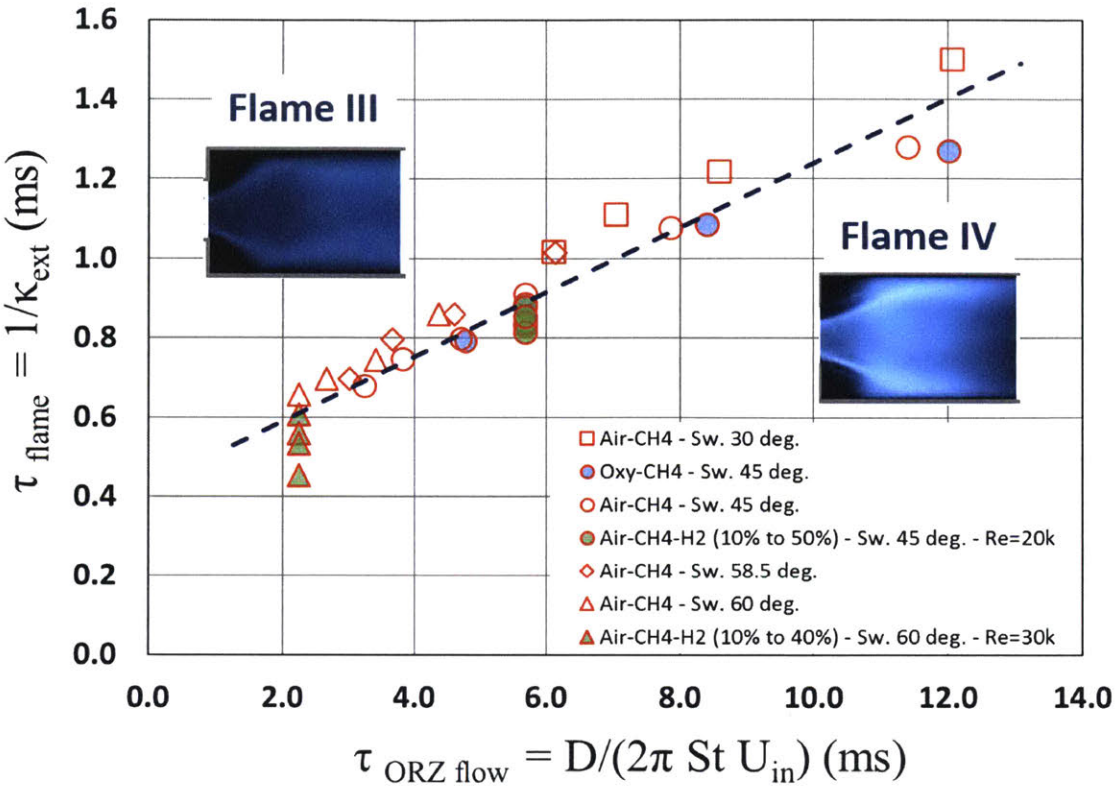

Figure 3-11: ORZ scaling curve for CH_4/H_2/Air and $CH_4/O_2/CO_2$ flames at different Reynolds numbers and Swirl numbers. Flame times are all computed at 400 K.

slow chemistry both collapse onto the same curve in the τ_{flame}-$\tau_{ORZ\ flow}$ space is a novel finding. Therefore, one of the most important outcomes from this plot is the establishment of the extinction strain rate as a critical flame parameter for understanding and scaling these premixed reacting flows. This point will be emphasized and expanded upon throughout the rest of this thesis.

3.3 Conclusions

In this chapter, we examined the specific flame transition linked to the occurrence of combustion instabilities in a gas turbine combustor for methane oxy-combustion mixtures. The following conclusions were reached:

1. The spinning frequency of this ORZ flame is a purely kinematic phenomenon with a fixed Strouhal number independent of the Reynolds number. This makes

the inlet velocity a more relevant parameter for maintaining similar flow conditions in the ORZ and isolating thermo-chemical effects, when comparing air to oxy-combustion.

2. There exists a flame transition point where the onset of flame stabilization in the ORZ takes place at the same equivalence ratio and inlet velocity in both air and oxy-combustion. This equi-transition point occurs at a point where the laminar burning velocities between the two mixtures are much different.

3. By defining the inverse of the ORZ spinning frequency as a characteristic flow time and the inverse of the extinction strain rate as a characteristic flame time scale, we constructed a map with a single line separating two different flame stabilization modes, valid for a whole range of different inlet conditions (Swirl numbers, Reynolds numbers, fuels and oxidizers).

4. In order to successfully scale this data for the different mixtures (CH_4/H_2/Air and $CH_4/O_2/CO_2$), the extinction strain rate must be computed at the realistic temperature of the ORZ reactants.

These results serve to promote a better understanding of the governing mechanism behind flame stabilization in turbulent swirling oxy-combustion systems. The most novel finding is the importance of the extinction strain rate as a flame parameter for scaling these flows. In the next chapter we delve deeper into what exactly impacts extinction strain rates in oxy-combustion mixtures, and also why we observe this dependence of extinction strain rate on the inlet temperature. In the other forthcoming chapters, we investigate what other flow features (ex. recirculation zone lengths) also scale with extinction strain rate and whether LES can capture the correct ORZ flame transition mechanism.

Chapter 4

Response of Flames to Strain; Role of Chemistry and Transport

4.1 Introduction

Prior works have shown that when changing the fuel by adding hydrogen to a gaseous-hydrocarbon, it is the extinction strain rate that determines the flame shape [110, 4], flow-structure[5] and combustion instability triggering point [107]. This naturally leads to the question of what drives the extinction strain rate effect: Is it due to the fuel chemistry – which we refer to as the chemical effect – or due to the transport properties such as diffusivity, viscosity, etc. ?

In the previous chapter, we compared the conditions leading to the stabilization of lean turbulent methane air and oxy-flames in the outer recirculation zone (ORZ) of a premixed swirl combustor. We found that when similar bulk flow conditions are imposed, the transition in the flame macrostructure to an ORZ flame, scaled according to the extinction strain rate and can occur at different adiabatic flame temperatures. Two key points are the importance of calculating the extinction strain rates at realistic thermal conditions (in the ORZ), and the existence of a crossover point in the extinction strain rate curves for air and oxy combustion. As the inlet reactant temperature was changed, this crossover point was found to occur at different equivalence ratios portraying the different sensitivities for air versus oxy combustion. In the cur-

rent study, the explanation for these different sensitivities will be investigated further as a way to fundamentally understand the differences in air versus oxy combustion and the importance of the CO_2 effect.

4.1.1 Literature Review

The impact of these fundamental differences on the turbulent oxy-flame was also in a study by Watanabe at el. [18], where they also examined the structure of lean turbulent premixed CH_4/air and $CH_4/O_2/CO_2$ flames in a swirl-stabilized combustor at the macro and micro-scales. The CO_2 dilution in the oxy-flame was adjusted to achieve the same adiabatic flame temperature for both flames while keeping the equivalence ratio (=0.65) and Reynolds number (=20,000) the same. At these conditions, it was observed that the oxy-flame length was noticeably shorter than the air flame and the oxy-flame also appeared to burn more intensely. A similar observation was made for stoichiometric oxy flames in experiments by Shroll [39]. Although laminar burning velocities of oxy flames are lower as has been extensively reported in the literature, the turbulent dynamics properties such as the small scale wrinkling of the flame were shown to explain these observed trends. The flame surface density of the oxy flame at these conditions was found to be higher than of the air flame downstream of the expansion section. The formation of smaller wrinkles in the oxy flame was attributed to the Lewis number effects i.e. oxy-flames being more thermo-diffusively unstable.

There have not been many studies that investigate the specific role CO_2 plays in changing important flame properties (ex. flame temperature, flame speed, extinction strain rates...). Song et al. [19] isolated the chemical effects of CO_2 from the physical effects (thermochemical, transport, radiation) in methane oxy-combustion, and found that the chemical effects were primarily responsible for the reduction in combustion temperature when compared to methane-air combustion with the same oxygen concentration. For the opposed diffusion flame they studied, an oxidizer composition of 36% O_2/64% CO_2 was required for the oxy-flame to achieve the same temperature as the air-flame. They also found that the heat release rate of $CO_2 + H \rightleftarrows CO + OH$ to be most heavily impacted by CO_2 addition (see Figure 4-1). The importance of this

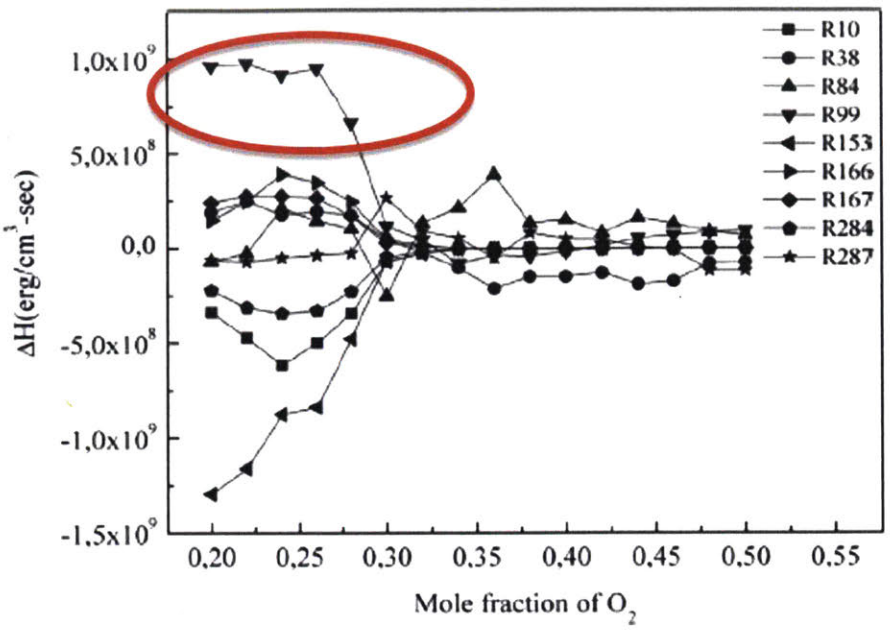

Figure 4-1: The heat release rate of elementary reactions versus the mixture O_2 mole fraction [19]. The circled data corresponds to results from the reaction $CO_2 + H \rightleftarrows CO + OH$.

reaction will be further studied in this work as well.

In a computational study by Halter et al. [7], they predominately related the heat capacity effect to the decrease in the laminar burning speed of a stoichiometric methane-air flame diluted with CO_2. The CO_2 diluted flame also caused a larger decrease in the burning speed compared to the N_2 diluted flame. In these calculations, they kept the equivalence ratio constant and equal to stoichiometry. In order to isolate the chemical effect of the CO_2 dilution, a new molecule was introduced (F-CO_2, for 'False' CO_2) which was chemically inactive. They observed the laminar burning speed for this F-CO_2 flame to be located between those corresponding to the CO_2 and N_2 diluted flames. The CO_2 dissociation effect was non-negligible but this effect became less important as the dilution level was increased.

In another study by Watanabe et al. [99], they also investigated the role of CO_2 versus N_2 transport properties on the flame consumption speed of lean premixed oxy-combustion of methane. The transport properties of CO_2 were changed to those of N_2

in the oxy calculation but the specific heat and density were kept the same in order to match the flame temperature with air-combustion. They found that the new oxy calculation (with N_2 transport properties) had a similar flame speed as the original oxy calculation but lower extinction strain rate. This shows that the CO_2 transport properties actually improve the stability of the flame by increasing the extinction strain rate. But the effect of transport properties does not affect the flame speed much, possibly implying that the chemical effect of CO_2 is mainly responsible. This will be verified and expanded upon in the current chapter.

Two types of chemical times were calculated by Amato et al. [2] for both CH_4/Air flames and near stoichiometric $CH_4/CO_2/O_2$ flames. The first time scale, the ratio of premixed flame thickness and flame speed, showed the air flame to have lower values than the oxy flame for an initial temperature of 533 K. Interestingly, the stoichiometric oxy flame had the largest chemical time and so at this point, which maximizes fuel and oxygen usage, the weakest flame stability is expected. For the other time scale, the inverse of the extinction strain rate, they showed the CO_2 dilution and near stoichiometric operation of the oxy flame had a major inhibiting effect. The air flame was found to have chemical times ten times faster at 1800 K. It is still unclear why exactly we see this difference between the two flames i.e. what exact role does the CO_2 play in the inhibiting effect?

4.1.2 Objectives

In this chapter, we aim to relate the differences in the response to strain between laminar air and stoichiometric oxy flames to help in explaining the turbulent flame structure differences. By investigating the effect of chemistry, reactant inlet temperature, product composition, heat transfer and transport properties of the CO_2 dilution in the stoichiometric oxy flame, a better understanding can be gained on the fundamental differences between these two flames. Specifically, the goals of this work are:

1. Understanding the flame stability characteristics of practical premixed stoichio-

metric oxy-combustion flames.

2. Why are there differences in the extinction strain rates and flame consumptions speeds between air and oxy flames ?

3. Since flame stabilization scaling is sensitive to the reactant inlet temperature, what effect does this inlet temperature have on the two flames ?

4.1.3 Cases Investigated

We mainly investigate five cases which are shown in Table 4.1. The two modified oxy cases were implemented by modifying the chemical mechanism and transport files used in the calculations. It should be noted that the $Oxy_{CO2\ inert}$ case is not technically "inert" since the CO_2 still participates in other reactions in the mechanism.

Case	**Label**	**Description**
Air (Lean)	Air	Lean CH_4/Air mixtures
Air (Stoichiometric)	Air_{stoich}	Stoichiometric CH_4/Air mixtures
Oxy (Base)	Oxy	Stoichiometric $CH_4/O_2/CO_2$ mixtures
Oxy (CO_2 inert)	$Oxy_{CO2\ inert}$	Stoichiometric $CH_4/O_2/CO_2$ mixtures with the forward reaction of $CO_2 + H \longleftrightarrow CO + OH$ removed
Oxy (CO_2 with N_2 transport properties)	$Oxy_{N2\ transport}$	Stoichiometric $CH_4/O_2/CO_2$ mixtures using CO_2 with N_2 transport properties (mass diffusivity, thermal conductivity, dynamic viscosity)

Table 4.1: The main cases tested in this chapter

The proper mixture compositions for given adiabatic flame temperatures for both air and oxy cases, are calculated using the open source software Cantera [23] by equilibrating the mixture at constant enthalpy and pressure (complete combustion is not assumed).

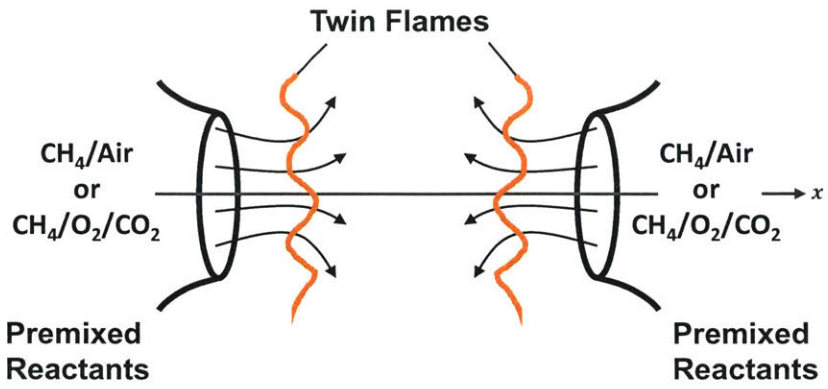

Figure 4-2: Numerical premixed laminar twin flame configuration setup

CHEMKIN-PRO [108] is used to perform all of the consumption speed and extinction strain rate calculations as explained in section 2.2.2. We use the symmetric opposed reactants setup as shown in Figure 4-2. As we show in Chapter 6, the asymmetric opposed reactants and products configuration should be used in order to better capture the effects of heat loss in the turbulent flame near the walls. The conventional definition of extinction strain rate is used (see [111]), and it is defined as the maximum axial velocity gradient just before the flame. This type of extinction model was shown to capture the turbulent flame behavior in the previous Chapter and will also be used in the rest of this thesis.

Besides the adiabatic flame, gaseous radiation for oxy-flames was included using an optically thin radiation model with a Plank mean absorption coefficient. The simple optically thin model has been frequently used in studies to examine the effects of CO_2 dilution on the flame radiation for $CH_4/O_2/CO_2$ mixtures [96, 97, 98]. In recent work [18], simulations adopting this radiation model were found to produce the most accurate extinction strain rates when compared to experimental results. By using this radiation model, we are considering the maximum impact of radiation on extinction for these mixtures since it generally over-predicts radiative losses. Effects of radiation led to changes on the order of 10% and 1% for oxy-flames and air-flames respectively. Therefore, we only included radiation in the oxy computations.

Once again the air-flame ($CH_4/O_2/N_2$) is modeled using the commonly used GRI-

Mech 3.0 [54]. For the oxy-flame ($CH_4/O_2/CO_2$) kinetics, the mechanism proposed by Mendiara and Glarborg [109] is used. As was shown in the previous chapter, this mechanism had a better extinction strain rate agreement with non-premixed experiments by Maruta et al [66], compared to calculations using GRI-Mech 3.0. The results using GRI-Mech 3.0 underpredicted extinction strain rates. Premixed experimental extinction strain rates for these oxy-combustion mixtures are not yet available in the literature in order to further validate the mechanism under the conditions studied in this chapter.

Also from the previous chapter, where we scaled the transition between flame stabilization modes in a premixed swirl combustor using characteristic flow and flame time scales, we showed that in order to successfully scale air and oxy data, the extinction strain rate must be computed at a temperature that reflects realistic thermal conditions in the outer recirculation zone. We measured this temperature to be 400 K. Therefore, in this chapter, we will continue using this criteria and so all of our strained calculations are performed with inlet reactants at 400 K unless stated otherwise.

4.2 Transport Properties

The change in diluent from N_2 to CO_2 for oxy-combustion of methane impacts the flame and combustion process due to numerous changes in some attributes including, flame temperature and mixture heat capacities, important transport properties, chemical kinetics and radiative heat transfer. In this section, the transport properties are explored by looking at how different they impact air versus oxy-combustion.

4.2.1 Flame Temperature

We start off at the common reference point of comparing the adiabatic flame temperature for air and oxy-combustion. As we mentioned before, we are looking at stoichiometric oxy-flames in this chapter. By fixing the equivalence ratio in oxy-combustion there is one more degree of freedom in mixture composition: diluent mole fraction. In order to have a fair comparison for the oxy and air flames, the same adiabatic flame

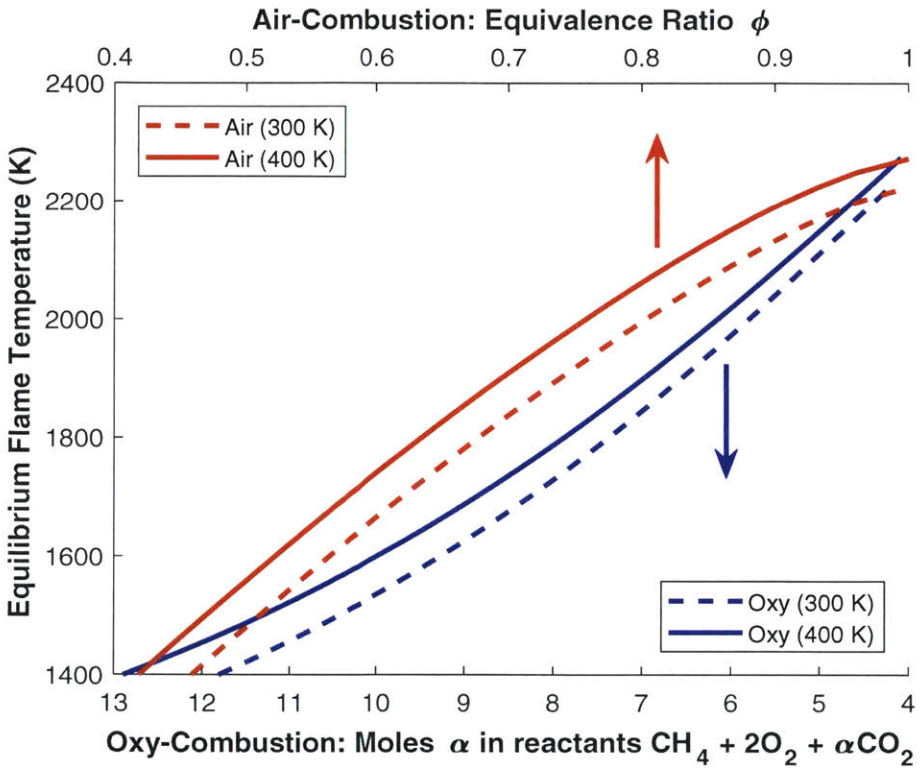

Figure 4-3: Equilibrium flame temperatures for air and oxy-combustion mixtures calculated at 300 and 400 K

temperature is used in the comparisons by varying the CO_2 diluent mole fraction in oxy-combustion and varying the equivalence ratio in air-combustion. This is the same approach throughout most of the chapter. In section 4.3 we additionally consider an air case where we have a stoichiometric mixture of CH_4 and O_2 and we vary the N_2 diluent to achieve the same adiabatic flame temperature as in the other cases ($CH_4 + 2\,O_2 + \beta N_2$).

Figure 4-3 shows equilibrium flame temperatures plotted against the equivalence ratio for air combustion and the stoichiometric oxy-combustion temperature is plotted versus a reversed axis of moles of CO_2 in the reactants to make comparisons convenient. These equilibrium calculations were done using the open source software, Cantera [23] at atmospheric pressure and for two reactant temperatures (300 and 400 K).

In other words, the main reactant mixtures are $\phi\,CH_4 + 2\,(O_2 + 3.76\,N_2)$ for air and $CH_4 + 2\,O_2 + \alpha\,CO_2$ for oxy-combustion, where ϕ and α are varied to achieve the same flame temperature. The adiabatic flame temperature given in the figure is the calculated equilibrium temperatures for reactant inlet temperatures of 300 K and 400 K at a pressure of 1 atm, since these are the conditions in our oxy-combustion experiments (see previous chapter). In all of the references to mole fractions in this chapter, the mole fraction is defined as the mole fraction in the whole reactant or product mixture, not the mole fraction in the oxidizer for example.

The heat capacity of CO_2 is about 1.7 times greater than that of N_2, therefore for oxy-combustion, one requires a greater mole fraction of O_2 in the reactants, in order to achieve the same flame temperature as in air-combustion and for the same equivalence ratio. For example, a stoichiometric equivalence ratio in both air and oxy-combustion, the O_2 mole fraction is around 33% for the oxy case compared to 21% for air.

4.2.2 Lewis Number

The diluent gas transport properties has an important influence on flame characteristics and quantities such as flame speed and stretch sensitivity. Table 4.2 compares val-

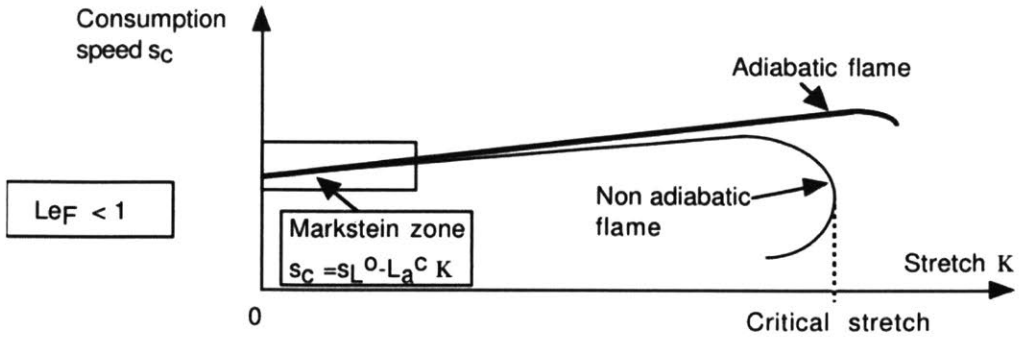

Figure 4-4: Effect of stretch on the consumption speed for fuel with Le < 1 [20]

ues of the density, thermal diffusivity, mass diffusivity (CH_4 into diluent and O_2 into diluent), and the Lewis number, Le, for air, CO_2, CH_4-Air, and CH_4-Oxy mixtures, assuming unity stoichiometry and atmospheric temperature and pressure, obtained using Cantera. The Lewis numbers for the CH_4/Air and stoichiometric $CH_4/O_2/CO_2$ mixtures are plotted versus the adiabatic flame temperature for a reactant mixture at 300 K in Figure 4-6. Since the oxy-fuel mixture is stoichiometric, we plot both the fuel Lewis number and the oxidizer Lewis number. The Lewis number is defined as:

$$Le = \frac{\alpha}{D_{k,m}} \tag{4.1}$$

where α is the thermal diffusivity and $D_{k,m}$ is the mass diffusivity between species, k, and the mixture, m. For air-combustion, the Lewis number is calculated simply using the mass diffusivity between the fuel (CH_4) and the mixture.

The Lewis number (Le) is an indirect measure of the flame intensity's sensitivity to stretch. When Le<1 the relative mass diffusion is higher than heat diffusion, therefore increasing the burning rate when the Markstein length is negative (Figure 4-4). However for Le>1, the opposite should be expected but very high strain will always lead to extinction [90] (Figure 4-5).

The Lewis number for air-combustion is around unity, as is commonly seen in the literature [110], but the stoichiometric oxy-combustion Lewis numbers are both less than one and increase with the flame temperature. This impacts the response to

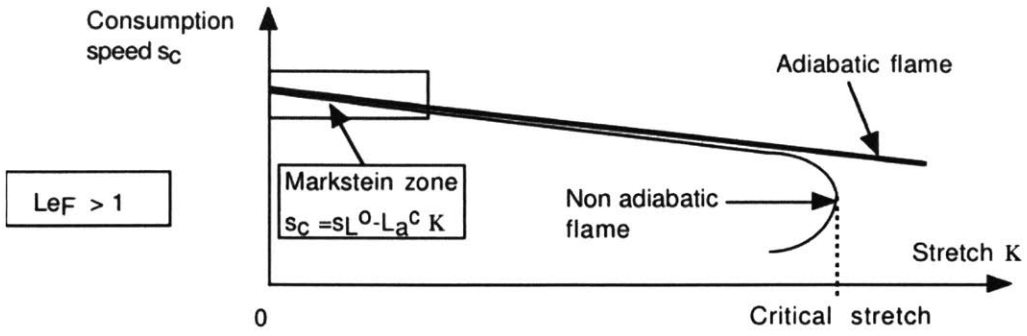

Figure 4-5: Effect of stretch on the consumption speed for fuel with Le > 1 [20]

	ρ kg/m^3	α 10^{-6} m/s^2	$D_{k,m}$ 10^{-6} m/s^2	Le (for mixtures)
Air	1.172	22.28	-	-
CO_2	1.788	11.52	-	-
CH_4	0.652	24.57	-	-
CH_4 + Air	1.123	22.44	22.40	1.002
$CH_4 + (O_2 + CO_2)$	1.495	15.27	17.16, 20.28	0.889 (O_2/CO_2), 0.753 (CH_4/CO_2)

Table 4.2: Some important transport properties for air and oxy-combustion mixtures at 300 K and 1 atm (source: Cantera [23])

strain of the two flames. As a result, the oxy flames display enhanced flame speeds as the flame is strained whereas the air flame's response is almost flat. But fuel stream Lewis numbers in general had much stronger impacts on flame location, heat release and flame dynamics than the oxidizer Lewis number [112, 113]. As can also be seen in the figure, at the higher temperatures for oxy-combustion, where there is less CO_2 in the mixture, the Lewis number approaches that of air-combustion.

Despite these differences in the Lewis numbers between the air and oxy mixtures, if we compare the mass diffusivities of the radicals into these two mixtures we do not see a significant change. Figure 4-7 shows the mass diffusivities of certain radicals into the two mixtures in order to have a better idea about the transport properties effect on the flames and Table 4.3 presents the percentage differences of these values between air and oxy. The average difference in diffusivities is only around 13% for an

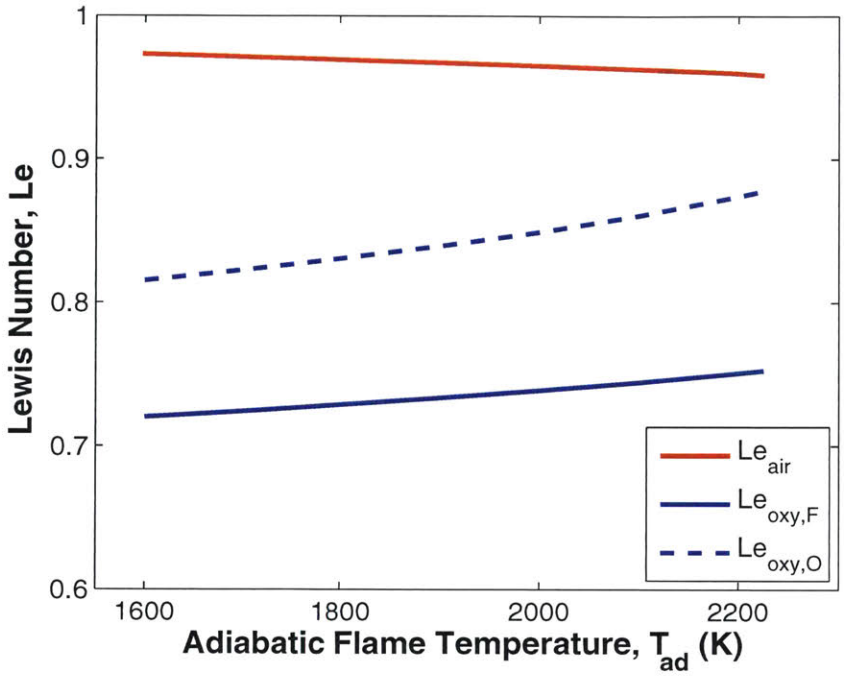

Figure 4-6: Lewis numbers of lean methane-air and stoichiometric methane-oxy flames

T_{in} (K)		300	400	600	800	1000	1200	1500
% Diff.	O	13.9%	12.7%	11.6%	11.1%	10.8%	10.7%	10.6%
	H	12.3%	10.8%	9.2%	8.4%	8.0%	7.8%	7.5%
	OH	14.1%	12.9%	11.8%	11.3%	11.0%	10.9%	10.7%
	Average	13.4%	12.1%	10.9%	10.3%	10.0%	9.8%	9.6%

Table 4.3: Differences in the mass diffusivities of radicals into the mixtures between air and oxy versus inlet temperature

inlet mixture at 300 K and this difference decreases with the inlet temperature down to 9.6% for 1500 K. This small change in the transport of the radicals when one goes from a CH_4-air mixture to a CH_4-oxy mixture, solely, does not seriously impact the flame's response to strain and stability as we show later.

4.3 Consumption Speed

The consumption speed is calculated for all of the cases for the setup in Figure 4-2 and using equation 2.12. This symmetric, opposed reactants setup was described in

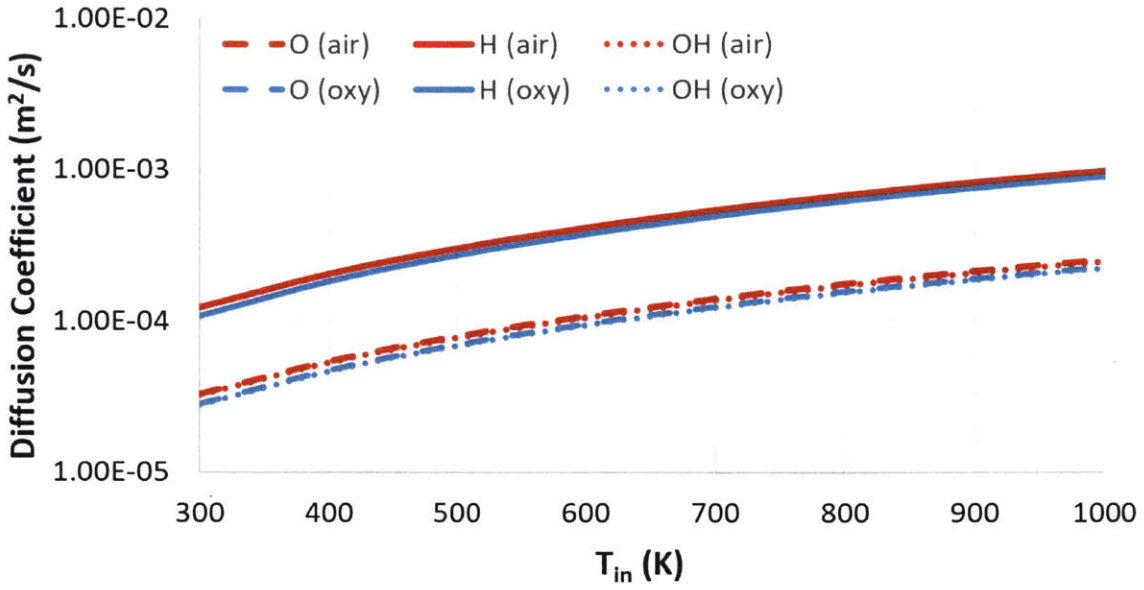

Figure 4-7: Diffusion coefficients of important radicals into the two air and oxy mixtures as a function of inlet temperature

greater detail in Section 2.2.2. The strain rate was increased until extinction and at each point, the speed was calculated. Flame extinction occurs at the turning point of the flame consumption speed. The conventional definition of extinction strain rate is used (see [111]), and it is defined as the maximum axial velocity gradient just before the flame. This type of extinction model was shown to capture the turbulent flame behavior in the previous Chapter and will also be used in the rest of this thesis. Figures 4-8 and 4-9 show the calculated consumption speeds for all of the air and oxy cases for adiabatic flame temperatures of 1800 K and 2100 K respectively.

As can be seen in the figures, at 1800 K the air case has a much higher consumption speed than all of the three oxy cases (almost double). Due to very high concentrations of CO_2 under oxy-fuel conditions, this enhances the forward reaction of:

$$CO_2 + H \longleftrightarrow CO + OH \tag{4.2}$$

and along with the single most important chain branching reaction,:

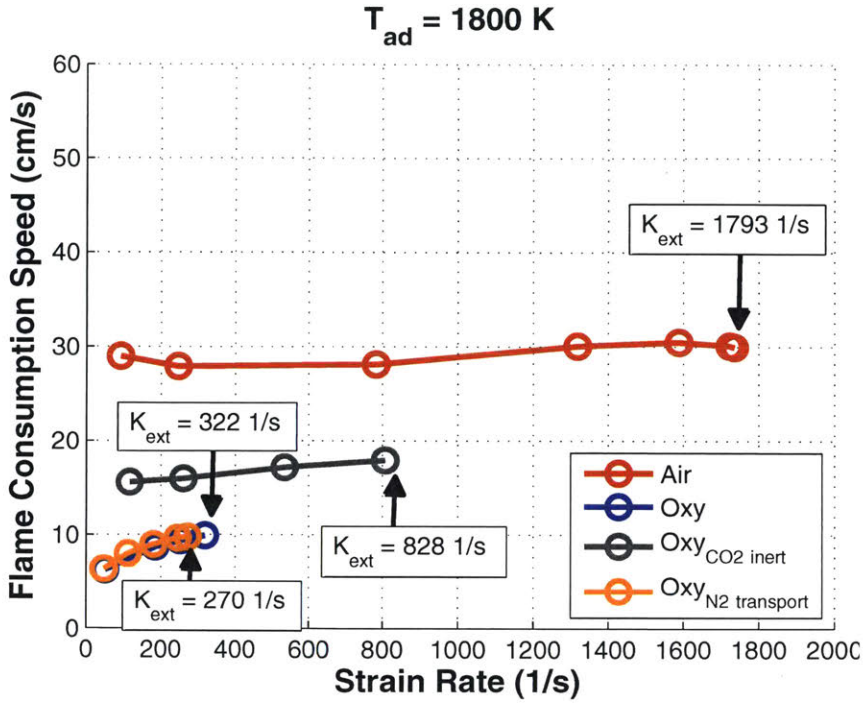

Figure 4-8: Consumption speeds at T_{ad}=1800 K for inlet reactants at 400 K.

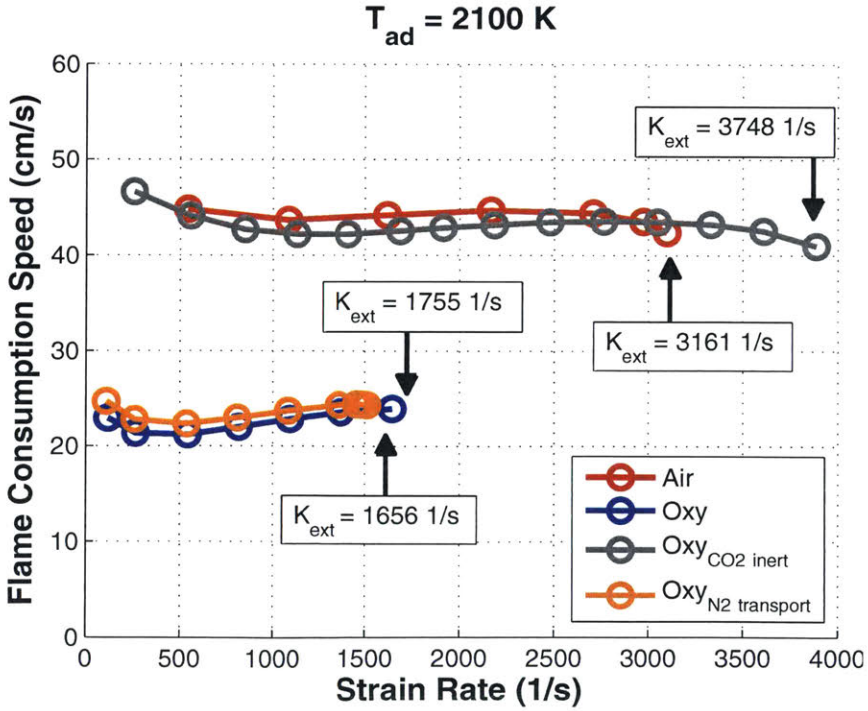

Figure 4-9: Consumption speeds at T_{ad}=2100 K for inlet reactants at 400 K.

$$H + O_2 \longleftrightarrow O + OH \tag{4.3}$$

this significantly reduces the concentrations of important radicals, leading to the significant reduction of the fuel burning rate [62]. This then reduces the consumption speed as is seen in the figures.

Moreover, the flame consumption speed and extinction strain significantly increases in the $\text{oxy}_{CO2\ inert}$ flame compared to the base oxy flame. This is again due to the effect of reaction 4.2. When the forward reaction rate of this reaction is set to zero, there is no longer that competitive reaction for H radicals and so both the flame consumption speed and extinction strain rate are increased in this special oxy case.

The effect of the CO_2 transport properties have less of an impact on the oxy flame. The flame consumption speed is almost identical to that of the base oxy case. But the extinction strain rate of the $\text{oxy}_{N2\ transport}$ flame decreases, indicating that the CO_2 transport properties actually improve the flame stability and have a positive effect of helping to increase the extinction strain rate. These responses agree with what Watanabe et al. [18] also found for lean oxy-combustion. Our work here is a follow up but for practical conditions of stoichiometric oxy-combustion and looking closer at the effect of the reactant temperature. Since the Lewis Number in the CO_2 environment is lower, this results in an increase in its extinction strain rate, purely due to transport [114].

In Figure 4-9, for the higher temperature, it is observed that the air and $\text{oxy}_{CO2\ inert}$ cases start to have similar consumption speeds and the $\text{oxy}_{CO2\ inert}$ flame actually has a larger extinction strain rate. As will be seen in the next section, when we plot the extinction strain rate dependence on temperature, there exists a cross point between these two cases and for the higher temperatures, the air case starts to have lower extinction strain rates than that special $\text{oxy}_{CO2\ inert}$ case.

There is also a Lewis number effect observed in the plots. From section 4.2.2 we saw that the air flame has a unity Lewis number whereas the oxy flame has a Lewis number that is less than one and increases as the temperature increases. This effect

is again seen here at the lower temperature where the Lewis number is lower, the oxy cases have a clear increase in the consumption speed as the strain rate increases from zero up until extinction. The air flame's consumption speed has almost no response to stretch as was expected. However at the higher temperature of 2100 K, heat loss from radiation starts to play a bigger role and counteracts this Lewis number effect and so the strain rate has less of an effect on the consumption speed for the oxy cases compared to those at 1800 K.

In Figure 4-10 we additionally model the air case which has a stoichiometric mixture of CH_4 and O_2 and the N_2 diluent is varied to achieve the same adiabatic flame temperature as in the other cases ($CH_4 + 2\,O_2 + \beta N_2$), the corresponding results are referred to as "air_{stoich}" in the figure. Since CO_2 has a higher specific heat capacity than N_2, less moles of CO_2 diluent is needed in the oxy mixture than moles of N_2 diluent in the stoichiometric air mixture in order to achieve the same flame temperature. For example at T_{ad}=2100 K, 5 moles of CO_2 are needed in the oxy mixture compared to 9 moles of N_2 in the air mixture. Since N_2 transport properties reduce extinction strain rates as we showed for the oxy cases, this transport effect is also reflected in the air-flame results in Figure 4-10. The stoichiometric air case has much lower extinction strain rate values than the original lean air combustion case partially due to the greater fractions of N_2 present. If we also compare the O_2 mole fractions in the reactants for these two air cases, we see that the stoichiometric case has a lower O_2 concentration of 17% versus 19% in the lean air case at T_{ad}=2100 K. The fuel mole fraction is about the same for the two air cases ($\approx$ 8.5 %). Since there is less oxygen but the same amount of fuel in the reactants of the stoichiometric air mixture, the consumption speed of this flame is lower as a result of the reduced heat release.

4.3.1 Chemical Effect of CO_2

We also modified the chemical mechanism used for the air case (GRI) in order to run a new case, "$air_{CO2\ inert}$", just to see how the chemical effect of CO_2 now affects the air flame. The results are shown in Figure 4-11 where the consumption speeds

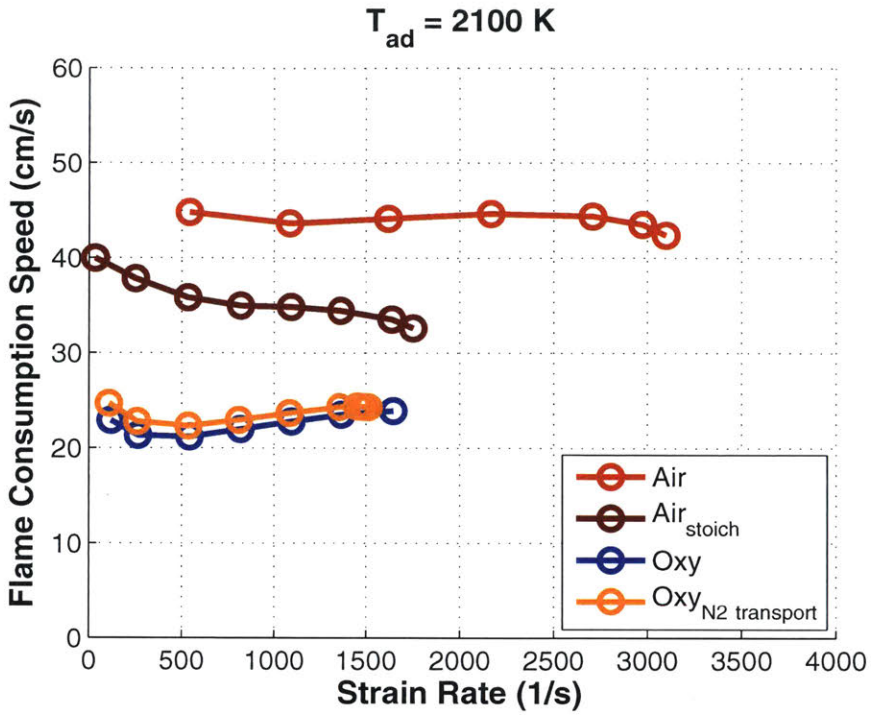

Figure 4-10: Consumption speeds at T_{ad}=2100 K showing the additional stoichiometric air case (brown line).

are plotted versus the strain rate for the adiabatic flame temperature of 2100 K. The two air and oxy CO_2-inert cases are compared. We observe the same trend in the air cases that was seen earlier for the oxy cases in that both the consumption speed and extinction strain rates increase after modifying the chemical mechanism such that the CO_2 is considered "inert". However due to the much higher concentrations of CO_2 in the oxy cases (as will be shown later), this effect is magnified. Both the consumption speed and extinction strain rate almost double after modifying the mechanism for the oxy case whereas in the air cases the increase in consumption speed and extinction strain rate is much milder. This highlights the differences between the air and oxy flames and the important role the presence of CO_2 plays.

These results show us that the chemical effect of CO_2 has a much larger impact on the flame extinction strain rate than the transport effect. Since the CO_2 diluent participates in the chemical reactions, it is mainly responsible for the decrease in flame consumption speed when running oxy-combustion compared to air.

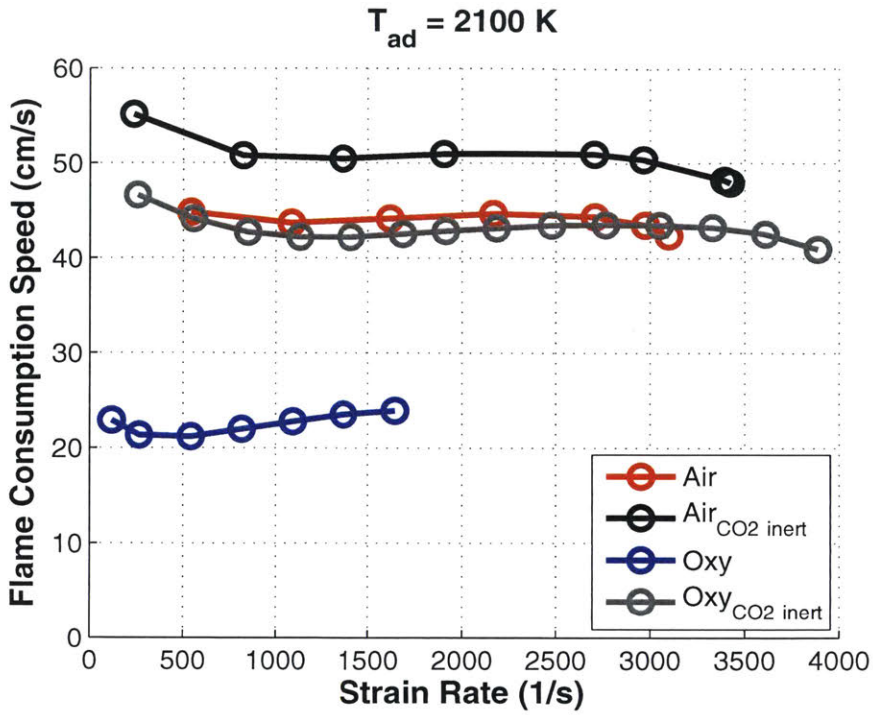

Figure 4-11: Consumption speeds at T_{ad}=2100 K showing the chemical effect of CO_2.

4.3.2 Effect of Inlet Temperature

Next we look at the impact of the inlet temperature on the consumption speed. Figure 4-12 shows the consumption speed plotted for the two temperatures of 300 K and 400 K for the adiabatic flame temperature of 2100 K. As expected, the consumption speed increases with the increasing inlet temperature. This variation with temperature shows the importance of choosing the right temperature when calculating these values in order to accurately reflect the conditions present in the combustor regions being investigated. The absolute values of the change in speeds is higher for the air and $oxy_{CO2\ inert}$ cases, as seen, but the percentage differences are almost the same for all four cases. The consumption speed increases by approximately 66% when the inlet temperature is increased from 300 K to 400 K. We see here that the absolute change in consumption speed with temperature is different for the air and base oxy cases, which agrees well with our results and observations previously.

Most studies in the literature perform flame calculations at atmospheric conditions but as we showed previously, choosing the right reactant temperature for these

calculations is very important. Therefore we next look at the sensitivity of Reaction 4.2 to reactant temperature since they are not the same for the air and oxy cases (see Figure 4-13) due to the differing concentrations of CO_2 as we will also show in section 4.5. Figure 4-13 shows the sensitivity of reaction $CO + OH \rightleftharpoons CO_2 + H$ to the inlet reactant temperature for the same twin flame configuration. The reaction rates for the net, forward and reverse reaction are plotted versus inlet temperature for air and oxy cases. The results in the plot help explain why we see the different extents to which the consumption speed and extinction strain rate change with inlet temperature for the air and oxy cases. For the air case, the net reaction rate (solid line) shows an increase with the inlet temperature whereas for oxy-combustion, the net reaction rate remains almost flat. This can also be seen from the forward and reverse rates lines where they diverge at higher temperatures for air but their difference is almost constant for oxy. These differing sensitivities to the inlet temperature by this reaction rate, causes the effect we saw in the previous figure with the different responses for air versus oxy in the flame characteristics. For air-combustion, since the reaction rate is more sensitive to the inlet temperature than oxy, we see it's consumption speed and extinction strain are also affected more by the inlet temperature than oxy (Figures 4-12 and 4-19). This further proves the point that the chemical effect of CO_2 is what causes the main differences between air and oxy combustion when the flames have different reactant temperatures. Practically speaking, the different zones in the combustor might have reactants at different temperatures and so flame extinction and stability behaves differently for air and oxy combustion as shown experimentally for turbulent flames in the previous chapter.

4.4 Extinction Strain Rate

Next the extinction strain rate is calculated by looking at the strain rate at which the turning point in the temperature response plot occurs. Results with and without considering radiation for the oxy cases are considered as well as the effect of inlet temperature.

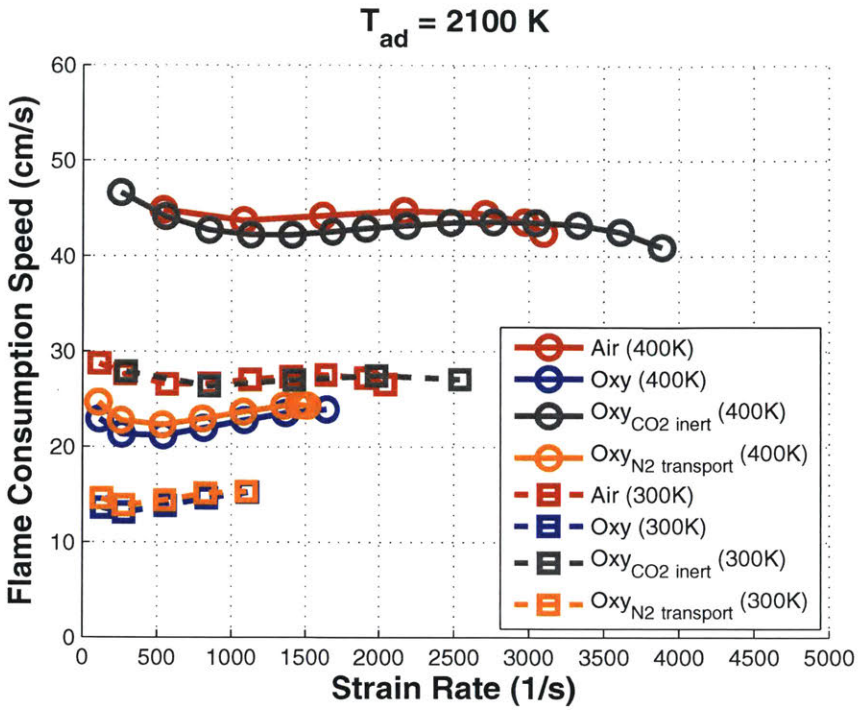

Figure 4-12: Consumption speeds at T_{ad}=2100 K showing the effect of reactant inlet temperature.

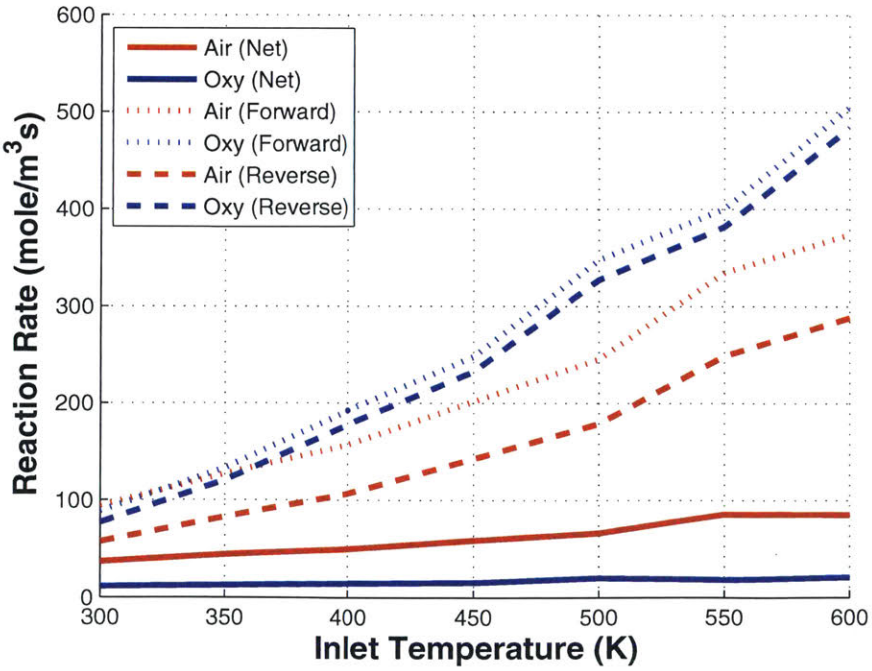

Figure 4-13: Forward, reverse, and net reaction rates for reaction CO + OH $\rightleftharpoons$ CO_2 + H as a function of inlet temperature.

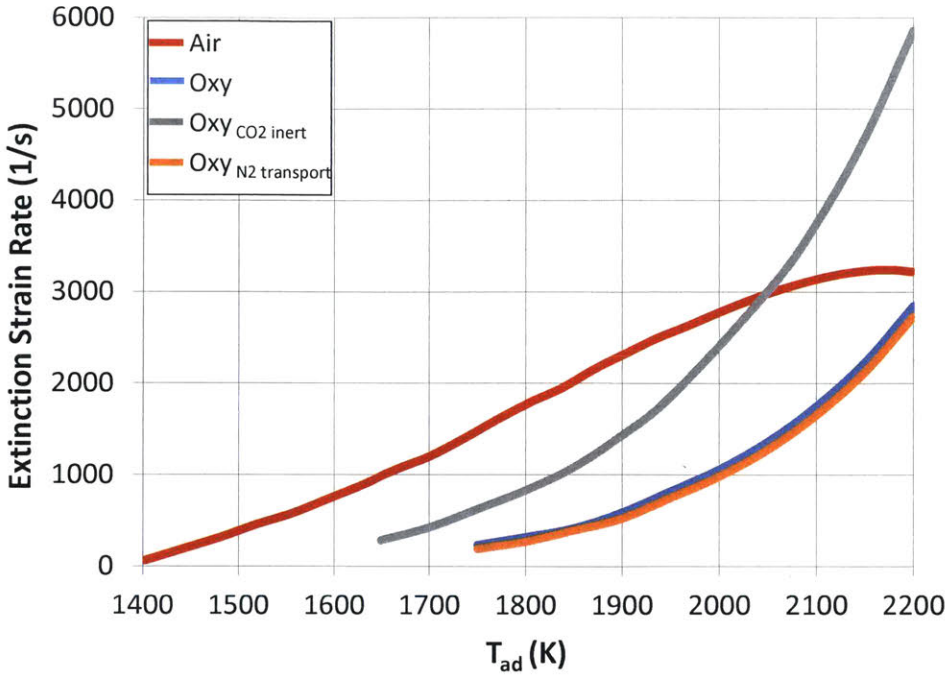

Figure 4-14: Extinction strain rates for inlet reactants at 400 K and radiation is considered for the oxy cases.

Figure 4-14 shows the calculated extinction strain rates for the three stoichiometric oxy cases and the air case plotted against the adiabatic flame temperature. The results verify what was seen earlier in the consumption speed calculations where the air flame's and the $oxy_{CO2\ inert}$ flame's curves cross at a temperature around 2050 K. Also as was seen earlier, the air flame has higher extinction strain rates than the oxy cases for most temperatures up until 2050 K. This is mainly due the high fractions of CO_2 enhancing the forward reaction of 4.2 and reducing radical concentrations which significantly affects the methane oxidation rate (Figure 4-21). When the forward reaction rate of reaction 4.2 is set to zero, thus making the CO_2 significantly less reactive, the extinction strain rate more than doubles over the base oxy case.

It can also be seen that the transport properties of CO_2 have a small effect on the flame stability and extinction strain rate where the $oxy_{N2\ transport}$ curve is very similar and values are a little lower than the base oxy case. This suggests that the CO_2 transport effect actually improves the flame's resistance to extinction.

In order to visualize the two competing effects: chemical versus transport, Figure

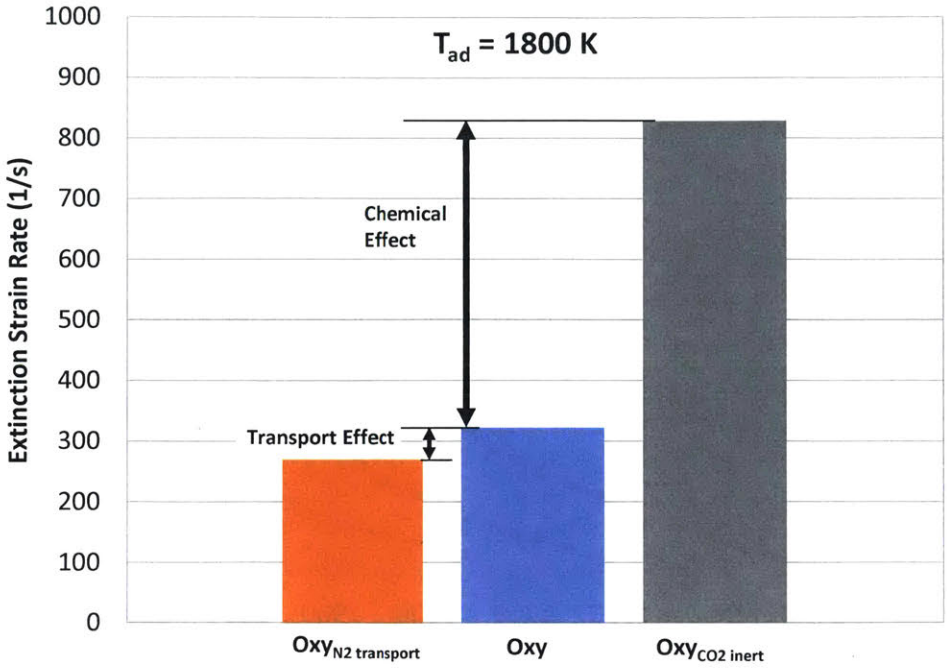

Figure 4-15: Extinction strain rate comparison showing the effect of chemistry versus transport for T_{ad}=1800 K

4-15 shows the extinction strain rate for the three oxy cases at an adiabatic flame temperature of 1800 K. The chemical effect of the CO_2 dilution on the oxy flame has a much larger impact on the extinction strain as shown than the transport effect. This clearly shows the difference between air and oxy combustion in that a passive diluent (N_2) compared to a chemically reactive diluent (CO_2) plays a big role in flame stability. Although the CO_2 does have a positive effect by slightly improving flame stability due to the favorable transport properties, the negative chemical effect ultimately results in a weaker flame with respect to the lower burning rate.

In Figure 4-16, the additional stoichiometric air case results are shown. This case serves as another way for comparing extinction strain rates of air and oxy flames by keeping both equivalence ratio and flame temperature the same, which is not the norm in literature studies. As mentioned, since CO_2 has a higher specific heat capacity than N_2, less moles of CO_2 diluent is needed in the oxy mixture than moles of N_2 diluent in the stoichiometric air mixture in order to achieve the same flame temperature. The extinction strain rate results from this additional case show an

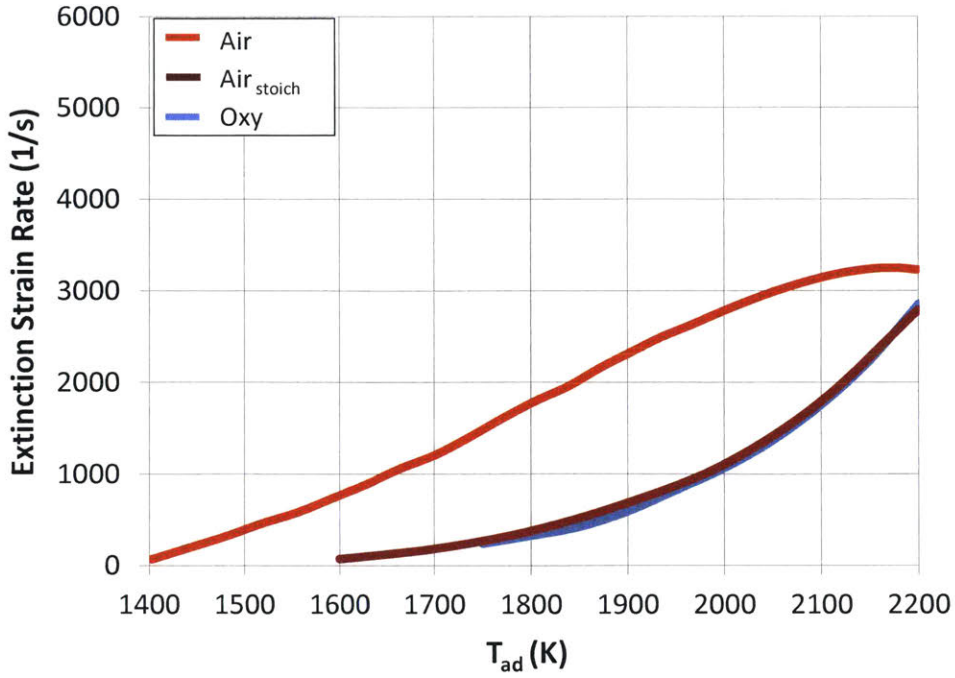

Figure 4-16: Extinction strain rates showing the additional stoichiometric air case (brown line).

interesting trend. Both the stoichiometric air and oxy cases have similar extinction strain rates and the stoichiometric air case has much lower values and a different shaped curve than the original lean air combustion case. Both the increased N_2 and decreased O_2 fractions in the stoichiometric air case contribute to the effects observed. Therefore if we want to compare air and oxy flames by keeping both the equivalence ratio and flame temperature the same in a stoichiometric mixture, the flame stability characteristics appear to be similar.

4.4.1 Effect of Radiation

Another important aspect in oxy-combustion is the effect of radiative heat transfer due to the presence of CO_2 and H_2O. As has been extensively shown in the literature [2, 67, 68, 69, 70, 71, 66, 72, 115, 116, 73], these species are far more effective absorbers and emitters of thermal radiation than O_2 and N_2. Some simulations have indicated that the CO_2 and H_2O present in the reactive gases, can either lead to enhanced preheating

through the effects of radiative absorption from the hot product gases or could lead to increased heat loss of the flame. Numerical investigations of the extinction limits of strained premixed and non-premixed $CH_4/O_2/CO_2$ flames at atmospheric conditions showed that while significant preheating can in fact occur, the net effect seems to be easier extinction due to increased heat loss [69, 66]. While the current radiation modeling approach (optically thin) does not allow for radiative preheating effects, we do see the effect of heat loss on extinction in our calculations at higher reactant inlet temperatures. Figure 4-17 shows the extinction strain rates without including the heat loss due to radiation; the extinction limits for the oxy cases shift to lower temperatures than in the case where radiation is considered (Figure 4-14). Figure 4-18 presents the variation in the extinction strain rate when radiation is and is not accounted for. As expected, the increased heat loss from the flame due to radiation weakens the flame by decreasing the extinction strain rate. However the impact of CO_2 radiation is limited and still much smaller than the chemical effect of CO_2. The Planck mean absorption coefficient of CO_2 is also much larger than those of other species [96] and so flame radiation increases with increasing CO_2 fraction (decrease in T_{ad}). There is on average a 60 1/s decrease in the extinction strain rate when radiation is accounted for, which amounts to percentage decreases of 17%, 15%, and 7% for the $oxy_{N2\ transport}$, oxy, and $oxy_{CO2\ inert}$ cases respectively.

4.4.2 Effect of Inlet Temperature

The effect of the inlet temperature also plays a role in the extinction strain rate values, as shown in Figure 4-19. One expected observation is the extinction of the flames at higher adiabatic temperatures for the lower inlet temperature. The extinction strain rate also appears to be more sensitive to the inlet temperature especially for the air and $oxy_{CO2\ inert}$ flames. The crossover point in the extinction strain rate between them occurs at an adiabatic flame temperature of around 2050 K for the inlet temperature of 400 K. However this crossover point remains at that same mixture flame temperature of 2050 K when the inlet temperature is decreased to 300 K. For the oxy and $oxy_{N2\ transport}$ cases, there is a smaller decrease in the extinction strain

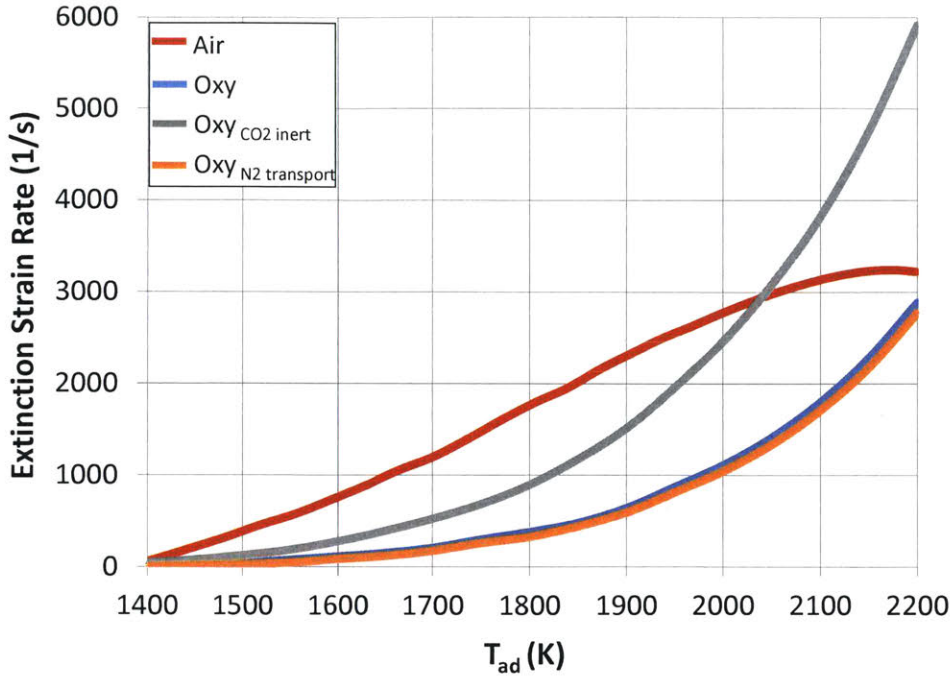

Figure 4-17: Extinction strain rates for inlet reactants at 400 K and radiation is not considered for the oxy cases.

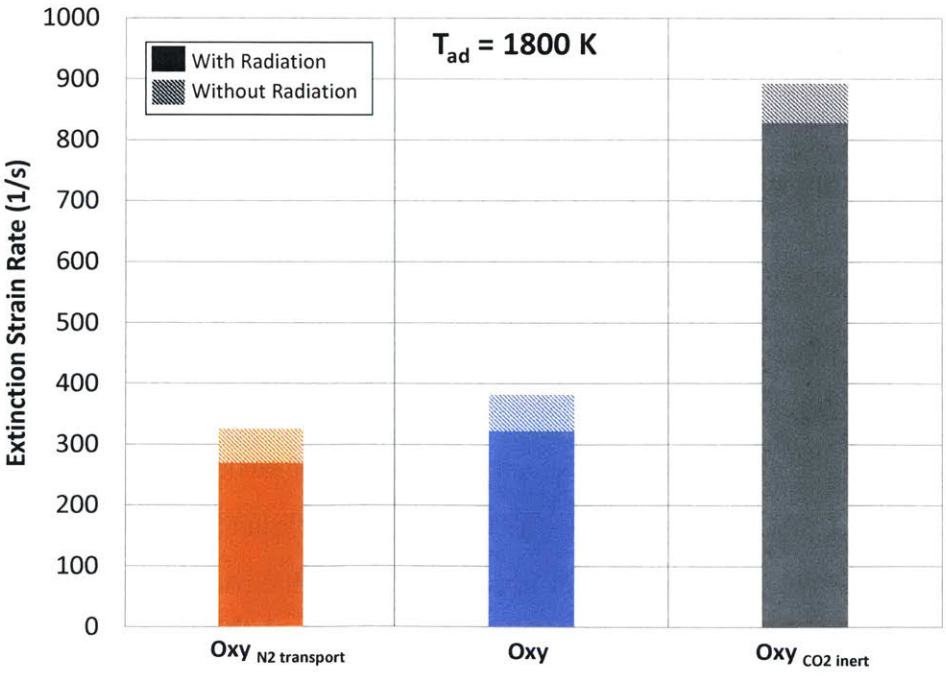

Figure 4-18: Extinction strain rate comparison showing the effect of including radiation for T_{ad}=1800 K

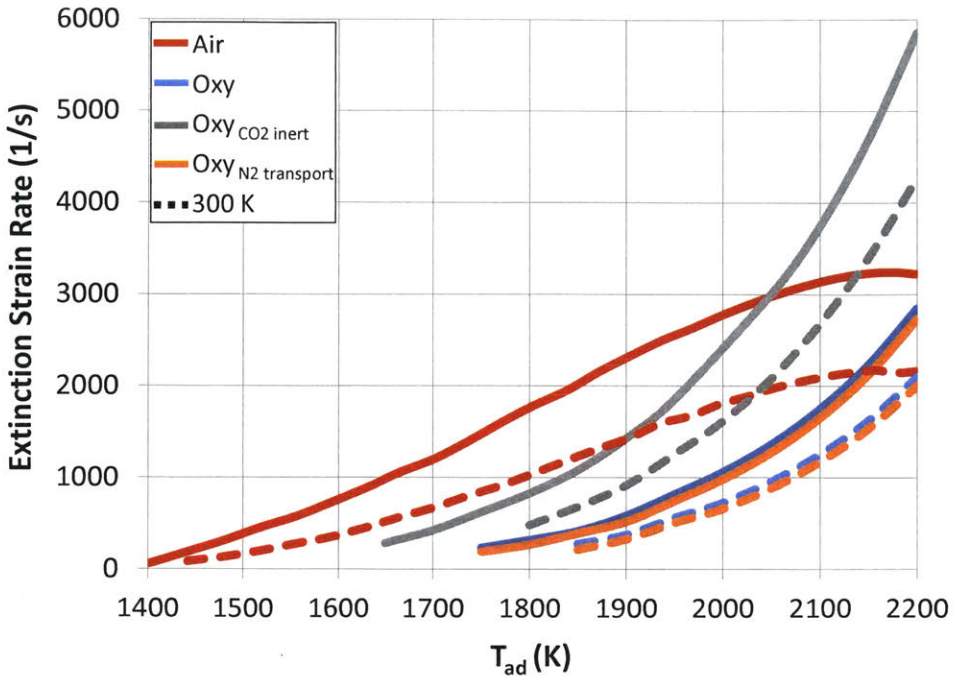

Figure 4-19: Extinction strain rates showing effect of reactant inlet temperature: 400 K (–), 300 K (- -).

rate when the inlet temperature is decreased from 400 K to 300 K. The chemical effect of the CO_2 appears to also play a large role here in the flame sensitivity to the inlet temperature. The important reaction mainly responsible for the decrease in fuel burning rate (reaction 4.2), appears to reduce the sensitivity of the flame extinction to the inlet temperature. When this reaction is not considered in the chemistry as is the case for the $oxy_{CO2\ inert}$ flame, there is a large change in the extinction strain rate with inlet temperature. This shows that the inlet temperature will affect the air and base oxy flames differently (also seen in Figure 4-12). Thus inlet temperature has a bigger impact on the flame extinction for the air flame due to the lower concentration of CO_2. These laminar calculations give important insights into the expected behavior of the turbulent flames. At the conditions where the extinction strain rates cross for different reactant temperatures, we would expect similar flame stability characteristics for the turbulent air and oxy flames.

	Reaction
1.	$OH + H_2 \longleftrightarrow H + H_2O$
2.	$CO + OH \longleftrightarrow CO_2 + H$
3.	$H + O_2 \longleftrightarrow O + OH$
4.	$2\,OH \longleftrightarrow O + H_2O$
5.	$HCO \longleftrightarrow H + CO$
6.	$CH_4 + OH \longleftrightarrow CH_3 + H_2O$
7.	$CH_2O + OH \longleftrightarrow HCO + H_2O$
8.	$O + H_2 \longleftrightarrow OH + H$
9.	$CH_2OH + H \longleftrightarrow CH_3 + OH$
10.	$CH_4 + H \longleftrightarrow CH_3 + H_2$

Table 4.4: Top elementary reactions with the highest maximum reaction rate in oxy-combustion

4.4.3 Effect of Reactions

Many studies in the literature have identified the reaction $CO + OH \longleftrightarrow CO_2 + H$ as being one of the most important pathways to how CO_2 present in oxy-combustion impacts the chemical kinetics [13, 19, 9, 2]. We have also shown throughout the previous results that this reaction specifically, significantly affects important flame stability parameters such as consumption speeds and extinction strain rates. To solidify our understanding of the chemical pathways that primarily affect extinction strain rates in oxy-combustion, the sensitivity of K_{ext} to certain reactions is investigated. This was done by isolating and removing individual reactions from the chemical mechanism in the simulation. Grinberg et al. [117] similarly studied the sensitivity of K_{ext} to important species during the process of generating a reduced skeletal mechanism for methane oxy-combustion. Unsurprisingly, O_2, H, O, and OH had the highest K_{ext} sensitivity coefficients since these are the most important radicals in methane combustion.

The maximum reaction rate of all the elementary reactions in the Glarborg mechanism are calculated and the top 10 reactions with the highest reaction rates are listed in Table 4.4 to help identify which reactions to investigate. In our short analysis, we identified the top 3 reactions in the table to study their impact on K_{ext} (Figure 4-20). The same reactions were also identified by Song et al. [19] as being the most

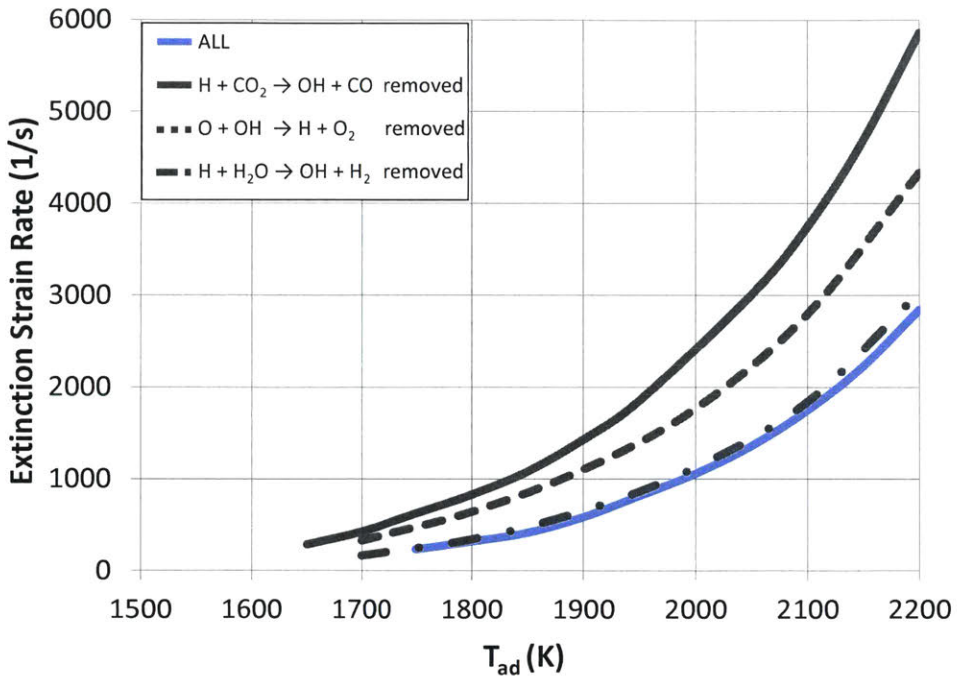

Figure 4-20: Extinction strain rates for a stoichiometric oxy flame looking at the effect of certain reactions.

heavily influenced by CO_2 through their individual heat release rates. Figure 4-20 shows the significance of reaction $CO + OH \longleftrightarrow CO_2 + H$ once again through its impact on K_{ext}. The removal of the reverse of this reaction results in the highest increase in K_{ext} compared to the impact of the other two reactions. The main chain branching reaction $H + O_2 \longleftrightarrow O + OH$ also impacts K_{ext} but not as heavily. The third reaction $OH + H_2 \longleftrightarrow H + H_2O$ barely had any affect even though it had one of the highest reaction rates. This analysis shows the importance of including these sensitive reactions if one wishes to construct a reduced mechanism for stoichiometric oxy-combustion that correctly predicts extinction strain rates.

4.5 Product Composition

Finally we now compare the products composition of the air and oxy flames to further strengthen our conclusions and explain the trends we saw earlier. Figure 4-21 shows profiles of CO_2, O_2, CO, H and OH radical concentrations for the twin premixed air

and oxy-flames at a strain rate right before extinction. The profiles at this specific strain rate condition are shown here since the concentration profiles showed similar trends at other strain rates. Profiles are shown for two adiabatic flame temperatures of 1800 K (a) and 2100 K (b). All of the profiles were calculated at the standard conditions we have been using before of the inlet temperature of 400 K and with the presence of radiation.

4.5.1 Air versus Oxy

At the lower adiabatic temperature, more CO_2 is added as a diluent in the oxy-combustion cases in order to reduce the temperature than at the higher flame temperature. Thus we expect the CO_2 concentrations in the products for T_{ad}=1800 K naturally to be higher due to this, as is seen in the plot. This will then also increase the CO mole fractions for the oxy cases and if you compare the base oxy (blue) to the air case (red), the oxy case has about three times more CO emissions for both flame temperatures. This is the common theme for skepticism and complaints related to oxy-combustion.

There is also a difference in CO levels when changing the adiabatic flame temperature. This is due to both the increased rates of reactions with increasing temperature, and the change in the reactants' compositions which will then affect emissions through the same important reactions mentioned previously, and are again shown below.

$$CO_2 + H \longleftrightarrow CO + OH \tag{4.4}$$

$$H + O_2 \longleftrightarrow O + OH \tag{4.5}$$

Looking at the important radicals, H and OH, Figure 4-21 mainly shows that the air flame has higher radical concentrations than the base oxy. Due to the high competition for radicals in oxy-combustion through the two reactions above, the radical concentrations are lower and so the flame speed is reduced as we showed before. In fact many researchers have shown that the high levels of CO_2 present in oxy-combustion

reduce the H radical through reaction 4.4, leading to a lower concentration of chain carriers via reaction 4.5 [64, 118, 119]. We have a similar conclusion from our calculations but at higher reactant temperatures.

4.5.2 Chemical Effect of CO_2

Any differences we see in the emissions between the $oxy_{CO2\ inert}$ flame and the other oxy flames will be due to reaction 4.4 which we are not modeling, thus isolating its effect. As we showed earlier, this reaction is mainly responsible for explaining the differences in the flame stability we see between air and oxy-combustion, and now looking at emissions we see this reaction is again very important.

We stated earlier that the high levels of CO_2 and the competition for radicals leads to the reduced radical concentrations in oxy-combustion when compared to air. Thus if we reduce this competition for radicals by setting the forward reaction of reaction 4.4 to zero, we should expect the radical concentrations to rise when compared to the base oxy flame with all reactions included. As we see in Figure 4-21, this is indeed the case. The $oxy_{CO2\ inert}$ even has higher radical concentrations than the air flame thus proving reaction 4.4's importance.

It can also be seen from Figure 4-21 that the CO_2 fraction in the products for the $oxy_{CO2\ inert}$ flame (grey) is higher than the other oxy cases (blue and orange). This is shown as a sharp peak at a distance of 1 cm. Since the CO_2 is considered "inert", reaction 4.4 does not occur and therefore much less CO is produced which is also shown in the figure.

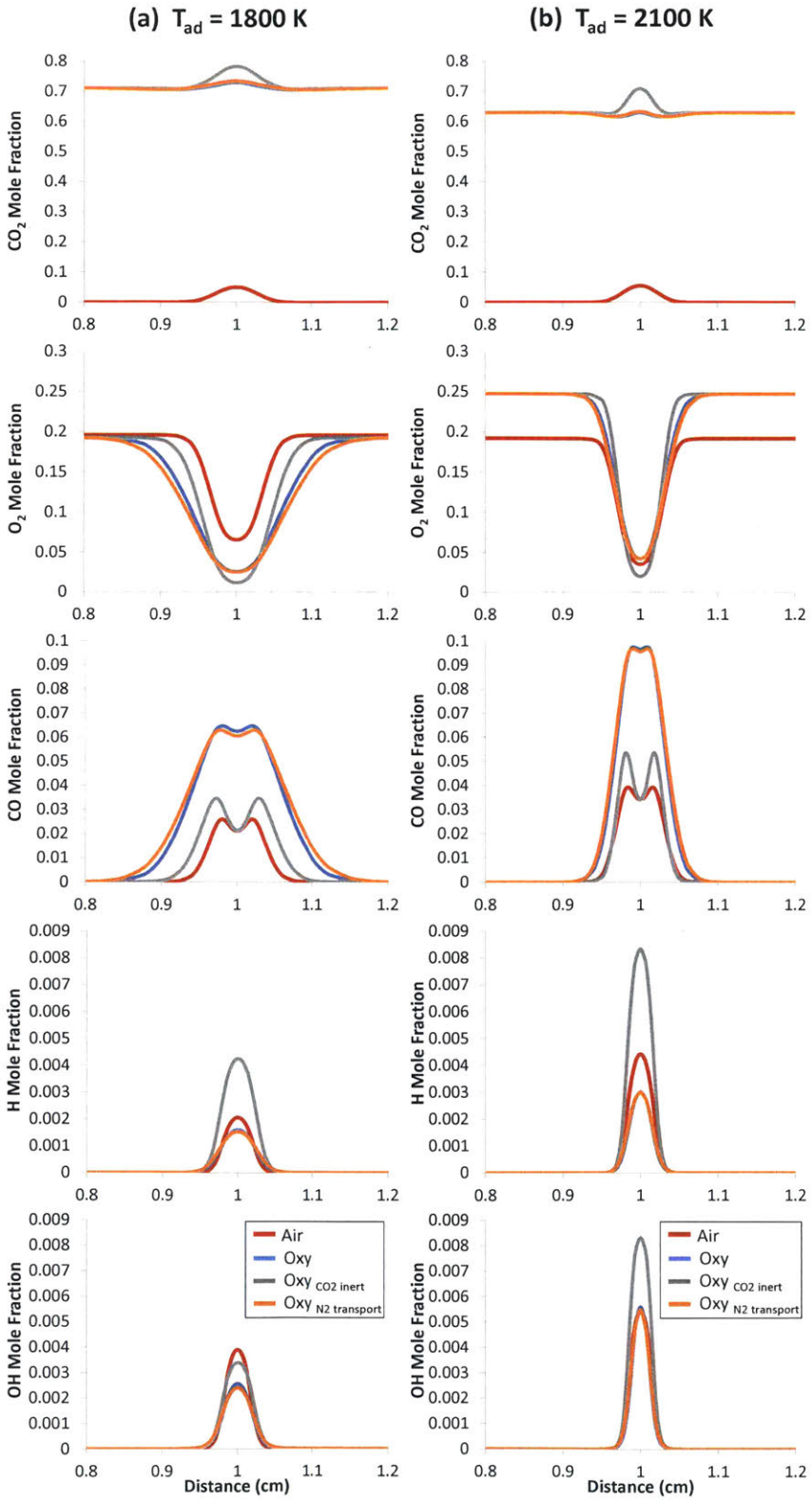

Figure 4-21: Profiles of CO_2, O_2, CO, H and OH mole fractions for (a) T_{ad} = 1800 K and (b) T_{ad} = 2100 K.

4.6 Conclusions

The work here builds on conclusions made from the previous chapter observations by investigating why there are differences in extinction strain rates and flame consumptions speeds, and what effect the reactant inlet temperature has on air and oxy flames. After examining the impact of CO_2 in stoichiometric oxy-combustion, by looking at both transport and chemistry effects, we conclude the following on why we see these differences in flame stability between air and oxy flames.

The Lewis number for stoichiometric oxy flames is less than 1, whereas for the air flame it is unity. This impacts the response to strain of the two flames by affecting the shape of the consumption speed curves. For lower flame temperatures, the oxy flames display enhanced flame speeds as the flame is strained whereas the air flame's response is almost flat. But at higher temperatures, heat loss from radiation is more significant and the mixture Lewis number is higher resulting in flatter curves for the oxy flame.

The chemical effect of CO_2 present in oxy-combustion has a bigger impact on the consumption speed and flame extinction strain rate than the effect of transport properties change. This is mainly due to the competition for radicals of the important reaction: $CO_2 + H \longleftrightarrow CO + OH$ when high levels of CO_2 are present in oxy-combustion as has been suggested in the literature.

This work also reveals that this reaction affects the sensitivity of the flame properties to changes in the inlet temperature with the air-combustion flame being more sensitive. This variation with temperature shows the importance of choosing the right inlet temperature when calculating these flame values in order to accurately reflect the conditions present in the combustor regions being investigated.

Contrary to what is observed in air flames, the CO_2 transport properties actually positively impact the flame stability characteristics. For the $\text{oxy}_{CO2\ inert}$ case, both the consumption speed and extinction strain rate significantly increase compared to the base oxy flame.

Looking at emissions, the $\text{oxy}_{CO2\ inert}$ flame has higher radical concentrations and

also much lower CO fractions compared to the other oxy cases, leading to the increased flame stability observed in the consumption speed and extinction strain rate results.

Practically speaking, these calculations serve to explain the different flame stability characteristics of air and oxy combustion in the different zones in a gas turbine combustor. We have demonstrated that it is the extinction strain rate and not the laminar burning velocity which is the important property for determining and comparing flame stability. The novelty here is building on this discovery by explaining why we see the differences in the response to strain of the air and oxy flames and in their sensitivity to the reactant inlet temperature.

Chapter 5

The Role of Chemical Kinetics Modeling in the LES of Premixed Combustors

5.1 Introduction

Modern lean premixed gas turbines rely on wake flows for flame stabilization because they create recirculation zones that can anchor flames. However these combustors are also prone to combustion instabilities due to the coupling between their wake flow dynamics and system acoustics [45]. The size and structure of these recirculation zones is dictated by the combustor geometry (Figure 5-1) and these recirculating flows in the wake of a bluff body, behind a sudden expansion or downstream of a swirler, are pivotal for anchoring the flame and expanding the stability range [5].

Large eddy simulation (LES) techniques are important tools in fundamental studies of these flows and by having an appropriate combustion model and reaction mechanism, they afford a balance between computational complexity and predictive accuracy.

Chemical kinetic mechanisms designed for gas turbine combustion modeling have traditionally focused on the ability to reproduce quantities such as fuel conversion

or pollutant formation. On the other hand, little attention has been paid to their suitability for predicting parameters related to flame-stabilization. When evaluating which reduced mechanisms to apply in LES, characteristics such as the laminar flame speed and ignition delay times are commonly used. However, in the previous chapters, it was shown that it is important that a chemical mechanism is able to predict the correct extinction strain rate, if it is expected to accurately capture and scale flame macrostructure transitions. This importance of the extinction strain rate has also been documented in a number of other recent studies [99, 107, 6, 120].

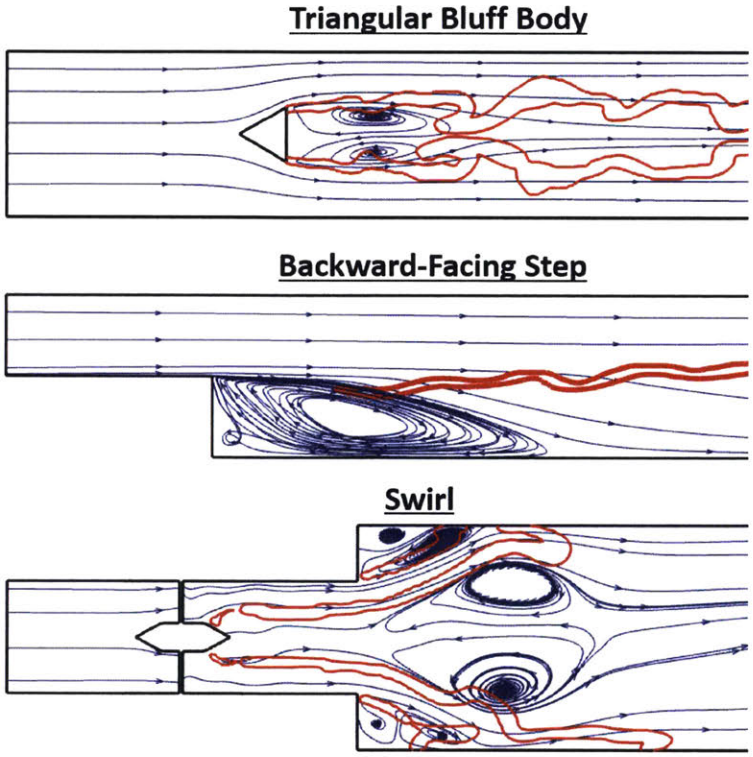

Figure 5-1: Mean streamlines (blue) and instantaneous heat release contours (red) for three combustor geometries: Bluff Body, Backward-Step, and Swirl.

5.1.1 Literature Review

Cocks et al. [52] questioned the ability of LES to predict large scale structures in reacting flows such as the recirculation zone. They used the same Volvo test case that is examined in this chapter and they showed a dependence of the unsteady dynamics on

the numerical schemes in different CFD solvers. In the same geometry, Sardeshmukh et al. [121] studied the impact of chemical kinetics on the combustion dynamics of bluff-body flames. They tried to show that the mechanism that accurately captured ignition delay: the detailed kinetics mechanism, resulted in a significantly more distributed heat release in the bluff-body wake and shear layer regions. However there was not a significant difference in the prediction of recirculation zone length using the two mechanisms they tested even though they had vastly different ignition delay times. This raises an important question. What attribute of chemical mechanisms is important in order to accurately predict recirculation zones in simulations?

There have been a number of studies in the literature looking at the importance of reduced chemistries in reproducing turbulent flames in LES and DNS of premixed and non-premixed combustors [122, 123, 124, 125]. However most of the studies compare reduced mechanisms on the basis of laminar flame speed and adiabatic flame temperature in simple geometries. Only the study by Franzelli et al. [124] studies a partially premixed swirled methane/air flame with different kinetic models compared on the basis of their laminar strained flame performance. They mainly looked at temperature and CO profiles to evaluate the mechanisms for one flame macrostructure simulation. Their ability to predict important flow structures such as recirculation zones was not considered.

But it was recently demonstrated that in CFD simulations, predicting the extinction strain rate is an important indicator so that multi-dimensional simulations can be expected to reproduce accurate flow and combustion features. In Michaels et al. [6], DNS of laminar premixed bluff body stabilized CH_4/H_2/Air flames at various temperature ratios were conducted. A sample of the results are shown in Figure 5-2 where the recirculation zone length (taken to define the flow time scale) is plotted against two different chemical time scales. The top plot shows that when the laminar unstretched burning velocity is considered in defining the chemical time scale, the data is widely scattered and no clear trend is observed. However when the data is plotted using the extinction strain rate to define the chemical time scale (bottom plot), there is a clear trend showing how the recirculation zone length scales well with

the extinction strain rate. This type of scaling is also seen in experiments as well. In another study by Shanbhogue et al. [107], experiments on turbulent premixed swirl-stabilized CH_4/H_2/Air flames showed that different flame macrostructures occurred at distinct equivalence ratios. But when these macrostructures are plotted against the extinction strain rate, these shapes collapse to fixed values of K_{ext} across the different mixtures. This scaling further strengthens our hypothesis that the extinction strain rate is an important parameter that dictates flame stabilization in premixed combustion, and that the chemistry mechanism in CFD models must be able to predict correct values of K_{ext} if the simulations are expected to accurately capture realistic flow and flame features.

5.1.2 Objectives

In this chapter, we use LES to model premixed mixtures and test multiple fuels (propane and methane) and oxidizers (air and oxygen) in multiple geometries (bluff body, backward step, and swirl). Specifically the goals of this work are:

1. Validating the LES code with the Artificially Thickened Flame (ATF) combustion model in geomtries ranging from simplex to very complex.

2. Showing the impact of the chemical kinetic mechanism on predicting recirculation zones.

3. Proving the importance of K_{ext} on scaling recirculation zone lengths in different combustor geometries.

5.2 Simulation Setups

We test our hypothesis in three combustor geometries: triangular bluff body, backward-facing step and swirl combustors. The LES code and corresponding models used were described in detail in Section 2.2.1.

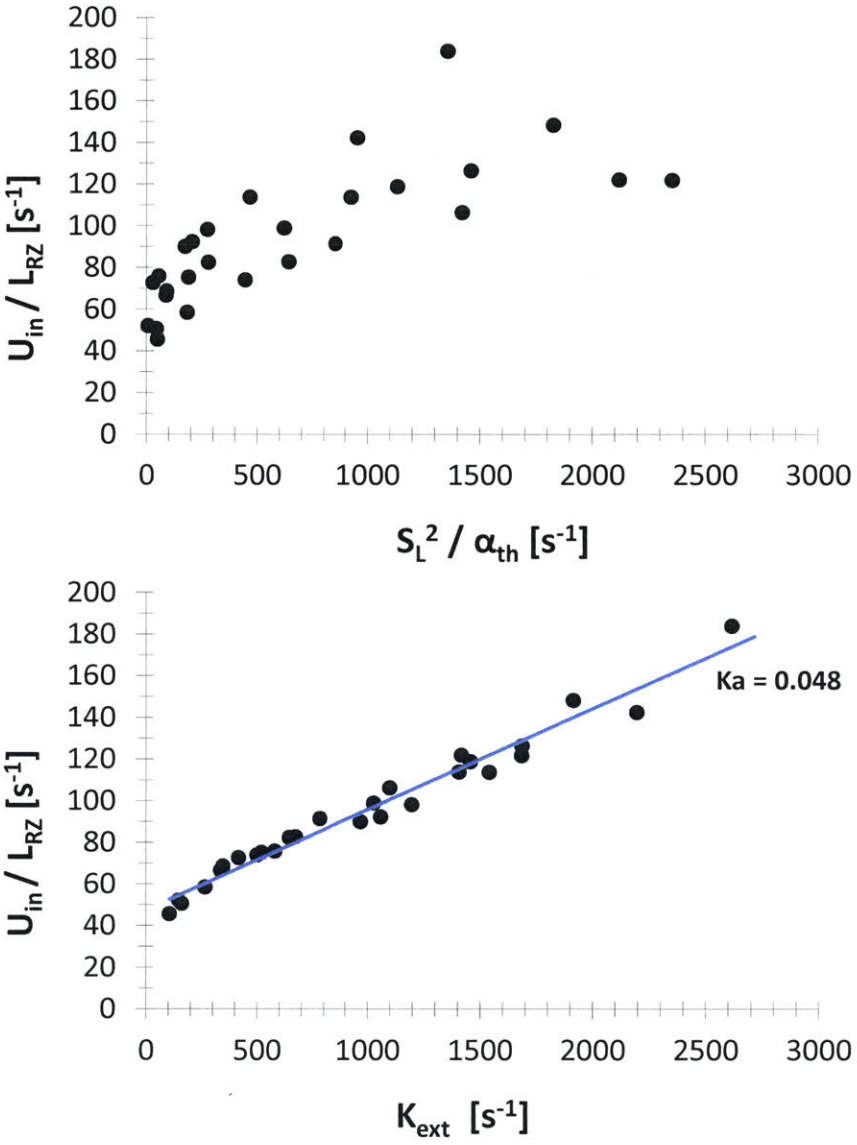

Figure 5-2: Flow vs chemical time scales for different fuels and inlet temperatures from DNS simulations of premixed laminar CH_4/H_2/Air mixtures in a bluff body stabilized combustor. The flow time scale is associated with a recirculation zone length while the chemical time scale is either represented by the flame speed (top) or extinction strain rate (bottom) of the chemical mechanism. Figures were generated using data from Michaels et al. [6].

Geometry	Bluff Body	Backward Step	Swirl
Fuel	Propane	Propane	Methane
Oxidizer	Air	Air	Oxygen
Reynold's Number	48,000	6500	15,000-30,000
Inlet Temperature	288.2 K	293 K	300-500 K
Equivalence Ratio	0.65	0.63-0.85	0.56-0.7

Table 5.1: Operating conditions simulated in the three combustors

5.2.1 Bluff Body

Figure 5-3 shows the computational domain dimensions for the premixed bluff body configuration, which is based on the Volvo test case in Refs. [126, 127]. The combustor is a rectangular duct with a flameholder centered in the duct. The flameholders cross section is a 40 mm equilateral triangle. The duct is 882 mm long with the bluff body situated at 200 mm from the inlet. The inlet operating conditions tested are shown in Table 5.1. A similar bluff body simulation was performed by Kewlani et al. [86] using a similar code and combustion model as this study but with a different chemistry mechanism. They obtained good agreements between the simulation results and the experimental data and so the same type of meshes were used in this work also. The non-uniform meshes (fine and coarse) are comprised of 1.54 million and 0.51 million hexahedral cells respectively, and the cells get coarser as you move downstream. The average cell sizes in the whole domain are 2 mm for the fine mesh and 3 mm for the coarse mesh with maximum and minimum cell sizes of 3.6 mm and 0.7 mm for the fine mesh and 4.1 mm and 1 mm for the coarse mesh, respectively. For the fine mesh, immediately downstream of the bluff body, $\overline{\Delta x}$=0.7 mm and $\overline{\Delta y}$=0.9 mm but the mesh is slightly more refined in the shear layer regions ($\overline{\Delta x}$=0.7 mm and $\overline{\Delta y}$=0.7 mm), while $\overline{\Delta x}$=1 mm and $\overline{\Delta y}$=0.9 mm on average further downstream. For the coarse mesh, immediately downstream of the bluff body, $\overline{\Delta x}$=1 mm and $\overline{\Delta y}$=1.3 mm and the mesh is also more refined in the shear layer regions ($\overline{\Delta x}$=1 mm and $\overline{\Delta y}$=1 mm), while $\overline{\Delta x}$=1.9 mm and $\overline{\Delta y}$=1.3 mm on average further downstream.

Periodic boundary conditions are used in the span-wise directions, and no-slip conditions are applied for the flow at the top and bottom walls of the duct as well as

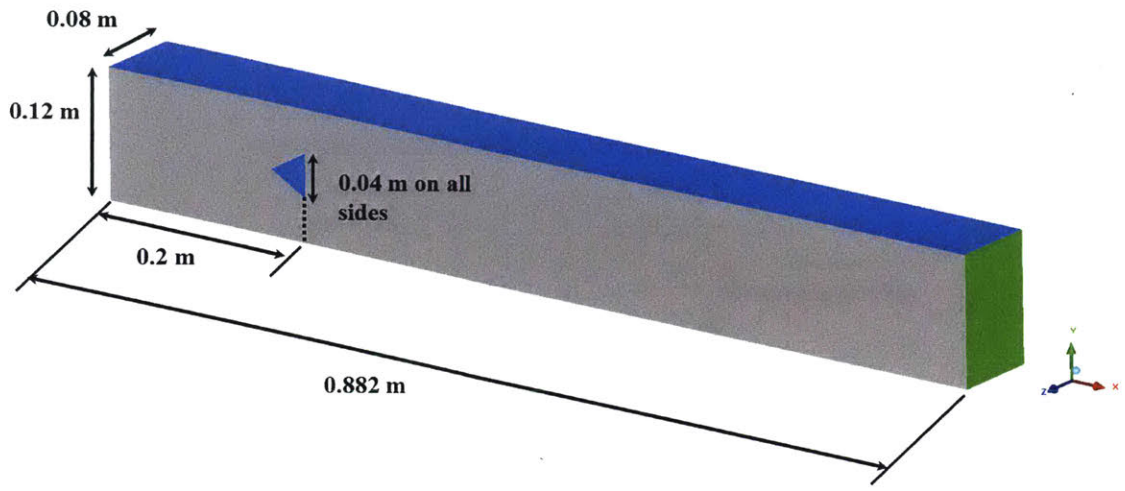

Figure 5-3: Computational domain dimensions for the bluff body case studied in this work (reproduced from [21]).

the bluff body. We fix the mass flow rate as 0.2083 kg/s at the inlet, fix the stagnation temperature of 288.2 K, zero inlet turbulence and a premixed propane-air mixture at an equivalence ratio of 0.65. Dirichlet conditions are used for all variables at the inlet except the pressure for which zero-gradient conditions are specified. Similarly at the exit, zero-gradients are specified for all variables except the pressure for which wave-transmissive conditions are used [86]. The top and bottom walls are also modeled as adiabatic and the other variables are specified as zero-gradient. The time step used in the simulations is 2 μs and the average values are calculated after sufficient times such that steady state conditions are established.

5.2.2 Backward Facing Step

The backward-facing step combustor configuration is shown in figure 5-4 and is based on the same combustor geometry as in our previous work [128, 5]. The inlet channel is 20 mm in height and 50 mm long and the step height is also 20 mm. After the sudden expansion, the length of the remaining combustor is 350 mm with a depth of 160 mm. The inlet conditions tested are shown in Table 5.1 where a propane-air mixture is introduced at various equivalence ratios and at an inlet velocity of 5.1 m/s corresponding to a Reynold's Number of 6500 similar to our experiments [128, 5].

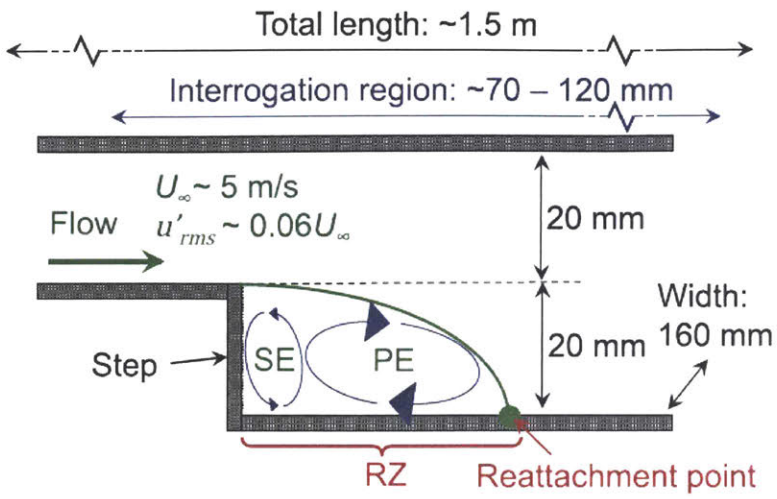

Figure 5-4: Computational domain dimensions for the backward-facing step case studied in this work (reproduced from [5]).

The code and mesh for the step combustor has been previously tested and validated [129] and so only the chemical mechanism has been modified in the present work; the goal here being to study the effect of the extinction strain rate of the kinetic model on the results. Details of the experimental study were reported in Hong et al. [5]. The mesh consists of 0.35 million cells with an average cell size of 2 mm. The mesh is also non-uniform with hexahedral cells. The time step for the simulations is 1 μs and this conservative value was chosen in order to adequately resolve the chemical time scales and consider local refinement and acceleration of the fluid above the bulk inlet velocity [129]. Averaging of the desired variables is done after sufficient times such that steady state conditions are observed.

The step simulations were performed in 3D with periodic boundary conditions in the z-direction (perpendicular to the step), and at atmospheric pressure. A uniform inlet velocity with fluctuations of around 5% of the inlet average value are considered based on measured experimental values close to the inlet section [5]. No-slip conditions are applied along all walls while zero-gradient conditions are used for other variables. Similarly at the exit, zero-gradient conditions are specified for all variables except pressure for which wave-transmissive conditions are used. Convection heat transfer from the top and bottom walls is also considered to realistically reflect the

wall's thermal boundary conditions in the experiments [128, 5].

5.2.3 Swirl

The swirl combustor configuration is shown in Figure 5-5 and is based on the same combustor geometry as the experiment (Chapter 2). The inlet conditions tested are shown in Table 5.1 where $CH_4/O_2/CO_2$ mixtures are introduced at various equivalence ratios, inlet temperatures and Reynold's Numbers similar to the experiments [18]. The code and mesh for the swirl combustor has been tested and validated before [87] for CH_4/Air mixtures and so in this study we change the inlet mixture to study methane oxy-combustion and the effect of the extinction strain rate of the kinetic model on the results. Details of the experimental study for a $CH_4/O_2/CO_2$ mixture at an equivalence ratio of 0.65 and Reynold's Number of 20,000 in the same geometry are reported in Watanabe et al. [18].

The mesh consists of 0.65 million cells and the cells get coarser as you move downstream. The average cell sizes in the whole domain is 1 mm with maximum and minimum cell sizes of 1.6 mm and 0.32 mm. The mesh is also non-uniform with a mix of tetrahedral and hexahedral cells. Tetrahedral cells are used around the swirler to better model its geometry. The swirler has 8 blades each inclined at 45^o to the cylinder cross-section, with an estimated swirl number of 0.7. Grid sensitivity tests were performed up to a 2 million cells grid [17, 85, 86]. The computational time increased by a factor of three and the results did not show significant improvements, when compared to experiments, in order to justify this increased time. The computational times using these fine grids were also too long to allow a practical use of LES in this case.

Dirichlet conditions are used for all variables at the inlet except the pressure for which zero-gradient conditions are specified. The inlet velocity is uniform with turbulent fluctuations imposed. No-slip conditions are applied along all walls while zero-gradient conditions are used for other variables. Similarly at the exit, zero-gradient conditions are specified for all variables except pressure for which wave-transmissive conditions are used. Convection heat transfer from the walls is considered, while

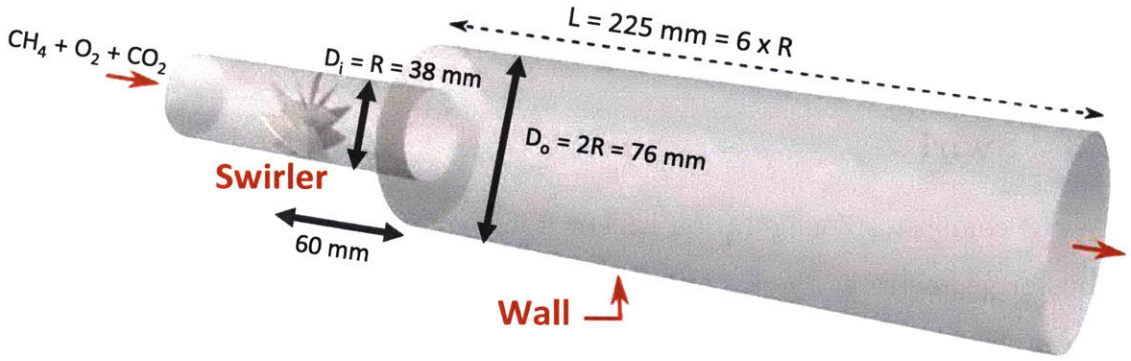

Figure 5-5: Computational domain dimensions for the swirl case studied in this work.

radiation within the gases and with the wall is neglected. The thermal boundary condition used at the wall is a Robin (mixed) type boundary condition that takes into account an effective external heat transfer coefficient.

5.3 Propane-Air Combustion Results

We start the analysis by first investigating propane-air mixtures in the simple geometries of triangular bluff body and backward-facing step combustors. This will also serve as a validation of the LES code and to initially support the idea that chemistry is important.

5.3.1 Chemical Kinetics Modeling

CHEMKIN-PRO is used to perform the extinction strain rate calculations. More details about these calculations and models can be found in Section 2.2.2.

Propane-air combustion is modeled using a reduced mechanism by Ghani et al. [130] containing 5 species and 2 reactions. This mechanism gave acceptable approximations of adiabatic flame temperatures and laminar burning velocities in a laminar premixed flame setup [130]. As we will show, this mechanism also gave reasonable extinction strain rates as well for certain cases.

We begin by comparing extinction strain rates calculated with the 2-step mechanism developed by Ghani et al. [130] and the detailed UC San Diego (UCSD)

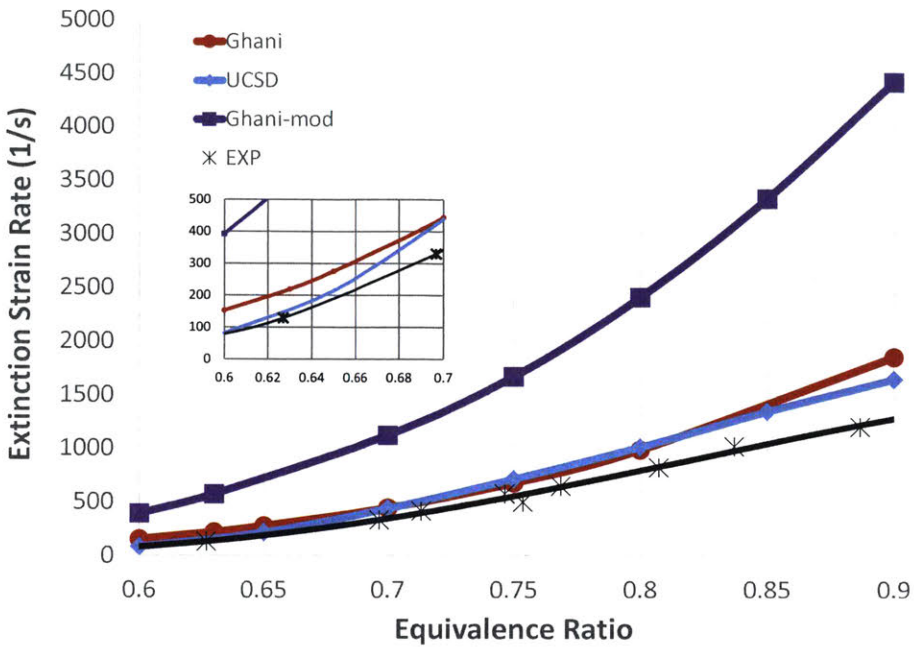

Figure 5-6: Extinction strain rates for C_3H_8/Air mixtures at atmospheric conditions calculated by the three mechanisms and measured in experiments [22].

mechanism [131] in Figure 5-6. Measured extinction strain rates from experiments by Law et al. [22] are also plotted in the figure. In our LES simulations, we can only use small kinetic models [86, 87], such as the Ghani mechanism, and so these comparisons serve to determine the accuracy of this mechanism on the basis of extinction strain rate predictions.

The 2-step Ghani mechanism reasonably predicts extinction strain rates in comparison to the UCSD mechanism and experiments in the equivalence ratio range we are concerned about: 0.6-0.85. But in the zoomed-in section of the plot, the Ghani mechanism predicts extinction strain rates about 1.5x those of the experiments. This difference still impacts the bluff body LES results as we will show later. This strained flame response was not the target variable during the development of the Ghani mechanism [130] and is "coincidentally" in fair agreement, however for our purposes we will use this kinetic model in the simulations since it is commonly used in LES of propane mixtures [132, 133] and has the fairest agreement out of some of the other reduced mechanisms in the literature [78]. The extinction strain rate results also show

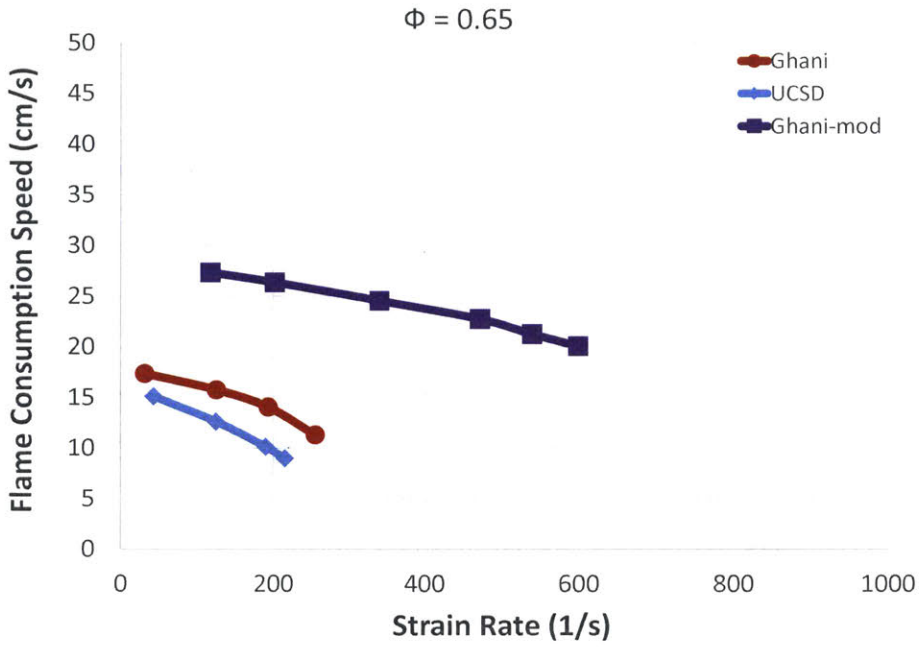

Figure 5-7: Calculated consumption speeds for C_3H_8/Air at equivalence ratio of 0.65 at atmospheric conditions for the three mechanisms.

that the values for the Ghani mechanism and experiments diverge as the equivalence ratio increases. Once again this divergence in extinction strain rates will impact the accuracy of LES results in the backward-facing step combustor (Section 5.3.3). The flame consumption speeds of the two mechanisms at equivalence ratio of 0.65 also show a small disagreement (Figure 5-7) as well as a difference in extinction strain rates at this condition.

In order to study the effect of the extinction strain rate of the chemical mechanism on LES, we wanted to test another mechanism that had worse agreement than the original Ghani mechanism. Therefore we modified the reaction orders of the original Ghani mechanism in order to intentionally obtain an extinction strain rate curve that is far different than the original one as shown by the purple line in Figure 5-6. This incorrect extinction strain rate curve, also leads to a much different flame consumption speed curve as is seen in figure 5-7. Moving forward, this new modified mechanism will be referred to as "Ghani-mod". The flame response to strain of the modified mechanism performs worse than the original Ghani mechanism and so we

expect this to have the least accurate LES results out of the two.

5.3.2 Bluff Body Combustor Results

Results from the non-reacting simulations of the bluff body case are presented first for the two resolution grids, in order to establish the accuracy of the LES model. All profile comparisons throughout this chapter are done using normalized quantities. The spatial dimensions are normalized by the bluff body dimension (D = 40 mm), non-reacting velocities are normalized by the bulk inlet velocity of 16.6 m/s, and the reacting velocities are normalized by 17.3 m/s. Figures 5-8 and 5-9 show the mean and rms normalized axial velocity profiles at different cross-sections across the length of the combustor for Mesh A and B. Figures 5-10 and 5-11 present the centerline profiles for the mean axial velocity and 2D turbulence intensity i.e. fluctuation level. The 2D turbulence intensity is defined as:

$$TI_{2D} = \frac{\sqrt{u_{x,rms}^2 + u_{y,rms}^2}}{U_0}$$

It is observed that the underlying average flow field is well resolved for both grids but the velocity fluctuations do not compare as well with experiments which could be due to the periodic boundary conditions employed in this test case. However the recirculation zone length is well predicted for both meshes along with the turbulence intensity levels as can be seen in figures 5-10 and 5-11.

Therefore it can be concluded that the results from the non-reacting simulations for both meshes are in reasonable agreement with the experimental data and the coarse mesh is sufficient for capturing the non-reacting flow field. This demonstrates a validation of our LES model for this case and confirms that the turbulence model employed is sufficient to capture the physics associated with this non-reacting flow.

Next, results from reacting simulations are presented in this section using the coarse mesh in the bluff body geometry. The main goal here is investigating the importance of the chemistry on the accuracy of the simulations and the ability to predict flow structures. As mentioned previously, our hypothesis is that the chemistry mechanism in CFD models must be able to predict correct values of K_{ext} if

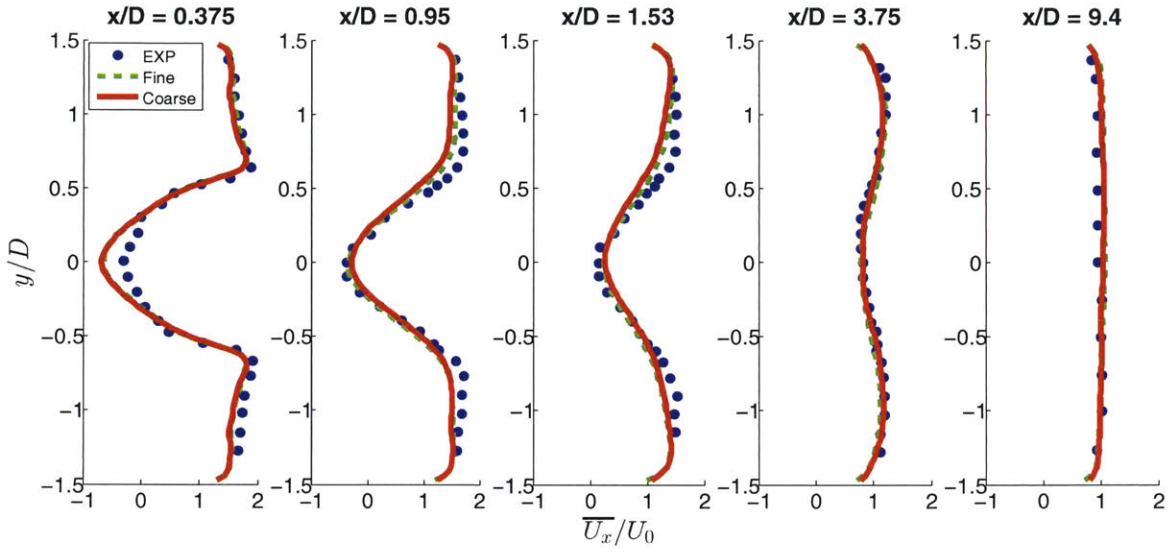

Figure 5-8: Normalized mean axial velocity profiles for the two grids at several axial (x/D) locations for the non-reacting bluff body case.

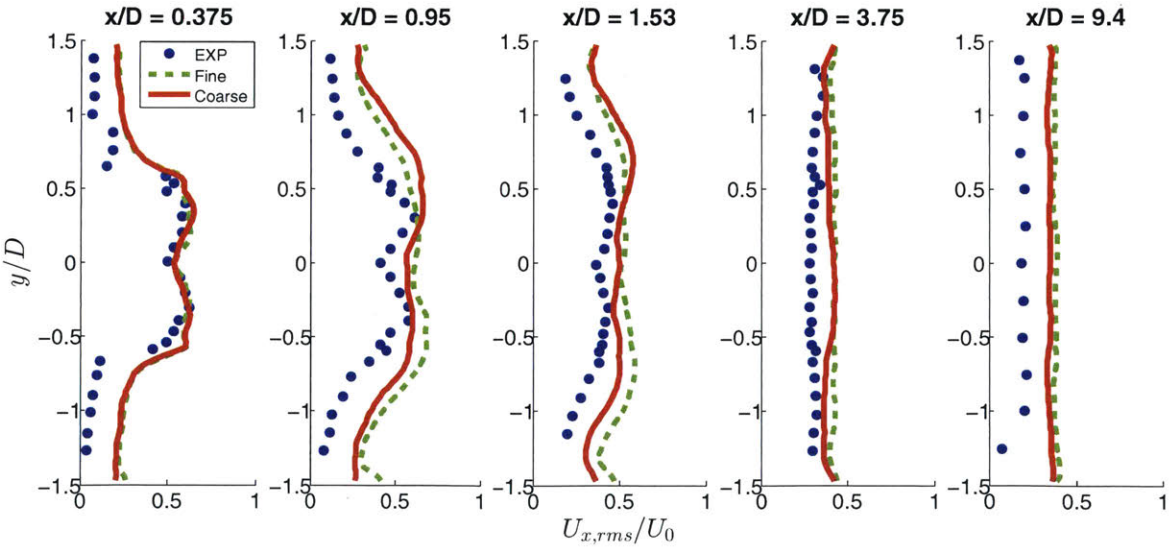

Figure 5-9: Normalized rms axial velocity profiles for the two grids at several axial (x/D) locations for the non-reacting bluff body case.

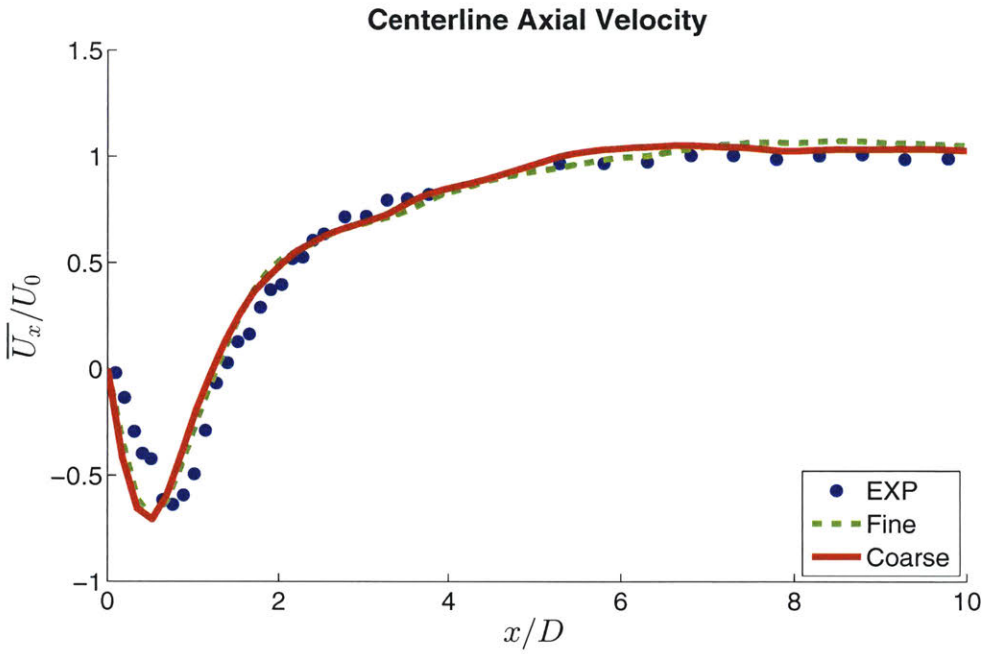

Figure 5-10: Centerline profiles of normalized mean axial velocity for the two grids for the non-reacting bluff body case.

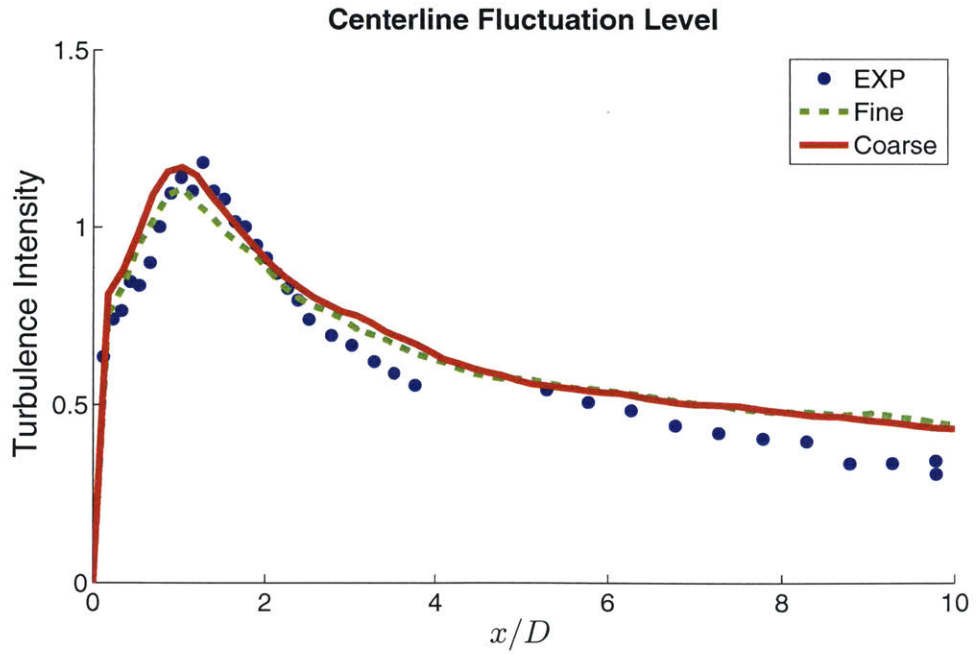

Figure 5-11: Centerline profiles of turbulence intensity for the two grids for the non-reacting bluff body case.

the simulations are expected to accurately capture realistic flow and flame features. This is because correct extinction strain rates prediction also leads to correct flame responses to strain.

Figure 5-12 shows the average velocity contours comparing the Ghani and modified Ghani mechanisms. A strong low-speed recirculation zone is predicted in both cases downstream of the bluff body which is consistent with the experimental data and theory [134] and helps to stabilize the flame. The original mechanism (top figure) predicts a slightly longer recirculation zone with higher speeds which is closer to the experimental measurements (see Figures 5-13 and 5-14). The recirculation zone length is measured by the location of the stagnation point (i.e. location at which the axial velocity along the centerline is zero). This can clearly be seen in the zoomed-in plot in Figure 5-14. The average axial velocity profiles are compared for the Ghani and modified Ghani mechanisms in Figures 5-13 and 5-14. Additional reacting flow profiles are shown in Figures 5-17 to 5-23 for further validation. The modified Ghani mechanism, with poor extinction strain rate predictions, performs worse than the simulation using the original mechanism. In Figure 5-14 which shows the centerline axial velocity, the simulation with the modified mechanism fails to reproduce the correct velocity magnitude inside the recirculation zone and also predicts a smaller recirculation zone length than the original mechanism. It was shown previously in DNS results [6] that the higher the K_{ext} of the flame, the shorter the recirculation zone predicted after the bluff body which is what is also observed here between the modified mechanism that predicts higher extinction strain rates and the original Ghani mechanism. It should be noted that the Ghani mechanism at ϕ=0.65 still predicts an extinction strain rate that is 1.5x that of the experiment. This can be a large source of error and could also lead to the difference in recirculation zones observed between the simulation and experiment in Figure 5-14. However both mechanisms over-predict the velocities further downstream in the combustor. This might be due to the over-prediction in temperature further downstream that we show next. Additionally, further refinement of the mesh in that downstream region could help reduce that error.

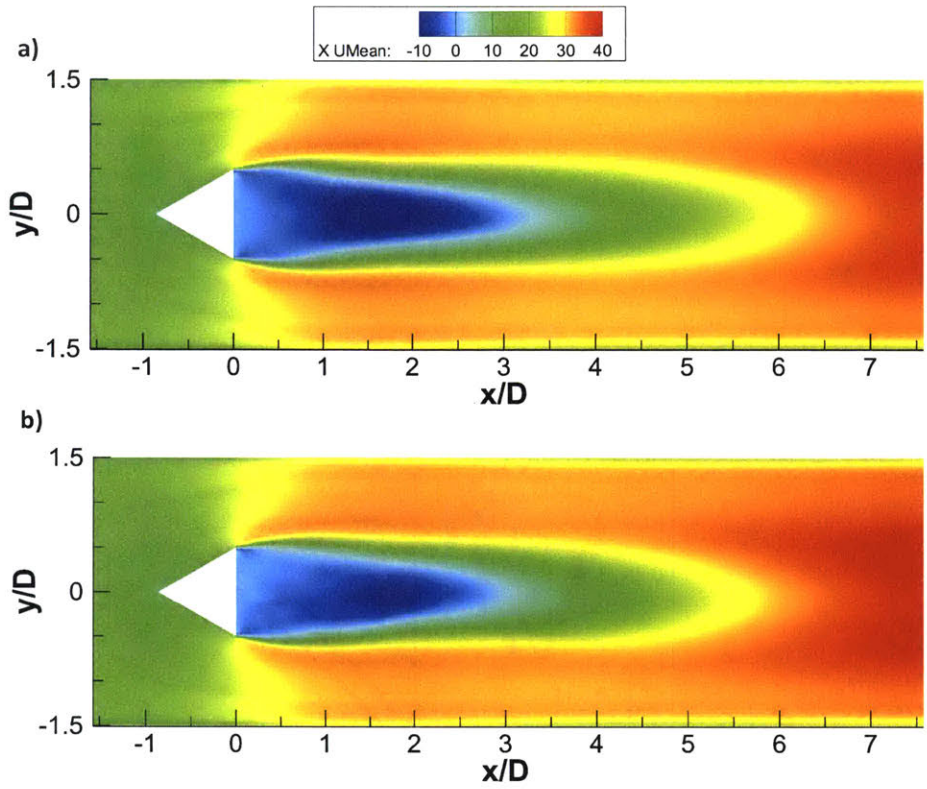

Figure 5-12: Mean axial velocity contours (m/s) for the two propane kinetic models for the reacting bluff body case at ϕ=0.65. a) Ghani mechanism, b) Ghani-mod mechanism.

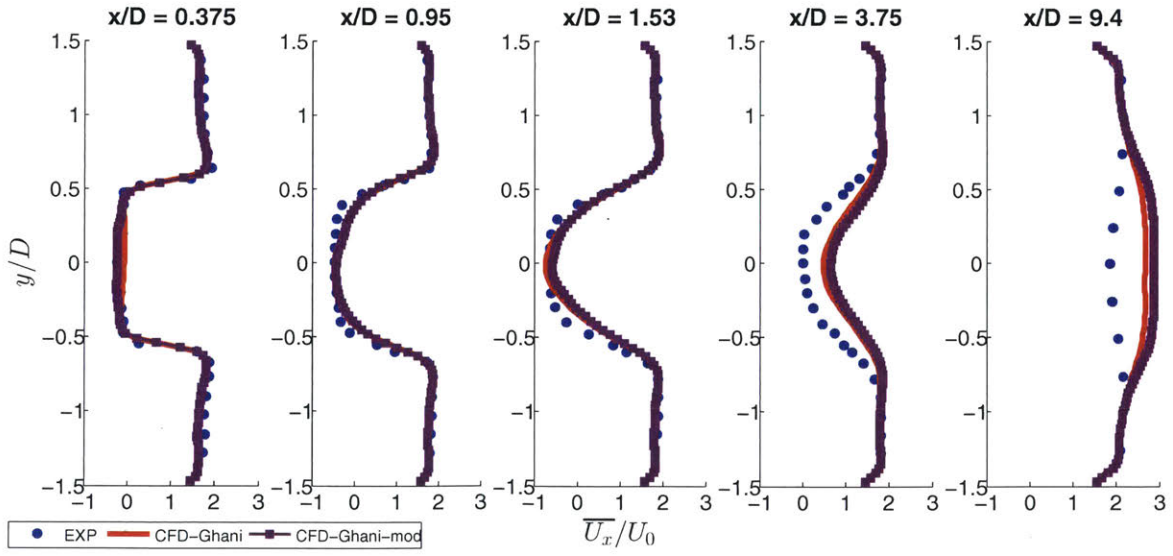

Figure 5-13: Normalized mean axial velocity profiles for two reduced kinetic models at several axial (x/D) locations in the reacting bluff body case for the propane-air mixture at ϕ=0.65.

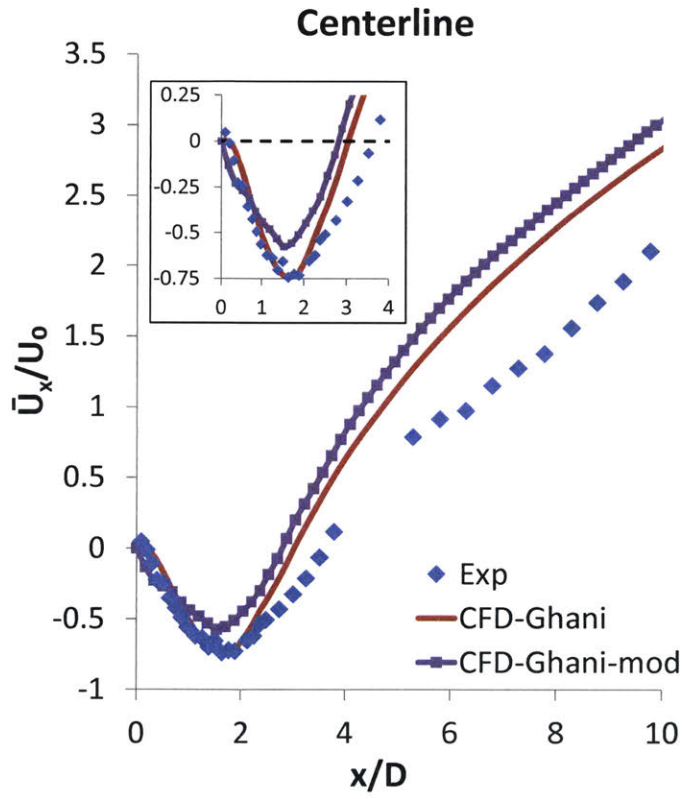

Figure 5-14: Centerline profiles of the normalized mean axial velocity for two reduced kinetic models in the reacting bluff body case for the propane-air mixture at ϕ=0.65.

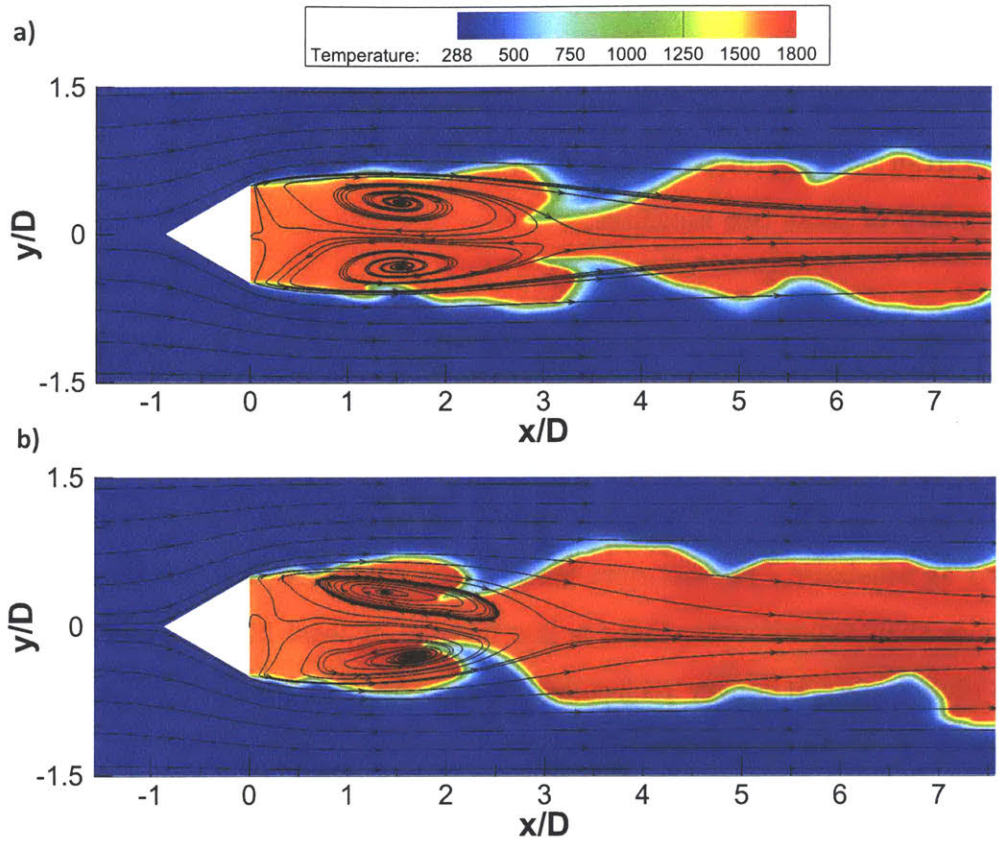

Figure 5-15: Instantaneous temperature contours (K) and mean streamlines using two reduced kinetic models in the reacting bluff body case for the propane-air mixture at ϕ=0.65. a) Ghani mechanism, b) Ghani-mod mechanism.

It has been shown that for a premixed bluff-body stabilized flame there is a significant change in the flow physics between the non-reacting to reacting flow fields, due to the suppression of the asymmetric vortex shedding seen in non-reacting flows, as a result of the heat release. This vortex suppression leads to a symmetric flame shape at high heat release [135, 136] and so capturing this correct physical solution to the problem is key.

Figure 5-15 shows instantaneous temperature contours with average velocity streamlines using the two chemical mechanisms in question. Unfortunately experimental flow field visualizations for this test case are not available which would have been very valuable in these qualitative comparisons. But we can still see that indeed the two LES runs predict symmetric flame shapes similar to those observed in previous

studies on this bluff body geometry [52]. Using the mean velocity streamlines we also see the difference in recirculation zone lengths once again and this key flow feature helps to anchor the flame as hot products are stored in the wake and their mixing with the fresh reactant mixture results in a flame forming at the shear layer and at the boundary of these two mixtures.

The average temperature profiles for each of the cases are also compared with the experimental data (Figure 5-16) and as can be seen, the kinetic models over-predict the temperature near the center especially further downstream. The higher predicted temperatures could be due to heat losses in the experiment while the combustor is modeled as adiabatic. Furthermore since the simulations predict shorter recirculation zones than experiments, there is less mixing, at least immediately downstream of the bluff body. If longer recirculation zones were predicted, allowing for more mixing, more of the cooler reactants would have been introduced into these zones possibly resulting in reduced temperatures near the center and better matching with the experimental values.

The two simulations also under-predict the spread rate of the flame and in Ref. [137] this is attributed to the fact that periodic boundary conditions are used and the effects of the four walls are not well represented. It should be mentioned that this under-prediction is also seen in other simulations on this test case utilizing other numerical schemes and CFD codes [52].

Now that we have provided elements pointing towards the importance of the kinetic models on the prediction of velocities, recirculation zones and temperatures, we will take this analysis a step further by testing these two chemical mechanisms in a combustor geometry where we have experimental data for multiple C_3H_8/Air equivalence ratios. Our aim is to provide further evidence of what we have observed so far in the bluff body combustor, but for a different geometry and other equivalence ratios.

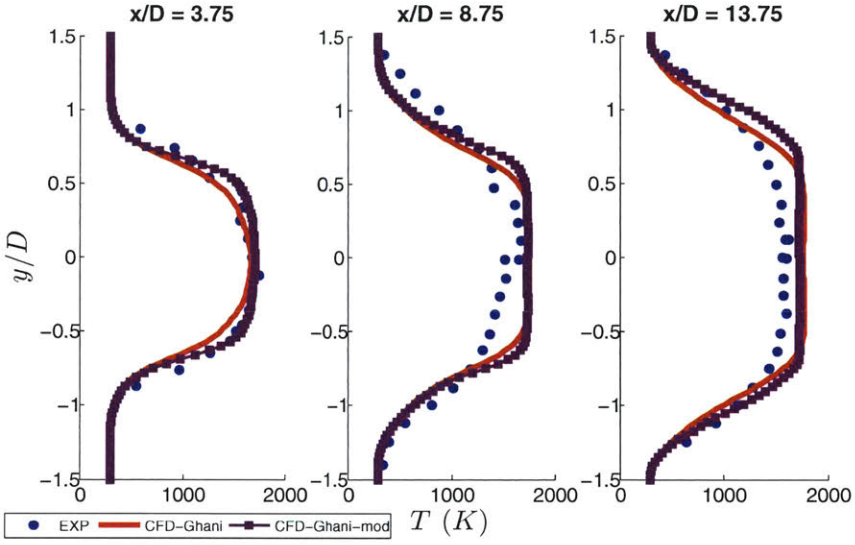

Figure 5-16: Mean temperature profiles for the two propane kinetic models at several axial (x/D) locations for the bluff body case at ϕ=0.65.

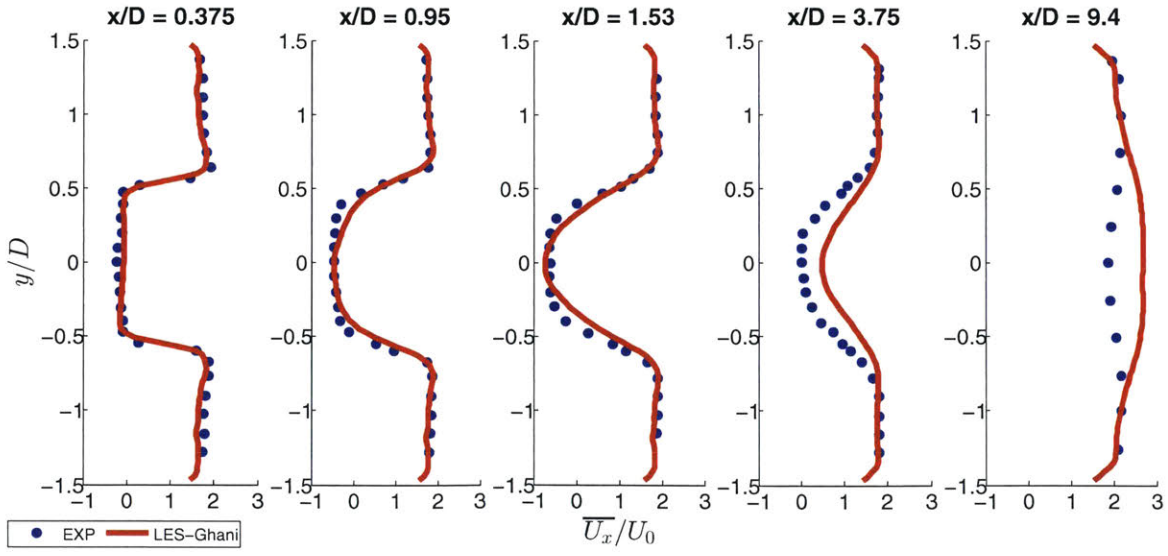

Figure 5-17: Normalized mean axial velocity profiles using the Ghani mechanism at several axial (x/D) locations for the reacting bluff body case at ϕ=0.65.

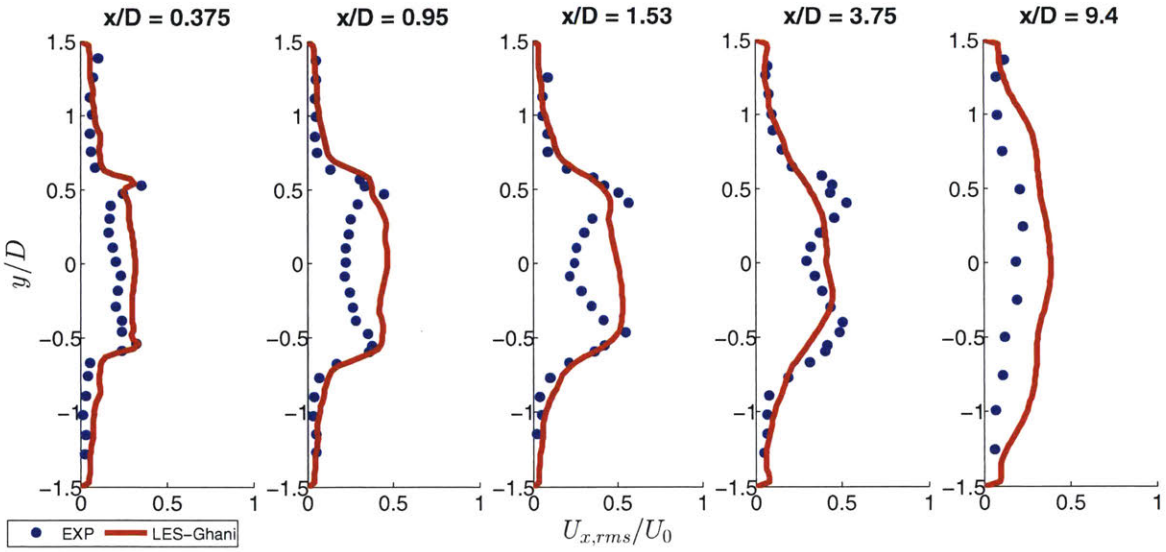

Figure 5-18: Normalized rms axial velocity profiles using the Ghani mechanism at several axial (x/D) locations for the reacting bluff body case at ϕ=0.65.

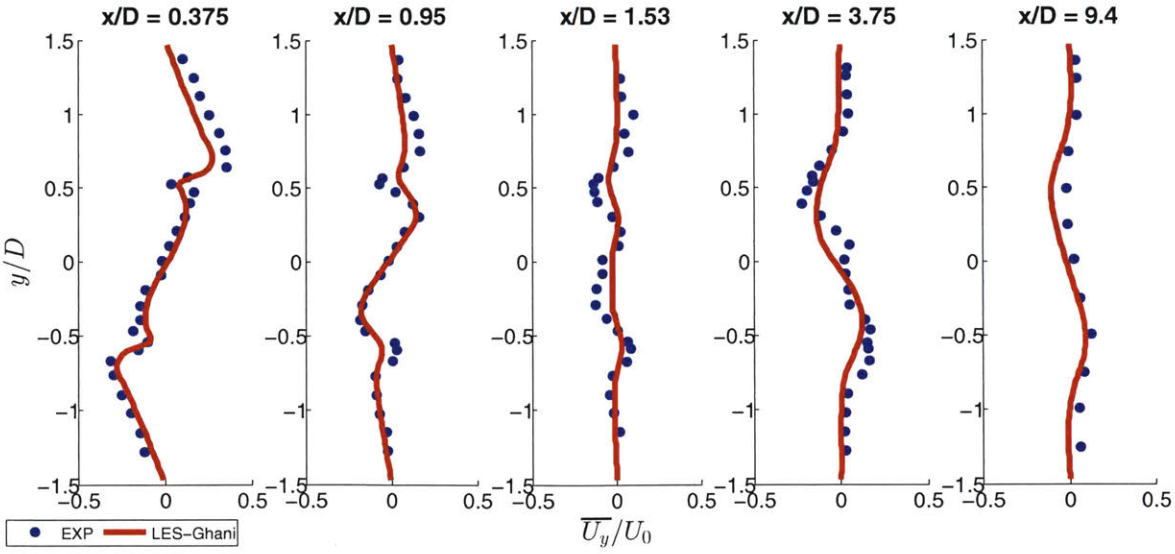

Figure 5-19: Normalized mean transverse velocity profiles using the Ghani mechanism at several axial (x/D) locations for the reacting bluff body case at ϕ=0.65.

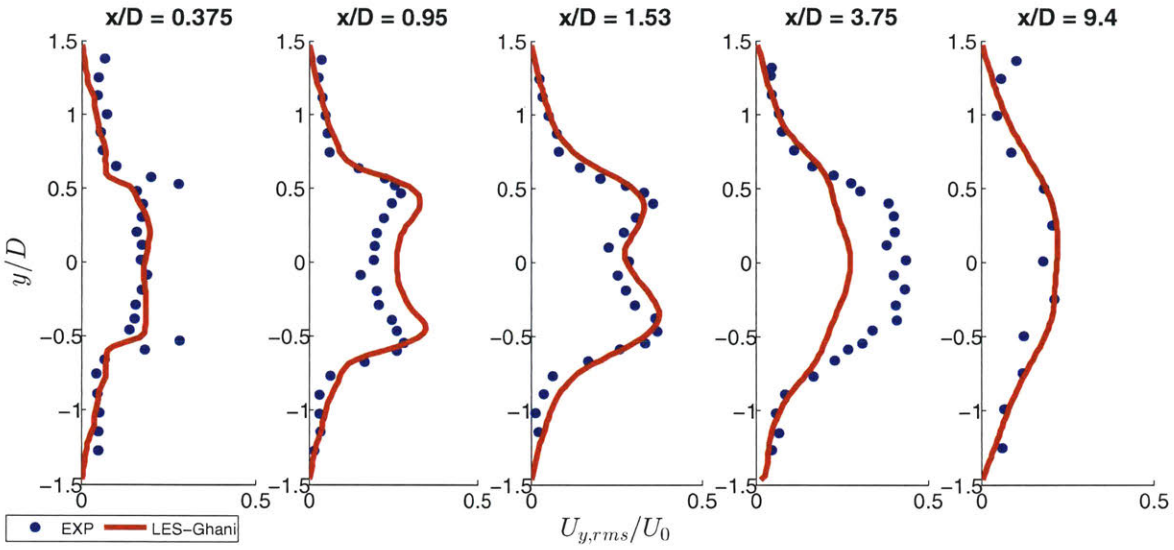

Figure 5-20: Normalized rms transverse velocity profiles using the Ghani mechanism at several axial (x/D) locations for the reacting bluff body case at ϕ=0.65.

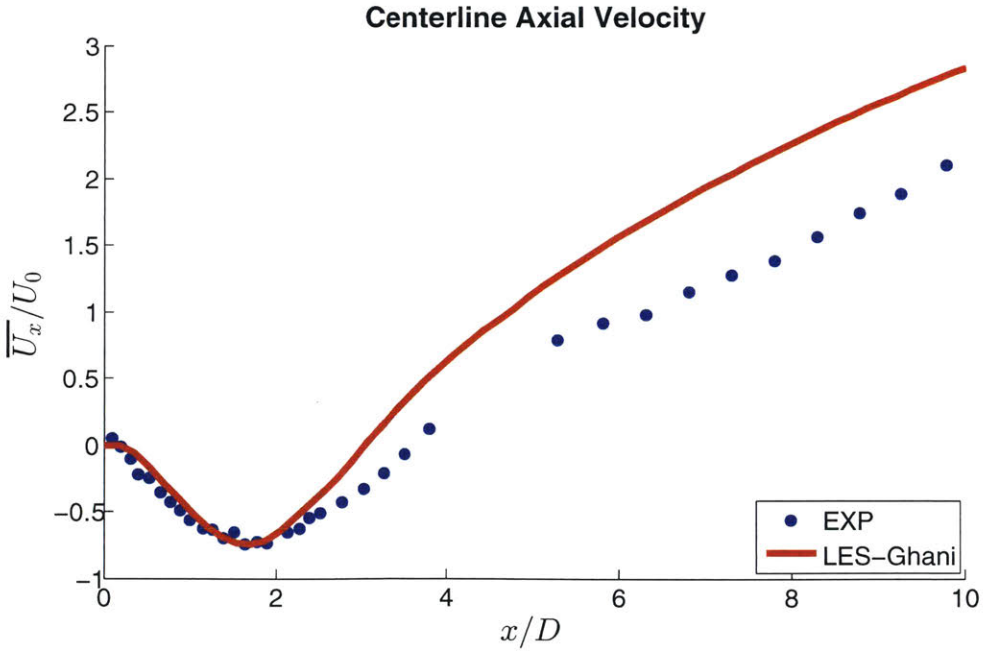

Figure 5-21: Centerline profiles of the normalized mean axial velocity using the Ghani mechanism for the reacting bluff body case at ϕ=0.65.

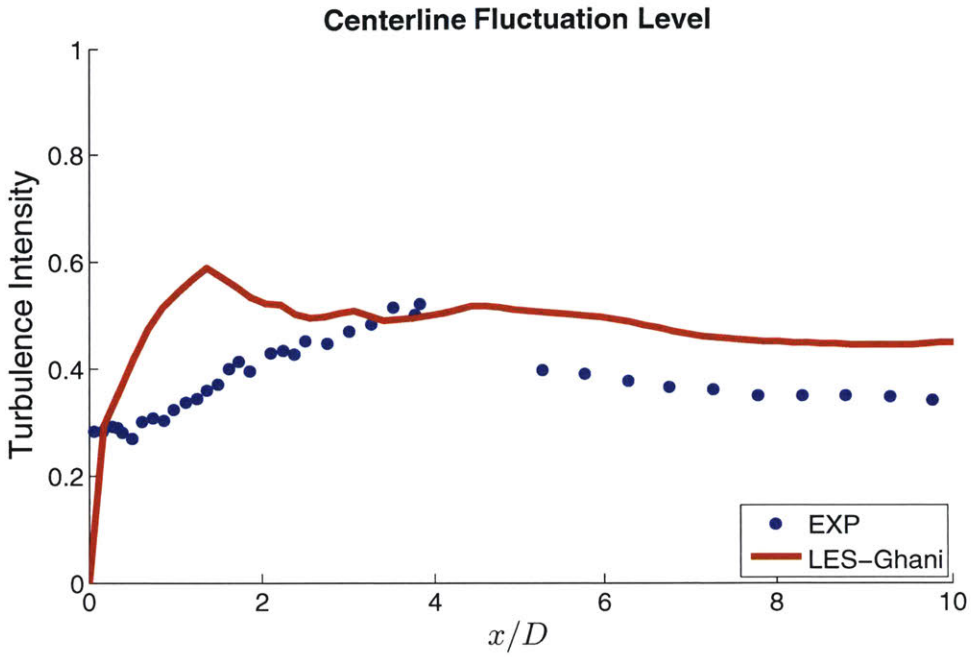

Figure 5-22: Centerline profiles of turbulence intensity using the Ghani mechanism for the reacting bluff body case at ϕ=0.65.

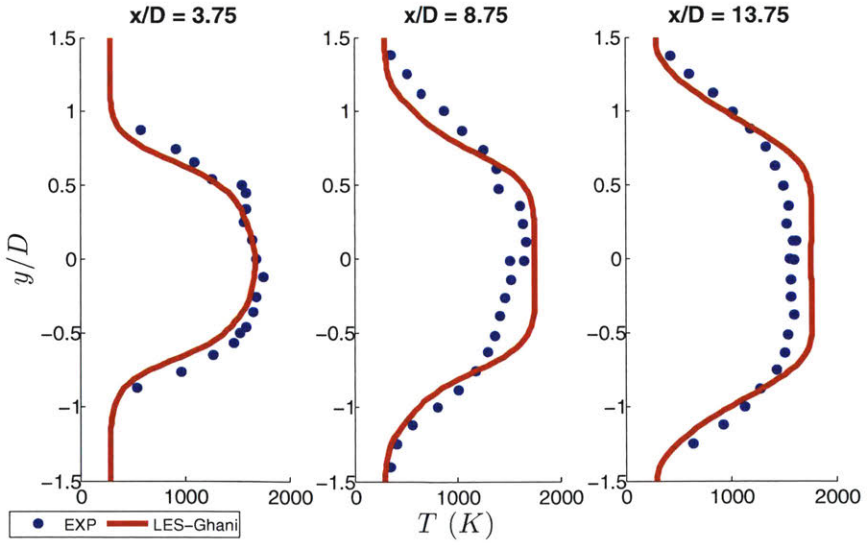

Figure 5-23: Mean temperature profiles using the Ghani mechanism at several axial (x/D) locations for the reacting bluff body case at ϕ=0.65.

5.3.3 Backward Facing Step Combustor Results

In this section, the two chemical mechanisms tested earlier in the bluff body geometry ("Ghani" and "Ghani-mod"), are compared in the backward-facing step combustor simulations. The LES code has already been tested extensively and validated against experimental data in Ref. [129] for the same step combustor geometry. In this study, only the kinetic model is changed in order to specifically look at the effect of the extinction strain rate on the prediction of important flow features.

Four C_3H_8/Air equivalence ratios were simulated: 0.63, 0.75, 0.79, 0.85. Figure 5-24 shows experimental mean streamlines at two equivalence ratios (ϕ=0.63 & 0.85) using PIV data obtained from Ref. [5]. Figure 5-25 depicts the instantaneous temperature contours along with mean velocity streamlines for the same two equivalence ratios and using the two mechanisms in order to show the reacting flow fields in LES. Figures 5-26 and 5-27 also show the mean axial velocities at several locations comparing experimental PIV data to LES with the two mechanisms. In general, as the equivalence ratio is raised, the size of the primary recirculation zone is reduced and its location moves further upstream towards the step. The higher temperature ratio across the flame reduces the velocity gradient in the shear layer and thus the overall recirculation zone length [5]. This strong dependence of the recirculation zone length on the equivalence ratio is also seen experimentally in Figure 5-24 where the length is almost halved. The simulations also predict the secondary recirculation zone at ϕ=0.63 which is in agreement with the experiments. Similar to what we saw in the bluff body combustor, the predicted recirculation zones using the modified Ghani mechanism were smaller than those with the original mechanism. As we show later in Table 5.2, the modified mechanism is much less accurate in predicting recirculation zone lengths compared to experiments than the original Ghani mechanism. This provides further evidence that the incorrect response to strain of the flame with the modified mechanism (Figure 5-6), negatively impacts the accuracy of the flow structures in LES.

Figure 5-25 also shows the flame tip or leading edge moving towards the step as

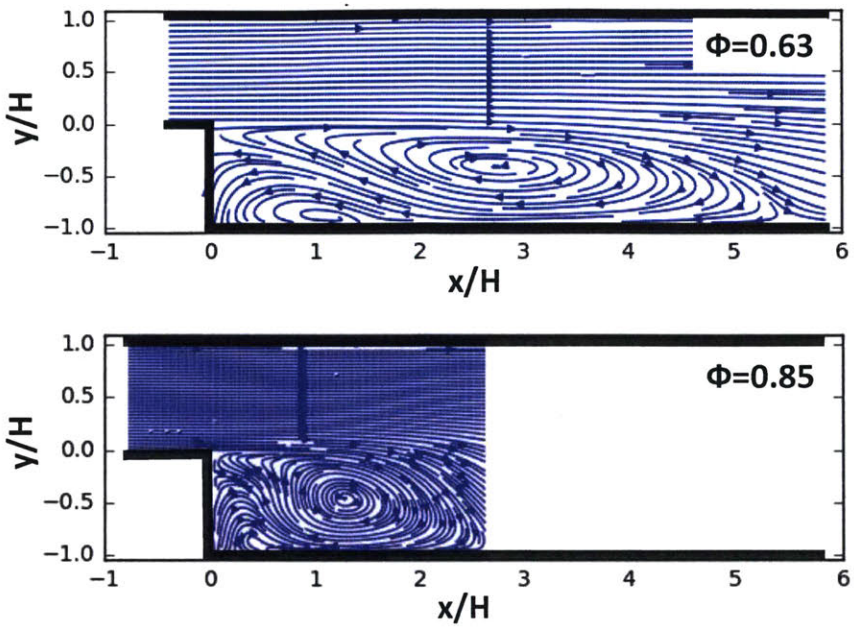

Figure 5-24: Experimental (PIV) mean streamlines for two propane-air equivalence ratios in the step combustor, ϕ=0.63 (top), ϕ=0.85 (bottom).

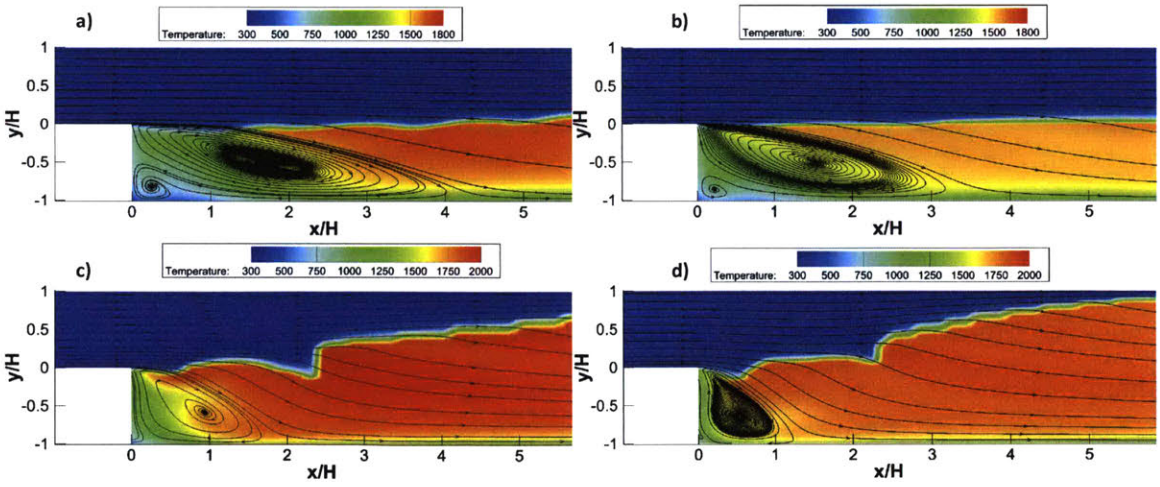

Figure 5-25: Instantaneous temperature contours (K) and mean streamlines for the Ghani and modified Ghani mechanisms and propane-air equivalence ratios in the step combustor: a) ϕ=0.63, Ghani mechanism, b) ϕ=0.63, Ghani-mod mechanism, c) ϕ=0.85, Ghani mechanism, d) ϕ=0.85, Ghani-mod mechanism.

the equivalence ratio is raised to 0.85. Since the flame at the higher equivalence ratio has a higher extinction strain rate, it is able to stabilize in regions of higher strain closer to the step. This is supported by experimental data [128] and also numerically in Ref. [6] with DNS. The flame angle also increases as can be seen at the higher equivalence ratios. The temperature inside the recirculation zones are lower as would be expected mainly due to the recirculating products mixing with reactants and also due to heat losses from the step walls. The temperatures in the simulations using the original mechanism (the two plots on the left) are higher especially downstream of the step. When the reaction orders are modified to produce the *Ghani-mod* mechanism, this will also slightly change the product concentrations predicted in simulations using this mechanism. Hence we might expect different temperatures downstream in the reacting flow field.

The solution using the *Ghani-mod* mechanism, which over-predicts extinction strain rates, behaves as though the reactants were at higher equivalence ratios. The simulations using this mechanism, have flames that stabilize closer to the step compared to flames predicted by simulations using the original Ghani mechanism, as can be seen in Figure 5-25. Since extinction strain rates of the *Ghani-mod* mechanism are higher, these flames can withstand regions of higher strain. This impacts the size of the recirculation zone and also results in erroneous velocity predictions as seen in Figures 5-26 and 5-27. Table 5.2 compares the accuracy of the predicted recirculation zone lengths in LES using the two reduced mechanisms. The measured lengths are obtained from experiments done in our previous work in Refs. [5] and [129]. The recirculation zone lengths are consistently under-predicted using both reduced mechanisms but the error is even worse using the *Ghani-mod* mechanism. The results obtained using the original Ghani mechanism also don't accurately predict the lengths and this could partly be due to the differences in calculated extinction strain rates with experimental values. As was seen in Figure 5-6, the extinction strain rate agreement with experiments gets worse as the equivalence ratio increases and Table 5.2 shows that this is responsible for also increasing the error at higher equivalence ratios. Developing and implementing another reduced C_3H_8/Air mechanism that more

ϕ	$L_{RZ,EXP}$ (mm)	$L_{RZ,Ghani}$ (mm)	Error	$L_{RZ,Ghani-mod}$ (mm)	Error
0.63	108	86	21 %	69	36 %
0.75	80	55	31 %	45	43 %
0.79	70	47	32 %	34	56 %
0.85	57	37	36 %	25	57%

Table 5.2: Comparison between the experimental recirculation zone lengths and LES using the two reduced mechanisms in the step combustor

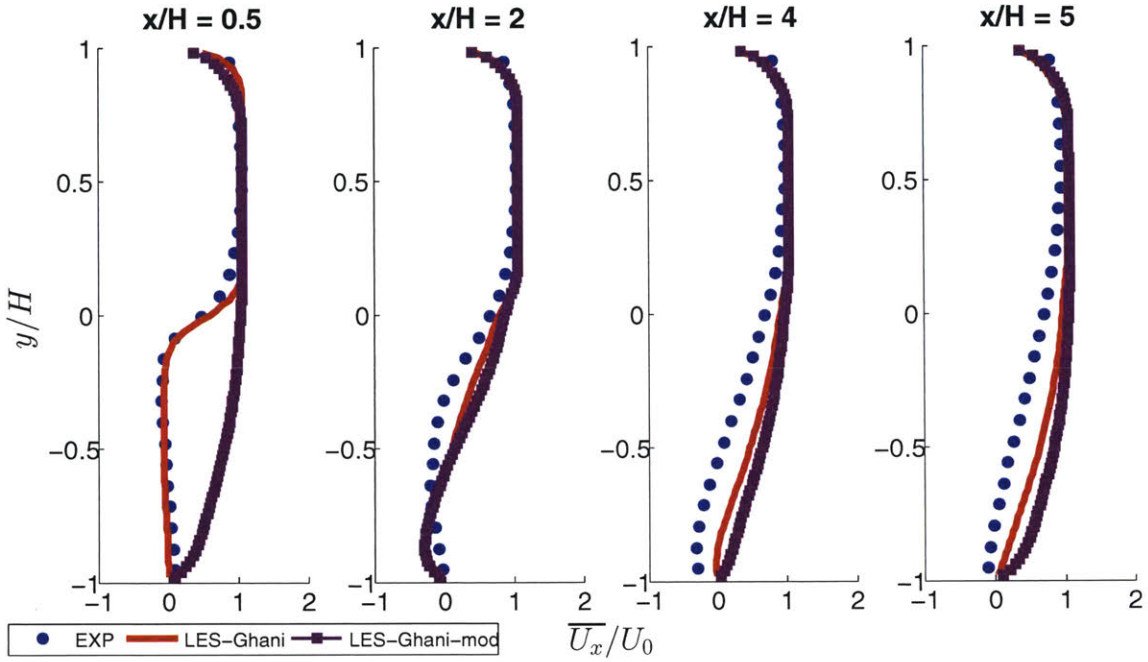

Figure 5-26: Normalized mean axial velocity profiles for two reduced kinetic models at several axial (x/H) locations in the step case for the propane-air mixture at ϕ=0.63.

accurately predicts extinction strain rate curves and values would help reduce this recirculation zone length error. Consequently, this analysis suggests that simulations done using chemical mechanisms that don't correctly match extinction strain rates, could incorrectly predict recirculation zone lengths in sudden expansion flows.

5.4 Methane Oxy-Combustion Results

Natural gas oxy-fuel combustion cycles are some of the leading technologies for carbon capture and sequestration (CCS) in power plants [38]. These cycles require combus-

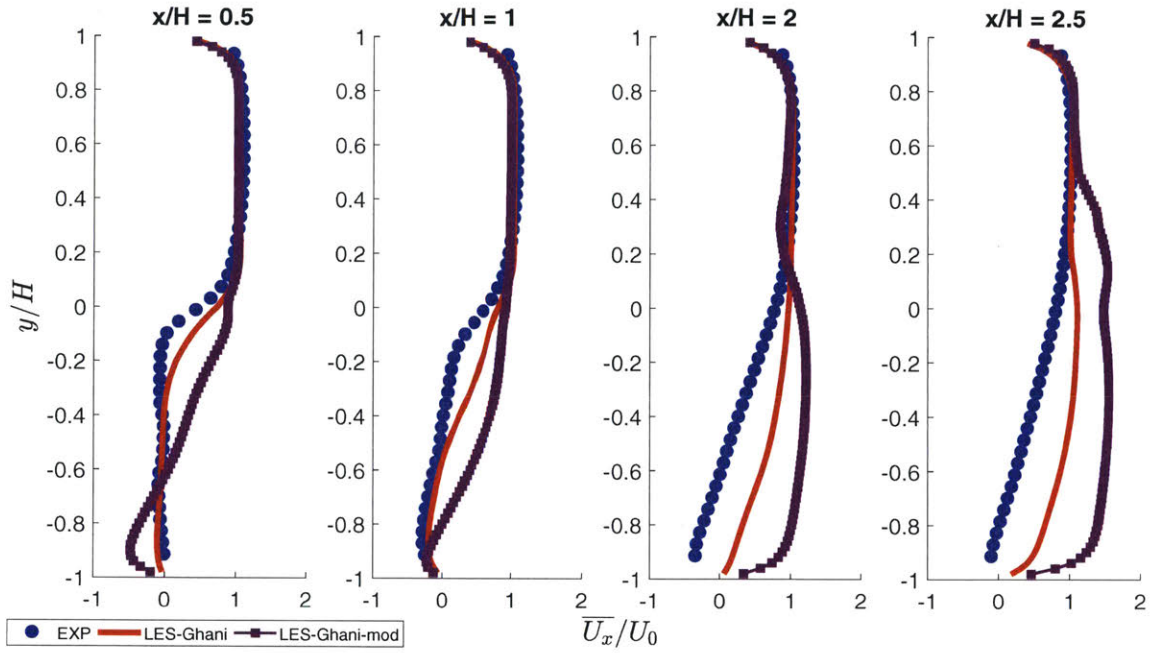

Figure 5-27: Normalized mean axial velocity profiles for two reduced kinetic models at several axial (x/H) locations in the step case for the propane-air mixture at ϕ=0.85.

tors that can burn fuel and an oxygen stream along with some diluent, typically CO_2, to control flame temperatures. The ability to accurately simulate these mixtures and understand the characteristics of oxy-combustion flames, are important for the design of combustors in these power plants. Therefore the aims of this section are to firstly show the importance of chemical kinetics modeling in simulations of complex swirling flows, and secondly to provide a validation for our LES code in the swirl combustor for these $CH_4/O_2/CO_2$ mixtures (methane-oxy mixtures).

5.4.1 Chemical Kinetics Modeling

Once again we begin by comparing kinetic mechanisms to use for LES in the swirl combustor. Until now there is no clear consensus on which reduced reaction mechanism should be used for CFD modeling of oxy-combustion as was discussed in Chapter 1. Frassoldati et al. [14] generated a new mechanism for methane oxy-combustion by tuning the widely used Jones and Lindstedt (JL) [78] mechanism for methane-air. They reported improved agreement of temperature and CO_2-profiles in a laminar

Reactions	A	B	E_a	Reaction Orders
$CH_4 + 1.5O_2 \rightarrow CO + 2H_2O$	1.59×10^{13}	0	47.8×10^3	$[CH_4]^{0.7}[O_2]^{0.8}$
$CO + 0.5O_2 \rightarrow CO_2$	3.98×10^8	0	10×10^3	$[CO][O_2]^{0.25}[H_2O]^{0.5}$
$CO_2 \rightarrow CO + 0.5O_2$	6.16×10^{13}	-0.97	78.4×10^3	$[CO_2][H_2O]^{0.5}[O_2]^{-0.25}$

Table 5.3: Andersen mechanism with kinetic rate data, units are: cm, s, cal, mol

Reactions	A	B	E_a	Reaction Orders
$CH_4 + 0.5O_2 \rightarrow CO + 2H_2$	7.69×10^{12}	0	3×10^4	$[CH_4]^{0.5}[O_2]^{1.3}$
$CH_4 + H_2O \rightarrow CO + 3H_2$	3.84×10^{12}	0	3×10^4	$[CH_4][H_2O]$
$CO + H_2O \leftrightarrow CO_2 + H_2$	2.01×10^{12}	0	2×10^4	$[CO][H_2]$
$H_2 + 0.5O_2 \leftrightarrow H_2O$	2.85×10^{19}	-1	4×10^4	$[H_2]^{0.3}[O_2]^{1.55}$
$O_2 \leftrightarrow 2O$	1.5×10^9	0	11.3×10^4	$[O_2]$
$H_2O \leftrightarrow H + OH$	2.3×10^{22}	-3	12×10^4	$[H_2O]$

Table 5.4: Frassoldati mechanism with kinetic rate data, units are: cm, s, cal, mol

diffusion flame.

Almost simultaneously, Andersen et al. [15] presented their own modified oxy-fuel version of the well-known Westbrook and Dryer (WD) [77] mechanism. They left the fuel consumption reactions unchanged and modified the CO-CO_2 reactions to better fit plug flow reactor results using a detailed mechanism by Glarborg and Bentzen [13] under CO_2-diluted oxy-fuel condition. They found the modified mechanism to give a closer agreement for CO concentrations and equilibrium temperature values for a laminar diffusion flame. These two mechanisms are summarized in tables 5.3 and 5.4. The Frassoldati mechanism includes 3 more reactions and 4 more species thus it would seem that it should perform better in terms of predicting emissions and flame characteristics.

The laminar burning velocities are compared first for the oxy-fuel chemical mechanisms in Figure 5-28 (Adiabatic flame temperatures and CO profiles were similar for both reduced mechanisms). It is clear that both reduced mechanisms (Frassoldati and Andersen) fail to match flame speeds with the detailed mechanism proposed by

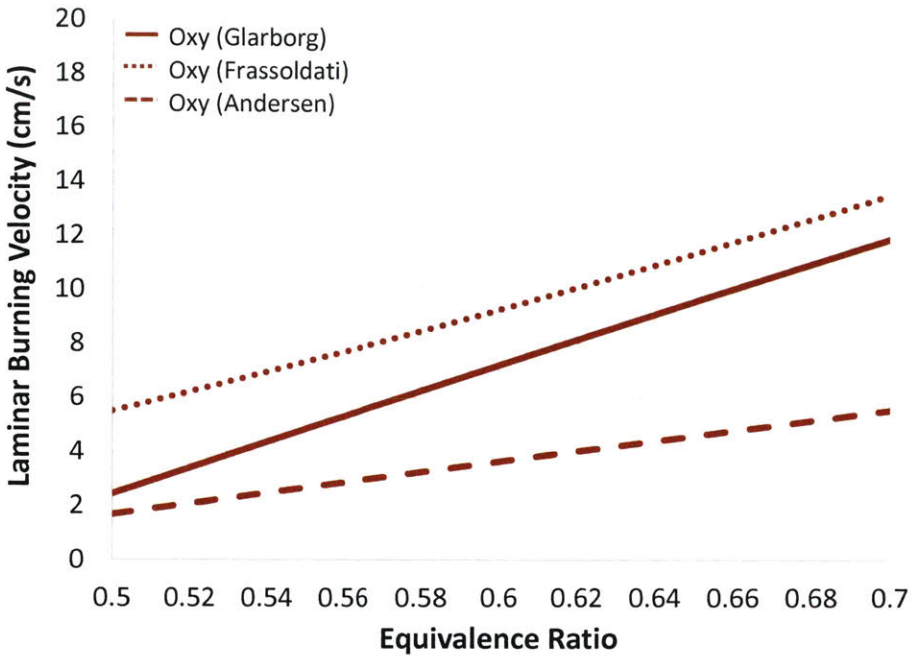

Figure 5-28: Laminar burning velocities for $CH_4/O_2/CO_2$ mixtures calculated by the three mechanisms.

Mendiara and Glarborg [109] with one reduced mechanism overpredicting and another underpredicting the speeds. The Frassoldati mechanism, however, has much closer values especially at the higher equivalence ratios.

Noting that neither of these two mechanisms were optimized for the extinction strain rate, we calculate extinction strain rates at a range of equivalence ratios using these two reduced mechanisms and compare the results to those with the detailed Glarborg mechanism (Figure 5-29).

Figure 5-29 shows a clear difference in extinction strain rates between the two reduced mechanisms in comparison to the detailed Glarborg mechanism. Values calculated with the Andersen mechanism extremely underpredict extinction strain rates whereas the Frassoldati mechanism performs much better. Therefore we expect a significant difference in the results for LES of the swirl combustor using these two reduced mechanisms in Section 5.4.2, with the Frassoldati mechanism expected to perform better. Predicting extinction strain rates well also doesn't necessarily translate to good laminar flame speed predictions as the figures show. Therefore by testing

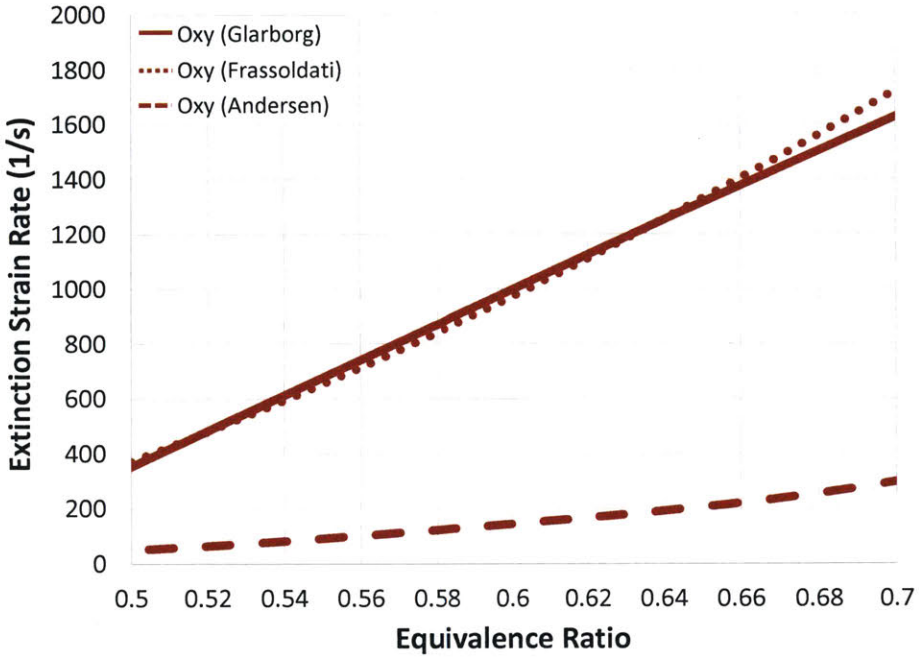

Figure 5-29: Extinction strain rates for $CH_4/O_2/CO_2$ mixtures calculated by the three mechanisms.

these oxy-fuel reduced mechanisms in the swirl combustor, we can evaluate the performance of mechanisms when extinction strain rates are well predicted while other flame characteristics might still be off.

5.4.2 Swirl Combustor Results

The preferred way to stabilize flames in modern gas turbine combustors is by vortex breakdown. As the swirling jet expands in the radial direction, an adverse pressure gradient is created along the centerline which results in an inner recirculation zone (IRZ). If the swirl number, defined as the ratio of angular momentum to axial momentum, is large enough, breakdown of the vortex occurs and a reversed flow is formed in the center. Besides the IRZ, an outer recirculation zone (ORZ) is also formed due to the sudden expansion and the presence of the combustor walls. These recirculation zones help to anchor the flame. However coupling between the wake flow dynamics and system acoustics can result in combustion instabilities [45]. These flow features are shown visually in Figure 5-30 along with the outer and inner shear layers (OSL

& ISL).

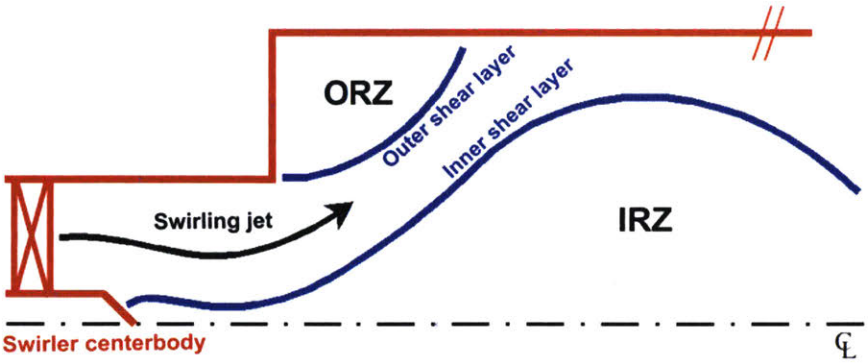

Figure 5-30: Main flow features of the swirling flow studied in this work. IRZ: Inner Recirculation Zone, ORZ: Outer Recirculation Zone (adapted from [17]).

In Chapter 1, we summarized the studies on methane oxy-combustion CFD simulations. We found a clear need for CFD simulations of methane oxy-combustion flames in practical gas turbine combustors. Experiments in the swirl combustor for a methane-oxy mixture at equivalence ratio of 0.65 generated results which included mean flame images and flow field data from Particle Image Velocimetry (PIV) measurements. These are described in greater detail in Section 2.1.2. Figure 5-31 shows images generated from the aforementioned experiments and temperature contours resulting from LES in the swirl combustor using the two reduced chemical mechanisms described in the previous section. These images show the macro-scale flame locations in each of the three cases. As a reminder, the mechanism by Andersen grossly underpredicted extinction strain rates whereas the Frassoldati mechanism had very good agreement at this equivalence ratio of 0.65. These extinction strain rate trends are also reflected in the marco-scale flame observations. LES results using the Frassoldati mechanism are able to correctly predict the same flame shape as in experiments; flame stabilizing in both the outer and inner shear layers (commonly referred to as flame IV [3]). On the other hand, simulations using the Andersen mechanism were only able to predict a flame III configuration (flame stabilizing in the inner shear layer only). A plausible explanation is the very low extinction strain rates predicted by the mechanism at these conditions are unable to overcome the high strain rates present in

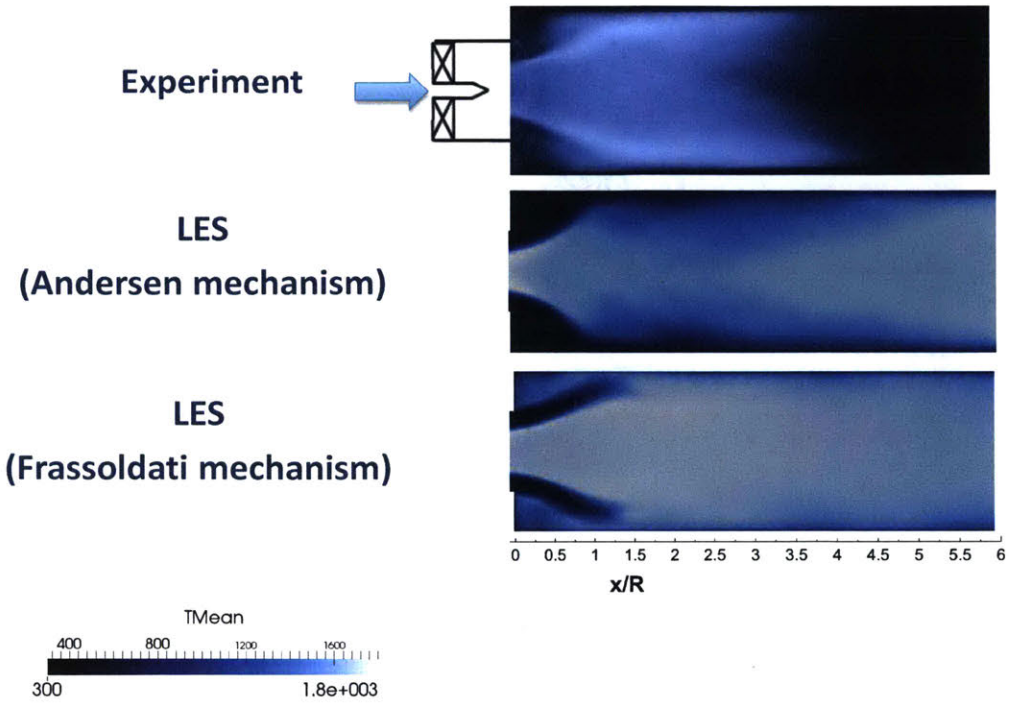

Figure 5-31: Mean flame structures of methane-oxy flames at ϕ=0.65 from experiments and LES using the two chemical mechanisms.

the outer shear layer and recirculation zone [16]. In fact the laminar burning velocity input to the combustion model was artificially increased by almost double to see if a change occurs but the flame macrostructure remained the same; providing further evidence that the extinction strain rate is the more important parameter. From these results alone we can already see that the Frassoldati mechanism will perform better than the Andersen mechanism since it predicts the correct flame shape, hence it is also expected to match better with experiments when we look at the flow fields next.

Figure 5-32 shows the time-averaged flow fields for the oxy-flames in the three cases. Experimental data is obtained from PIV measurements on the swirl combustor as described in Section 2.1.2. The velocity vectors are shown along with their color bars to depict the direction and magnitude of the flow. The zero-velocity contour is also added to show the location and structure of the recirculation zones. The mean flow fields from the two mechanisms in LES are significantly different as evident. The flow field generated by the Andersen mechanism closely resembles that seen in flame

III configurations in the swirl combustor [4]. The IRZ extends upstream towards the swirler and is also long and wide while the axial velocity magnitude in the jet is weaker than in the experiment. On the other hand, the flow field generated by the Frassoldati mechanism closely matches with that of the experiment. Since it has a flame IV configuration (outer + inner shear layer stabilized flame), the IRZ is shorter and narrower and this flame is more compact. But the IRZ length is slightly longer than in the experiment. There is also a reduction in the spreading angle of the jet but an increase in it's thickness and magnitude compared to that by the Andersen mechanism.

Next, we compare the mean axial velocity profiles produced by these two mechanisms with the data from experiments at several axial locations (Figure 5-33). The profile comparisons for the swirl combustor are normalized by the radius of the outlet tube (R = 38 mm) spatially, and velocities are normalized by the bulk inlet velocity of 5.4 m/s which corresponds to a Reynold's number of 20,000. Figure 5-33 also shows a contrast in the results between the two mechanisms compared to the experiment. Since an incorrect IRZ is predicted by the Andersen mechanism (one which extends upstream), negative velocities are observed at the upstream axial locations whereas experiments show positive values. Comparing results between experiments and LES using the Frassoldati mechanism show fairly good agreement especially in predicting the correct velocity magnitude in the annular jet. Additional flow profile comparisons and quantities are presented below for further validation of the Frassoldati mechanism in LES of methane oxy-combustion. The Andersen mechanism fails to reproduce the correct spreading angle of the jet and also fails to predict the correct velocity magnitudes and directions along the centerline.

Another important comparison is how well CO is predicted by the two mechanisms and how it is influenced by wall heat transfer. As was described in Section 2.2.1, convection heat transfer is included at the wall in the simulations. Figure 5-34 presents the CO mass fraction profiles predicted by the Frassoldati and Andersen mechanisms at different axial locations within the flow. The flame macrostructures predicted by the two mechanisms are different and the CO distributions are also very different.

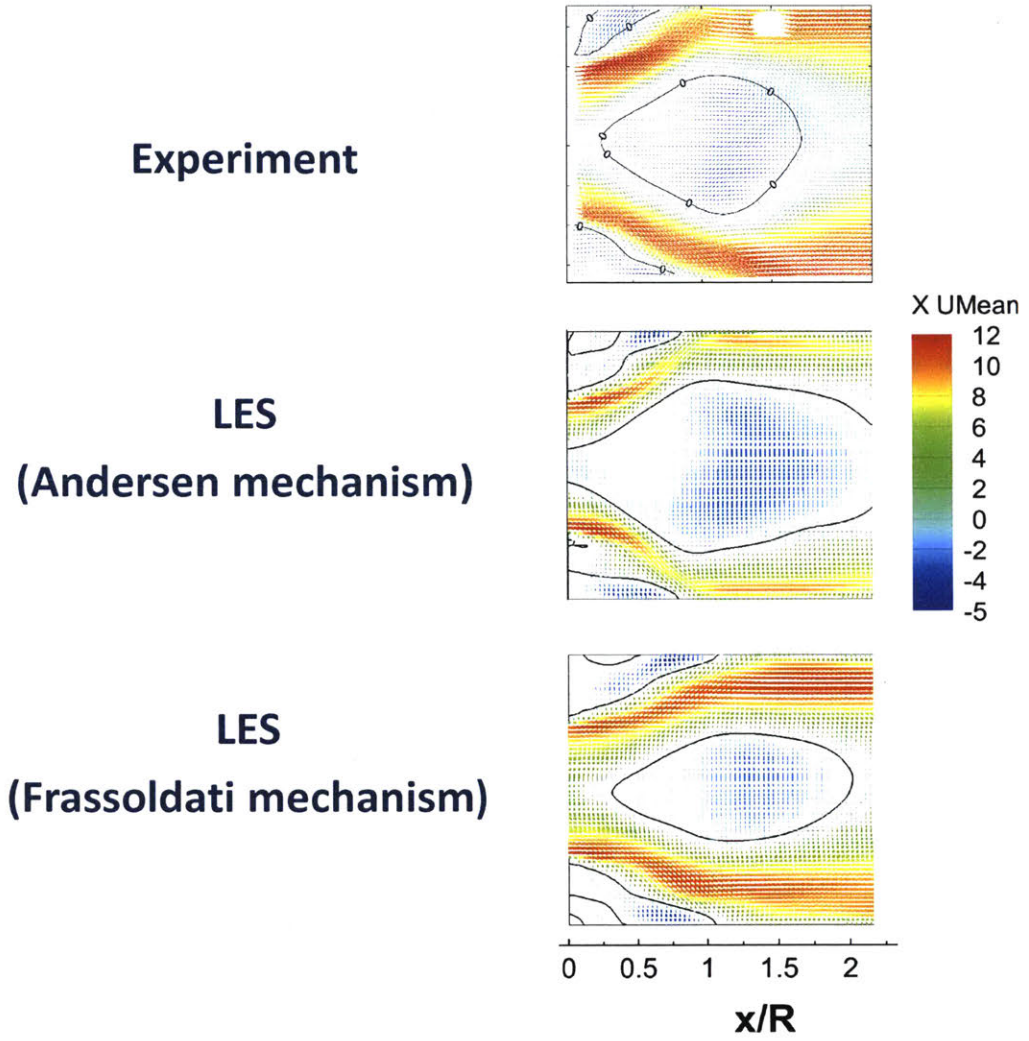

Figure 5-32: Mean flow fields of methane-oxy flames at ϕ=0.65 from experiments and LES using the two chemical mechanisms. The solid black line represents the zero-velocity contour to show the recirculation zones.

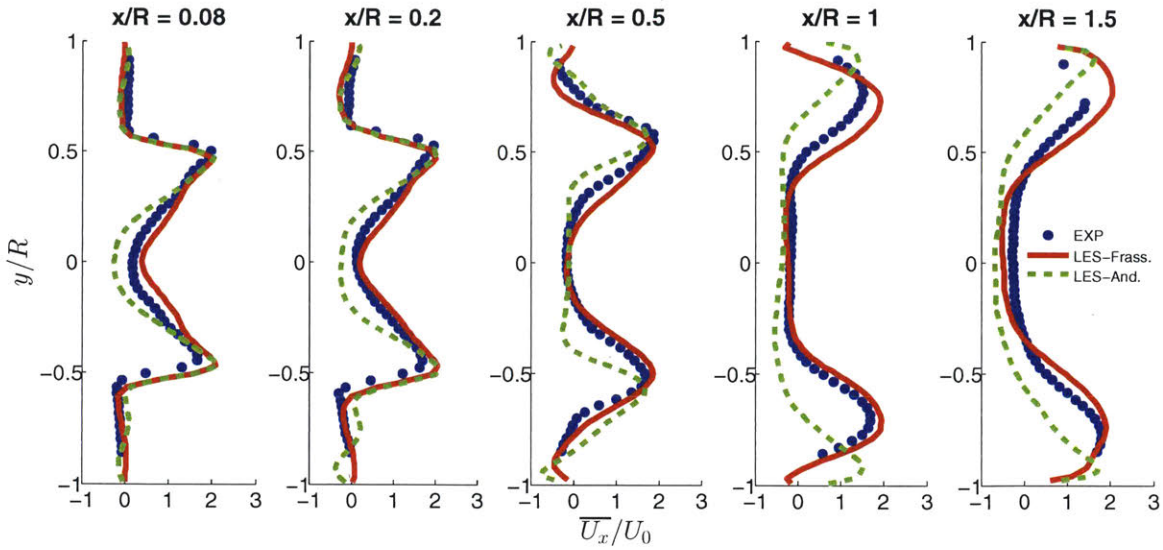

Figure 5-33: Normalized mean axial velocity profiles using the Frassoldati and Andersen mechanisms at several axial (x/R) locations in the swirl combustor for the methane-oxy mixture at ϕ=0.65.

The peaks in the CO fractions indicate the location of the flame front. The flame length using the Andersen mechanism is much longer and only stabilized along the inner shear layer. This explains why CO fractions are high further downstream using this mechanism whereas the CO fractions by the Frassoldati mechanism are lower.

The wall heat transfer also plays a role in determining the flame stabilizations. In Figure 5-36, we plot the gas temperature distribution along the wall of the combustor and in Figure 5-35 we plot the temperature profiles at different axial locations predicted by the different mechanisms. There is a clear difference between the two results. The temperatures predicted by the Andersen mechanism are much lower than the Frassoldati mechanism near the walls because of the flame's proximity to the wall. The extinction strain rates of the Andersen flame are very low and so a flame is not able to survive in the outer recirculation zone region. This will also cause the flame to propagate near the wall and the gas temperature to be lower in that outer zone near the walls. This role of heat transfer and strain effects between different flame macrostructures will be investigated and analyzed in greater detail in Section 6.3. The Frassoldati mechanism predicts a flame stabilized in the outer shear

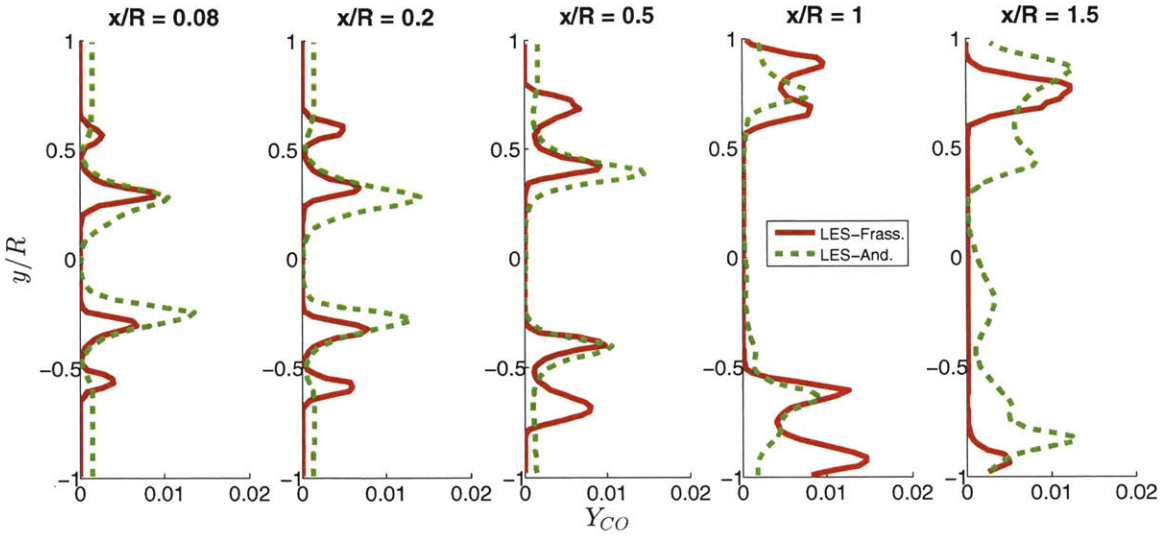

Figure 5-34: CO mass fraction profiles using the Frassoldati and Andersen mechanisms at several axial (x/R) locations in the swirl combustor for the methane-oxy mixture at ϕ=0.65.

layer and so temperature is higher in the ORZ and the flame is shorter and does not propagate near the walls. We also notice that the temperature predicted near the center of the combustor is almost the same between the two oxy mechanisms since wall heat transfer has a negligible effect on that region.

This analysis once again shows that for a different combustor geometry, fuel and oxidizer, the chemical mechanism which correctly predicts extinction strain rates will not only predict the correct flame macrostructure, but also the correct velocities and flow field. *Thus it is very important that a chemical mechanism is able to correctly predict extinction strain rates if it is to be used in CFD simulations.*

5.5 RZ Scaling

We observed in Figure 5-25 that the recirculation zone length varies as you vary the equivalence ratio and hence extinction strain rate. Since we have also shown that the extinction strain rate of the chemical mechanism is an important parameter to predict correctly, can K_{ext} also be used as a surrogate to scale these lengths? This question was answered previously by Michaels et al. [6] but for laminar flows in a bluff body

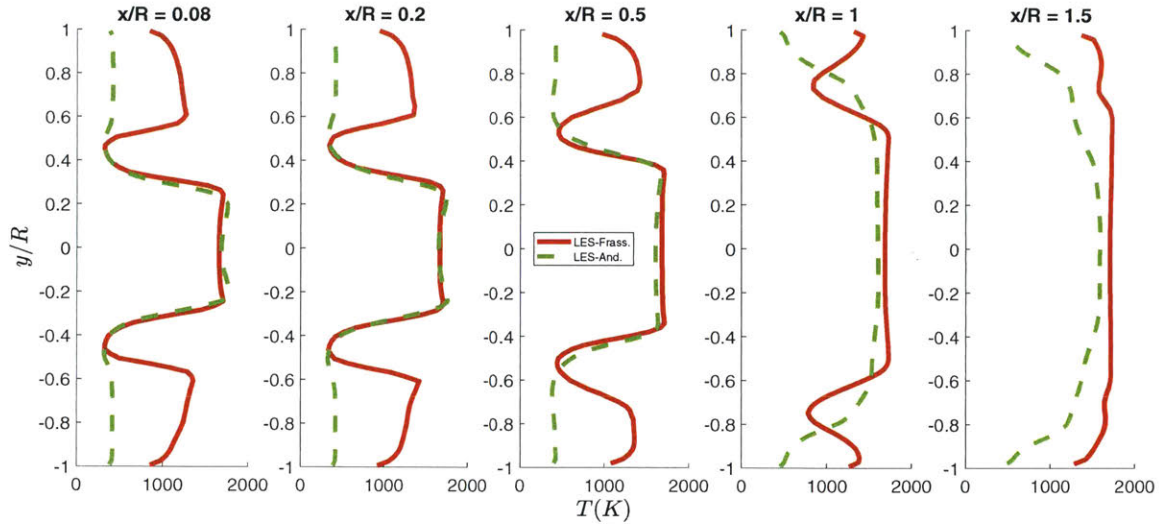

Figure 5-35: Mean temperature profiles using the Frassoldati and Andersen mechanisms at several axial (x/R) locations in the swirl combustor for the methane-oxy mixture at ϕ=0.65.

stabilized flame. The novelty in the present work is extending and validating this hypothesis for more realistic cases in complex geometries and turbulent flows which has not been conducted before in the literature.

In order to try and scale recirculation zone lengths in the swirl combustor, we first need to identify which recirculation zone should be the focus. Figure 5-41 depicts how these recirculation zones in the swirl combustor change with varying $CH_4/O_2/CO_2$ equivalence ratios and flame shapes. As evident from the figure, only the IRZ appears to have a noticeable change in length as you increase mixture equivalence ratio. Therefore we will focus on examining this length and its relation to extinction strain rates in the forthcoming analyses. It can also be seen from this figure that the flame shape evolves, as equivalence ratio increases, from a flame III (ISL stabilized flame) to flame IV configuration (OSL stabilized flame). The flame becomes more compact which in turn reduces the size of the IRZ. Similar experimental observations were made for methane-air mixtures in the swirl combustor [4].

A comprehensive simulation study is done in the swirl combustor for these methane-oxy mixtures for a range of inlet temperatures, equivalence ratios and Reynold's numbers as was shown in Table 5.1. The goal is to calculate IRZ lengths at all of

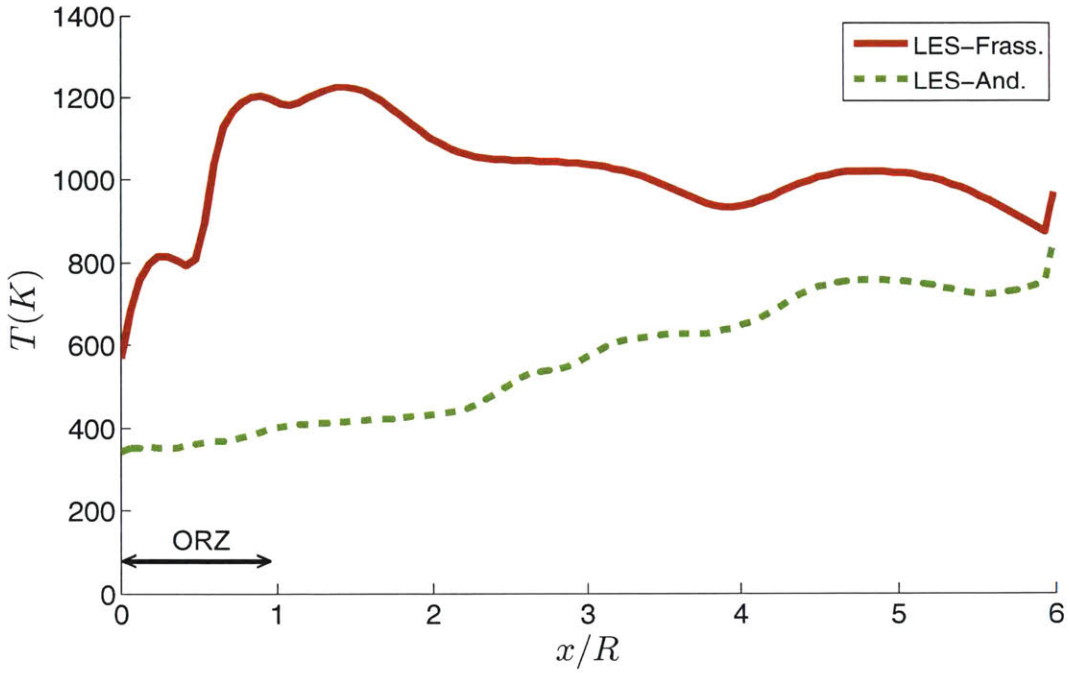

Figure 5-36: Mean temperature distribution of the gases near the wall using the Frassoldati and Andersen mechanisms in the swirl combustor for the methane-oxy mixture at ϕ=0.65.

these different conditions and correlate the results with the inlet reactant mixture's extinction strain rate at those conditions. The simulations are performed using the Frassoldati mechanism which was validated in the previous section. The results from these extensive simulations are shown in Figure 5-42. The different colors correspond to different inlet temperatures while the flame shape is also indicated. For each simulation, there are also error bars associated with the variance in the IRZ length data. Since these simulations are turbulent and performed in a complex geometry, the IRZ length fluctuates quite significantly especially at the higher equivalence ratios as seen in the figure. The mean IRZ length reaches a steady state value after a certain point and this value is plotted along with the maximum and minimum lengths during this fixed period of time. The data appears to linearly scale fairly well (R^2=62%) when plotted using the flow time scale (U_{in}/L_{RZ}) versus the extinction strain rate at all of the different inlet conditions.

In order to asses the reliability of this scaling, we also plot the experimental

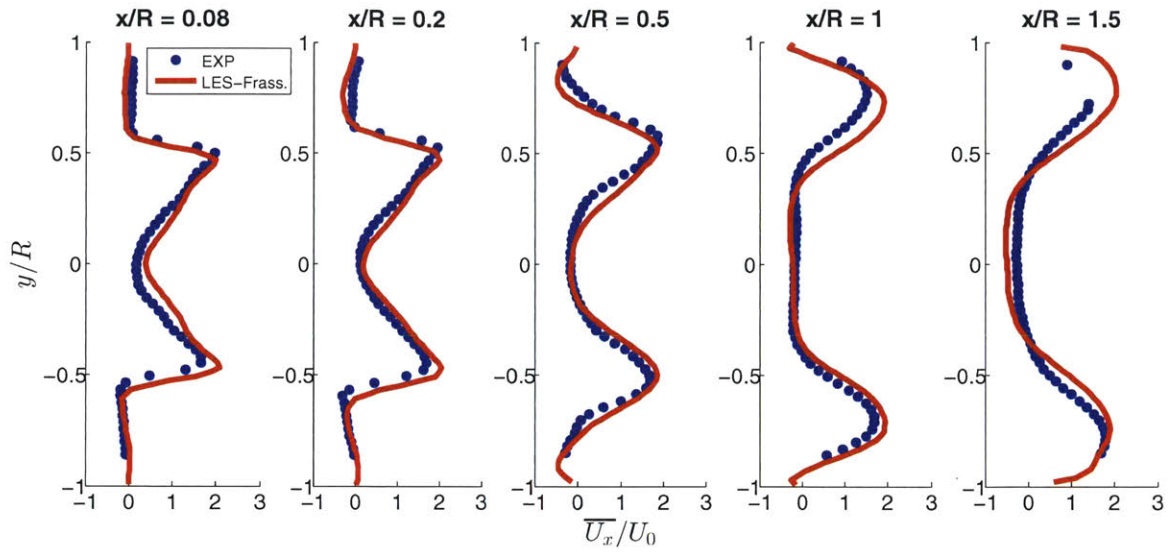

Figure 5-37: Normalized mean axial velocity profiles using the Frassoldati mechanism at several axial (x/R) locations in the swirl combustor for the methane-oxy mixture at ϕ=0.65.

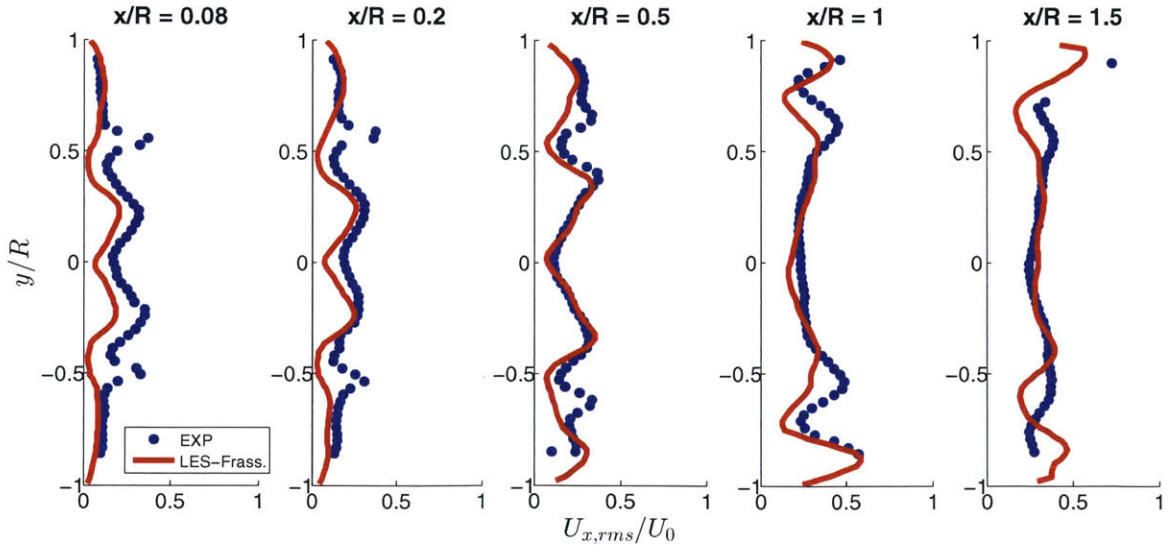

Figure 5-38: Normalized rms transverse velocity profiles using the Frassoldati mechanism at several axial (x/R) locations in the swirl combustor for the methane-oxy mixture at ϕ=0.65.

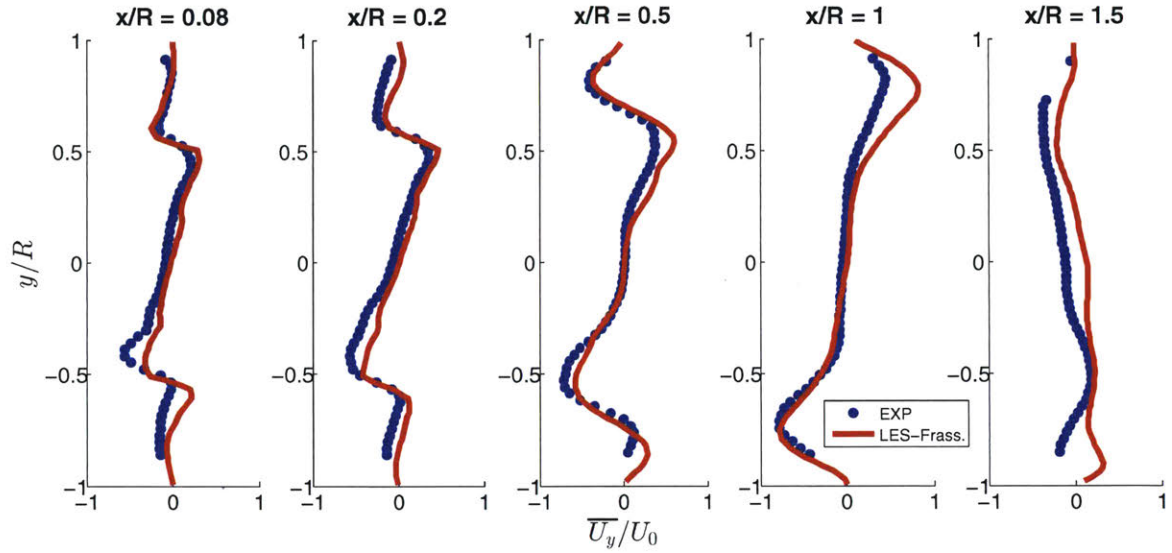

Figure 5-39: Normalized mean transverse velocity profiles using the Frassoldati mechanism at several axial (x/R) locations in the swirl combustor for the methane-oxy mixture at ϕ=0.65.

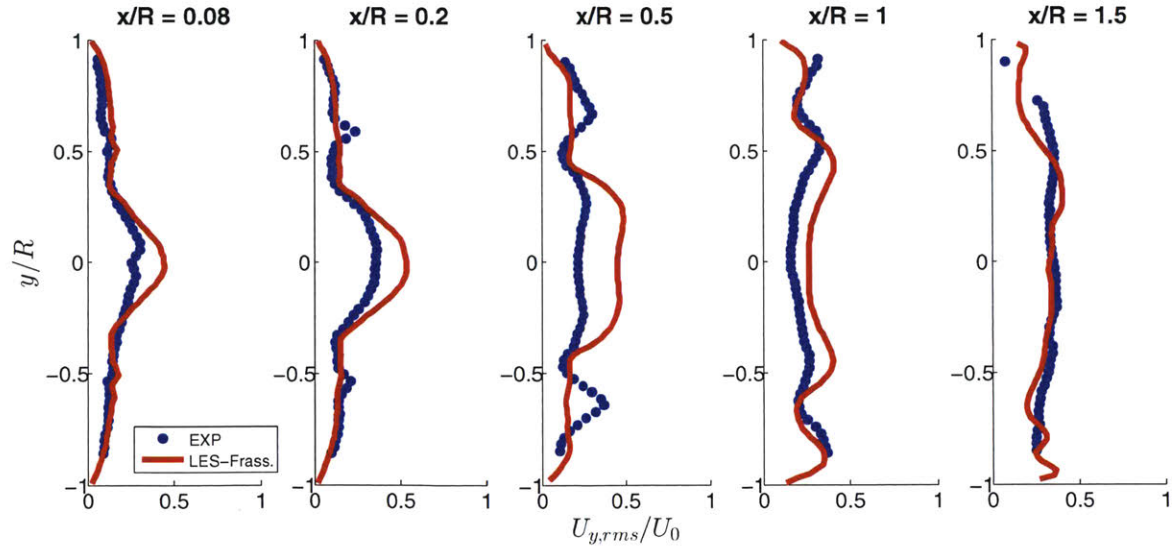

Figure 5-40: Normalized rms transverse velocity profiles using the Frassoldati mechanism at several axial (x/R) locations in the swirl combustor for the methane-oxy mixture at ϕ=0.65.

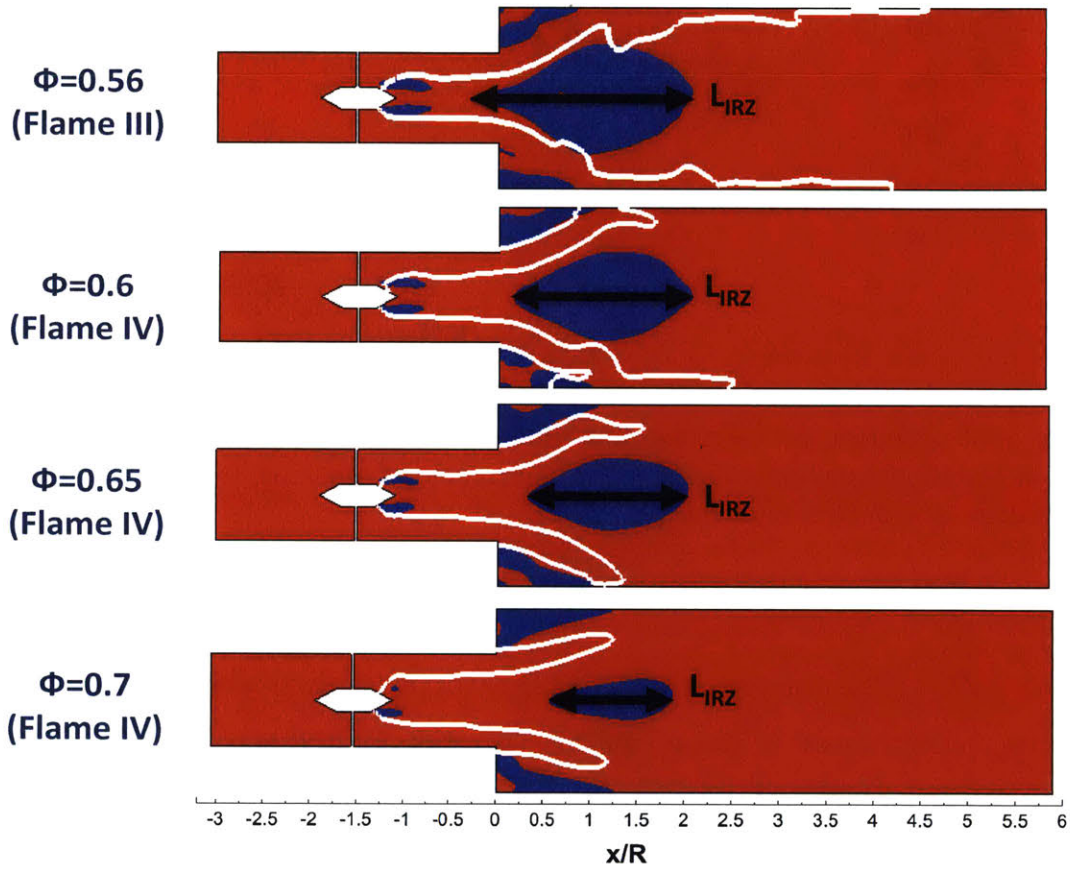

Figure 5-41: Mean axial velocity contours showing positive (red) and negative velocities (blue) in order to visualize recirculation zones for various methane-oxy mixture equivalence ratios using the Frassoldati mechanism. The instantaneous progress variable contour (c=0.8) is also plotted (white line) as a way to locate the flame front.

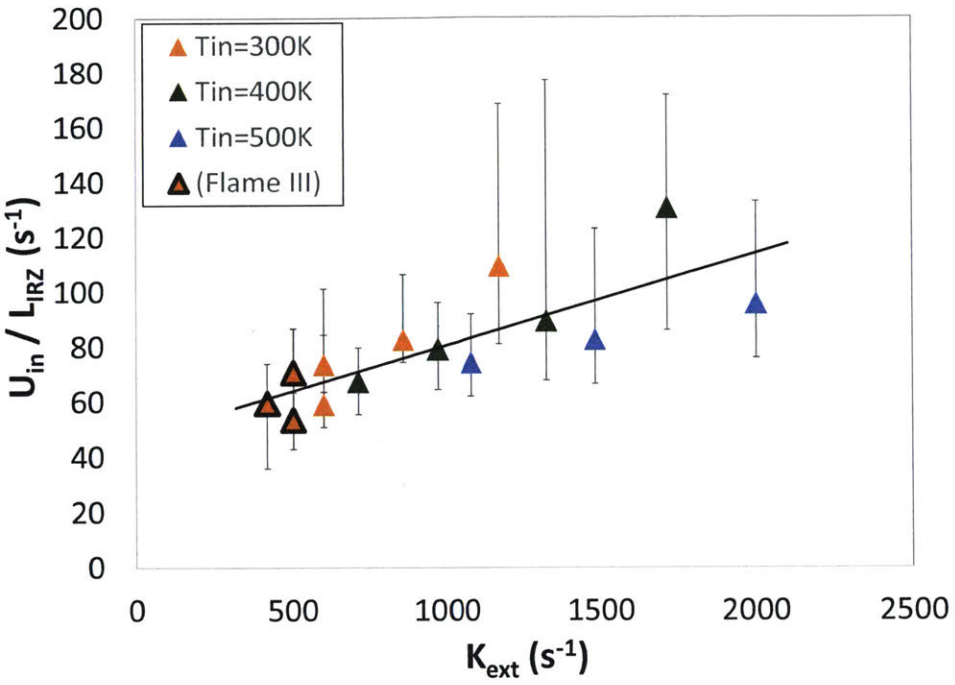

Figure 5-42: Relation between the flow time scale, U_{in}/L_{RZ}, and chemical time scale, K_{ext}, in the swirl combustor for LES of methane-oxy mixtures using the Frassoldati mechanism at different inlet temperatures.

data from the backward-facing step combustor for the different propane-air mixtures (Figure 5-43). The comprehensive UCSD mechanism [131] was used to calculate extinction strain rates at those equivalence ratios for the experimental step data (red) in the figure. The LES swirl methane-oxy data from Figure 5-42 is also plotted in Figure 5-43 for comparison (blue).

Interestingly enough the plot shows that, as we hypothesized, turbulent flame stabilization also appears to be mainly correlated with the extinction strain rate. Therefore regardless of the fuel or oxidizer type, Reynold's number, inlet temperature, or combustor geometry, this scaling still holds and a flow time scale represented by a recirculation zone length correlates well with a chemical time scale associated with extinction strain rate. The ratio of these time scales (i.e. gradient of the lines) is the Karlovitz number and the value is very similar for both curves. It should also be noted that the Karlovitz number for DNS of the laminar 2D bluff body stabilized flame (see Figure 5-2) is also close to that of the turbulent flames (0.048 vs 0.039

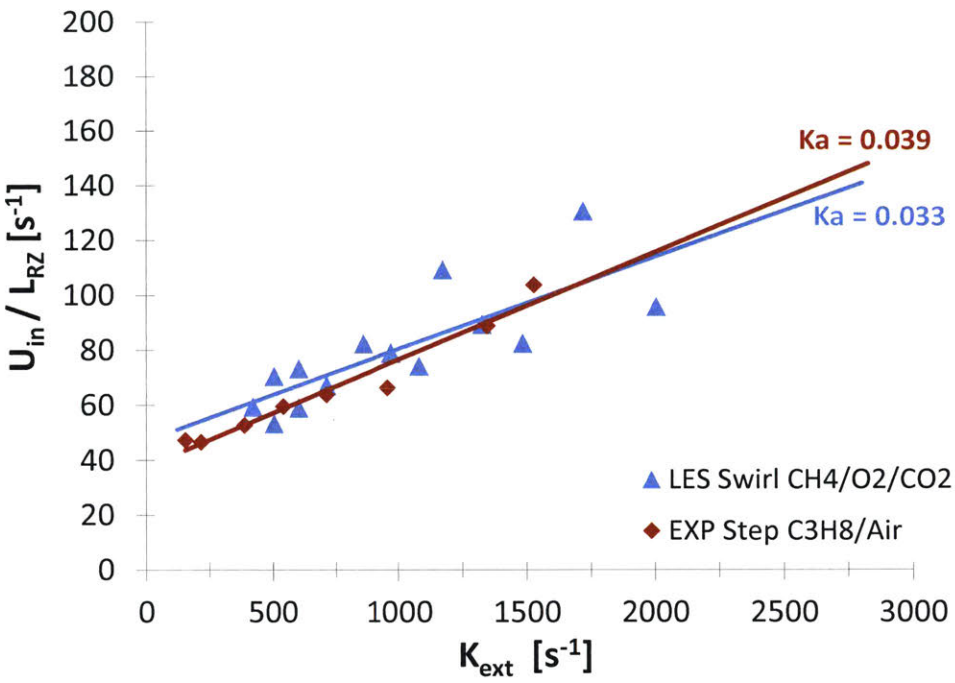

Figure 5-43: Relation between the flow time scale, U_{in}/L_{RZ}, and chemical time scale, K_{ext}, in the backward facing step combustor for propane-air experiments (red) and in the swirl combustor for methane-oxy LES using the Frassoldati mechanism (blue).

& 0.033). This could be a very powerful tool because these scaling curves can allow for the accurate prediction of recirculation zone lengths at a certain K_{ext}, therefore aiding in the design of combustor lengths based on their operating conditions.

5.6 Conclusions

In this chapter, propane-air mixtures were simulated in bluff-body and backward-facing step combustors, and then methane-oxy mixtures were simulated in a swirl combustor. The main goal was to investigate the attributes of a chemical mechanism which are important for predicting important flow features such as recirculation zones in simple and complex geometries.

For the propane-air cases, we used a 2-step mechanism which had reasonable extinction strain rate agreement with experimental values. We also modified that reduced mechanism to form a new mechanism which intentionally had far worse

agreement and over-predicted extinction strain rates. We found that simulations in these two geometries using the modified mechanism under-predicted recirculation zone lengths compared to results using the original mechanism.

In the swirl combustor, oxy-combustion simulations using the Frassoldati mechanism, which had very good extinction strain rate values, were able to predict the correct flame macrostructure and flow profiles compared to the Andersen mechanism which had much worse extinction strain rate prediction. The response to strain of the flames with the inaccurate mechanisms are unrealistic and so this negatively impacts the accuracy of the predicted flow structures.

Recirculation zone lengths in the backward-facing step and swirl combustors linearly scaled well with extinction strain rate. This scaling held regardless of fuel or oxidizer type, Reynold's number, inlet temperature, or combustor geometry. These scaling curves can also allow for accurate prediction of recirculation zone lengths for a certain inlet mixture extinction strain rate, and therefore this tool can help in designing premixed combustors. We conclude that it is very important that a chemical mechanism is able to correctly predict extinction strain rates if it is to be used in CFD simulations.

Chapter 6

Flame Macrostructure Transitions in LES; Mechanism and Modeling

6.1 Introduction

In this chapter, we bring together a lot of the knowledge gained from the previous chapters and results to help answer outstanding questions mainly related to the important flame macrostructure transition in the swirl combustor: Flame III to Flame IV. In Chapter 3, we discussed the importance of these flame macrostructures and how they relate to the stability of the oxy-combustor. We were able to successfully model and scale the behavior of these 3D turbulent oxy-flames using simple 1D laminar flame calculations of extinction strain rates.

In Chapter 5, LES models were validated for oxy-combustion flames in the swirl combustor. Important flow structures such as recirculation zones were found to also scale with extinction strain rates for both flame macrostructures. Similar to experimental observations, the simulations also predicted a decrease in the size of the inner recirculation zone as the flame shape evolved from an inner shear layer stabilized flame (Flame III) to an inner + outer shear layer stabilized flame (Flame IV).

Investigations by other researchers have also identified these different flame macrostructures at different equivalence ratios for methane-air mixtures in swirling flows [138, 139, 140]. They also use LES to show how the flow topology changes for the different

flame shapes. However, the current gap in the literature is the explanation for why exactly recirculation zones change sizes and structures at different flame macrostructures. Additionally, many LES studies fail to correctly capture this ORZ flame transition mechanism due to the difficulty in modeling this unsteady phenomenon with heat loss, strain, and chemical kinetics effects all present in that region.

Experiments by Taamallah et al. [4] for methane-air mixtures, in the same swirl combustor studied in this thesis, captured the ignition of the ORZ recirculating reactants using a dual camera chemiluminescence imaging setup. Figure 6-1 shows consecutive binarized images from this setup showing how the ORZ flame is established. Initially, a flame front extends out from the ISL flame then a flame kernel detaches from that flame and moves into the ORZ. It propagates and ignites the recirculating reactants only if it can overcome the strain it is subjected to. Due to the rotation of the flow in the ORZ, the flame kernel then travels behind the flame out of the field of view and appears on the other side before igniting that whole region of unburnt reactants. The three dimensional and complex nature of this ORZ flame origin was also seen visually during the experiments performed for the results in Chapter 3.

As was shown in the previous chapter, the flame significantly impacts the flow field in the swirl combustor especially with respect to recirculation zone sizes. Michaels et al. [6] observed similar flame-flow interactions in DNS of methane-air-hydrogen mixtures in a bluff body stabilized premixed flame. Figure 6-2 shows normalized vorticity maps along with the flame heat release zone and the stagnation streamline in these simulations. An obvious but important outcome from these images is how the vorticity decays faster as the flame moves closer to the shear layer. The recirculation zone also shrinks for the higher heat release mixtures as was shown earlier in Figure 1-6, similar to the results of the simulations in the previous chapter.

In this chapter, we use LES to model the Flame III to Flame IV transition in the swirl combustor for the $CH_4/O_2/CO_2$ mixtures. Specifically we aim to answer the following questions:

1. Do we observe the correct flame macrostructure transition mechanism as in

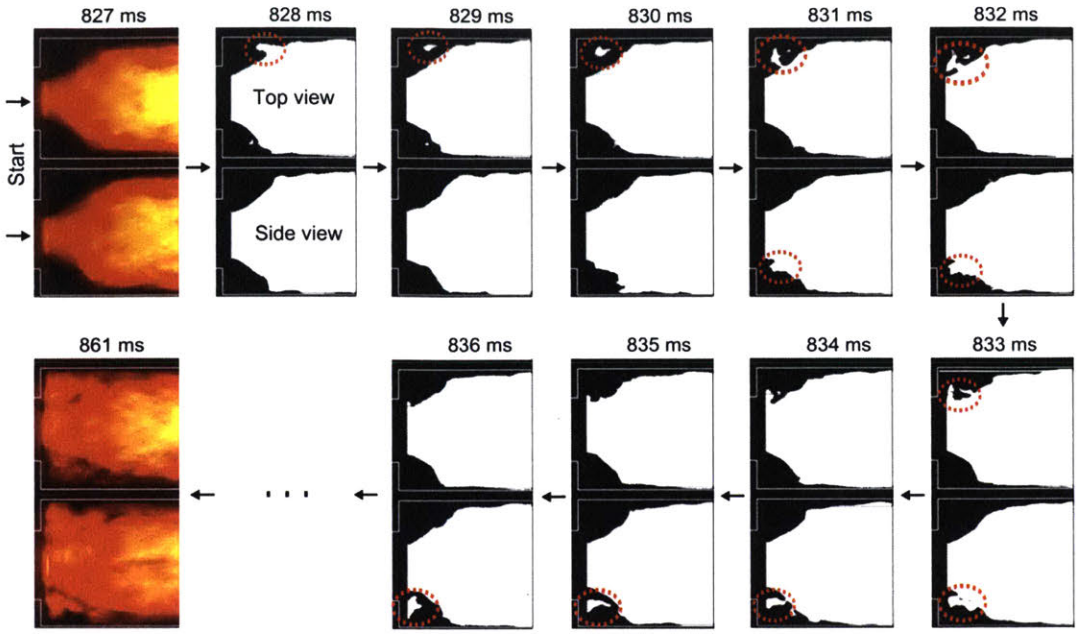

Figure 6-1: Consecutive binarized chemiluminescence images showing the ignition of the ORZ recirculating reactants (CH_4/Air at ϕ=0.62). Adapted from Ref. [4].

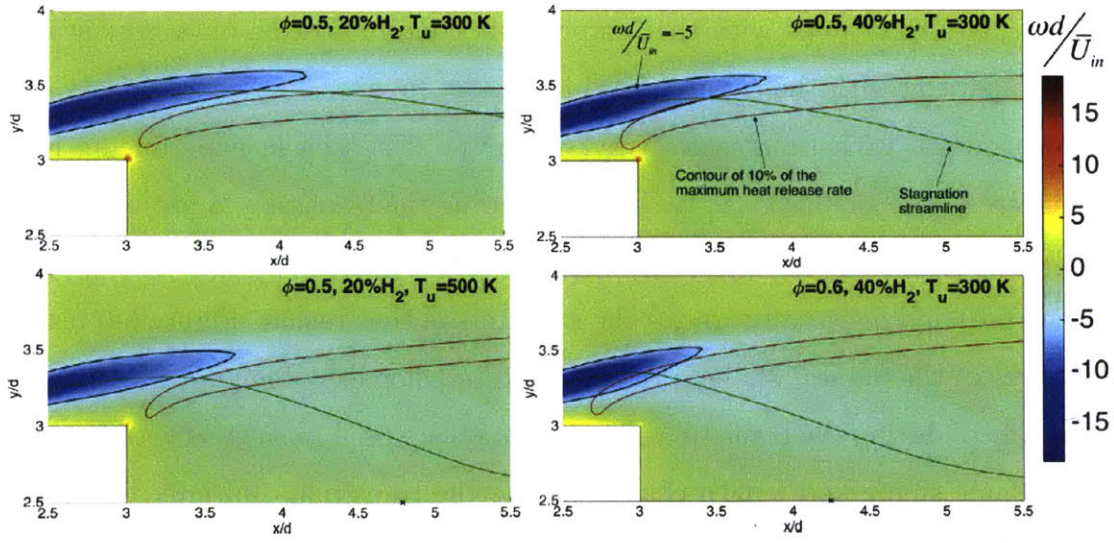

Figure 6-2: Normalized vorticity maps of different reactant mixture compositions (CH_4/Air), with lines marking the iso-surface of $\omega d/U_{in} = -5$, the flame heat release zone (contour of 10% of the maximum heat release) and the stagnation stream line. These results are from DNS in a bluff body combustor. Adapted from Ref. [6].

experiments?

2. Why do laminar flame calculations appear to capture the behavior of these turbulent flame macrostructures?

3. How do the flame-flow interactions compare for the two flame macrostructures?

6.2 Flame III to IV Stabilization Mechanism

The Flame III to Flame IV transition is simulated in the swirl combustor geometry (see Figure 5-5) using LES that was validated in the previous chapter with the Frassoldati [14] chemical mechanism. Beginning with the $CH_4/O_2/CO_2$ mixture at an equivalence ratio of 0.58, where the flame is stabilized only along the inner shear layer (Flame III), the reactants' equivalence ratio is slowly raised until a flame stabilizes along the outer shear layer as well (Flame IV). The exact time steps during this transition phenomenon is identified and the images are recorded for comparison with the experimental images in Figure 6-1. Figure 6-3 presents these LES images for consecutive time steps with the temperature contour plotted on a gray scale for easier comparison with the experimental images.

A mechanism with time scales very similar to that seen in experiments is also evident here in the simulations. We see that during the transition, a hot flame kernel detaches from the inner shear layer flame, spins in the ORZ to other side (as shown in Figure 6-4) and eventually ignites the reactants in that region. Figure 6-5 presents side images of the flames' 3D heat release contour colored by temperature at various time instances during the transition. These images are used to show how temperature profiles, flame shape and length change during the transition. Initially the flame is long and very wrinkled with temperatures around 1000 K. Then as the equivalence ratio is raised, the temperature increases gradually and the flame begins to shorten. We can also observe how that pocket of hot products enter the ORZ, igniting the whole region as it is spinning in a highly erratic and unsteady process. As the OSL flame is establishing, the flame becomes much more compact and the resulting flame

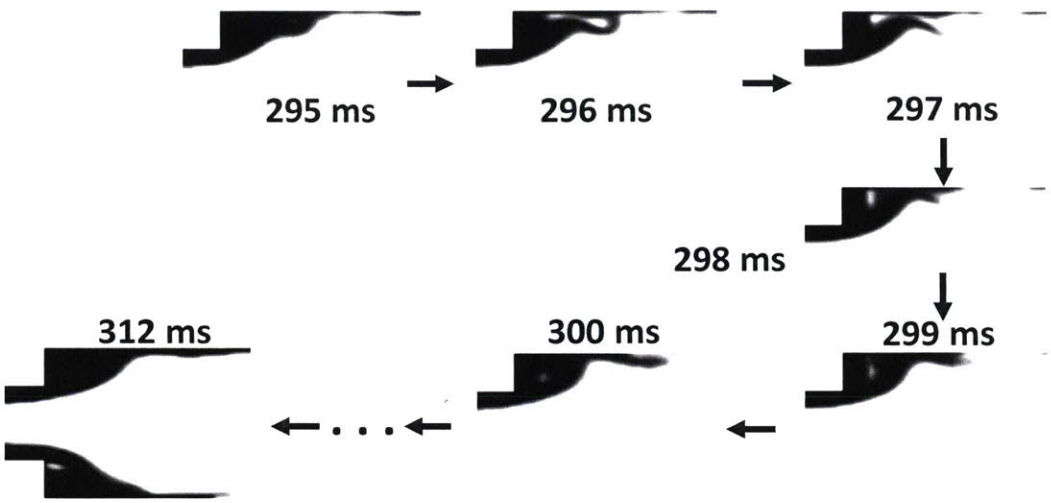

Figure 6-3: Consecutive 2D flame images from LES of the methane-oxy mixture in the swirl combustor during the flame transition. The time instances shown are for a mixture equivalence ratio of 0.625 and T_{ad}=1710 K. The different images represent the temperature contour plotted on a gray scale.

shape (Flame IV) is shown in the last image.

6.3 Flame III vs Flame IV: Flamelet Structures

After establishing the ORZ flame's transition mechanism, in the subsequent sections, we mainly focus on comparing these two important flame macrostructures to better understand their different behaviors.

One important benefit from having a reliable LES model for the swirl combustor is its use for understanding and explaining experimental observations. In Chapter 3, it was identified that extinction strain rates calculated using a 1-D laminar flame configuration could be used to scale and model the ORZ flame transition. The hypothesis is that these turbulent flames are impacted by the local strain and their structure should resemble that of strained laminar flames under certain conditions. This might explain why extinction strain rates have been able to model these flames so far, as we have shown in the previous chapters.

The dependence of these macrostructures on strain and heat loss effects was investigated by several researchers [141, 142, 95]. Proch et al. [142] performed large eddy

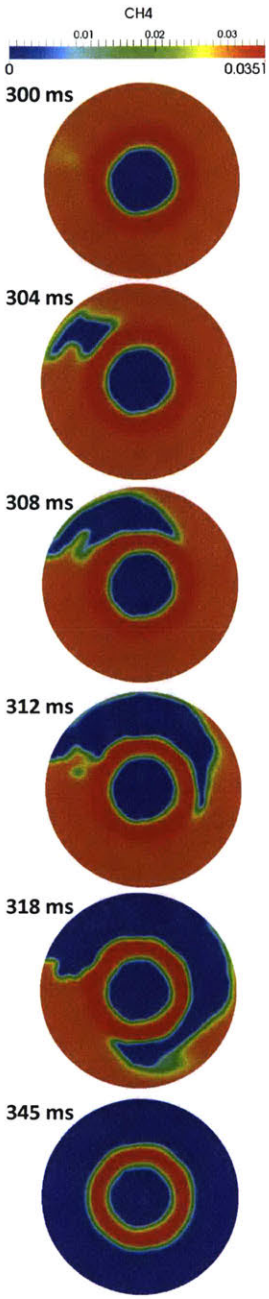

Figure 6-4: 2D flame images from LES of the methane-oxy mixture in the swirl combustor during the flame transition at x/R=0.2. The time instances shown are for a mixture equivalence ratio of 0.625 and T_{ad}=1710 K. The cross-sectional images represent the fuel (CH_4) mass fractions at various points during the transition.

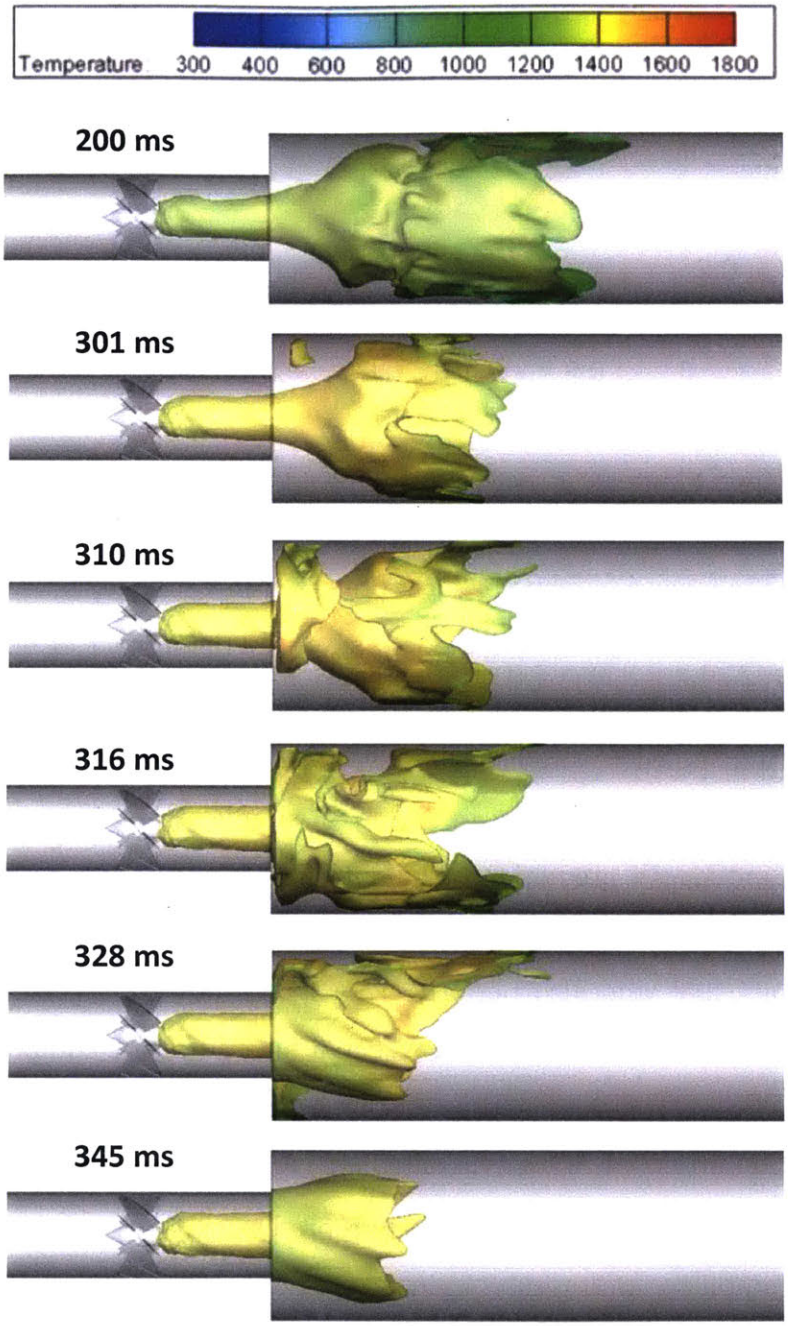

Figure 6-5: 3D flame images from LES of the methane-oxy mixture in the swirl combustor during the flame transition. The time instances shown are for a mixture equivalence ratio of 0.625 and T_{ad}=1710 K. The side images represent the 3D heat release contours colored by temperature at various non-consecutive points during the transition.

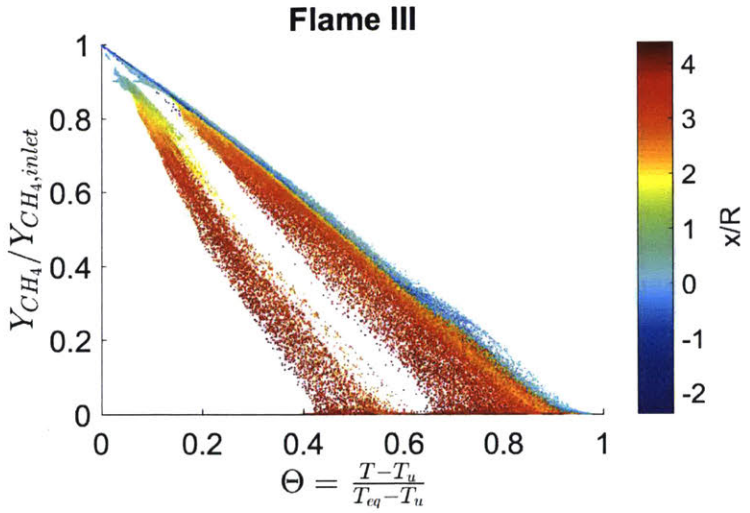

Figure 6-6: Flamelet structure of Flame III (ϕ=0.56) with heat loss.

simulations also in a swirl combustor for a premixed methane-air mixture. They also use the thickened flame combustion model and study the impact of heat loss modeling. Their adiabatic simulations over-predicted the temperature by several hundred degrees kelvin and failed to predict the flow field correctly. However, after including heat loss, it was also necessary to include a simple strain correction method to improve the flame length prediction. The authors reported that the physical mechanism behind this required further investigation. A similar conclusion was reached by Mercier et al. [95] who also performed an LES study on a premixed methane-hydrogen-air mixture in a swirl injector. When a fully adiabatic combustion chamber was assumed, LES always predicted an M flame (flame IV) and did not capture the V to M transition observed in experiments.

All these studies show that inadequately representing the thermal boundary conditions of the combustor wall results in incorrect predictions of the flame macrostructure found in experiments. Our work serves to better understand the roles of strain and heat transfer for methane oxy-combustion mixtures which has not been investigated yet. As we will show in this section, heat loss also significantly impacts the microstructures of flames as well.

It is common to use a phase diagram or scatter plots in which the fuel fraction distribution is the coordinate that compares turbulent LES and laminar flame structures

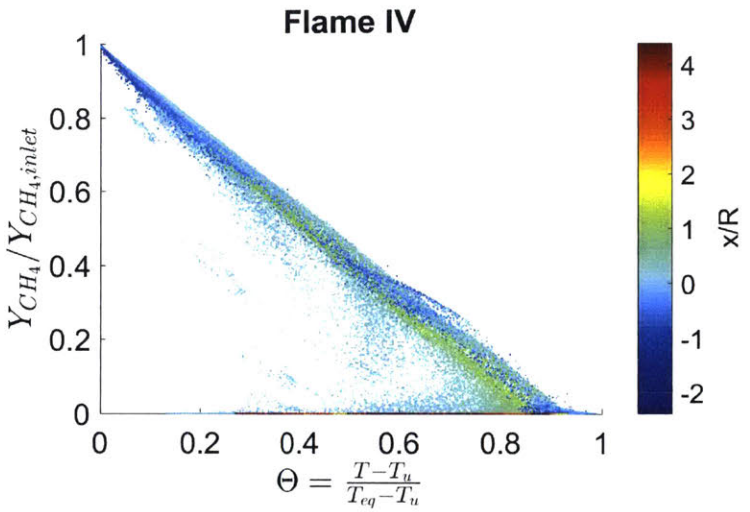

Figure 6-7: Flamelet structure of Flame IV (ϕ=0.7) with heat loss.

[143, 144, 145]. These studies primarily looked at DNS studies of higher hydrocarbon mixtures in simple geometries. In a recent 2015 DNS study on $n-C_7H_{16}/air$ flames, Savard et al. [146] show that even under intense turbulence (Karlovitz numbers > 200), the structure of turbulent flames are similar to those of laminar flamelets. In Figures 6-6 and 6-7 we plot the flamelet structures of Flames III and IV for methane-oxy in the swirl combustor, with the data colored by their axial location. The LES data is constructed by extracting methane mixture fraction and temperatures for all points in the 3D domain at a single instance of time. The x-axis is the normalized temperature, Θ, where T_{eq} is the equilibrium temperature of the two mixtures (1590 K and 1838 K for Flames III and IV respectively) and T_u is the inlet atmospheric temperature of 300 K. The results presented do not depend on the time instant chosen. The fuel mass fraction begins at the reactant composition and temperature, and drops all the way to temperatures close to their equilibrium values. For Flame IV, the majority of the points lie along a curve extending from top left to bottom right. Flame III scatter plot, and its underlying flamelet structure, is more complex. We observe a large cluster of points, located further downstream in the flow, below the flamelet structure observed in Flame IV. The location within the flow of these low temperature data are extracted, and they are all found along the outer walls of the combustor; suggesting that they have a different structure, perhaps determined by

heat loss along the wall.

Next, we plot the flamelet structures of these two cases but with LES simulations assuming adiabatic boundary conditions in Figures 6-8 and 6-9. All the other swirl simulations in this thesis assume heat loss at the wall as was described in section 5.2.3. For reference, results from an unstretched flame and simulations of a strained flame very near extinction, are added. The laminar flame profiles were constructed using the same symmetric opposed reactants configuration in Chemkin described in section 2.2.2 and using the same Frassoldati mechanism [14] as in LES.

We also plot the temperature contours, comparing the two thermal boundary conditions for each flame type in Figures 6-10 to 6-13. Similar to the results by Proch et al. [142], we also notice that the adiabatic simulations predict a much shorter flame for Flame III. We do not see large differences in the flame structures for Flame IV, however, and the flamelet plots reach a similar conclusion as we will show later. The temperatures in the ORZ and along the wall are also higher for the adiabatic cases.

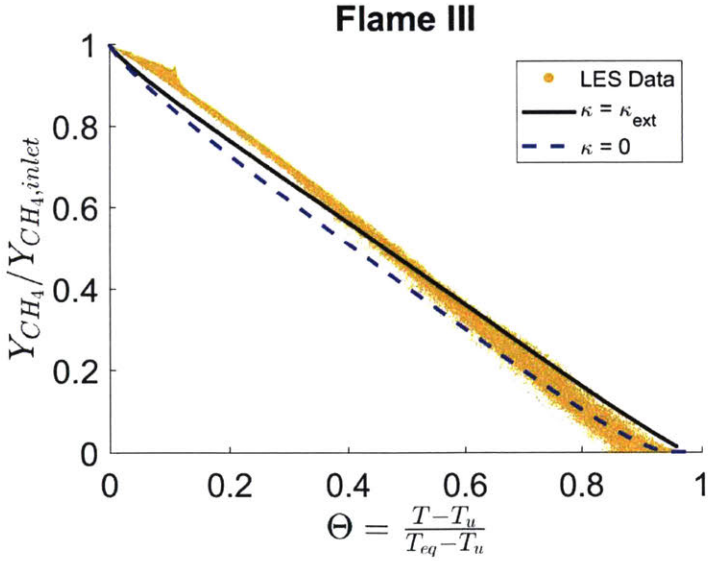

Figure 6-8: Flamelet structure of Flame III (ϕ=0.56) with adiabatic boundary conditions, and symmetric laminar flame profiles.

For Flame III, notice that the flamelet from the LES data agrees well with the laminar flame profiles especially at higher temperatures. Now consider the flamelet in Flame IV (Figure 6-9). In this figure, we also display unstretched flame profiles

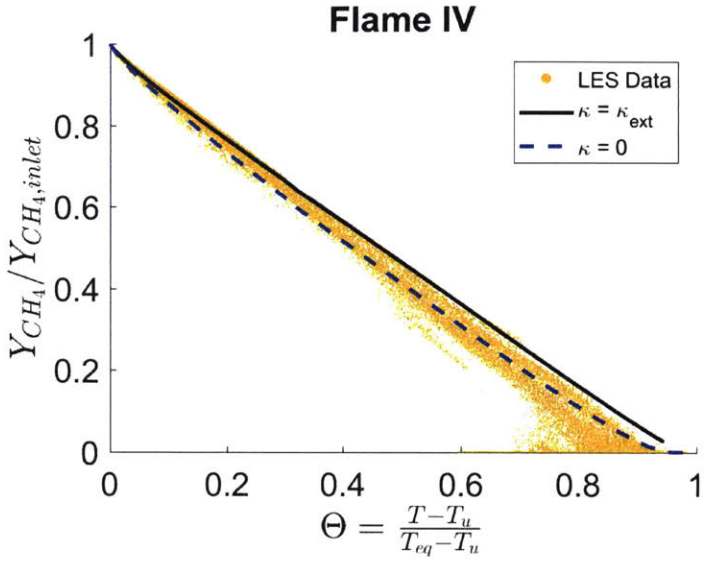

Figure 6-9: Flamelet structure of Flame IV (ϕ=0.7) with adiabatic boundary conditions, and symmetric laminar flame profiles.

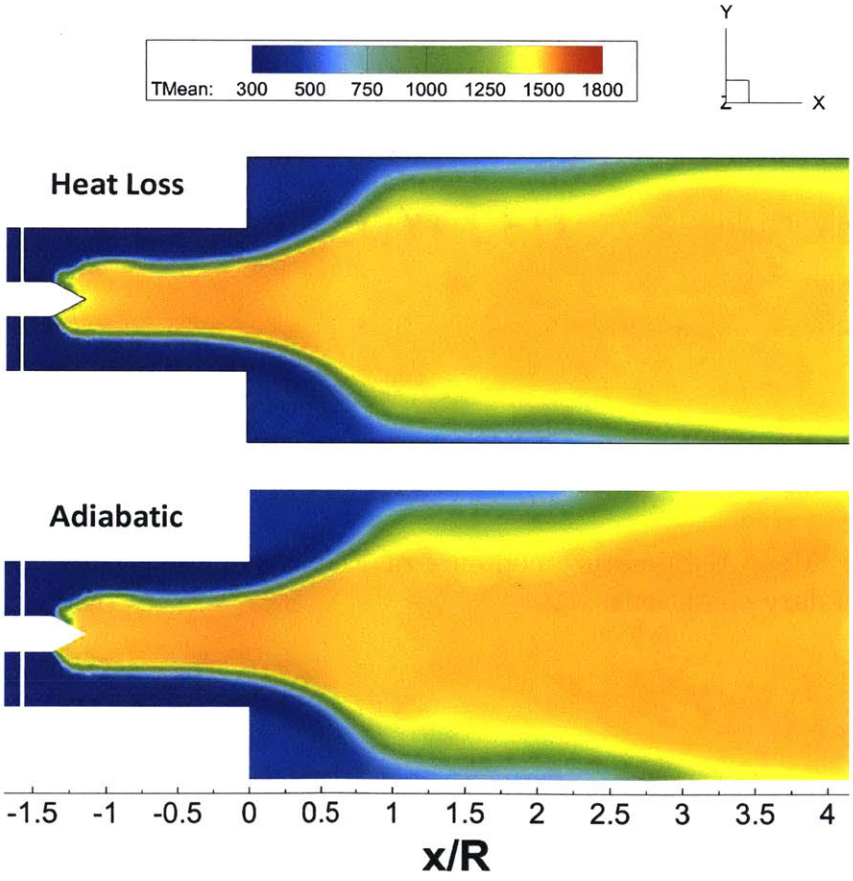

Figure 6-10: Mean temperature contours of Flame III (ϕ=0.56) with two different thermal boundary conditions.

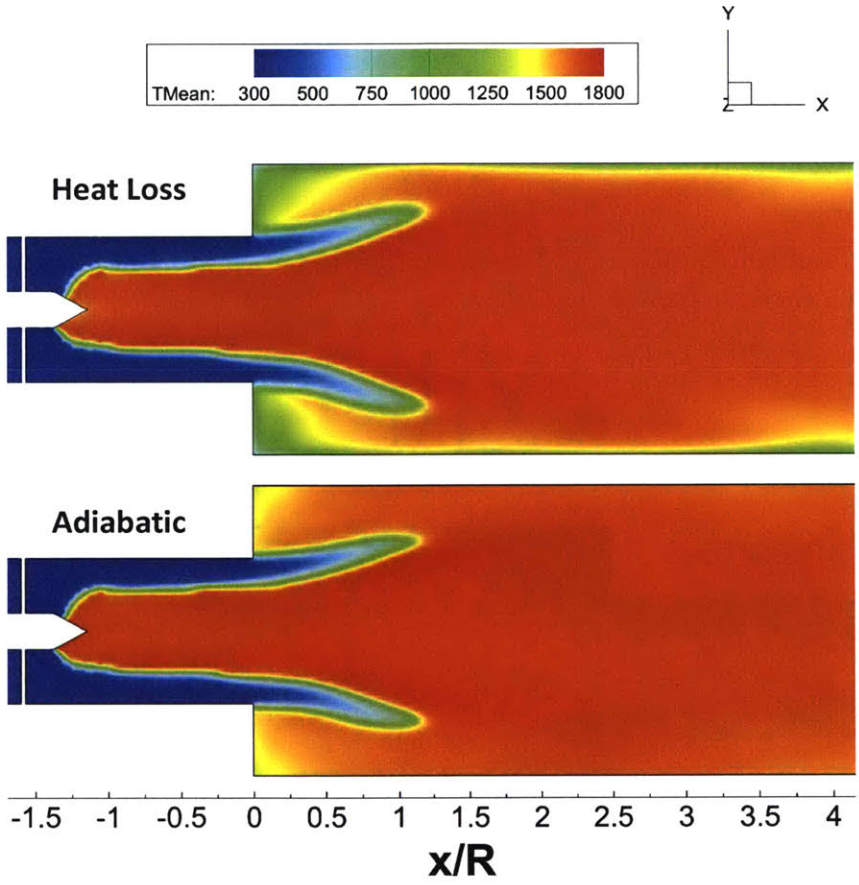

Figure 6-11: Mean temperature contours of Flame IV (ϕ=0.7) with two different thermal boundary conditions.

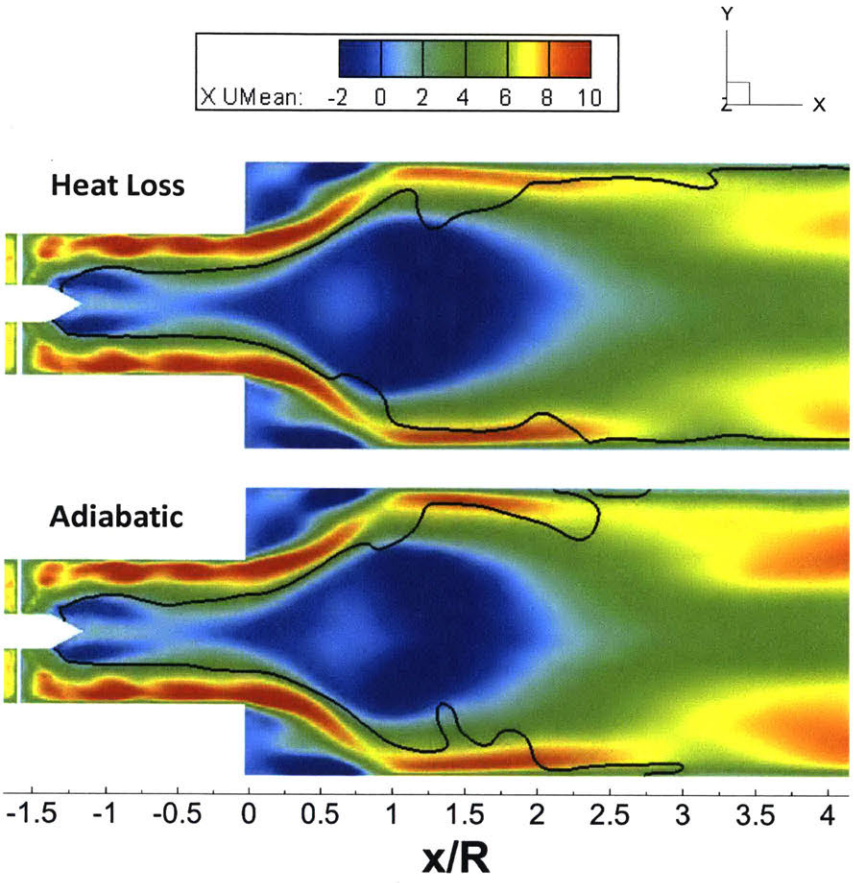

Figure 6-12: The instantaneous progress variable contour (c=0.8) is plotted (black line) as a way to locate the flame front along with the mean axial velocity contours of Flame III (ϕ=0.56) with two different thermal boundary conditions.

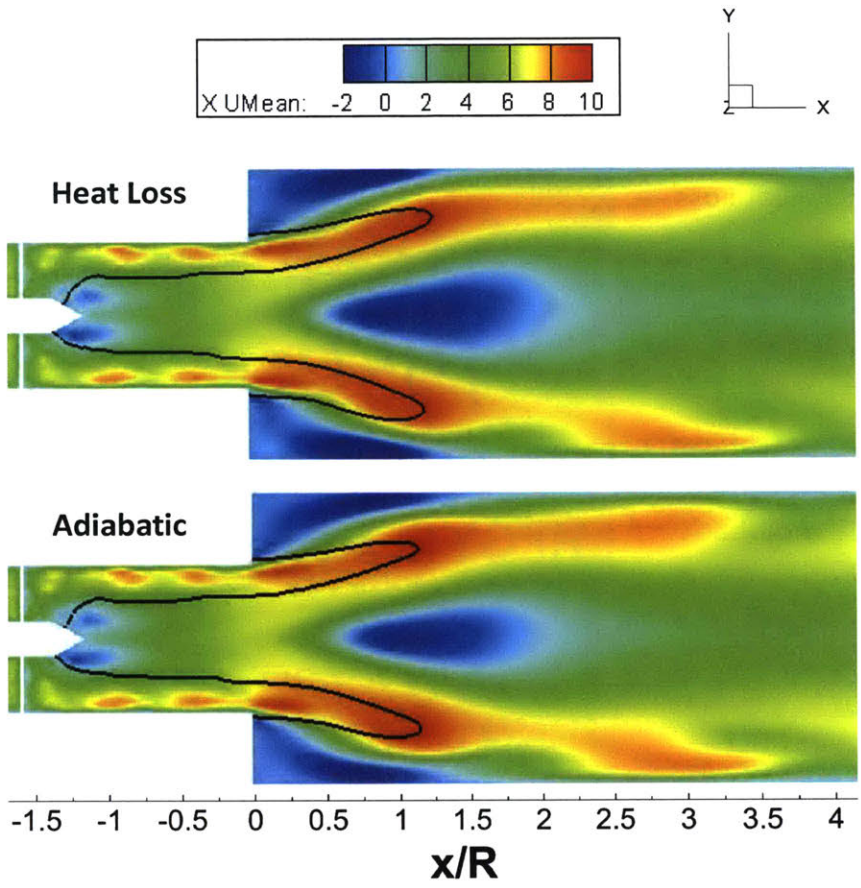

Figure 6-13: The instantaneous progress variable contour (c=0.8) is plotted (black line) as a way to locate the flame front along with the mean axial velocity contours of Flame IV (ϕ=0.7) with two different thermal boundary conditions.

($\kappa = 0$) and profiles of the same at the extinction strain rate ($\kappa = \kappa_{ext}$= 989 1/s). The latter forms the upper bound of the LES data, while the unstretched flame forms the lower bound. This is also seen for Flame III near the highest temperatures. The spread in the LES data is almost equal to the difference between the strained and unstrained laminar profiles. Both figures show that the scatter plot of the LES data are bounded by laminar flame profiles at different strain rates. These adiabatic LES results indicate turbulence impacts these flames primarily by subjecting them to different strain rates. Furthermore, we see that overall, the turbulent flamelet structures are similar to those of laminar strained flames.

We perform a similar analysis in this section, to try and capture the turbulent flame structure of the non-adiabatic flames using 1-D laminar flamelets. Data from Figures 6-6 and 6-7 are now plotted in Figures 6-14 and 6-16 but with different laminar profiles added for comparisons.

Clear differences are observed between the two wall boundary conditions for Flame III in Figures 6-8 and 6-14. Heat loss results in significant increases in the LES data scatter with more points located below the main flamelet. We also noticed clear differences in the macrostructure of the flames with these two boundary conditions in Figure 6-12 with the adiabatic case having a shorter flame, and thus the reactants are consumed only at high temperatures. This is what is also indicated from the flamelet plots. We attempt to reproduce this turbulent flame behavior for Flame III with heat loss using laminar flame simulations but with varying product gas temperatures as shown in the figure, hence modeling the impact of heat loss on the flamelet structure. Note that $\Theta_b = (T_b - T_u)/(T_{eq} - T_u)$, where T_b is the product gas temperature and T_{eq} the equilibrium temperature. These laminar flamelets simulate the different product temperatures present along the wall of the combustor (see Figure 6-15). In the downstream regions of the flow (x/R $>$ 3), it is mainly the product gases that interact with the wall ($\Theta > 0.4$.).

Figure 6-14 shows that we are able to successfully capture the spread in the LES data using these laminar calculations. For these flamelet simulations, in order to reproduce the impact of heat loss, a different laminar flame model is used with

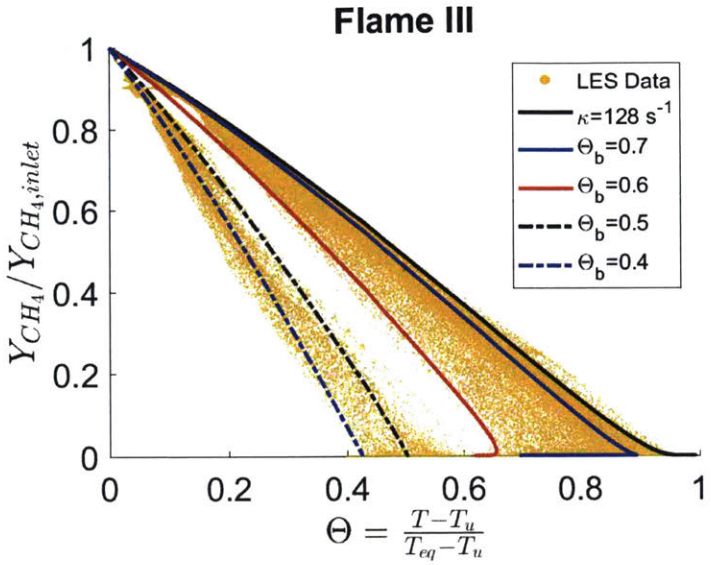

Figure 6-14: Flamelet structure of Flame III (ϕ=0.56) with heat loss, and laminar flame profiles constructed using the asymmetric laminar setup.

opposed reactants and products stream at different equilibrium temperatures as was described in Section 2.2.2 in the asymmetric flame model. We also add a strained flamelet at an intermediate level of strain to capture the upper bound of the data. Therefore for Flame III, symmetric laminar strained profiles alone are not sufficient to capture the LES data spread; implying that heat loss has a bigger impact than strain for this flame macrostructure.

On the other hand, the effects of heat loss on the Flame IV structure is pretty minimal. From Figure 6-13 it is evident that the Flame IV macrostructure is more compact and has less interaction with the combustor wall. Therefore we expect the thermal boundary conditions not to impact the flame as much. Adiabatic unstrained and strained laminar flames, can thus reasonably reproduce the microstructure of this flame; implying that strain effects are larger than the role of heat transfer for this flame macrostructure.

These results show that the 1D laminar strained flames that we have previously used to describe the 3D turbulent oxy-flame (ex. Figure 3-11), appears to be valid in the flow regions we are concerned about (IRZ & ORZ). These results also attempt to explain the differing roles of heat transfer and strain to try and decouple their effects

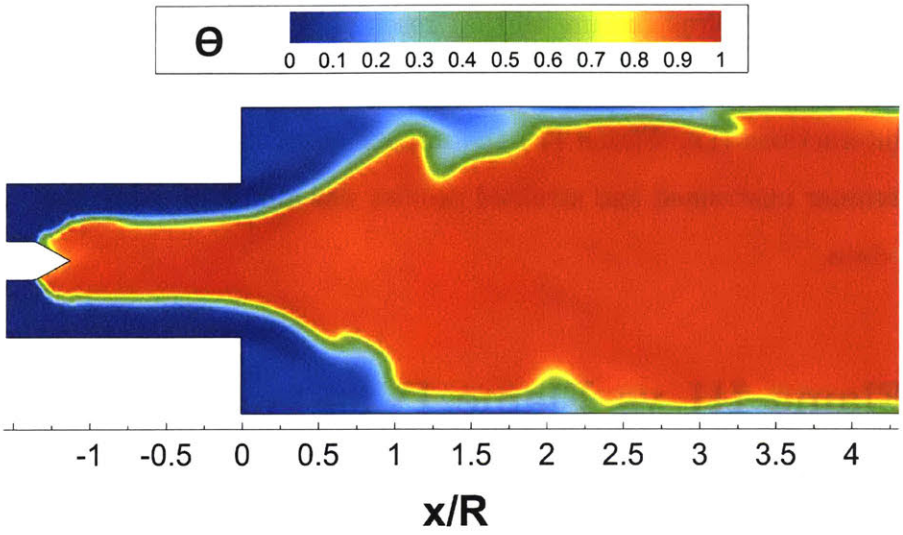

Figure 6-15: Instantaneous normalized temperature ($\Theta = (T - T_u)/(T_{eq} - T_u)$) contours for Flame III with heat loss.

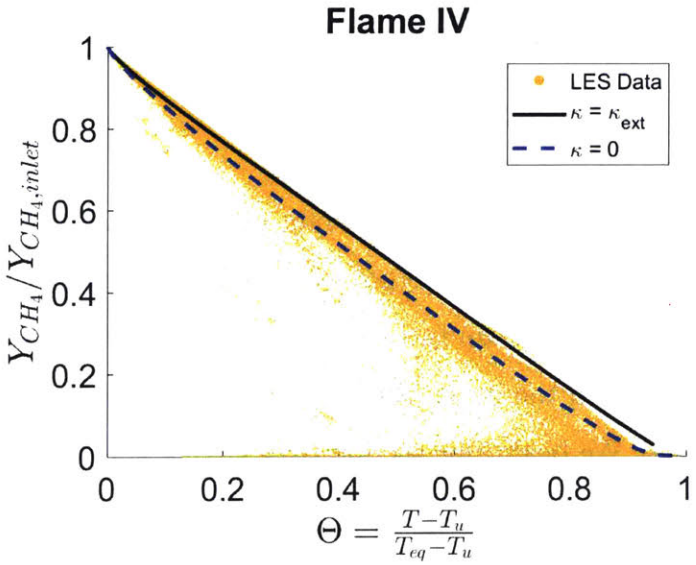

Figure 6-16: Flamelet structure of Flame IV (ϕ=0.7) with heat loss, and symmetric laminar flame profiles.

since it is not well understood in the literature [141, 142, 95]. Heat transfer impacts the flame type that has the greatest interaction with the wall (i.e. Flame III) by changing it's flame microstructure to that resembling an asymmetric laminar flame with different product equilibrium temperatures. On the other hand for flames with less wall interactions (i.e. Flame IV) the impact of strain is larger since the spread between laminar unstrained and strained profiles was almost equal to that of the LES turbulent data.

6.4 Flame III vs Flame IV: Flame-Flow Interactions

The Flame III to IV transition is dependent on the strain rates in the ORZ region. Additionally, from the previous chapter, it was clearly seen that the recirculation zone size significantly varies and scales with the extinction strain rate of the reactant mixture (Fig. 5-42. There are certain flame-flow interactions that cause these and using LES gives access to the important variables in the flow to help understand these phenomena.

6.4.1 Strain Rates

In Chapter 3 it was shown how extinction strain rates are able to model and scale the flame transition to the ORZ. The hypothesis was that the flame survives in the ORZ only when it's extinction strain rate exceeds the local strain rates in the flow in that region. We also showed the importance of calculating extinction strain rates at the ORZ temperatures. We begin this section by verifying this hypothesis using our flame transition LES simulations which consider heat loss for practical considerations. The shear strain rate contour of the flow is plotted along with the flame edge at the moment when a flame kernel is seen entering the ORZ in Figure 6-17. We analyze the strain rates in the red region highlighted in the figure in order to assess how they change as equivalence ratio increases and hence extinction strain rates of the mixture.

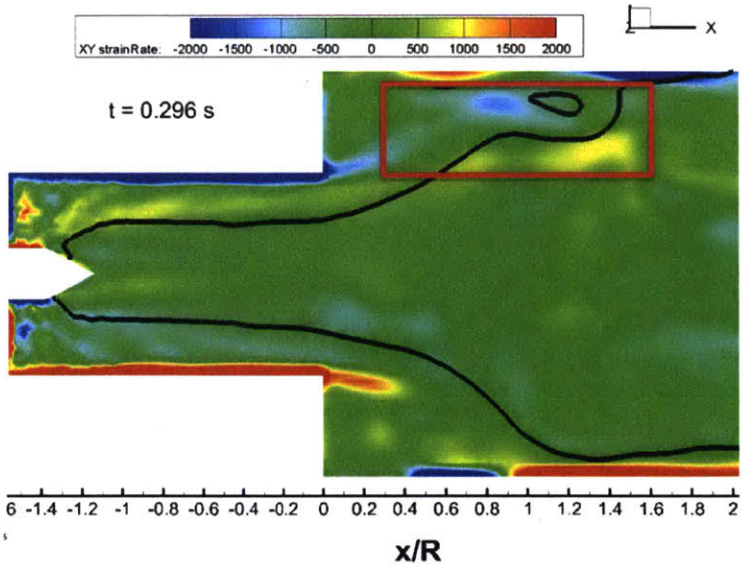

Figure 6-17: XY strain rate contours along with the flame edge at the instant right before a flame kernel enters the ORZ. The strain rate analysis is performed on the area highlighted.

Before calculating extinction strain rates of the reactant mixture in the ORZ, we plot temperature profiles at various axial locations in the flow and at two different time instances during the transition process as shown in Figure 6-18. It can be seen that the temperature of the reactants in that ORZ region (y/R≈0.8) is on the order of 450 K before a flame stabilizes there. Therefore for the strain rate analysis shown in Figure 6-19, extinction strain rates are calculated at 450 K.

The shear (S_{xy}) and normal (S_{xx} and S_{xy}) components of the strain rates in the flow are normalized by the extinction strain rate and plotted versus time. Predicting the ORZ flame stabilization requires a further understanding of the local strain characteristics of the flow field. The shear strain rate causes extensional flame straining leading to positive stretching of the flame. The normal strains of the flow causes compressive flame straining leading to negative stretching or compression of the flame [147].

Therefore we plot all of these strain rate terms versus time to determine the relative importance of each as well. As time moves forward, the equivalence ratio increases, so does the corresponding extinction strain rate and thus normalized strain

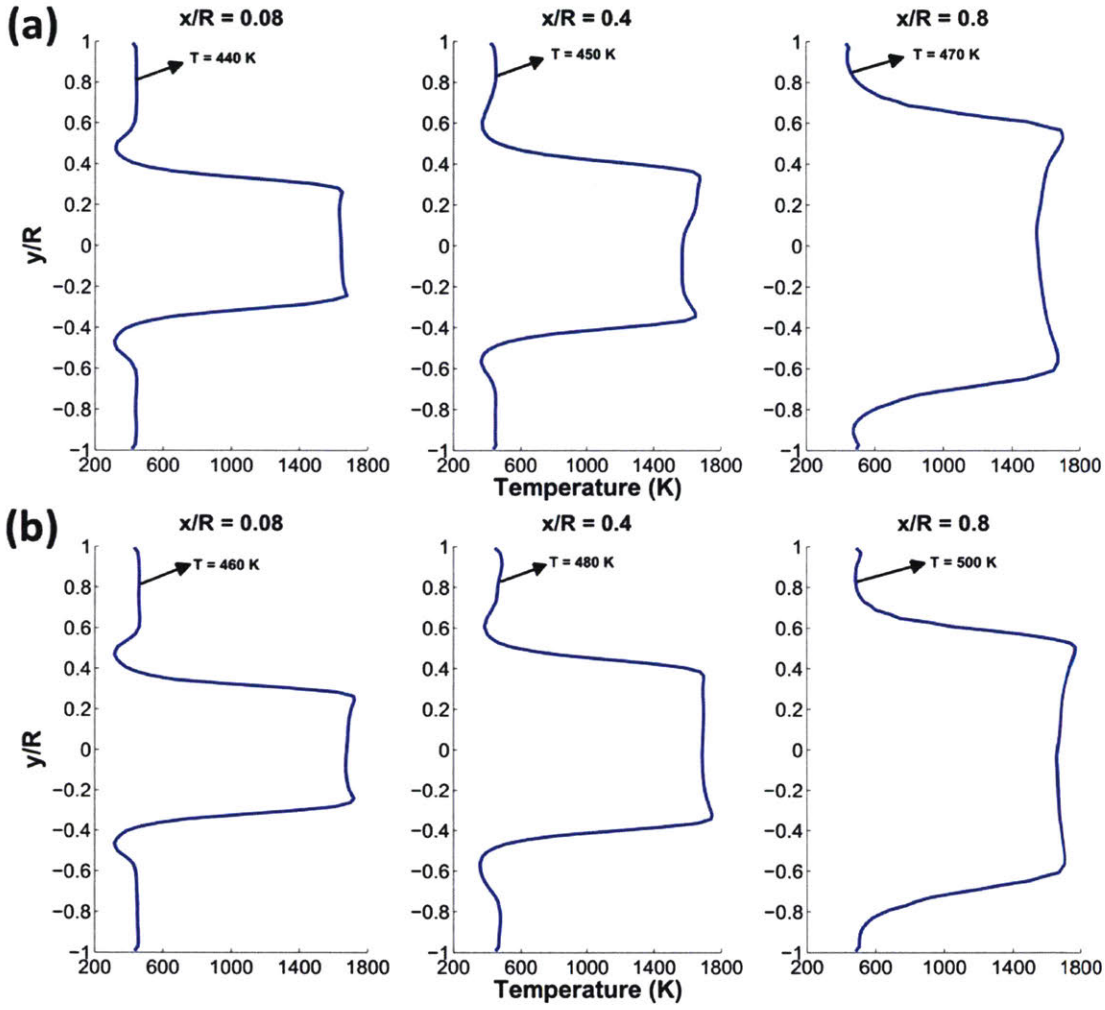

Figure 6-18: Instantaneous temperature profiles at several axial locations for (a) Flame III (ϕ=0.58) and (b) Right before the transition to Flame IV (ϕ=0.625).

rates start to trend downwards. The vertical line shows the point at which the flame kernel enters and survives in the ORZ. Before this point the strain rates in the flow are greater than the extinction strain rate for the majority of the time. Therefore a flame would not be able to survive there. However after this point is reached, at a certain equivalence ratio, there is a dramatic shift in the three curves as the strain rates in the flow become much smaller than the extinction strain rate. These results give additional proof that the Flame III to IV transition is very dependent on the strain rates in the ORZ region, and the transition occurs when the extinction strain rate of the mixture, computed at the ORZ temperature, can overcome these strains. It also appears that the shear strain rate term (S_{xy}) is less impacted by the flame transition, since we observe a very sharp decrease in the normalized strain rate, only for the normal components of strain.

From the previous section we saw that heat loss has a greater impact on Flame III than IV due its greater interaction with the wall. We also noticed a slight increase in the ORZ temperature when adiabatic boundary conditions were assumed. The increase in ORZ reactants temperature will increase the corresponding extinction strain rate in that region. Therefore we would expect the Flame III to IV transition to happen at slightly leaner equivalence ratios for the adiabatic case than the simulation with heat loss.

6.4.2 Recirculation Zones

We now compare recirculation zone structures and flow profiles for the two flame types. Figure 6-20 presents the mean temperature contours and streamlines for each flame. The inner recirculation zone becomes much smaller for Flame IV as the two main eddies in that region also shrink. This reduction in recirculation zone size causes the flame to become more compact; consistent with experimental observations [16].

Next, taking a look at mean axial profiles at two different locations in the flow (Figure 6-21), distinct differences are present between the two flames' flow profiles. The jet is thicker for Flame IV and is at a different vertical location within the flow. The inner recirculation zone is also clearly seen to be larger for Flame III.

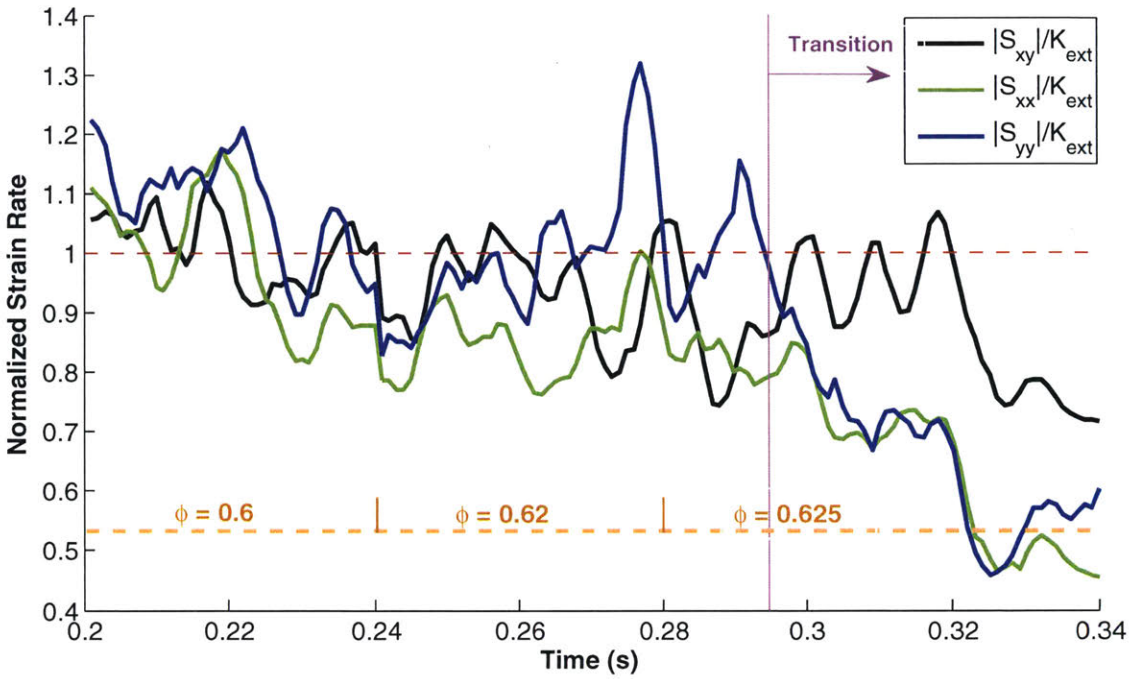

Figure 6-19: Normalized strain rate terms plotted during the flame III to flame IV transition. The strain rates are normalized by the extinction strain rate calculated at 450 K.

This reduction in the spreading angle of the annular jet for Flame IV is also seen by Kewlani et al. [87] for methane-air mixtures in the swirl combustor. This takes place as a result of higher heat release and thermal expansion in the ORZ region as will be shown in detail in the next section.

6.4.3 Vorticity Fields

In this section, we investigate the vorticity field and its effect on the flow and flame profiles. In Figures 6-22 and 6-23, we compare the out-of-plane vorticity field and its impact on the recirculation zone and the flame front in both flame configurations at consecutive time instances. The shear layers are characterized by high vorticity. Flame III is simulated at an equivalence ratio of 0.56 and Flame IV refers to an equivalence ratio of 0.7.

The eddies appear to be quite different for each flame type. For Flame IV, the eddies are more circular and distinct compared to those in Flame III. These vortical

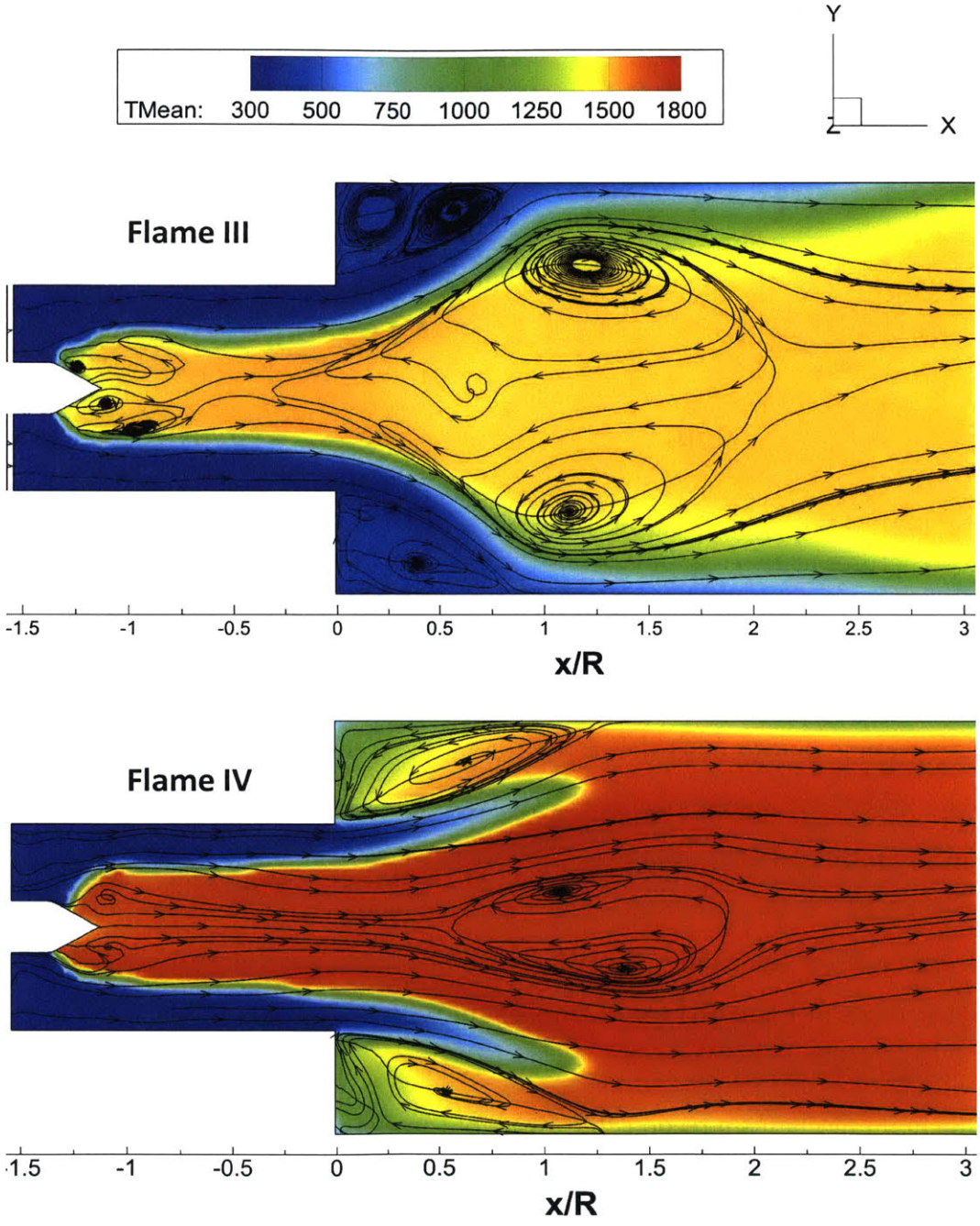

Figure 6-20: Mean temperature contours and streamlines of methane-oxy flames from LES at the two flame macrostructures.

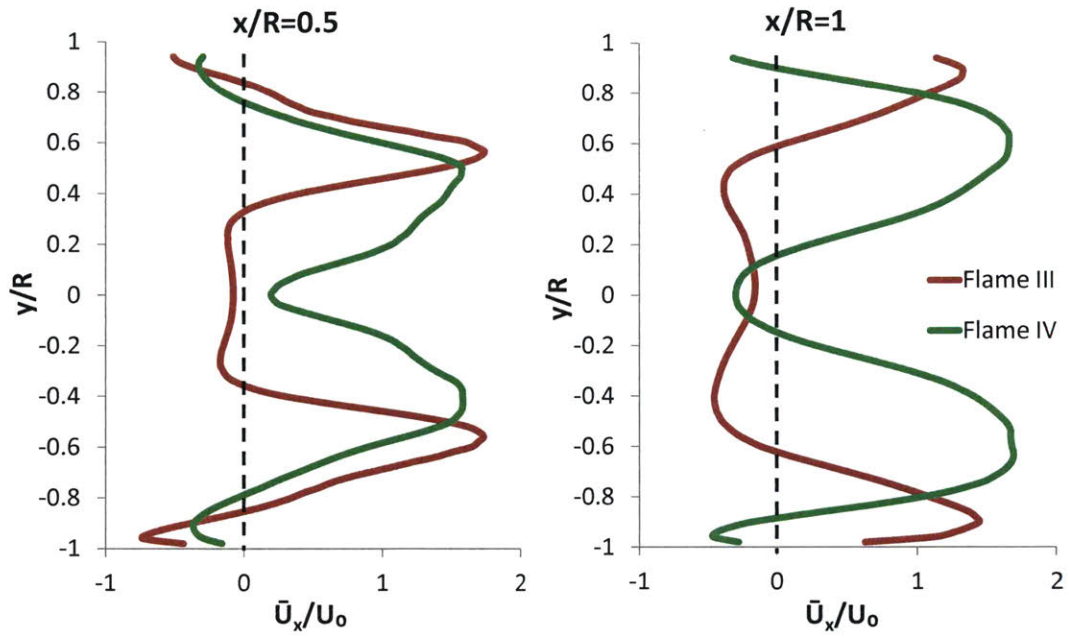

Figure 6-21: Normalized mean axial velocity profiles comparing the two flame macrostructures at two axial locations (x/R) in the swirl combustor for the methane-oxy mixture.

structures originate from the swirler centerbody and shed along the shear layers. The spreading angle is also much lower for Flame IV and so the dominant positive and negative eddies are closer together. This can clearly be seen in Figure 6-24 if we look at the mean vorticity contours. This effect causes the inner recirculation zone to decrease for Flame IV as a result. This figure also shows the differences in the relative mean strengths of the eddies, with the eddies being weaker for Flame IV. Therefore only the eddies in Flame III are able to significantly impact flame wrinkling as is also seen in Fig. 6-23.

The main mechanism responsible for all of these observations is the impact of heat release on vorticity. As several researchers have shown [87, 6, 148, 149], increasing heat release rates increases vorticity damping mainly through the dilatation term (stretching). This is consistent with what is seen qualitatively in Figures 6-22 and 6-23 for Flame III as significant vortex stretching is clearly evident compared to Flame IV.

Furthermore, Michaels et al. [6] compared the impacts of the different terms in

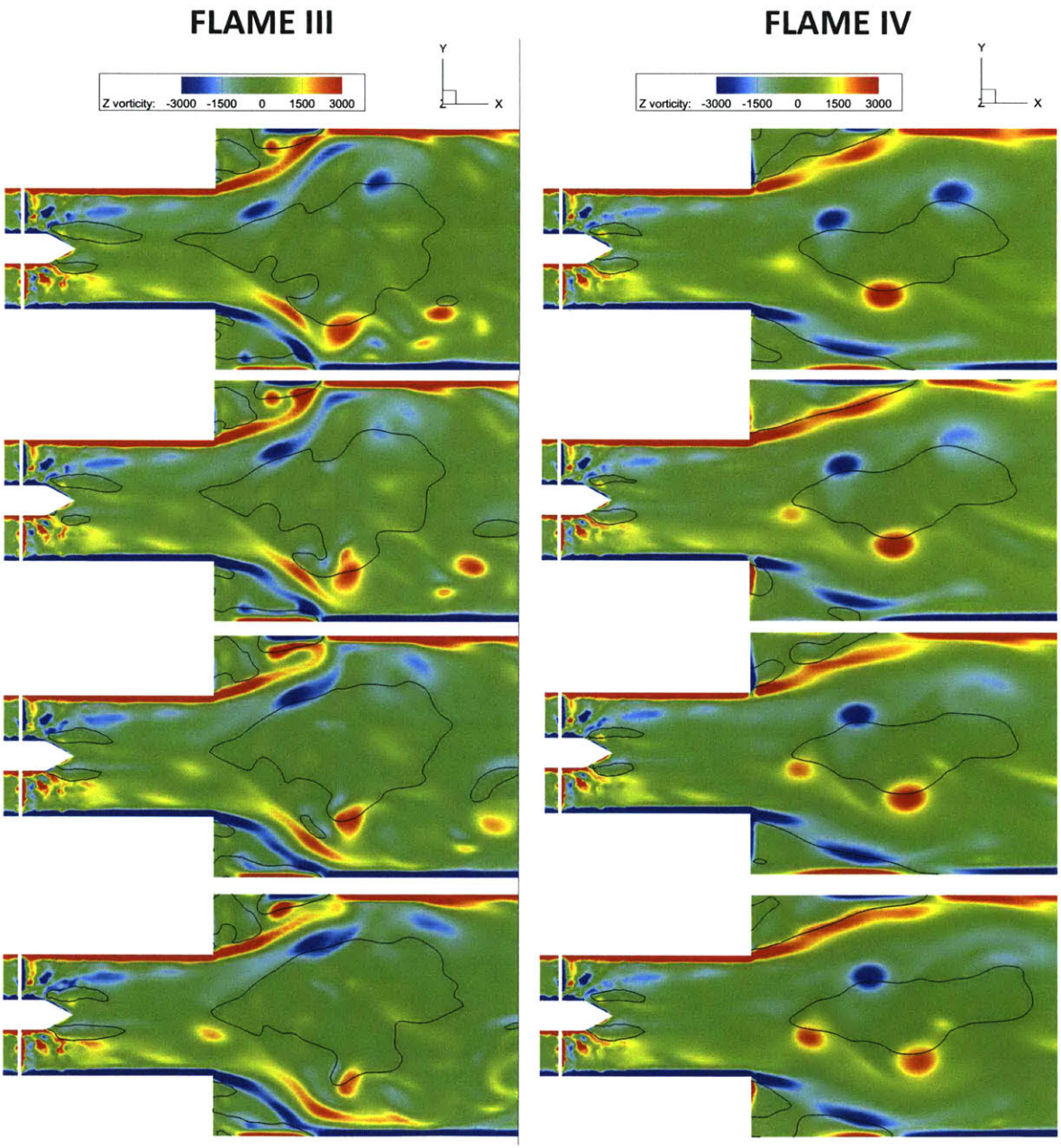

Figure 6-22: Instantaneous out-of-plane vorticity contours along with the stagnation velocity line (black line) to locate the recirculation zones of methane-oxy flames from LES at the two flame macrostructures. 1 ms separates each frame.

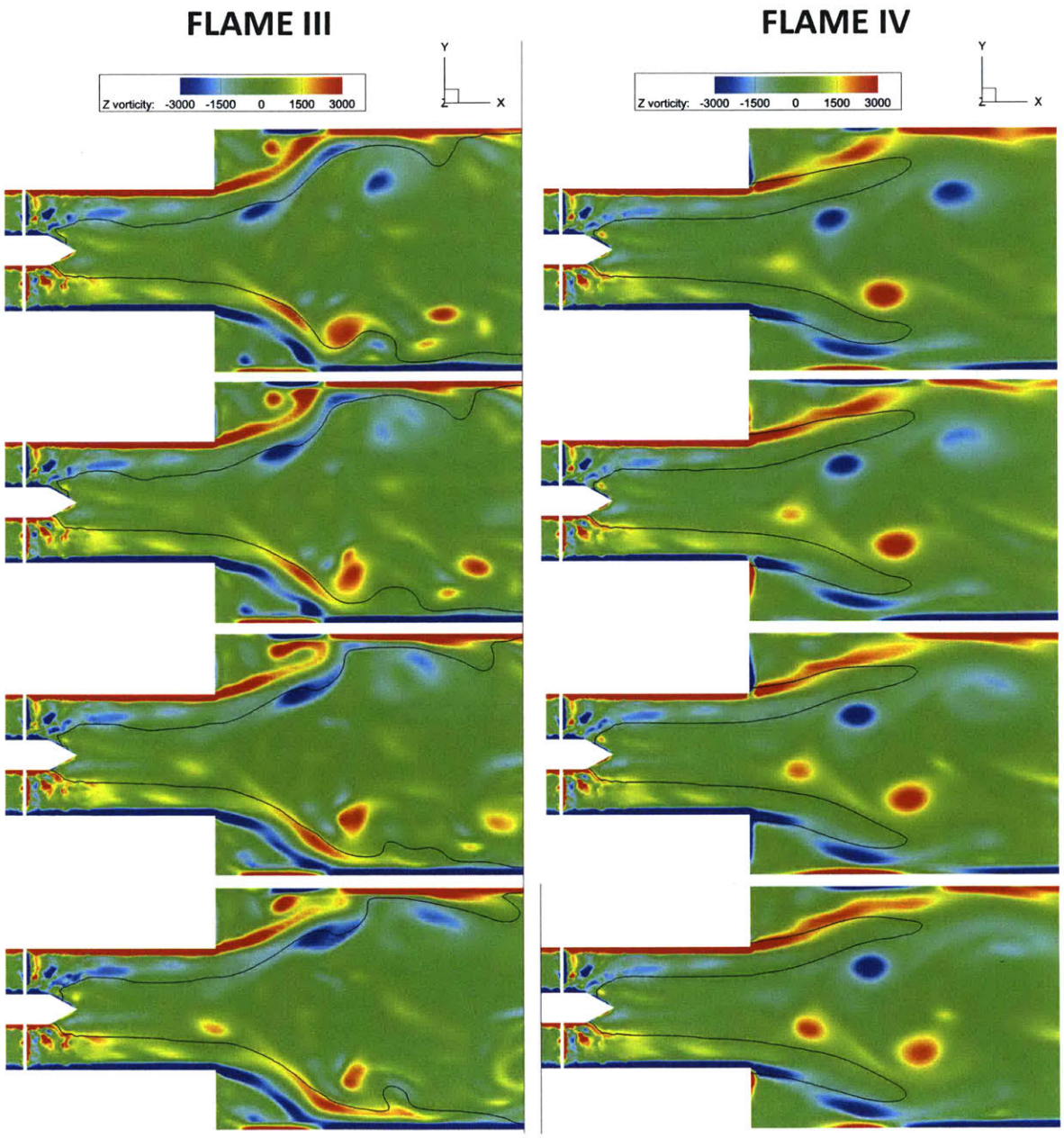

Figure 6-23: Instantaneous out-of-plane vorticity contours along with the progress variable contour c=0.8 (black line) to locate the flame front of methane-oxy flames from LES at the two flame macrostructures. 1 ms separates each frame.

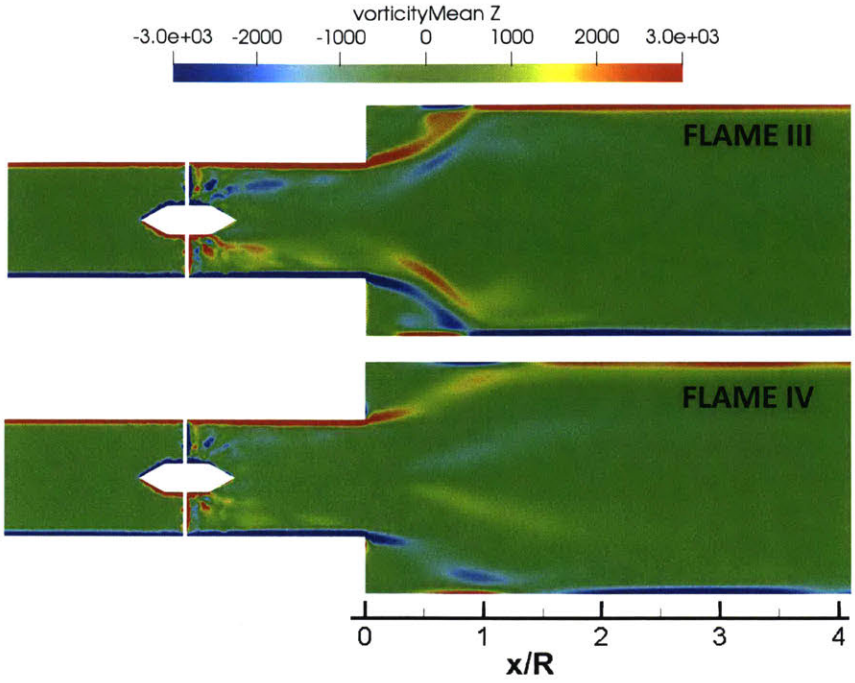

Figure 6-24: Mean out-of-plane vorticity contours of methane-oxy flames from LES at the two flame macrostructures.

the vorticity equation and also showed the dilatation effect to be the highest and increased with higher heat release. A similar conclusion was reached by Bobbitt et al. [148] for premixed flames with low Karlovitz numbers.

To verify these outcomes from the literature in the swirl combustor geometry for methane-oxy mixtures, the dilatation vorticity source term ($\omega(\nabla \cdot u)$) is calculated for the whole region in the flow for both flames and the results are shown in Figures 6-25 and 6-26. The dilatation term clearly has a big impact on the flame since it's value is greatest in the regions of the flow where the flame front is located 6-26. The two flames also have different values near the flame as is shown in Fig. 6-25 with the higher heat release flame type (Flame IV) having higher dilatation values as expected.

We also compare mean vorticity and heat release profiles for each flame macrostructure in Figure 6-27. There is a clear contrast in the results between the two flames. Firstly, the heat release rates are much higher for Flame IV as is expected in both the inner and outer shear layers. These high heat release rates result in gas expansion

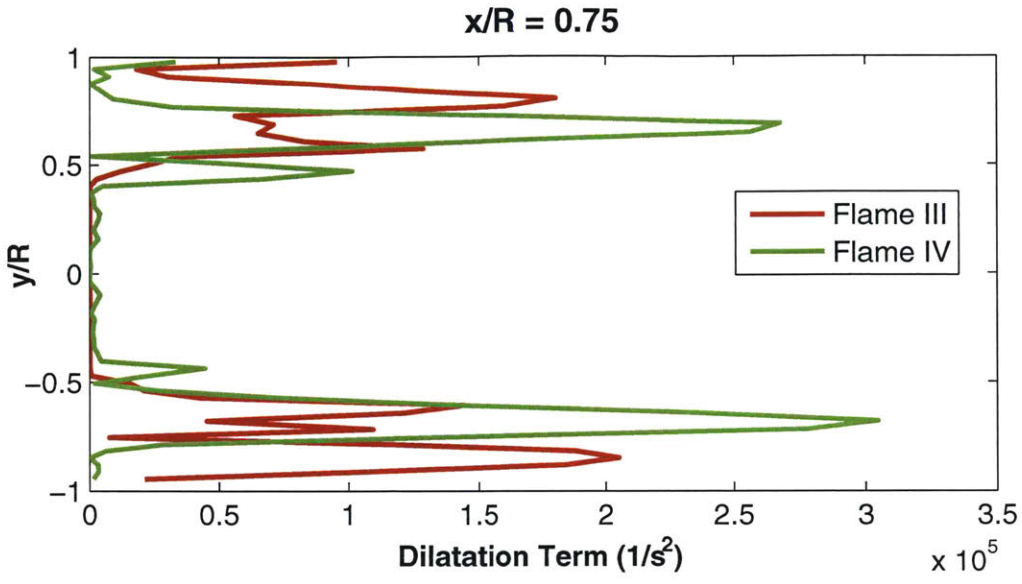

Figure 6-25: Mean dilatation vorticity source term profiles comparing the two flame macrostructures at x/R=0.75 in the swirl combustor for the methane-oxy mixture.

in those regions which reduces the spreading angle of the jet. The high heat release rates also increases the dilatation impact on vorticity 6-25 which in turn increases the vorticity damping as is also seen in the left figure. Vorticity damping coupled with the reduction in jet angle causes the inner recirculation zone to shrink for Flame IV as observed in simulation results from the previous and current chapter.

These important outcomes are consistent with all of the numerical observations we have seen so far and also serve to explain how the flow impacts the flame in experiments as well. Watanabe et al. [16] also observed experimentally the reduction in flame length of methane-oxy flames in a swirl combustor as the flame transitioned from Flame III to IV. The LES results in this thesis have now shown that this reduction in flame length occurs as a result of the change in size and shape of the inner recirculation zones which is due to vorticity damping at high release as we have shown. This interplay between flow and flame is visually represented in Figure 6-28. The flame is impacted by the flow; vorticity damping reduces the size of the recirculation zone which makes the flame more compact during the Flame III to IV transition. The flow is also impacted the flame; higher heat release results in gas expansion which causes this vorticity damping. Therefore there is this continuous

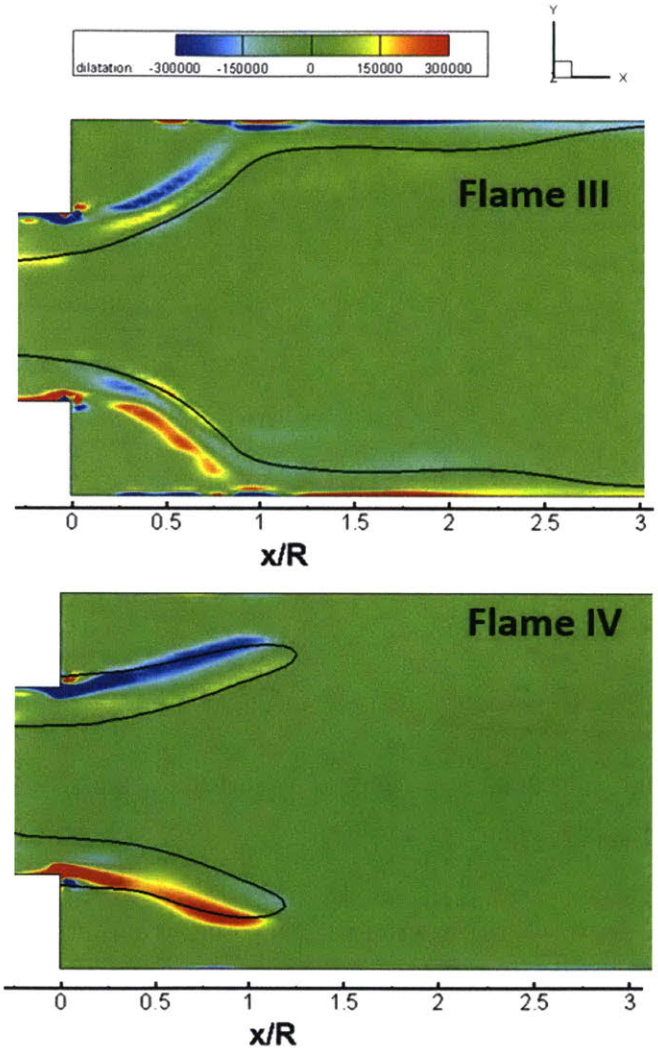

Figure 6-26: Mean dilatation vorticity source term contours comparing the two flame macrostructures in the swirl combustor for the methane-oxy mixture.

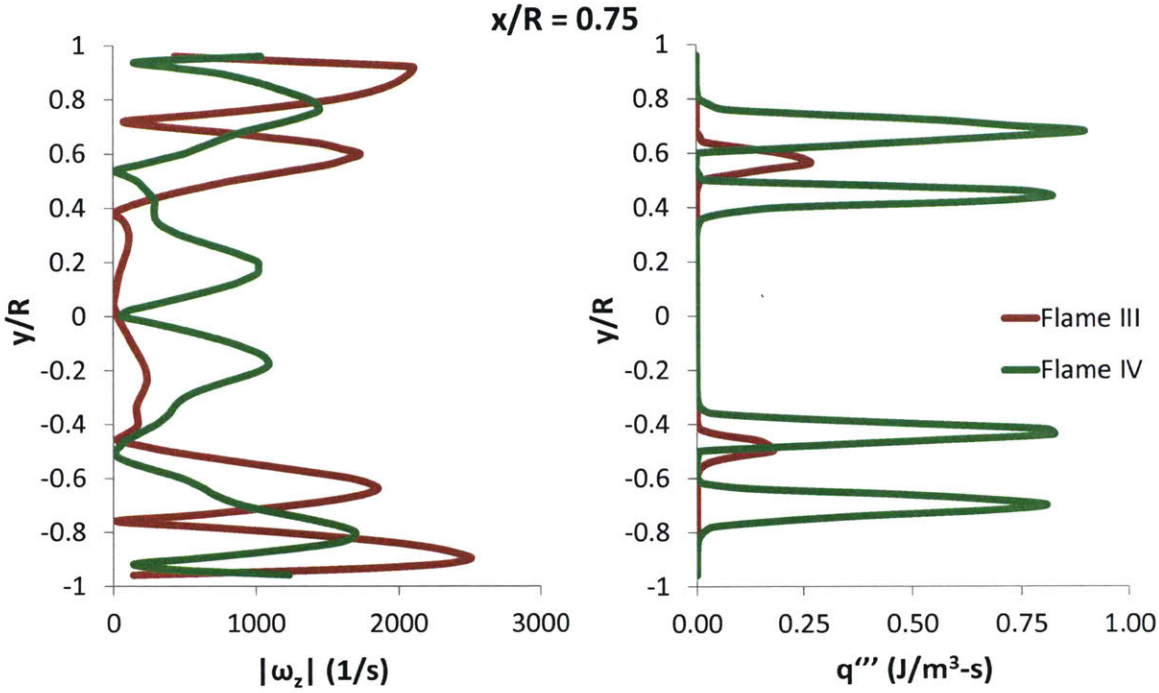

Figure 6-27: Mean out-of-plane vorticity (left) and volumetric heat release (right) profiles comparing the two flame macrostructures at x/R=0.75 in the swirl combustor for the methane-oxy mixture.

feedback loop present.

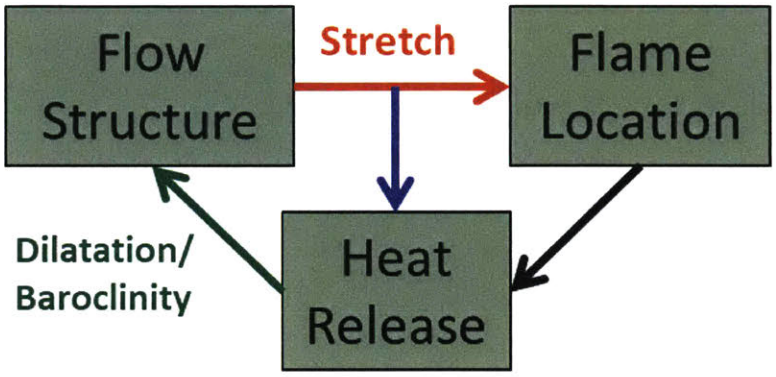

Figure 6-28: Visual representation of the interactions between the flow and flame.

6.5 Conclusions

In this chapter, we used LES to model the Flame III to Flame IV transition in the swirl combustor for $CH_4/O_2/CO_2$ (methane-oxy) mixtures. The simulations were successfully able to capture the correct flame macrostructure transition mechanism for these methane-oxy flames. We also investigated the flamelet structure of these two flame macrostructures. The combustor wall boundary conditions had a significant impact on the flamelet structure of these two flames. For the adiabatic cases, the flamelets of both macrostructures behaved like strained laminar flames subjected to varying levels of strain. When wall heat transfer is included, Flame III flamelet results in larger scatter of the data because the fuel is consumed at lower temperatures along the combustor wall. In addition, the direct correspondence of the 1D laminar flame structures to the 3D turbulent flames, proves the validity of using laminar flame calculations (ex. extinction strain rate) to model and scale these turbulent flame macrostructures (Chapter 3). We also showed how the flame stabilizes in the ORZ only when the extinction strain rate of the mixture, at the ORZ temperature, exceeds strain rates in the region. The flame becomes much shorter during the transition to higher equivalence ratios due to the decreasing size of the inner recirculation zone and the flame folding phenomenon that happens. This was explained by vorticity damping

due to gas expansion at the higher high release rates during the flame transition. These important outcomes are consistent with all of the numerical observations we have seen so far and also serve to explain the interplay between the flow and flame dynamics in the swirl combustor for oxy-combustion.

Chapter 7

Conclusions

7.1 Summary

Oxy-fuel combustion is a leading technology for carbon capture and sequestration (CCS) in power plants. Natural gas cycles with CCS can be cost-competitive with renewable energy technologies, making them important for transitioning to low CO_2 energy sources using fossil fuels. Methane oxy-combustion cycles require combustors that can burn fuel and an oxygen stream along with some diluent, so that the CO_2 in the flue gases can easily be captured by condensing out the water. Cycles with CO_2 recycle are found to be more attractive due to their higher efficiencies and lower costs but the combustor technology still requires development and that is the focus of this thesis. A combined experimental and numerical approach is used to take advantage of both types of tools in exploring the combustion dynamics of oxy-fuel flames.

In Chapter 3, we established the stability characteristics for flame macrostructure transitions for turbulent oxy-flames in a gas turbine combustor. We examined the specific flame transition linked to the occurrence of combustion instabilities in a gas turbine combustor for methane oxy-combustion mixtures. There existed a flame transition point where the onset of flame stabilization in the ORZ took place at the same equivalence ratio and inlet velocity in both air and oxy-combustion. The spinning frequency of this ORZ flame was found to be a purely kinematic phenomenon with a fixed Strouhal number independent of the Reynolds number. Therefore the inlet

velocity is a more relevant parameter for maintaining similar flow conditions in the ORZ. By defining the inverse of the ORZ spinning frequency as a characteristic flow time, and the inverse of the extinction strain rate as a characteristic flame time scale, we constructed a map with a single line separating two different flame stabilization modes, valid for a whole range of different inlet conditions.

The work in Chapter 4 then builds on these results by investigating the role of kinetics vs transport on the response to strain of these oxy-flames. The Lewis number for stoichiometric oxy flames is less than 1, whereas for the air flame it is unity. This impacts the response to strain of the two flames by affecting the shape of the consumption speed curves. For lower flame temperatures, the oxy flames display enhanced flame speeds as the flame is strained whereas the air flame's response is almost flat. But at higher temperatures, heat loss from radiation is more significant and the mixture Lewis number is higher resulting in flatter curves for the oxy flame. The chemical effect of CO_2 present in oxy-combustion has a bigger impact on the consumption speed and flame extinction strain rate than the effect of transport properties change. This is mainly due to the competition for radicals of the important reaction: $CO_2 + H \longleftrightarrow CO + OH$ when high levels of CO_2 are present in oxy-combustion. It is also revealed that this reaction affects the sensitivity of the flame properties to changes in the inlet temperature, with the air-combustion flame being more sensitive. This variation with temperature shows the importance of choosing the right inlet temperature when calculating these flame values in order to accurately reflect the conditions present in the combustor regions being investigated.

In Chapter 5, LES models were validated for propane-air mixtures in bluff-body and backward-facing step combustors, and for methane-oxy mixtures in the swirl combustor. The main goal was also to investigate the attributes of a chemical mechanism which are important for predicting important flow features such as recirculation zones in these simple and complex geometries. For the propane-air cases, we used a 2-step mechanism which had reasonable extinction strain rate agreement with experimental values. We also modified that reduced mechanism to form a new mechanism which intentionally had far worse agreement and over-predicted extinction strain rates. We

found that simulations in these two geometries using the modified mechanism under-predicted recirculation zone lengths compared to results using the original mechanism. In the swirl combustor, oxy-combustion simulations using the Frassoldati mechanism, which had very good extinction strain rate values, were able to predict the correct flame macrostructure and flow profiles compared to the Andersen mechanism which had much worse extinction strain rate prediction. Recirculation zone lengths in the backward-facing step and swirl combustors linearly scaled well with extinction strain rate. This scaling held regardless of fuel or oxidizer type, Reynold's number, inlet temperature, or combustor geometry. We conclude that it is very important that a chemical mechanism is able to correctly predict extinction strain rates if it is to be used in CFD simulations.

Finally, in Chapter 6, we used our LES framework to model the Flame III to Flame IV transition in the swirl combustor for methane-oxy mixtures. The simulations were successfully able to capture the correct flame macrostructure transition mechanism for these methane-oxy flames. 1D laminar flamelets were also found to reasonably represent 3D turbulent flame structures, explaining why laminar calculations have been able to capture more complex turbulent behaviors. We also showed how the flame stabilizes in the ORZ only when the extinction strain rate of the mixture, at the ORZ temperature, exceeds strain rates in the region; confirming an important hypothesis in this thesis. The flame becomes much shorter during the transition to higher equivalence ratios due to the decreasing size of the inner recirculation zone. This was explained by vorticity damping due to gas expansion at the higher high release rates during the flame transition. These important outcomes are consistent with all of the numerical observations we have seen so far and also serve to explain the interplay between the flow and flame dynamics in an oxy-fuel gas turbine combustor.

Overall, the contributions from this thesis are pivotal for advancing the fundamental understanding of methane oxy-combustion flames which ultimately supports in the design of these novel gas turbine combustors.

7.2 List of Publications

Peer-Reviewed Journal Articles

- **Chakroun, N. W.**, Shanbhogue, S. J., Dagan, Y., Ghoniem, A. F. (2017). Flamelet structure in turbulent premixed swirling oxy-combustion of methane. *Proceedings of the Combustion Institute*, under review.

- Dagan, Y., **Chakroun, N. W.**, Shanbhogue, S. J., Ghoniem, A. F. (2017). Role of intermediate temperature kinetics and radical transport in LES and the prediction of leading edge structure of turbulent lean premixed flames. *Proceedings of the Combustion Institute*, under review.

- **Chakroun, N. W.**, Shanbhogue, S. J., Taamallah, S., Michaels, D., Kewlani, G., Ghoniem, A. F. (2017). For accurate LES of lean premixed combustion, reduced kinetics mechanisms must predict correct extinction strain rates. To be submitted.

- **Chakroun, N. W.**, Michaels, D., Shanbhogue, S. J., Ghoniem, A. F. (2017). Response of premixed stoichiometric oxy-flames to strain; role of chemistry and transport. *Journal of Propulsion and Power.*

- Taamallah, S., **Chakroun, N. W.**, Watanabe, H., Shanbhogue, S. J., Ghoniem, A. F. (2016). On the characteristic flow and flame times for scaling oxy and air flame stabilization modes in premixed swirl combustion. *Proceedings of the Combustion Institute*, 36(3), 3799-3807.

- Watanabe, H., Shanbhogue, S. J., Taamallah, S., **Chakroun, N. W.**, Ghoniem, A. F. (2016). The structure of swirl-stabilized turbulent premixed CH4/air and $CH_4/O_2/CO_2$ flames and mechanisms of intense burning of oxy-flames. *Combustion and Flame*, 174, 111-119.

Peer-Reviewed or Abstract-Reviewed Conference Proceedings

- Dana, A. G., Gudiyella, S., Shanbhogue, S. J., Michaels, D., **Chakroun, N. W.**, Ghoniem, A. F., Green, W. H. (2017). Automated generation of chemical mechanisms for predicting extinction strain rates with applications in flame stabilization and combustion instabilities. *55th AIAA Aerospace Sciences Meeting*, AIAA 2017-0835.

- **Chakroun, N. W.**, Michaels, D., Shanbhogue, S. J., Ghoniem, A. F. (2017). Response of premixed stoichiometric $CH_4/O_2/CO_2$ flames to strain; the role of chemistry and transport. *55th AIAA Aerospace Sciences Meeting*, AIAA 2017-1800.

- **Chakroun, N. W.**, Shanbhogue, S. J., Kewlani, G., Taamallah, S., Michaels, D., Ghoniem, A. F. (2017). On the role of chemical kinetics modeling in the LES of premixed bluff body and backward-facing step combustors. *55th AIAA Aerospace Sciences Meeting*, AIAA 2017-1572.

Bibliography

[1] Tyler Bryant, Keith Burnard, Pierpaolo Cazzola, John Dulac, Araceli Fernandez, Joerg Husar, Peter Janoska, Eric Masanet, Luis Munuera, Uwe Remme, Jacob Teter, and Kira West. Energy technology perspectives 2016 - towards sustainable urban energy systems. Technical report, International Energy Agency, 2016.

[2] A Amato, B Hudak, P DCarlo, D Noble, D Scarborough, J Seitzman, and T Lieuwen. Methane oxycombustion for low co2 cycles: Blowoff measurements and analysis. *Journal of Engineering for Gas Turbines and Power*, 133(6):061503, 2011.

[3] Soufien Taamallah, Zachary A LaBry, Santosh J Shanbhogue, and Ahmed F Ghoniem. Thermo-acoustic instabilities in lean premixed swirl-stabilized combustion and their link to acoustically coupled and decoupled flame macrostructures. In *Proceedings of the Combustion Institute*. Elsevier, 2014.

[4] Soufien Taamallah, Santosh J. Shanbhogue, and Ahmed F. Ghoniem. Turbulent flame stabilization modes in premixed swirl combustion: Physical mechanism and karlovitz number-based criterion. *Combustion and Flame*, pages –, 2016.

[5] Seunghyuck Hong, Santosh J Shanbhogue, and Ahmed F Ghoniem. Impact of fuel composition on the recirculation zone structure and its role in lean premixed flame anchoring. *Proceedings of the Combustion Institute*, 35(2):1493–1500, 2015.

[6] D. Michaels, S.J. Shanbhogue, and A.F. Ghoniem. The impact of reactants composition and temperature on the flow structure in a wake stabilized laminar lean premixed ch4/h2/air flames; mechanism and scaling. *Combustion and Flame*, 176:151 – 161, 2017.

[7] F. Halter, F. Foucher, L. Landry, and C. Mounam-Rousselle. Effect of dilution by nitrogen and/or carbon dioxide on methane and iso-octane air flames. *Combustion Science and Technology*, 181(6):813–827, 2009.

[8] V Ratna Kishore, Nipun Duhan, MR Ravi, and Anjan Ray. Measurement of adiabatic burning velocity in natural gas-like mixtures. *Experimental Thermal and Fluid Science*, 33(1):10–16, 2008.

[9] Dominik Bongartz and Ahmed F Ghoniem. Chemical kinetics mechanism for oxy-fuel combustion of mixtures of hydrogen sulfide and methane. *Combustion and Flame*, 162(3):544–553, 2015.

[10] Eric Albin, Holger Nawroth, Sebastian Gke, Yves D'Angelo, and Christian Oliver Paschereit. Experimental investigation of burning velocities of ultra-wet methaneairsteam mixtures. *Fuel Processing Technology*, 107:27 – 35, 2013. Selected Papers from the Eleventh International Conference on Combustion and Energy Utilization (11th ICCEU).

[11] A.N. Mazas, B. Fiorina, D.A. Lacoste, and T. Schuller. Effects of water vapor addition on the laminar burning velocity of oxygen-enriched methane flames. *Combustion and Flame*, 158(12):2428 – 2440, 2011.

[12] V. S. Babkin and A. V. V'yun. Effect of water vapor on the normal burning velocity of a methane-air mixture at high pressures. *Combustion, Explosion and Shock Waves*, 7(3):339–341.

[13] Peter Glarborg and Line LB Bentzen. Chemical effects of a high co2 concentration in oxy-fuel combustion of methane. *Energy & Fuels*, 22(1):291–296, 2007.

[14] A Frassoldati, A Cuoci, T Faravelli, E Ranzi, C Candusso, and D Tolazzi. Simplified kinetic schemes for oxy-fuel combustion. In *1st International conference on sustainable fossil fuels for future energy*, pages 6–10, 2009.

[15] Jimmy Andersen, Christian Lund Rasmussen, Trine Giselsson, and Peter Glarborg. Global combustion mechanisms for use in cfd modeling under oxy-fuel conditions. *Energy & Fuels*, 23(3):1379–1389, 2009.

[16] Hirotatsu Watanabe, Santosh J Shanbhogue, and Ahmed F Ghoniem. Impact of equivalence ratio on the macrostructure of premixed swirling ch4/air and ch4/o2/co2 flames. In *ASME Turbo Expo 2015: Turbine Technical Conference and Exposition*, pages V04BT04A014–V04BT04A014. American Society of Mechanical Engineers, 2015.

[17] Soufien Taamallah. *Impact of fuel and oxidizer composition on premixed flame stabilization in turbulent swirling flows: dynamics and scaling.* PhD thesis, Massachusetts Institute of Technology, 2016.

[18] Hirotatsu Watanabe, Santosh J Shanbhogue, Soufien Taamallah, Nadim W Chakroun, and Ahmed F Ghoniem. The structure of swirl-stabilized turbulent premixed ch4/air and ch4/o2/co2 flames and why oxy-flames seem to burn more intensely. *Combustion and Flame*, 2016.

[19] Yu Song, Chun Zou, Yizhuo He, and Chuguagn Zheng. The chemical mechanism of the effect of {CO2} on the temperature in methane oxy-fuel combustion. *International Journal of Heat and Mass Transfer*, 86:622 – 628, 2015.

[20] Glassman Irvin and Yetter Richard. *Combustion.* Academic Press, 2008.

[21] MVP Workshop SciTech 2017 Case. `http://web.stanford.edu/group/ihmegroup/cgi-bin/mvpws/development/`.

[22] CK Law, DL Zhu, and G Yu. Propagation and extinction of stretched premixed flames. In *Symposium (International) on Combustion*, volume 21, pages 1419–1426. Elsevier, 1988.

[23] DG Goodwin, N Malaya, H Moffat, and R Speth. Cantera: An object-oriented software toolkit for chemical kinetics, thermodynamics, and transport processes, 2012. *URL: http://code. google. com/p/cantera.*

[24] Intergovernmental Panel on Climate Change. *Climate change 2014: mitigation of climate change*, volume 3. Cambridge University Press, 2015.

[25] Energy Information Administration. International Energy Outlook, report DOE/EIA-0484, 2013.

[26] Dolf Gielen. The future role of CO_2 capture and storage: results of the IEA-ETP Model, report no. EET/2003/04. `http://www.iea.org/textbase/papers/2003/eet04.pdf`, 2003.

[27] Vittorio Tola and Alberto Pettinau. Power generation plants with carbon capture and storage: A techno-economic comparison between coal combustion and gasification technologies. *Applied Energy*, 113(0):1461 – 1474, 2014.

[28] Alberto Pettinau, Francesca Ferrara, and Carlo Amorino. Techno-economic comparison between different technologies for a {CCS} power generation plant integrated with a sub-bituminous coal mine in italy. *Applied Energy*, 99(0):32 – 39, 2012.

[29] Medhat A Nemitallah and Mohamed A Habib. Experimental and numerical investigations of an atmospheric diffusion oxy-combustion flame in a gas turbine model combustor. *Applied Energy*, 111:401–415, 2013.

[30] Bert Metz, Ogunlade Davidson, HC De Coninck, Manuela Loos, and LA Meyer. IPCC, 2005: IPCC special report on carbon dioxide capture and storage. Prepared by Working Group III of the Intergovernmental Panel on Climate Change. *Cambridge, United Kingdom and New York, NY, USA, 442 pp*, 2005.

[31] United States Environmental Protection Agency (EPA). Global Greenhouse Gas Emissions Data. `http://www.epa.gov/climatechange/ghgemissions/global.html`, 2013.

[32] US Energy Information Administration. Average national levelized costs for generating technologies in 2018, 2011.

[33] Olav Bolland and Philippe Mathieu. Comparison of two CO_2 removal options in combined cycle power plants. *Energy Conversion and Management*, 39(1618):1653 – 1663, 1998.

[34] Hanne M. Kvamsdal, Kristin Jordal, and Olav Bolland. A quantitative comparison of gas turbine cycles with capture. *Energy*, 32(1):10 – 24, 2007.

[35] Wolfgang Sanz, Herbert Jericha, Bernhard Bauer, and Emil GÃķttlich. Qualitative and quantitative comparison of two promising oxy-fuel power cycles for CO_2 capture. *Journal of Engineering for Gas Turbines and Power*, 130(3):031702, 2008.

[36] G Corchero, VP Timon, and JL Montanes. A natural gas oxy-fuel semiclosed combined cycle for zero CO_2 emissions: a thermodynamic optimization. *Proceedings of the Institution of Mechanical Engineers, Part A: Journal of Power and Energy*, 225(4):377–388, 2011.

[37] Adrian Dahlquist, Magnus Genrup, Mats Sjoedin, and Klas Jonshagen. Optimization of an oxyfuel combined cycle regarding performance and complexity level. In *ASME Turbo Expo 2013: Turbine Technical Conference and Exposition*, pages V002T07A011–V002T07A011. American Society of Mechanical Engineers, 2013.

[38] N.W. Chakroun and A.F. Ghoniem. High-efficiency low lcoe combined cycles for sour gas oxy-combustion with co2 capture. *International Journal of Greenhouse Gas Control*, 41:163 – 173, 2015.

[39] Andrew Philip Shroll. *Dynamic stability, blowoff, and flame characteristics of oxy-fuel combustion.* PhD thesis, Massachusetts Institute of Technology, 2011.

[40] Mohamed A Habib, Medhat A Nemitallah, Pervez Ahmed, Mostafa H Sharqawy, Hassan M Badr, Inam Muhammad, and Mohamed Yaqub. Experimental analysis of oxygen-methane combustion inside a gas turbine reactor under various operating conditions. *Energy*, 86:105–114, 2015.

[41] Charles E Baukal Jr. *Oxygen-enhanced combustion.* CRC press, 2013.

[42] Donald M Wicksall and Ajay K Agrawal. Effects of fuel composition on flammability limit of a lean premixed combustor. In *ASME Turbo Expo 2001: Power for Land, Sea, and Air*, pages V002T01A007–V002T01A007. American Society of Mechanical Engineers, 2001.

[43] Arthur H Lefebvre. *Gas turbine combustion.* CRC Press, 2010.

[44] Timothy C Lieuwen and Vigor Yang. Combustion instabilities in gas turbine engines(operational experience, fundamental mechanisms and modeling). *Progress in astronautics and aeronautics*, 2005.

[45] Ying Huang and Vigor Yang. Dynamics and stability of lean-premixed swirl-stabilized combustion. *Progress in Energy and Combustion Science*, 35(4):293–364, 2009.

[46] Andrew P Shroll, Santosh J Shanbhogue, and Ahmed F Ghoniem. Dynamic-stability characteristics of premixed methane oxy-combustion. *Journal of Engineering for Gas Turbines and Power*, 134(5):051504, 2012.

[47] Guo-neng Li, Hao Zhou, and Ke-fa Cen. Emission characteristics and combustion instabilities in an oxy-fuel swirl-stabilized combustor. *Journal of Zhejiang University SCIENCE A*, 9(11):1582–1589, 2008.

[48] Mario Ditaranto and Jørgen Hals. Combustion instabilities in sudden expansion oxy–fuel flames. *Combustion and Flame*, 146(3):493–512, 2006.

[49] H Murat Altay, Raymond L Speth, Duane E Hudgins, and Ahmed F Ghoniem. Flame–vortex interaction driven combustion dynamics in a backward-facing step combustor. *Combustion and Flame*, 156(5):1111–1125, 2009.

[50] Raymond L Speth and Ahmed F Ghoniem. Using a strained flame model to collapse dynamic mode data in a swirl-stabilized syngas combustor. *Proceedings of the Combustion Institute*, 32(2):2993–3000, 2009.

[51] S.J. Shanbhogue, Y.S. Sanusi, S. Taamallah, M.A. Habib, E.M.A. Mokheimer, and A.F. Ghoniem. Flame macrostructures, combustion instability and extinction strain scaling in swirl-stabilized premixed ch4/h2 combustion. *Combustion and Flame*, 163:494 – 507, 2016.

[52] Peter AT Cocks, Vaidyanathan Sankaran, and Marios C Soteriou. Is les of reacting flows predictive? part 1: Impact of numerics. In *51st AIAA Aerospace Sciences Meeting, Grapevine TX, January*, pages 7–10, 2013.

[53] Sivaji Seepana and Sreenivas Jayanti. Flame structure investigations of oxy-fuel combustion. *Fuel*, 93:52–58, 2012.

[54] Gregory P Smith, David M Golden, Michael Frenklach, Nigel W Moriarty, Boris Eiteneer, Mikhail Goldenberg, C Thomas Bowman, Ronald K Hanson, Soonho Song, William C Gardiner Jr, et al. Gri-mech 3.0. 1999.

[55] Teresa Mendiara and Peter Glarborg. Ammonia chemistry in oxy-fuel combustion of methane. *Combustion and Flame*, 156(10):1937–1949, 2009.

[56] Zhenyu Tian, Yuyang Li, Lidong Zhang, Peter Glarborg, and Fei Qi. An experimental and kinetic modeling study of premixed nh 3/ch 4/o 2/ar flames at low pressure. *Combustion and Flame*, 156(7):1413–1426, 2009.

[57] Wayne K Metcalfe, Sinéad M Burke, Syed S Ahmed, and Henry J Curran. A hierarchical and comparative kinetic modeling study of c1- c2 hydrocarbon and oxygenated fuels. *International Journal of Chemical Kinetics*, 45(10):638–675, 2013.

[58] Batikan Koroglu, Owen Pryor, Joseph Lopez, Leigh Nash, and Subith Vasu. Methane ignition delay times in co2 diluted mixtures in a shock tube. In *51st AIAA/SAE/ASEE Joint Propulsion Conference*, page 4088, 2015.

[59] Alan Kéromnès, Wayne K Metcalfe, Karl A Heufer, Nicola Donohoe, Apurba K Das, Chih-Jen Sung, Jürgen Herzler, Clemens Naumann, Peter Griebel, Olivier Mathieu, et al. An experimental and detailed chemical kinetic modeling study of hydrogen and syngas mixture oxidation at elevated pressures. *Combustion and Flame*, 160(6):995–1011, 2013.

[60] Zekai Hong, David F. Davidson, and Ronald K. Hanson. An improved h2/o2 mechanism based on recent shock tube/laser absorption measurements. *Combustion and Flame*, 158(4):633 – 644, 2011. Special Issue on Kinetics.

[61] Timothy C Williams, Christopher R Shaddix*, and Robert W Schefer. Effect of syngas composition and co2-diluted oxygen on performance of a premixed swirl-stabilized combustor. *Combustion Science and Technology*, 180(1):64–88, 2007.

[62] Fengsham Liu, Hongsheng Guo, and Gregory J Smallwood. The chemical effect of co2 replacement of n2 in air on the burning velocity of ch4 and h2 premixed flames. *Combustion and flame*, 133(4):495–497, 2003.

[63] Tanh Le Cong and Philippe Dagaut. Effect of water vapor on the kinetics of combustion of hydrogen and natural gas: experimental and detailed modeling study. In *ASME Turbo Expo 2008: Power for Land, Sea, and Air*, pages 319–328. American Society of Mechanical Engineers, 2008.

[64] Mara Abin, Jorge Gimnez-Lpez, Rafael Bilbao, and Mara U. Alzueta. Effect of different concentration levels of {CO2} and {H2O} on the oxidation of co: Experiments and modeling. *Proceedings of the Combustion Institute*, 33(1):317 – 323, 2011.

[65] P. GLARBORG, D. KUBEL, P. G. KRISTENSEN, J. HANSEN, and K. DAM-JOHANSEN. Interactions of co, nox and h2o under post-flame conditions. *Combustion Science and Technology*, 110-111(1):461–485, 1995.

[66] Kaoru Maruta, Kazuki Abe, Susumu Hasegawa, Shigenao Maruyama, and Junichi Sato. Extinction characteristics of ch4/co2 versus o2/co2 counterflow non-premixed flames at elevated pressures up to 0.7 mpa. *Proceedings of the Combustion Institute*, 31(1):1223–1230, 2007.

[67] Lei Chen, Sze Zheng Yong, and Ahmed F Ghoniem. Oxy-fuel combustion of pulverized coal: Characterization, fundamentals, stabilization and cfd modeling. *Progress in Energy and Combustion Science*, 38(2):156–214, 2012.

[68] Yiguang Ju, Goro Masuya, and Paul D Ronney. Effects of radiative emission and absorption on the propagation and extinction of premixed gas flames. In

Symposium (international) on combustion, volume 27, pages 2619–2626. Elsevier, 1998.

[69] H Guo, Y Ju, K Maruta, T Niioka, and Fengshan Liu. Numerical investigation of ch4/co2/air and ch4/co2/o2 counterflow premixed flames with radiation reabsorption. *Combustion science and technology*, 135:49–64, 1998.

[70] Jiongming Ruan, Hideaki Kobayashi, Takashi Niioka, and Yiguang Ju. Combined effects of nongray radiation and pressure on premixed ch¡ sub¿ 4¡/sub¿/o¡ sub¿ 2¡/sub¿/co¡ sub¿ 2¡/sub¿ flames. *Combustion and Flame*, 124(1):225–230, 2001.

[71] Zheng Chen, Xiao Qin, Bo Xu, Yiguang Ju, and Fengshan Liu. Studies of radiation absorption on flame speed and flammability limit of co2 diluted methane flames at elevated pressures. *Proceedings of the Combustion Institute*, 31(2):2693–2700, 2007.

[72] Klas Andersson and Filip Johnsson. Flame and radiation characteristics of gas-fired o2/co2 combustion. *Fuel*, 86(5):656–668, 2007.

[73] Chungen Yin, Lasse A Rosendahl, and Søren K Kær. Chemistry and radiation in oxy-fuel combustion: A computational fluid dynamics modeling study. *Fuel*, 90(7):2519–2529, 2011.

[74] Sivaji Seepana and Sreenivas Jayanti. Flame structure and no generation in oxy-fuel combustion at high pressures. *Energy Conversion and Management*, 50(4):1116–1123, 2009.

[75] A Amato, B Hudak, P DSouza, P DCarlo, D Noble, D Scarborough, J Seitzman, and T Lieuwen. Measurements and analysis of co and o¡ sub¿ 2¡/sub¿ emissions in ch¡ sub¿ 4¡/sub¿/co¡ sub¿ 2¡/sub¿/o¡ sub¿ 2¡/sub¿ flames. *Proceedings of the Combustion Institute*, 33(2):3399–3405, 2011.

[76] C.Y. Liu, G. Chen, N. Sipcz, M. Assadi, and X.S. Bai. Characteristics of oxy-fuel combustion in gas turbines. *Applied Energy*, 89(1):387 – 394, 2012. Special issue on Thermal Energy Management in the Process Industries.

[77] Charles K Westbrook and Frederick L Dryer. Simplified reaction mechanisms for the oxidation of hydrocarbon fuels in flames. *Combustion science and technology*, 27(1-2):31–43, 1981.

[78] WP Jones and RP Lindstedt. Global reaction schemes for hydrocarbon combustion. *Combustion and Flame*, 73(3):233–249, 1988.

[79] Faravelli T. Frassoldati A. Granata S. Ranzi, E. Wide range kinetic modeling study of the pyrolysis, partial oxydation and combustion of heavy n-alkanes. *Industrial and Engineering Chemistry Research*, 44:5170–5183, 2005.

[80] Chiara Galletti, Giovanni Coraggio, and Leonardo Tognotti. Numerical investigation of oxy-natural-gas combustion in a semi-industrial furnace: Validation of cfd sub-models. *Fuel*, 109:445–460, 2013.

[81] MA Habib, R Ben-Mansour, HM Badr, SF Ahmed, and AF Ghoniem. Computational fluid dynamic simulation of oxyfuel combustion in gas-fired water tube boilers. *Computers & Fluids*, 56:152–165, 2012.

[82] LCR Johansen. *RANS Simulation of Oxy-Natural Gas Combustion.* PhD thesis, MS Thesis, Aalborg University, Denmark, 2010.

[83] P Jourdaine, C Mirat, J Beaunier, Y Joumani, and T Schuller. A comparison of the structure of N2 and CO2 diluted CH4/O2 premixed flames in a swirled combustor. In *Proceedings of the European Combustion Meeting 2015.*

[84] Jon Runyon, Richard Marsh, Agustin Valera-Medina, Anthony Giles, Steve Morris, Daniel Pugh, Yura Sevcenco, and Phil Bowen. Methane-oxygen flame stability in a generic premixed gas turbine swirl combustor at varying thermal power and pressure. In *ASME Turbo Expo 2015: Turbine Technical Conference and Exposition*, pages V04BT04A043–V04BT04A043. American Society of Mechanical Engineers, 2015.

[85] Gaurav Kewlani, Zachary Labry, Neerav Abani, Santosh Shanbhogue, and Ahmed Ghoniem. Large eddy simulations and experimental investigation of flow in a swirl stabilized combustor. In *50th AIAA Aerospace Sciences Meeting including the New Horizons Forum and Aerospace Exposition.* American Institute of Aeronautics and Astronautics, 2012.

[86] Gaurav Kewlani, Konstantina Vogiatzaki, Santosh Shanbhogue, and Ahmed F Ghoniem. Validation study of large-eddy simulations of wake stabilized reacting flows using artificial flame thickening approaches. In *51st AIAA Aerospace Sciences Meeting including the New Horizons Forum and Aerospace Exposition*, page 169, 2013.

[87] Gaurav Kewlani, Santosh Shanbhogue, and Ahmed Ghoniem. Investigations into the impact of the equivalence ratio on turbulent premixed combustion using particle image velocimetry and large eddy simulation techniques:v and m flame configurations in a swirl combustor. *Energy & Fuels*, 30(4):3451–3462, 2016.

[88] O Colin, F Ducros, D Veynante, and Thierry Poinsot. A thickened flame model for large eddy simulations of turbulent premixed combustion. *Physics of Fluids (1994-present)*, 12(7):1843–1863, 2000.

[89] Shenghong Huang and QS Li. A new dynamic one-equation subgrid-scale model for large eddy simulations. *International Journal for Numerical Methods in Engineering*, 81(7):835–865, 2010.

[90] Thierry Poinsot and Denis Veynante. *Theoretical and numerical combustion.* RT Edwards, Inc., 2005.

[91] Jean-Philippe Legier, Thierry Poinsot, and Denis Veynante. Dynamically thickened flame les model for premixed and non-premixed turbulent combustion. In *Proc. of the summer program*, pages 157–168, 2000.

[92] Gaurav Kewlani. *Large eddy simulations of premixed turbulent flame dynamics: combustion modeling, validation and analysis.* PhD thesis, Massachusetts Institute of Technology, 2014.

[93] Ludovic Durand and Wolfgang Polifke. Implementation of the thickened flame model for large eddy simulation of turbulent premixed combustion in a commercial solver. In *ASME Turbo Expo 2007: Power for Land, Sea, and Air*, pages 869–878. American Society of Mechanical Engineers, 2007.

[94] A Hosseinzadeh, A Sadiki, and J Janicka. Assessment of the dynamic sgs wrinkling combustion modeling using the thickened flame approach coupled with fgm tabulated detailed chemistry. *Flow, Turbulence and Combustion*, 96(4):939–964, 2016.

[95] R Mercier, TF Guiberti, A Chatelier, D Durox, O Gicquel, N Darabiha, T Schuller, and B Fiorina. Experimental and numerical investigation of the influence of thermal boundary conditions on premixed swirling flame stabilization. *Combustion and Flame*, 171:42–58, 2016.

[96] Yongliang Xie, Jinhua Wang, Meng Zhang, Jing Gong, Wu Jin, and Zuohua Huang. Experimental and numerical study on laminar flame characteristics of methane oxy-fuel mixtures highly diluted with co2. *Energy & Fuels*, 27(10):6231–6237, 2013.

[97] Beth Anne V Bennett, Zhongxian Cheng, Robert W Pitz, and Mitchell D Smooke. Computational and experimental study of oxygen-enhanced axisymmetric laminar methane flames. *Combustion Theory and Modelling*, 12(3):497–527, 2008.

[98] Karnam Bhadraiah and Vasudevan Raghavan. Numerical simulation of laminar co-flow methane–oxygen diffusion flames: effect of chemical kinetic mechanisms. *Combustion Theory and Modelling*, 15(1):23–46, 2010.

[99] Hirotatsu Watanabe, Santosh J. Shanbhogue, and Ahmed F. Ghoniem. Impact of equivalence ratio on the macrostructure of premixed swirling CH4/Air and CH4/O2/CO2 flames. *Proceedings of ASME Turbo Expo*, (GT2015-43224), 2015.

[100] Peter Kutne, Bhavin K Kapadia, Wolfgang Meier, and Manfred Aigner. Experimental analysis of the combustion behaviour of oxyfuel flames in a gas turbine model combustor. *Proceedings of the Combustion Institute*, 33(2):3383–3390, 2011.

[101] Kyu Tae Kim, Jong Guen Lee, Hyung Ju Lee, Bryan D Quay, and Domenic A Santavicca. Characterization of forced flame response of swirl-stabilized turbulent lean-premixed flames in a gas turbine combustor. *Journal of Engineering for Gas Turbines and Power*, 132(4):041502, 2010.

[102] TF Guiberti, D Durox, P Scouflaire, and T Schuller. Impact of heat loss and hydrogen enrichment on the shape of confined swirling flames. *Proceedings of the Combustion Institute*, 2014.

[103] Soufien Taamallah, Zachary A. LaBry, Santosh J. Shanbhogue, and Ahmed F. Ghoniem. Thermo-acoustic instabilities in lean premixed swirl-stabilized combustion and their link to acoustically coupled and decoupled flame macrostructures. *Proceedings of the Combustion Institute*, 35(3):3273 – 3282, 2015.

[104] Ulrich Stopper, Wolfgang Meier, Rajesh Sadanandan, Michael Stohr, Manfred Aigner, and Ghenadie Bulat. Experimental study of industrial gas turbine flames including quantification of pressure influence on flow field, fuel/air premixing and flame shape. *Combustion and Flame*, 160(10):2103–2118, 2013.

[105] I. Chterev, C. W. Foley, D. Foti, S. Kostka, A. W. Caswell, N. Jiang, A. Lynch, D. R. Noble, S. Menon, J. M. Seitzman, and T. C. Lieuwen. Flame and flow topologies in an annular swirling flow. *Combustion Science and Technology*, 186(8):1041–1074, 2014.

[106] Thibault F. Guiberti, Daniel Durox, Laurent Zimmer, and Thierry Schuller. Analysis of topology transitions of swirl flames interacting with the combustor side wall. *Combustion and Flame*, 162(11):4342 – 4357, 2015.

[107] SJ Shanbhogue, YS Sanusi, S Taamallah, MA Habib, EMA Mokheimer, and AF Ghoniem. Flame macrostructures, combustion instability and extinction strain scaling in swirl-stabilized premixed ch 4/h 2 combustion. *Combustion and Flame*, 163:494–507, 2016.

[108] CHEMKIN-PRO Release. 15101, reaction design. *Inc., San Diego, CA*, 2010.

[109] Teresa Mendiara and Peter Glarborg. Ammonia chemistry in oxy-fuel combustion of methane. *Combustion and Flame*, 156(10):1937–1949, 2009.

[110] Soufien Taamallah, Santosh J. Shanbhogue, Yinka S. Sanusi, Esmail M.A. Mokhiemer, and Ahmed F. Ghoniem. Transition from a single to a double flame structure in swirling reacting flows: mechanism, dynamics, and effect of thermal boundary conditions. In *ASME Turbo Expo 2015 - Montreal, Canada. GT2015-43998*. ASME, 2015.

[111] Robert J Kee, Fran M Rupley, and James A Miller. Chemkin-ii: A fortran chemical kinetics package for the analysis of gas-phase chemical kinetics. Technical report, Sandia National Labs., Livermore, CA (USA), 1989.

[112] Tariq Shamim. Effect of unequal fuel and oxidizer lewis numbers on flame dynamics. *International journal of thermal sciences*, 45(12):1213–1223, 2006.

[113] Fengshan Liu, Gregory J Smallwood, ÖL Gülder, and Y Ju. Asymptotic analysis of radiative extinction in counterflow diffusion flames of nonunity lewis numbers. *Combustion and flame*, 121(1):275–287, 2000.

[114] CK Law and SH Chung. Steady state diffusion flame structure with lewis number variations. *Combustion Science and Technology*, 29(3-6):129–145, 1982.

[115] Klas Andersson, Robert Johansson, Filip Johnsson, and Bo Leckner. Radiation intensity of propane-fired oxy-fuel flames: implications for soot formation. *Energy & Fuels*, 22(3):1535–1541, 2008.

[116] L Wang, NE Endrud, SR Turns, MD D'agostini, and AG Slavejkov. A study of the influence of oxygen index on soot, radiation, and emission characteristics of turbulent jet flames. *Combustion science and technology*, 174(8):45–72, 2002.

[117] Alon Grinberg Dana, Soumya Gudiyella, William H Green, Santosh J Shanbhogue, Dan Michaels, Nadim W Chakroun, and Ahmed Ghoniem. Automated generation of chemical mechanisms for predicting extinction strain rates with applications in flame stabilization and combustion instabilities. In *55th AIAA Aerospace Sciences Meeting*, page 0835, 2017.

[118] Tanh Le Cong and Philippe Dagaut. Oxidation of h2/co2 mixtures and effect of hydrogen initial concentration on the combustion of {CH4} and ch4/co2 mixtures: Experiments and modeling. *Proceedings of the Combustion Institute*, 32(1):427 – 435, 2009.

[119] Anders Brink, Mikko Hupa, Frederic Breussin, Nicolas Lallemant, and Roman Weber. Modeling of oxy-natural gas combustion chemistry. *Journal of Propulsion and Power*, 16(4):609–614, 2000.

[120] Alon Grinberg Dana, Soumya Gudiyella, William H. Green, Santosh Shanbhogue, Dan Michaels, Nadim W. Chakroun, and Ahmed F. Ghoniem. Automated chemical mechanisms generation for predicting extinction strain rates with applications in flame stabilization and combustion instabilities. In *55th AIAA Aerospace Sciences Meeting*. American Institute of Aeronautics and Astronautics, 2017.

[121] SV Sardeshmukh, C Huang, and WE Anderson. Impact of chemical kinetics on the predictions of bluff body stabilized flames. In *54th AIAA Aerospace Sciences Meeting*, 2016.

[122] A Roux, LYM Gicquel, S Reichstadt, N Bertier, G Staffelbach, F Vuillot, and TJ Poinsot. Analysis of unsteady reacting flows and impact of chemistry description in large eddy simulations of side-dump ramjet combustors. *Combustion and Flame*, 157(1):176–191, 2010.

[123] Pierre Boivin, Antoine Dauptain, Carmen Jiménez, and Bénédicte Cuenot. Simulation of a supersonic hydrogen–air autoignition-stabilized flame using reduced chemistry. *Combustion and Flame*, 159(4):1779–1790, 2012.

[124] Benedetta Franzelli, Eleonore Riber, and Bénédicte Cuenot. Impact of the chemical description on a large eddy simulation of a lean partially premixed swirled flame. *Comptes Rendus Mécanique*, 341(1-2):247–256, 2013.

[125] Zacharias M Nikolaou, Nedunchezhian Swaminathan, and Jyh-Yuan Chen. Evaluation of a reduced mechanism for turbulent premixed combustion. *Combustion and Flame*, 161(12):3085–3099, 2014.

[126] A Sjunnesson, C Nelsson, and E Max. LDA measurements of velocities and turbulence in a bluff body stabilized flame. *Laser Anemometry*, 3:83–90, 1991.

[127] A Sjunnesson, S Olovsson, and B Sjoblom. Validation rig- a tool for flame studies. In *International Symposium on Air Breathing Engines, 10 th, Nottingham, England*, pages 385–393, 1991.

[128] Jongsup Hong, Patrick Kirchen, and Ahmed F Ghoniem. Laminar oxy-fuel diffusion flame supported by an oxygen-permeable-ion-transport membrane. *Combustion and Flame*, 160(3):704–717, 2013.

[129] Medhat A Nemitallah, Gaurav Kewlani, Seunghyuck Hong, Santosh J Shanbhogue, Mohamed A Habib, and Ahmed F Ghoniem. Investigation of a turbulent premixed combustion flame in a backward-facing step combustor; effect of equivalence ratio. *Energy*, 95:211–222, 2016.

[130] Abdulla Ghani, Thierry Poinsot, Laurent Gicquel, and Gabriel Staffelbach. Les of longitudinal and transverse self-excited combustion instabilities in a bluff-body stabilized turbulent premixed flame. *Combustion and Flame*, 162(11):4075–4083, 2015.

[131] Mechanical and Aerospace Engineering (Combustion Research), University of California at San Diego. Chemical-kinetic mechanisms for combustion applications. `http://combustion.ucsd.edu`, 2016.

[132] Adam L Comer, Swanand Sardeshmukh, Brent A Rankin, Matthew E Harvazinski, and Venkateswaran Sankaran. Grid convergence studies of bluff body stabilized turbulent premixed combustion. In *55th AIAA Aerospace Sciences Meeting*, page 0377, 2017.

[133] Hao Wu, Peter C Ma, Yu Lv, and Matthias Ihme. Mvp-workshop contribution: Modeling of volvo bluff flame experiment and comparison of finite-volume and discontinuous-galerkin schemes. In *55th AIAA Aerospace Sciences Meeting, AIAA SciTech Forum, AIAA*, volume 1573, 2017.

[134] I Glassman. Combustion, academic press orlando fl. 1987.

[135] RR Erickson and MC Soteriou. The influence of reactant temperature on the dynamics of bluff body stabilized premixed flames. *Combustion and Flame*, 158(12):2441–2457, 2011.

[136] Benjamin Emerson, Jacqueline OConnor, Matthew Juniper, and Tim Lieuwen. Density ratio effects on reacting bluff-body flow field characteristics. *Journal of Fluid Mechanics*, 706:219–250, 2012.

[137] Eugenio Giacomazzi, Valerio Battaglia, and Claudio Bruno. The coupling of turbulence and chemistry in a premixed bluff-body flame as studied by les. *Combustion and Flame*, 138(4):320–335, 2004.

[138] Christopher Foley, Ianko Chterev, Bobby Noble, Jerry Seitzman, and Tim Lieuwen. Shear layer flame stabilization sensitivities in a swirling flow. *International Journal of Spray and Combustion Dynamics*, 9(1):3–18, 2017.

[139] Ianko Chterev, Daniel Foti, Jerry Seitzman, Suresh Menon, and Tim Lieuwen. Flow field characterization in a premixed, swirling annular flow. *AIAA Paper*, (2012-0450), 2012.

[140] I Chterev, CW Foley, D Foti, S Kostka, AW Caswell, N Jiang, A Lynch, DR Noble, S Menon, JM Seitzman, et al. Flame and flow topologies in an annular swirling flow. *Combustion Science and Technology*, 186(8):1041–1074, 2014.

[141] Luis Tay-Wo-Chong, Mathieu Zellhuber, Thomas Komarek, Hong G Im, and Wolfgang Polifke. Combined influence of strain and heat loss on turbulent premixed flame stabilization. *Flow, Turbulence and Combustion*, 97(1):263–294, 2016.

[142] F Proch and AM Kempf. Modeling heat loss effects in the large eddy simulation of a model gas turbine combustor with premixed flamelet generated manifolds. *Proceedings of the Combustion Institute*, 35(3):3337–3345, 2015.

[143] AJ Aspden, MS Day, and JB Bell. Turbulence–flame interactions in lean premixed hydrogen: transition to the distributed burning regime. *Journal of Fluid mechanics*, 680:287–320, 2011.

[144] Jaesung Kwon, Yeongdo Park, and Kang Y Huh. Flamelet characteristics at the leading edge and through the flame brush of statistically steady incompressible turbulent premixed flames. *Combustion and Flame*, 164:85–98, 2016.

[145] Simon Lapointe, Bruno Savard, and Guillaume Blanquart. Differential diffusion effects, distributed burning, and local extinctions in high karlovitz premixed flames. *Combustion and Flame*, 162(9):3341–3355, 2015.

[146] Bruno Savard, Brock Bobbitt, and Guillaume Blanquart. Structure of a high karlovitz n-c 7 h 16 premixed turbulent flame. *Proceedings of the Combustion Institute*, 35(2):1377–1384, 2015.

[147] Qingguo Zhang, Santosh J Shanbhogue, Shreekrishna, Tim Lieuwen, and Jacqueline O'Connor. Strain characteristics near the flame attachment point in a swirling flow. *Combustion Science and Technology*, 183(7):665–685, 2011.

[148] Brock Bobbitt, Simon Lapointe, and Guillaume Blanquart. Vorticity transformation in high karlovitz number premixed flames. *Physics of Fluids*, 28(1):015101, 2016.

[149] JC Pan, MD Vangsness, and DR Ballal. Aerodynamics of bluff body stabilized confined turbulent premixed flames. In *ASME 1991 International Gas Turbine and Aeroengine Congress and Exposition*, pages V003T06A019–V003T06A019. American Society of Mechanical Engineers, 1991.